# GEOCHEMICAL MODELLING OF FLUID – ROCK INTERACTIONS IN AKKÖY AND EDREMİT GEOTHERMAL FIELDS (WESTERN ANATOLIA) AS PROSPECTIVE $CO_2$ STORAGE SITES

A THESIS SUBMITTED TO
THE GRADUATE SCHOOL OF NATURAL AND APPLIED SCIENCES
OF
MIDDLE EAST TECHNICAL UNIVERSITY

BY

SANEM ELİDEMİR

IN PARTIAL FULFILLMENT OF THE REQUIREMENTS
FOR
THE DEGREE OF DOCTOR OF PHILOSOPHY
IN
GEOLOGICAL ENGINEERING

MAY 2024

Approval of the thesis:

# GEOCHEMICAL MODELLING OF FLUID – ROCK INTERACTIONS IN AKKÖY AND EDREMİT GEOTHERMAL FIELDS (WESTERN ANATOLIA) AS PROSPECTIVE $CO_2$ STORAGE SITES

submitted by **SANEM ELİDEMİR** in partial fulfillment of the requirements for the degree of **Doctor of Philosophy** in **Geological Engineering, Middle East Technical University** by,

Prof. Dr. Naci Emre Altun
Dean, **Graduate School of Natural and Applied Sciences**

Prof. Dr. Erdin Bozkurt
Head of the Department, **Geological Engineering**

Prof. Dr. Nilgün Güleç
Supervisor, **Geological Engineering, METU**

**Examining Committee Members:**

Prof. Dr. Yusuf Kağan Kadıoğlu
Geological Engineering, Ankara University

Prof. Dr. Nilgün Güleç
Geological Engineering, METU

Assoc. Prof. Dr. Fatma Toksoy Köksal
Geological Engineering, METU

Assoc. Prof. Dr. Özgür Avşar
Geological Engineering, Muğla Sıtkı Koçman Uni.

Assist. Prof. Dr. Ali İmer
Geological Engineering, METU

Date: 15.05.2024

**I hereby declare that all information in this document has been obtained and presented in accordance with academic rules and ethical conduct. I also declare that, as required by these rules and conduct, I have fully cited and referenced all material and results that are not original to this work.**

Name Last name : Sanem Elidemir

Signature :

# ABSTRACT

## GEOCHEMICAL MODELLING OF FLUID – ROCK INTERACTIONS IN AKKÖY AND EDREMİT GEOTHERMAL FIELDS (WESTERN ANATOLIA) AS PROSPECTIVE $CO_2$ STORAGE SITES

Elidemir, Sanem
Doctor of Philosophy, Geological Engineering
Supervisor: Prof. Dr. Nilgün Güleç

May 2024, 250 pages

Lithogeochemical and hydrogeochemical characterizations of two geothermal fields located in western Anatolian region (Akköy – Denizli and Edremit – Balıkesir) are performed to simulate the $CO_2$-fluid-rock interactions in the systems through geochemical modelling studies.

Drill cuttings obtained from the fields are investigated in terms of their petrographic features, mineral compositions and elemental variations with depth. Calcareous rocks (marble/limestone/calcschist) and granitic rocks constitute the dominant rock fragments in the samples of Akköy and Edremit, respectively. Main mineral phases in Akköy include quartz, calcite and clay minerals whereas in Edremit, along with quartz, feldspars, micas, carbonates and amphiboles are the dominant phases. Hydrogeochemical analyses reveal that the hot waters are of $Na+K-HCO_3-SO_4$ type in Akköy and of $Na+K–SO_4$ type in Edremit field.

The results have led to the geochemical assessment of two fields as potential sites for $CO_2$ storage in the context of $CO_2$-fluid-rock interactions with the utilization of geochemical simulations performed by PHREEQC software. Modelling studies of Akköy samples point to ankerite as the principal carbonate phase that can trap $CO_2$. In Edremit, mineral trapping mainly occurs through the precipitation of dolomite. Clay mineral abundance seems to prolong the reaction times and smectite presence, in particular, increases the propagation distance. Due to the mineralogical differences, the reactions in Edremit samples are shorter both temporally and spatially than in Akköy. The geochemical outcome of a $CO_2$ addition to a system (e.g. trapping mechanisms) seems to be closely interconnected to the composition and assemblage of minerals in the reservoir.

Keywords: $CO_2$ Storage, Fluid-Rock Interactions, Geochemical Modelling, Lithogeochemistry, Hydrogeochemistry

# ÖZ

## OLASI $CO_2$ DEPOLAMA ALANLARI OLARAK AKKÖY VE EDREMİT JEOTERMAL SAHALARINDAKİ (BATI ANADOLU) AKIŞKAN – KAYAÇ ETKİLEŞİMLERİNİN JEOKİMYASAL MODELLEMESİ

Elidemir, Sanem
Doktora, Jeoloji Mühendisliği
Tez Yöneticisi: Prof. Dr. Nilgün Güleç

Mayıs 2024, 250 sayfa

Batı Anadolu bölgesinde bulunan iki jeotermal saha (Akköy – Denizli ve Edremit – Balıkesir), jeokimyasal modelleme çalışmaları yoluyla $CO_2$-akışkan-kayaç etkileşimleri simüle edilmek üzere litojeokimyasal ve hidrojeokimyasal olarak karekterize edilmiştir.

Sahalardan elde edilen kırıntı kayaç örnekleri, petrografik özellikler, mineral bileşimleri ve elementlerin derinliğe göre değişimleri bakımından incelenmiştir. Kalkerli kayaçlar (mermer/kireçtaşı/kalkşist) ve granitik kayaçlar sırasıyla Akköy ve Edremit sahalarına ait örneklerde egemen kırıntıları oluşturmaktadır. Ana mineral fazları Akköy'de kuvars, kalsit ve kil mineralleri iken, Edremit'teki hakim fazlar kuvarsın yanı sıra feldispat, mika, karbonat ve amfibol mineralleridir. Hidrojeokimyasal çalışmalar sıcak suların Akköy'de Na+K-$HCO_3$-$SO_4$ tipinde, Edremit'te Na+K–$SO_4$ tipinde olduğunu ortaya koymuştur.

Elde edilen sonuçlar bu iki sahanın olası $CO_2$ depolama sahaları olarak, $CO_2$-akışkan-kayaç etkileşimleri kapsamında, PHREEQC yazılımı ile yapılan jeokimyasal simülasyonlar aracılığıyla değerlendirilmelerini sağlamıştır. Akköy örnekleri üzerinde gerçekleştirilen modelleme çalışmaları, $CO_2$’nin tutulumunu sağlayan ana karbonat fazının ankerit olduğunu göstermiştir. Edremit’teki mineral kapanlanması ise başlıca dolomit çökelmesi yoluyla gerçekleşmiştir. Kil minerallerinin oranlarının artmasıyla reaksiyon sürelerinin uzadığı gözlemlenmiş ve özellikle smektitin varlığı reaksiyonların ilerleme mesafesini arttırmıştır. Mineralojik farklılıklardan dolayı, Edremit örneklerindeki reaksiyonların Akköy’e göre daha kısa süre ve mesafede gerçekleştiği belirlenmiştir. Bir sisteme eklenen $CO_2$’nin jeokimyasal akıbetinin (örn. kapanlanma mekanizmaları), rezervuardaki minerallerin bileşimlerine ve birlikte bulundukları mineral grubuna yakından bağlı olduğu görülmüştür.

Anahtar Kelimeler: $CO_2$ Depolama, Akışkan-Kayaç Etkileşimleri, Jeokimyasal Modelleme, Litojeokimya, Hidrojeokimya

Everything not saved will be lost.

*– Nintendo "Quit Screen" message*

# ACKNOWLEDGEMENTS

The realization of this challenging academic journey would not be possible without my supervisor, Dr. Nilgün Güleç. I consider myself privileged to have the chance to study under her guidance. Being a true mentor, she not only shared her exceptional scientific knowledge, but also insights from her life experiences which I deeply appreciate. I have learned precious lessons from her enthusiasm, discipline and wisdom.

I am indebted to Dr. Yusuf Kağan Kadıoğlu for his invaluable contributions, continuous support and encouragement. A significant part of this thesis would not be achievable without his guidance. I would like to thank Dr. Nurkan Karahanoğlu for his helpful remarks and support. I would like to express my gratitude to Dr. Özgür Avşar, Dr. Tamer Koralay, Pekdemir Seracılık and Edremit Jeotermal A.Ş. for sample provision.

Special thanks go to Dr. Kıymet Deniz Yağcıoğlu for her support, efforts and constructive comments.

I would like to thank Dr. Çağıl Kolat for her support and positivity. I will miss our comforting breaks with Nilgün Hoca.

My beloved friends Gamze, Seda, Çidem, Duygu, Görkem, Faruk, Zeynep, Barış, Bahadır deserve special thanks for cheering me up and encouraging me.

I would like to thank my colleagues in MTA who supported me; especially Taha Çapanoğlu, Oktay Çelmen, Uğur Ören, Engin Purtul.

I am deeply grateful for the infinite love, encouragement and understanding from my family. I especially want to thank my mother and my little tiger Sushi for always being there for me.

Finally, I would like to thank my husband, Uğurcan Özçamur, for all the love, courage and serenity. I am sincerely grateful for all the joyful moments in our lives and looking forward to creating more.

This thesis study is partially funded by Scientific and Technological Research Council of Turkiye under grant number TUBİTAK 119Y350.

# TABLE OF CONTENTS

CHAPTERS

APPENDICES

# LIST OF TABLES

TABLES

# LIST OF FIGURES

FIGURES

# CHAPTER 1

# INTRODUCTION

$CO_2$ Capture and Storage (CCS) is proved to be one of the most effective measures for the mitigation of the destructive effects of anthropogenic $CO_2$ emissions on climate change. The implementation of CCS in geothermal fields as deep saline aquifers can contribute both to reduce the $CO_2$ emissions and to increase the energy production within the context of Enhanced Geothermal Systems (EGS). The understanding and application of this technology are particularly critical for Turkiye which has a substantial geothermal energy potential. Turkish geothermal systems which have considerably higher $CO_2$ emissions than the global average, include $CO_2$ as the dominant component of gas phases in many of the reservoirs, creating the necessity to tend towards CCS as a feasible solution.

Given the limitations of experimental studies regarding the time span and reservoir conditions, the geochemical modelling studies are highly important in the CCS projects. Equilibrium, kinetic and reactive transport modelling are the methods which are used to determine the potential $CO_2$-fluid-rock interactions, to interpret the temporal and spatial behaviour of $CO_2$ in the system and to predict the fate of $CO_2$. The necessary input parameters for these simulations are i) modal mineralogy of the reservoir rocks and ii) hydrogeochemistry of the reservoir fluid. The quality of the input data can determine the accuracy of a geochemical model. To be able to construct a dataset, two geothermal fields selected from Western Anatolia (Akköy – Denizli and Edremit – Balıkesir) are thoroughly assessed in terms of their lithologic and hydrogeochemical properties as potential sites for EGS.

Lithogeochemical analyses are focused on the drill cuttings obtained from PS-1, PS-2 (Akköy field) and EDJ-12 (Edremit field) wells. The samples that belong to the various depths of the wells are studied macroscopically and microscopically for their mineralogic-petrographic properties, followed by the techniques of X-Ray Diffraction (XRD), Confocal Raman Spectroscopy (CRS) and Electron Probe Micro Analysis (EPMA) for detailed mineral characterizations. X-Ray Fluorescence (XRF) analyses are conducted for the examination of the elemental changes with depth. These analyses have led to the identification and quantification of mineral phases in the samples which distinctly affect the modelling results.

Hydrogeochemical characterization for Akköy geothermal field is performed through the analysis of two water samples collected from PS-1 well. The results provide an understanding regarding hydrogeochemical facies, hydrothermal effect of the water-rock interactions, possible reservoir temperature, source of fluids and scaling potential of the system. For Edremit geothermal field, on the other hand, since hydrogeochemical characterization of the field has been previously studied by Avşar et al. (2013), the results in their work are directly used in this thesis study.

In addition to the establishment of a complete dataset for relevant fields, lithogeochemical and hydrogeochemical studies complement each other by contributing to the knowledge on the systems with distinct information. The results are compiled to be used in geochemical modelling performed with PHREEQC software. Dominant reactions in each sample that occur with $CO_2$ addition to the system, are determined with equilibrium modelling results. These reactions are then investigated according to the temporal and spatial variations they may display and whether $CO_2$ is potentially stored in the reservoir by any of the trapping mechanisms. The results allow the interpretation of Akköy and Edremit geothermal fields in terms of $CO_2$-fluid-rock interactions.

## 1.1 Purpose and Scope

This thesis study is focused on the assessment of the fluid-rock interactions in two selected geothermal fields in the possible scenario of $CO_2$ injection to the systems. The main aim of this study is to geochemically characterize and model Akköy and

Edremit fields from Turkiye as potential sites for EGS. In this regard, rock and water samples are collected from the relevant fields. This approach is followed by the geochemical-mineralogical investigations on rock samples and hydrogeochemical and isotopic analyses of the water samples. Compiling the results of the analyses as input data, the potential geochemical reactions in the systems are identified and simulated in the context of $CO_2$-fluid-rock interactions with geochemical modelling studies which include batch model (equilibrium and kinetic modelling), integrated with reactive transport model.

## 1.2 Geographic Setting

Western Anatolia is the host for the numerous important geothermal fields of Turkiye which are distributed on the approximately E-W trending fault bounded basins (grabens). Two of these fields, Akköy and Edremit, are studied in this thesis.

Akköy geothermal field is situated in the relatively southern part of Western Anatolia and its location is in between Sarayköy and Akköy towns in Denizli province. Rock and water samples of two geothermal wells, PS-1 (676137 E, 4205869 N) and PS-2 (669046 E, 4196502 N), that have been drilled in the field are utilized for the lithogeochemical and hydrogeochemical characterization (Fig.1.1). Akköy field neighbours many well-known low to high temperature geothermal fields (e.g. Kızıldere, Tekkehamam, Yenice, Gölemezli, Karahayıt, Pamukkale) surrounding the Denizli Basin which are utilized for numerous purposes, including electricity generation and district heating for many years (Karakuş and Şimşek, 2013; Özgür and Çalışkan, 2014; Alçiçek et al., 2018; Alçiçek et al., 2019).

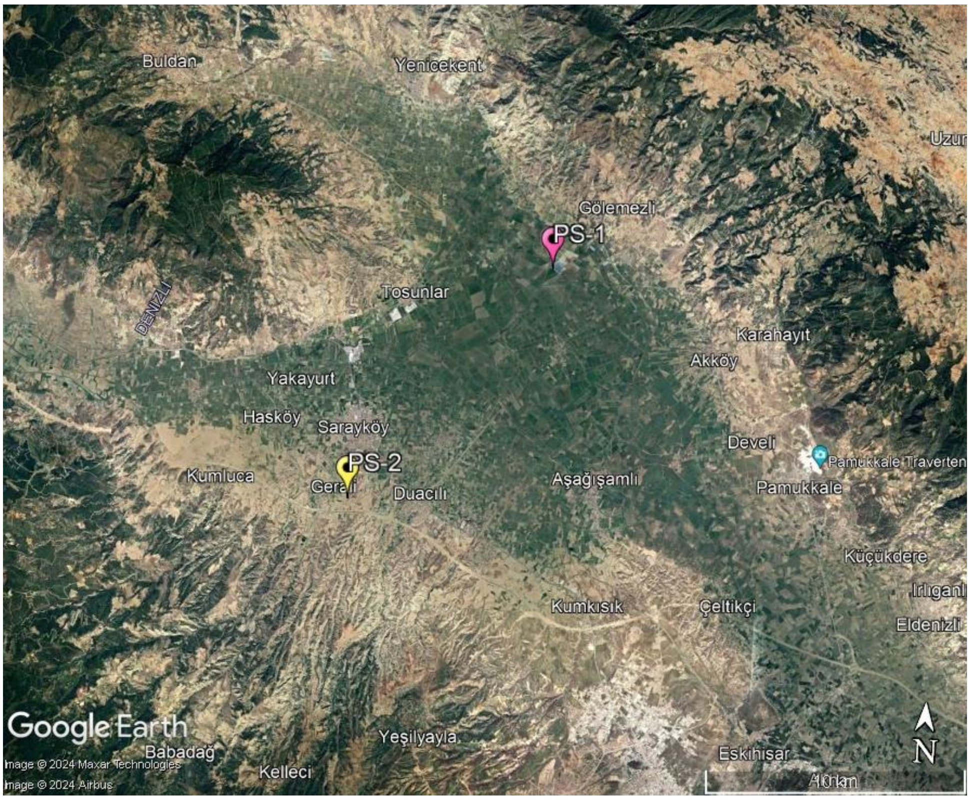

Figure 1.1. Google Earth view of PS-1 & PS-2 well locations

Edremit geothermal field is situated in northwest part of Western Anatolia, to the southwest of Edremit in Balıkesir province. In addition to the studied EDJ-12 well (503535 E, 4378962 N, Fig.1.2), a total of 27 wells have been drilled in the field. The field has been utilized productively over the last decades for district heating and irrigation purposes (Avşar et al., 2015; Edremit Jeotermal, 2018).

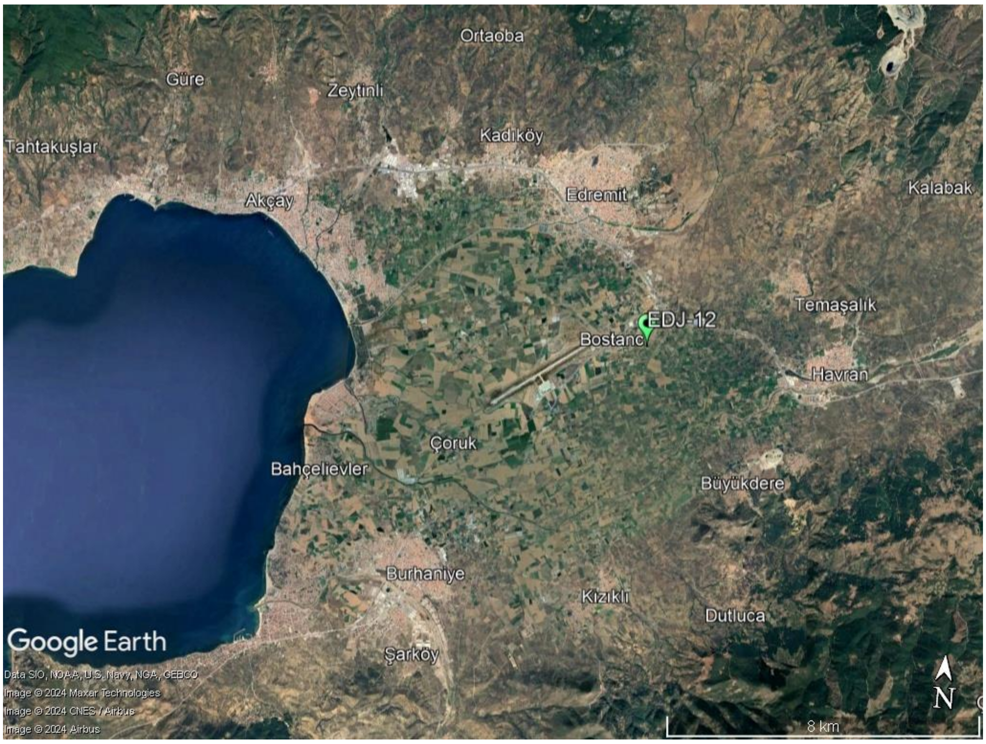

Figure 1.2. Google Earth view of EDJ-12 well location

## 1.3 Materials and Methods

The study was conducted in three main steps as i) sampling, ii) rock and water analyses, iii) data interpretation and modelling.

Drill cuttings were collected from Akköy and Edremit geothermal fields with a total of 109 and 70 samples, respectively. Two water samples were obtained from PS-1 well of Akköy field.

All the samples were geochemically analysed and examined for extensive lithogeochemical and hydrogeochemical characterizations. The analyses performed on the rock samples were macroscopic and microscopic examinations, X-Ray Diffraction (XRD), Confocal Raman Spectroscopy (CRS), Electron Probe Micro Analysis (EPMA) and X-Ray Fluorescence (XRF) techniques. The geochemical content of the water samples were determined with wet chemical methods (ion chromatography, colorimetric analysis, titration) and Inductively Coupled Plasma Mass Spectrometry (ICP-MS). Thermo Finnigan DeltaPlus XP Isotope Ratio Mass Spectrometer (IR-MS) was used for the determination of the isotopic composition. The results from the analyses were utilized as input data for the geochemical modelling studies in order to investigate $CO_2$-fluid-rock interactions in the case for a possible $CO_2$ addition to the system. The software program used in realization of the simulations was the PHREEQC code. Equilibrium, kinetic and reactive transport modelling studies were performed on the samples of both geothermal fields.

## 1.4 Layout of the Thesis

This thesis is divided into 9 chapters. Following this introduction chapter which is Chapter 1;

Chapter 2 is a literature review regarding the fundamental aspects of $CO_2$ storage process in a geochemical perspective.

Chapter 3 presents the geologic and hydrogeologic outline of the studied Akköy and Edremit geothermal fields.

Chapter 4 elaborates the methods used in this study.

Chapter 5 provides the results from the analyses performed for the lithogeochemical characterization of the fields.

Chapter 6 gives the results for hydrogeochemical analyses for Akköy field and the compiled hydrogeochemical information regarding Edremit field.

Chapter 7 is concerned with the investigation of samples and their dominant reactions in both fields in terms of $CO_2$-fluid-rock interactions through geochemical simulations.

Chapter 8 discusses dissolution-precipitation mechanisms and temporal as well as spatial evolutions of the reactions determined from the modelling studies and their significance in relation with $CO_2$ storage.

Chapter 9 summarizes the major conclusions derived from all the performed studies with the comparison of two fields.

# CHAPTER 2

# $CO_2$-FLUID-ROCK INTERACTIONS IN GEOTHERMAL FIELDS IN THE FRAMEWORK OF $CO_2$ STORAGE: A REVIEW

Over the past 250 years, burning of fossil fuels (coal, oil, gas) for power production, heating, industry and transportation has dramatically increased the amount of $CO_2$ emitted into the atmosphere. The atmospheric $CO_2$ concentration which has been reported as 280 ppm in the 19th century, increased up to 424 ppm as of March 2024 (Fig.2.1, Siegenthaler, 1984; Scripps Institution of Oceanography, 2024). This has resulted in the rise of the average global surface temperature by more than 1°C over this period (IPCC, 2018).

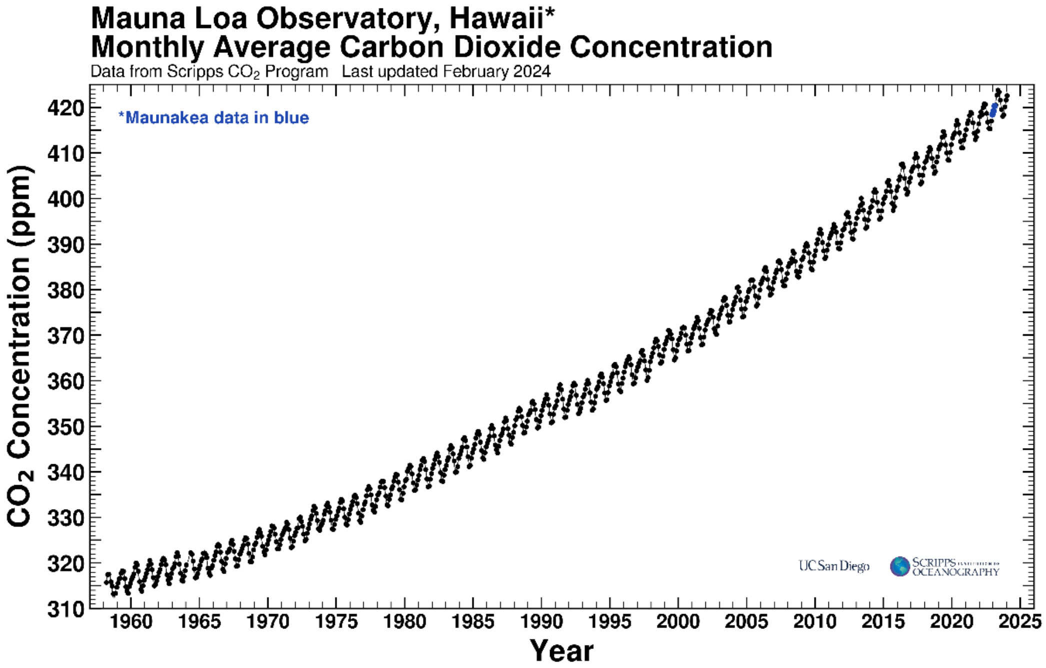

Figure 2.1. Monthly average atmospheric $CO_2$ concentration in time recorded at Mauna Loa Observatory (Scripps Institution of Oceanography, 2024)

## 2.1 Carbon Capture and Storage (CCS)

To reduce $CO_2$ emissions and to mitigate the effects of global warming and climate change, Carbon Capture and Storage (CCS) is considered to be one of the major strategies which is a process carried out in several stages: the separation of $CO_2$ from industrial and energy-related sources, the transportation to a storage location and the injection of $CO_2$ into deep geologic formations (such as deep saline aquifers, and depleted or active oil reservoirs) for long-term confinement from the atmosphere (Fig.2.2).

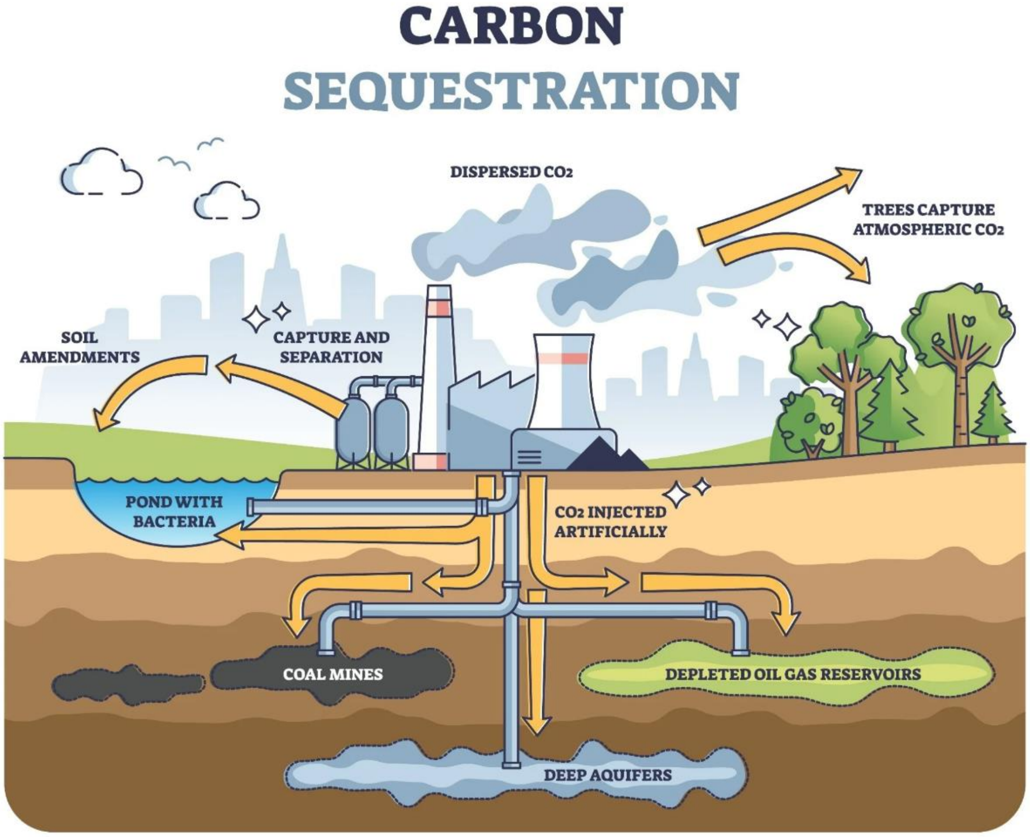

Figure 2.2. Schematic diagram of $CO_2$ storage processes (Wright, 2022)

Studies regarding $CO_2$ injection into subsurface formations started in the early 1970s in Texas, USA as a part of Enhanced Oil Recovery (EOR) project and many research projects have been performed since the 1990s in Europe, the United States, Canada, Australia and Japan. Some of the large-scale projects include, Norway – Sleipner (since 1996), Canada – Weyburn (since 2000), Algeria – In Salah (2004 – 2011), Norway – Snohvit (2007 – 2011), Australia – Otway (since 2008), Germany – Ketzin (2008 – 2009), USA – Cranfield (2009 – 2015) and Canada – Alberta Carbon Trunk Line (since 2018) (IPCC, 2005; Shukla et al., 2010; MIT, 2016; Kalam et al., 2021; $CO_2$GeoNet, 2024). According to the 2016 report of the Global CCS Institute, 38 large-scale worldwide CCS projects have been recorded for that year while in their latest study, a total number of 119 CCS facilities across Europe which involve capture, storage, transport applications have revealed to be in different phases of development (Global CCS Institute, 2016; 2023). Sleipner which is the first commercial-scale storage project started in 1996, demonstrated that a rate of 1 Mt/yr storage of $CO_2$ in saline aquifers is viable and safe (Kelemen et al., 2019). In fact, in the study of Zhang et al. (2022), it is reported that in the years between 1996 and 2020 the estimated cumulative $CO_2$ storage in industrial-scale projects (including EOR and deep saline aquifer injection) is 197 Mt.

Deep saline aquifers constitute one of the potential formations for geologic storage of $CO_2$. Having much larger storage capacity and being widespread than the alternatives, deep saline aquifers are considered to be an effective solution (Fig.2.3). In this regard, geothermal systems started to gain attention as prospective sites for $CO_2$ storage in recent years. $CO_2$ which constitutes the dominant gas phase in most of the geothermal systems, is injected into the reservoir not only to reduce the $CO_2$ emissions to the atmosphere but also to use $CO_2$ as working fluid to increase energy recovery (Enhanced Geothermal Systems, EGS). The potential synergy between $CO_2$ storage and geothermal energy utilization has been investigated in many studies (e.g. Randolph and Saar, 2011; Saar et al., 2015; Tutolo et al., 2015; Elidemir ve Güleç, 2018; Avanthi Isaka et al., 2019; Esteves et al., 2019).

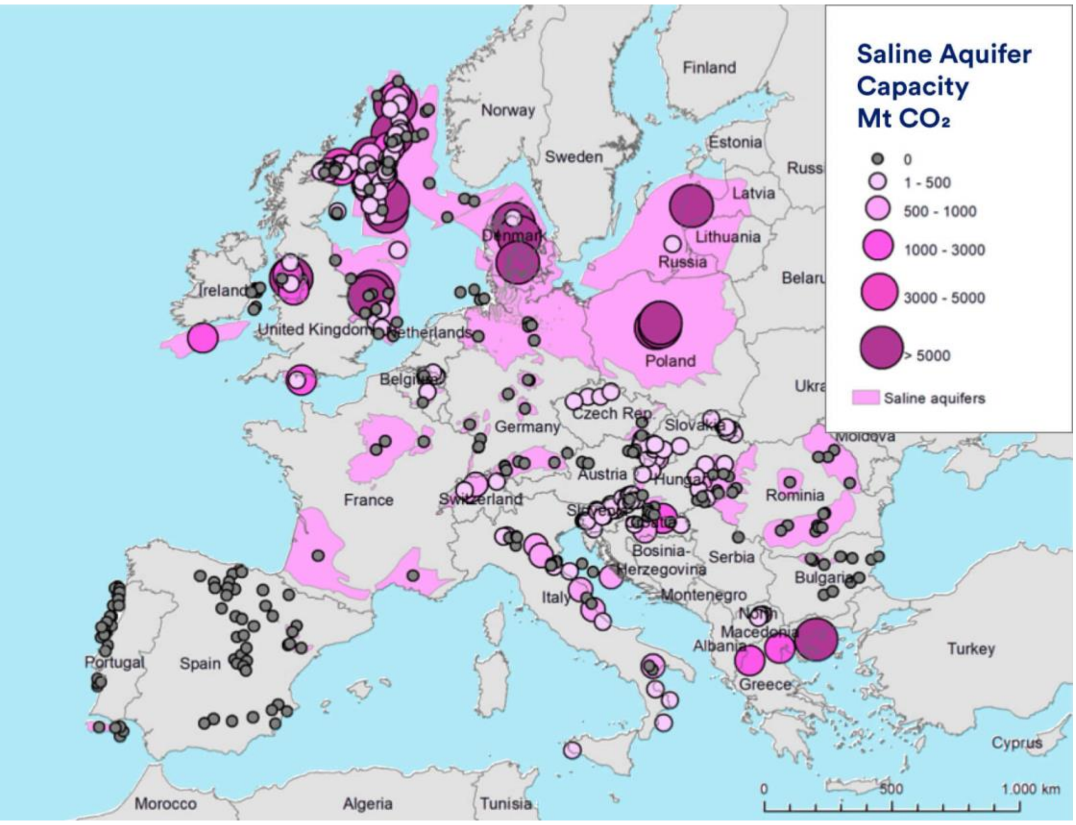

Figure 2.3. Locations of saline aquifers and associated storage capacities in Europe (Anthonsen and Christensen, 2021 in Grove, 2021)

## 2.2 The Fate of $CO_2$ in the Reservoir

The geochemical assessment of $CO_2$-fluid-rock interactions is an essential part of CCS, as both the movement and entrapment of $CO_2$ depend on the geochemical characteristics of the reservoir.

When $CO_2$ is injected into the reservoir, it initially fills the fractures and pore spaces of the permeable formation then, it slowly rises towards an impermeable layer (caprock). In time, $CO_2$ may dissolve into the reservoir fluid and/or may react with the host rocks leading to geochemical changes in the mineralogic as well as the hydrologic properties of the reservoir. These changes take place heterogeneously and they may have either positive or negative impact on the storage operation due to the complex relationship of multitude factors such as aquifer characteristics (porosity, permeability, mineral reactive surface areas, areal extent and thickness of the reservoir), injection rate and duration, number of the injection wells, injection strategy (Lamy-Chappuis et al., 2014; Bachu, 2015; Bensinger and Beckingham, 2020; Al-Khdheeawi et al., 2021; Wang et al., 2021; Gao et al., 2024).

The “storage” of $CO_2$ can be accomplished through various trapping mechanisms that would hold the injected $CO_2$ and prevent it from migrating upwards to the surface. These mechanisms depend on the local geology as well as the reservoir characteristics and may act together if more than one mechanism is present. The trapping mechanisms (Fig.2.4) include i) stratigraphic/structural trapping: traps in which $CO_2$ is trapped by impermeable rock, formed due to lithology change or shift of rocks by a fault, ii) residual trapping: $CO_2$ being stuck in pore spaces due to capillary forces, iii) solubility trapping: dissolution of $CO_2$ in groundwater, and iv) mineral trapping: precipitation of secondary carbonate minerals. Mineral trapping is considered to be the most secure mechanism for $CO_2$ storage (IPCC, 2005; IEAGHG, 2008; Pham et al., 2012; Lee et al., 2016; Zhang and Huisingh, 2017; Liu et al., 2019; Delerce et al., 2021; Mishra et al, 2021).

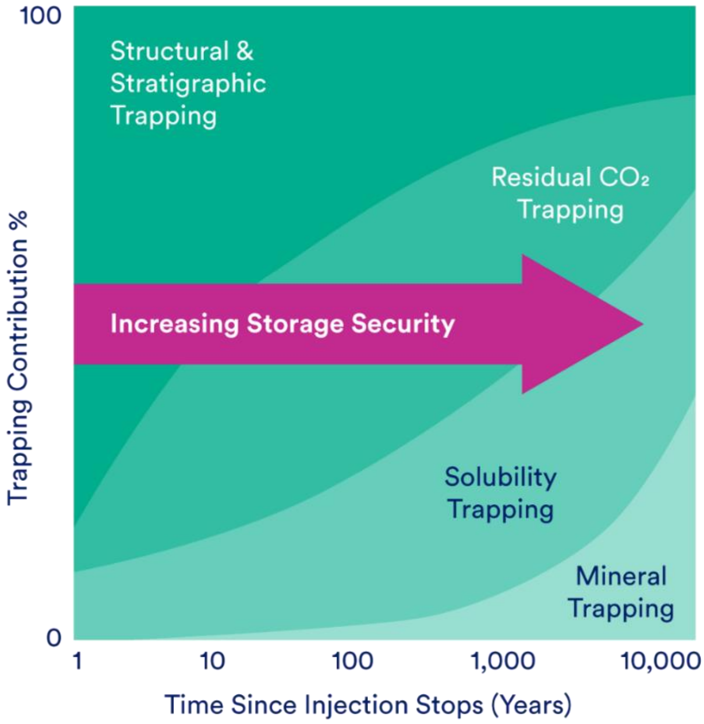

Figure 2.4. Development of trapping mechanisms over time in relation to storage safety (IPCC, 2005)

When $CO_2$ dissolves into the reservoir fluid, weak carbonic acid ($H_2CO_3$) is initially formed, followed by its dissociation to form bicarbonate ($HCO_3^-$) and carbonate ($CO_3^{2-}$) ions (solubility trapping) resulting in the instantaneous drop in pH. The increase in the acidity provokes the dissolution of the minerals in the reservoir (e.g. silicate minerals) which buffers low pH. The cations (e.g. $Ca^{2+}$, $Mg^{2+}$) released during the dissolution react with the dissolved bicarbonate species leading to the precipitation of stable secondary carbonate minerals such as calcite and magnesite (mineral trapping). These series of geochemical interactions of $CO_2$ with the reservoir fluid and rock can be expressed by the following reactions:

$CO_2\ (g) + H_2O \leftrightarrow H_2CO_3 \leftrightarrow HCO_3^- + H^+ \leftrightarrow CO_3^{2-} + 2H^+$

$HCO_3^- + Ca^{2+} \leftrightarrow CaCO_3(s) + H^+$ (calcite)

$HCO_3^- + Mg^{2+} \leftrightarrow MgCO_3(s) + H^+$ (magnesite)

Alumino-silicate minerals play a crucial role in permanent trapping of $CO_2$ by supplying the cations required to form the secondary carbonates (Assayag et al., 2009; Matter and Kelemen, 2009; Gaus, 2010; Rackley, 2010; Pham et al., 2011; Hellevang et al., 2013; Kaszuba et al., 2013; Zhang and DePaolo, 2017; Snaebjörnsdóttir et al., 2020; Mishra et al, 2021 and the references therein). As an example, chlorite alteration may provide iron and/or magnesium cations for $CO_2$ to be locked up in the form of dolomite and/or siderite (Gaus, 2010). The post-injection monitoring studies of some of the $CO_2$ storage projects reveal that the minerals which trap the injected $CO_2$ in these applications are calcite (CarbFix – Iceland, Nagaoka – Japan), ankerite (Wallula Basalt – USA) and siderite (Otway – Australia) (Romanov et al., 2015 and the references therein; McGrail et al., 2017; Pogge von Strandmann et al., 2019; White et al., 2020; Ratouis, 2022; $CO_2$ Storage Research Group, 2024).

Although the general conception is that development of mineral trapping is relatively slow (potentially taking a thousand years or longer) since the process is usually limited by the low reactivity of silicate minerals and the lack of Ca-, Mg-, and Fe-bearing minerals to release the necessary cations for carbonation, rapid mineralization has been reported in recent studies (CarbFix2 project: mineralization within two to nine months (Gunnarsson et al., 2018; Clark et al., 2020; Snaebjörnsdóttir et al., 2020) and in experimental studies: time scales of weeks to months (Kampman et al., 2014) and within five months (Voigt et al., 2021)). It is even disclosed in the 2020 study of Snaebjörnsdóttir et al. regarding CarbFix project that, no decrease in system permeability or in carbonation rates was observed since the start of injection in 2014. Thus, combined with its permenance of storage, mineral trapping is the most desirable outcome for long-term $CO_2$ storage.

Monitoring the CCS system is essential to reduce the uncertainties, to maintain a safe storage and to give early warnings about the potential risks. An indispensable part of a monitoring program is *geochemical monitoring* providing detailed information about the reservoir character, and the predictions regarding $CO_2$ migration and potential leakage pathways. Moreover, geochemical monitoring reveals the geochemical interactions between the fluids and reservoir rocks that may lead to either increased risks or entrapment of $CO_2$ (IPCC, 2005; Rütters et al., 2013; $CO_2$GeoNet, 2024). One of the phases of geochemical monitoring is the modelling studies performed using a software program (e.g. TOUGHREACT, PHREEQC or The Geochemist's Workbench), in which i) existing and potential geochemical reactions, ii) hydrogeochemical behaviour of the system, iii) temporal changes associated with $CO_2$ injection, iv) potential trapping mechanisms and v) long-term predictions about the fate of injected $CO_2$ can be investigated in detail.

# CHAPTER 3

# GEOLOGICAL BACKGROUND OF THE STUDIED GEOTHERMAL FIELDS

## 3.1 Tectonic Setting & Regional Geology

Situated in the tectonically active Alpine–Himalayan belt, Turkiye is continuously affected by the relative movements of the European and the Afro–Arabian plates. The northward subduction of the African plate in the west combined with the northward collision of the Arabian plate with Eurasia in the east, induce westward motion of the Anatolian plate bounded by the North Anatolian Fault Zone (NAFZ) and East Anatolian Fault Zone (EAFZ). Western Anatolia, a neotectonic province governed by active extension is characterized by dominantly E-W trending graben-horst structures formed as a result of active extension (Şengör et al., 1985; Taymaz et al., 2004; Bozkurt and Rojay, 2005). The widespread thermal manifestations (such as hot springs, fumaroles and hydrothermal alterations) are closely interrelated with the tectonics in this region and they are concentrated along within the major grabens (e.g. Büyük Menderes, Gediz grabens) or along their boundary faults (Şengör et al., 1985; Vengosh et al., 2002; Taymaz et al., 2004; Güleç and Hilton, 2006; de Leeuw et al., 2010; Baba and Sözbilir, 2012; Güleç and Hilton, 2016; Alçiçek et al., 2019; Karakuş et al., 2019). The studied Edremit (Balıkesir) and Akköy (Denizli) geothermal fields, are located in the northern and southern parts of western Anatolia, respectively (Fig.3.1).

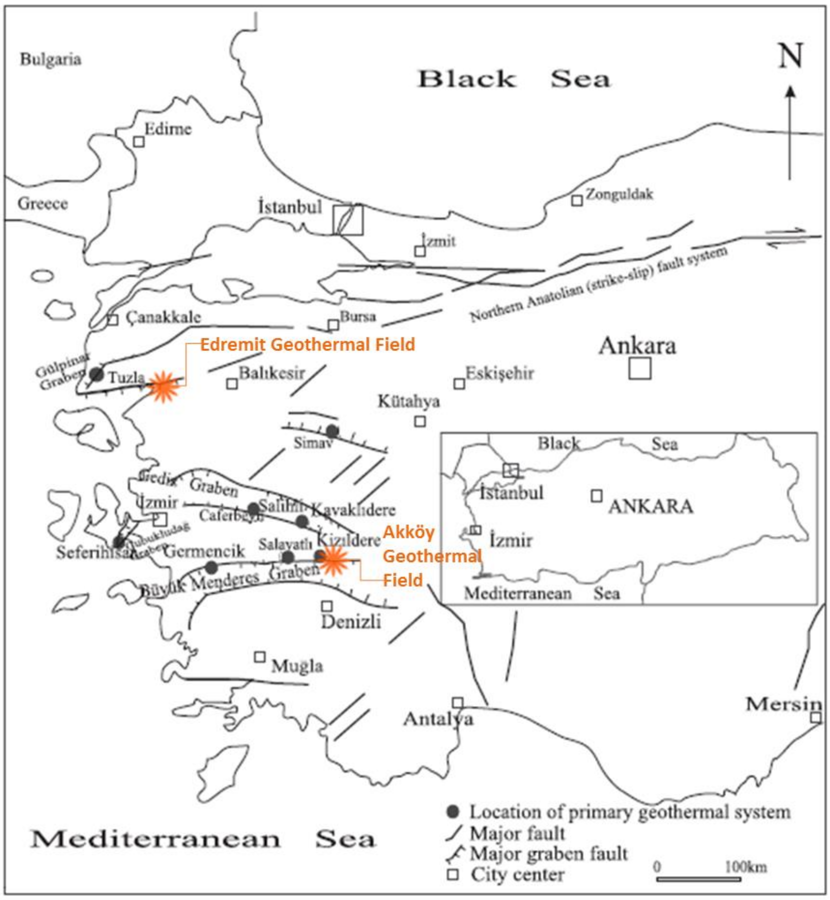

Figure 3.1. The location of Akköy and Edremit geothermal fields (shown with orange stars) along with some major geothermal fields (simplified geologic map is from Tarcan, 2005 and the references therein)

The studied Akköy geothermal field is situated in the Denizli Basin where two of the major grabens, namely E-trending Büyük Menderes and the NW-trending Gediz Graben intersect (Fig.3.1). Denizli Basin is 50 km wide and 70 km long bordered by NW- and SE-striking faults (Alçiçek et al., 2018; Alçiçek et al., 2019; Brogi et al., 2021 and the references therein).

Edremit geothermal field is located within the Edremit Graben. Tectonic position of the area corresponds to the western termination of the southern branch of the North Anatolian Fault Zone (NAFZ), controlled by dominantly NE–SW oriented right lateral strike slip and/or oblique faults (Herece, 1990; Avşar et al., 2013).

Akköy and Edremit geothermal fields are hosted by two major paleotectonic units of Turkiye, Menderes-Taurus Block and Sakarya Continent respectively which are separated by İzmir-Ankara suture (Fig.3.2). These units, along with other microcontinents bounded by suture zones and Tethyan oceans in between, are the products of the complex motions of Eurasia and the Afro–Arabian continents (Şengör and Yılmaz, 1981; Şengör, 1984).

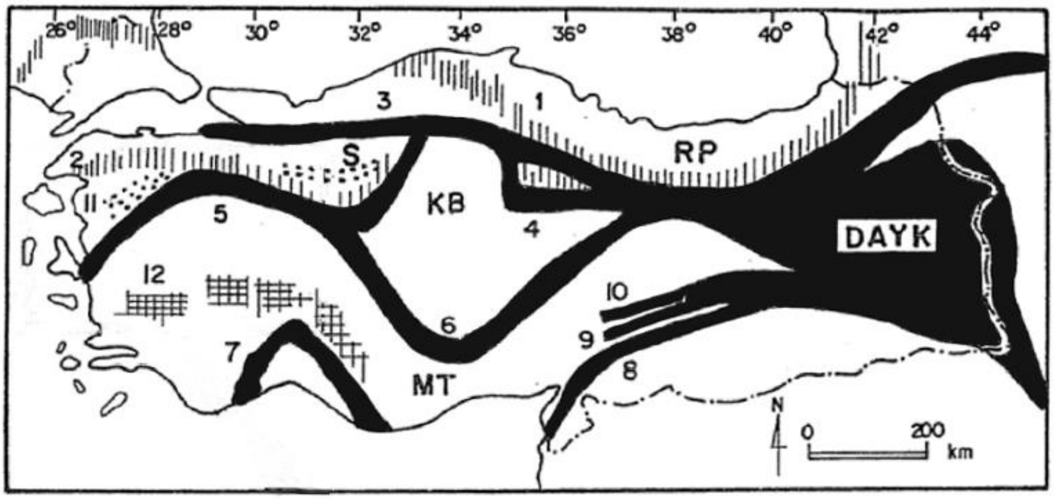

Figure 3.2. Paleotectonic provinces and the suture zones of Turkey. RP: Rodope-Pontide Fragment, KB: Kırşehir Block, S: Sakarya Continent, MT: Menderes-Taurus Block, DAYK: East Anatolian Accretionary Complex, 1: Main Palaeo-Tethys Suture, 2: Karakaya Suture, 3: Intra Pontide Suture, 4: Erzincan Suture, 5: İzmir-Ankara Suture, 6: Inner Tauride Suture, 7: Antalya Suture, 8: Asurid Suture, 9: Çüngüş Suture, 10: Maden Suture, 11: Hercinian Suture, 12: Pan-African Suture (Şengör, 1984)

Menderes-Taurus Block is composed of from basement to top, Menderes massif metamorphics which constitutes a gneiss core covered by schist and marble (Dürr, 1975; Şengör et al., 1984), Upper Cretaceous ophiolitic mélange (conglomerate, sandstone–shale, limestone, serpentinite, mafic volcanics, chert (Şengör & Yılmaz, 1981) and Neogene terrestrial sediments. Menderes massif comprises one of the oldest basements of Turkiye.

The highly deformed basement of Sakarya Continent consists of Palaeozoic to Triassic aged metamorphic rocks of Kazdağ Massif (amphibolites, gnesisses, phyllites, marbles, metaperidotites) and Karakaya Complex (schists, phyllites, marbles, metabasites). Tertiary clastic and carbonate rocks overlie the metamorphic basement (Bingöl, 1969; Bingöl et al., 1973; Bozkurt and Mittwede, 2001).

Magmatic activities characterized by widespread volcanic products and granitic intrusions of Neogene-Quaternary age seem to have considerable effects on both the Sakarya Continent and the Menderes-Taurus Block.

## 3.2 Geology of the Fields

### 3.2.1 Akköy Field

Paleozoic metamorphic rocks of the Menderes Massif constitute the basement of the Akköy geothermal field (Fig.3.3). These rocks are composed, at the lower levels, of gneisses alternating with quartzites and schists (micaschist unit). The uppermost part of the metamorphics, known as İğdecik Formation, consists of marble, calcschist, quartzite and schist alternations (Şimşek, 1985). Menderes Massif is tectonically overlain by Mesozoic dolomitic limestones, marbles, sandstones and ophiolitic melange of the Lycian nappes (Okay, 1989; Alçiçek et al., 2007, and the references therein). Lacustrine sediments overlie the basement units with an angular unconformity. The succession starts with alternating conglomerates, sandstones, shales, and lignite layers of Kızılburun Formation. These rocks are overlain, from bottom to top, by intercalated limestones, marls, siltstones and lake deposits (mudstone, gypsum, halite) of Sazak Formation, marls, siltstones and sandstones of Kolonkaya Formation and alternating units of poorly-consolidated conglomerates, sandstones and mudstones of Tosunlar Formation. The youngest unit of the area is the Quaternary alluvium (Şimşek et al., 2005).

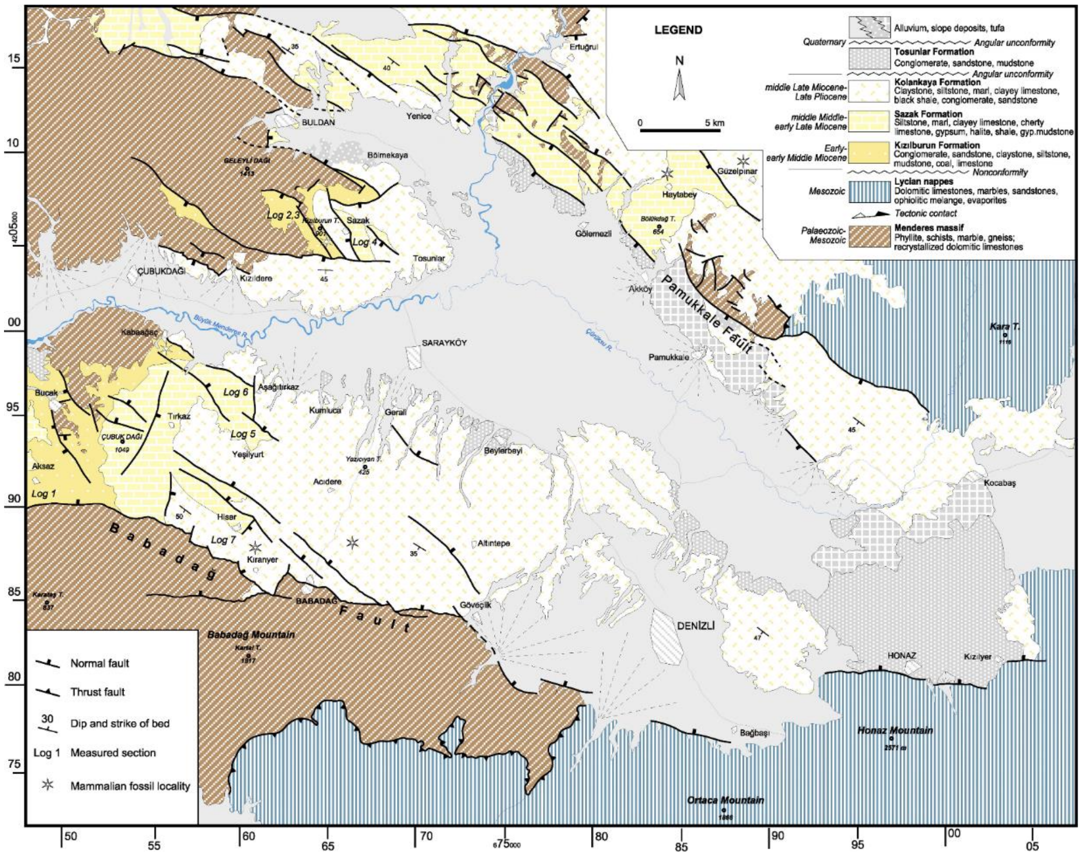

Figure 3.3. Geological map of Denizli Basin (Alçiçek et al., 2007 and the references therein)

### 3.2.2 Edremit Field

The basement of the region is represented by the Paleozoic aged metamorphic rocks of the Kazdağ Massif comprised of schists, gneisses, amphibolites, metadunites, migmatites and marbles (Fig.3.4). The basement is overlain by spilitic basalts, radiolarites and clastics of Karakaya Formation. Sandy limestones of Bilecik Formation overlies Karakaya Formation. These units are intruded by the Eybek Granodiorite which is reported to be genetically related to the overlying Upper Oligocene to Lower Miocene Hallaçlar volcanics. The youngest units in the field are the Ballıca Formation and the Plio-Quaternary sediments, the former unconformably overlying the Hallaçlar Formation (Avşar et al., 2013, and the references therein).

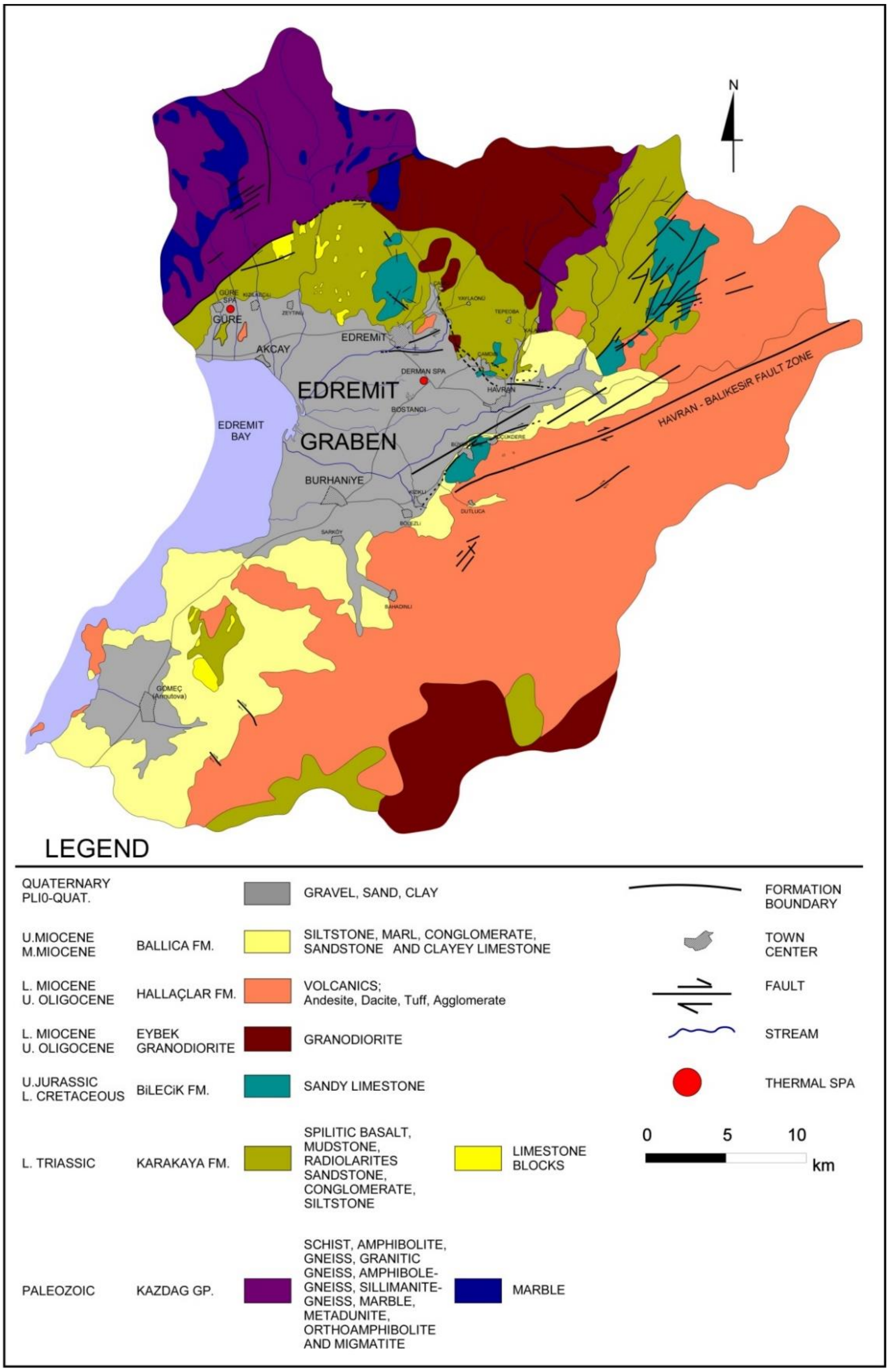

Figure 3.4. Geological map of the Edremit region (Avşar, 2011; Avşar et al., 2013 and the references therein)

## 3.3 Hydrogeologic Outline of the Fields

### 3.3.1 Akköy Field

Sazak Formation, İğdecik Formation and the lower levels of the Menderes Metamorphics are the three units identified as the reservoir rocks in the area, while relatively impermeable Kızılburun, Tosunlar, and Kolonkaya Formations act as the cap rocks (Şimşek, 1984; Şimşek et al., 2005; Tarcan et al., 2016). The reservoir and cap rocks of the Akköy field (schist-calcschist-marble-quartzite intercalations and the Neogene sedimentary units, respectively) are shown in well logs provided by Pekdemir Seracılık (Fig.3.5).

Two wells, PS-1 and PS-2, have been drilled in the field, among which PS-1 well is the production well and utilized in greenhouse heating.

Recharging of the system is sustained by the circulation of meteoric waters through the fault zones bounding the grabens, after being heated at depth. The rising hot water flows into the centre of the graben and subsequently, mixes with cold groundwater (Şimşek, 1985).

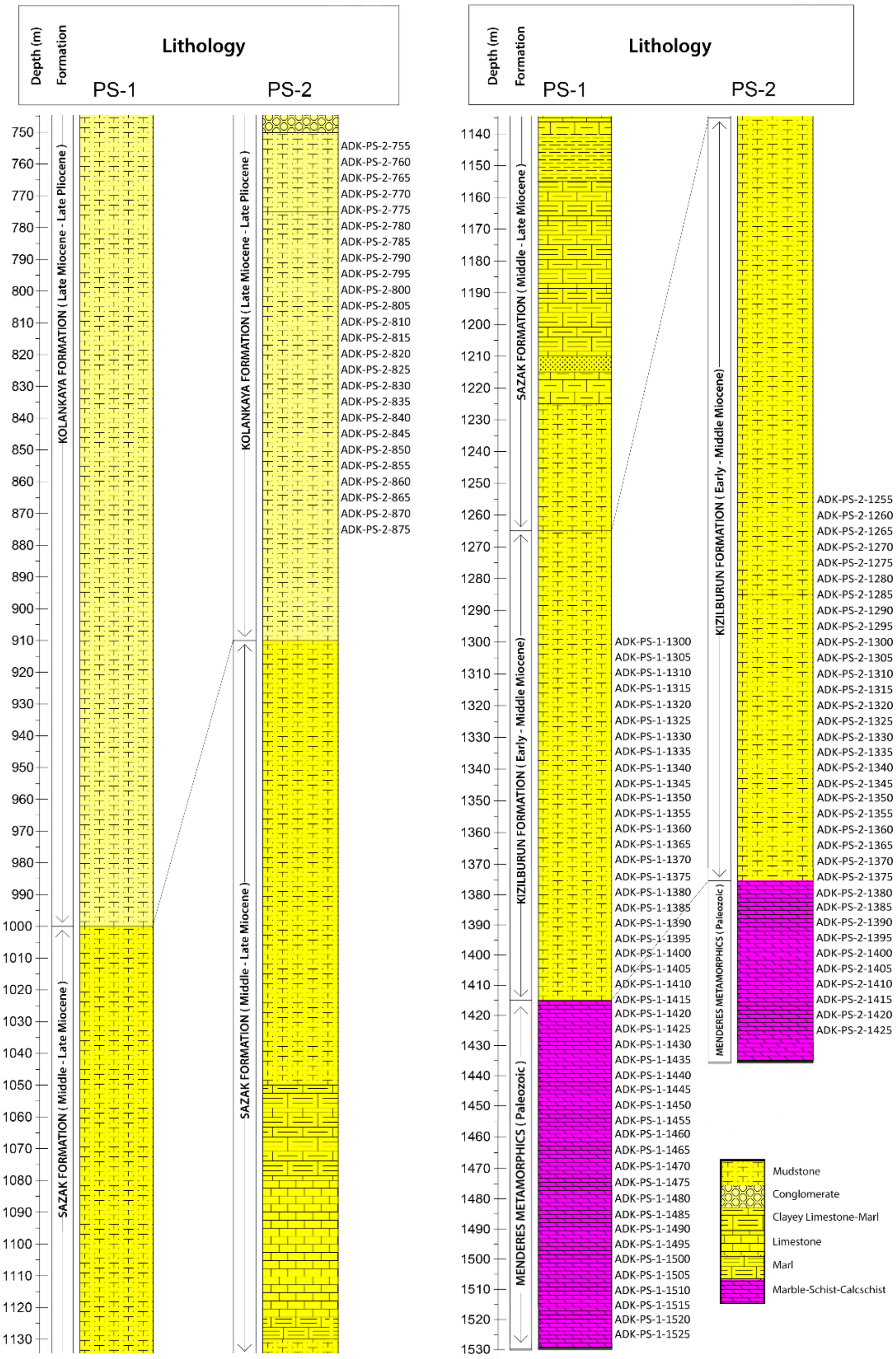

Figure 3.5. Well logs of PS-1 and PS-2 wells (Akköy field) with the sample numbers shown with respect to depth (the lithology after the depth of 1415 meter in PS-1 well was not shown in original document; this part was edited following the observations and analyses conducted in the thesis study)

]

### 3.3.2 Edremit Field

Based on the information obtained from the shallow and relatively deeper wells (with the depths of 30-496 m) drilled for irrigation purposes before 2013, the presence of two aquifers is identified around 0-90 m and 130-260 m levels in the Edremit field as reported by Avşar et al. (2013). For the second and relatively deeper aquifer, agglomerate and conglomerate units of Hallaçlar volcanics are determined to be the reservoir rocks while the cap rock is made up of siltstones, marls, conglomerates, sandstones and clayey limestones of Middle to Upper Miocene Ballıca Formation. However, it is inferred from the conceptual model of Avşar et al. (2013) that the hot geothermal fluid seems to be ascending along the fault zones from much greater depths and the basement units of metamorphic and granitic rocks act as the deep reservoir levels of the field (Fig.3.6, well log taken from the 2019 report of Parlaktuna and Avşar). In fact, the later conducted drillings have shown that water leakage zones are present in deeper levels. A total of 27 wells have been drilled in the field, which are used for heating and irrigation purposes (Avşar et al., 2015; Edremit Jeotermal, 2018). The well, on which this study is focused, is EDJ-12 well with a 1038 m depth which was drilled in 2013 (Edremit Geothermal Inc., 2018), but it is not currently utilized in production. In the well log of EDJ-12, 657, 864, 930 and 1015 meters are marked as probable water leakage zones.

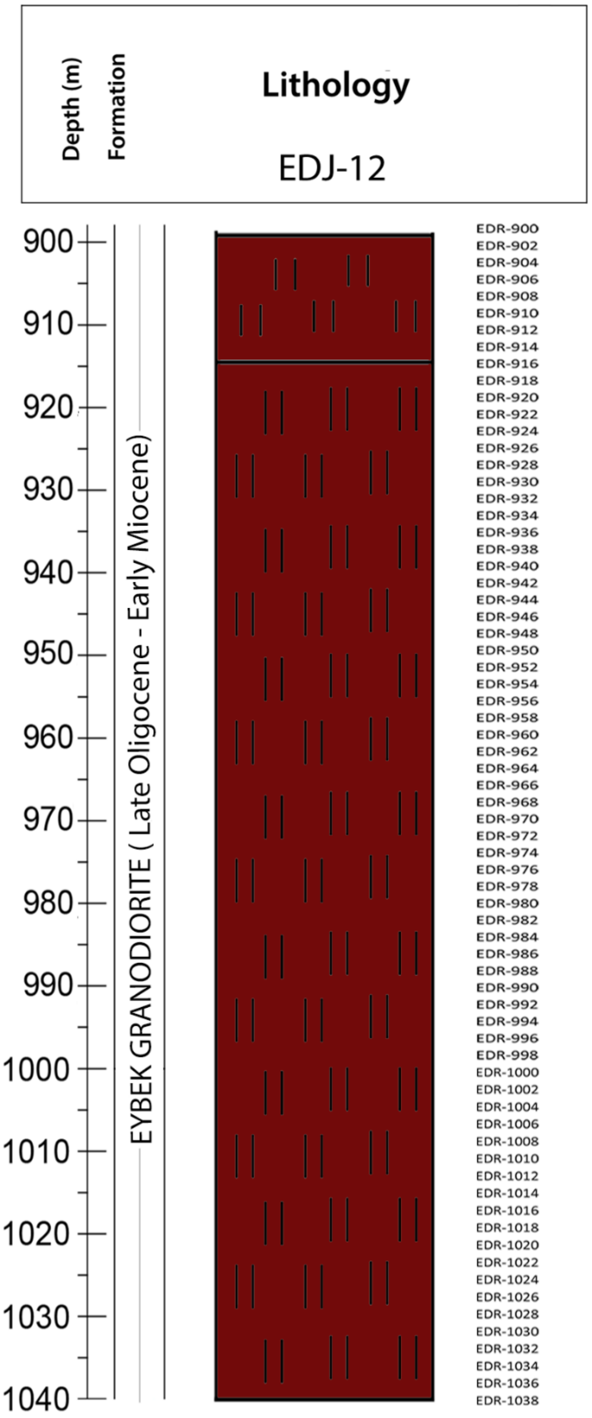

Figure 3.6. Well log of EDJ-12 well (Edremit field) with the sample numbers shown with respect to depth (modified from Parlaktuna and Avşar, 2019)

# CHAPTER 4

# METHODS OF STUDY

The construction of this thesis study is based on three main phases; i) sample acquisition, ii) analyses, iii) modelling. Rock and water samples are collected from Akköy (Denizli) and Edremit (Balıkesir) geothermal fields and the investigation of the samples is realized by means of mineralogic-petrographic and geochemical analyses. The results of the analyses are utilized as input data for the modelling studies in the context of $CO_2$-water-rock interactions.

## 4.1 Sampling

A field trip was conducted to Akköy geothermal field on 14 December 2018. Water sample from PS-1 well-head and drill cuttings that belong to various depths of both PS-1 and PS-2 wells were provided by Pekdemir Seracılık that owns the Akköy field (Fig.4.1). From a total of 109 rock samples, i) 46 samples collected in every five meters from 1300-1525 m depth belong to PS-1 well, ii) 60 samples collected in every five meters from 755-875 m and 1255-1425 m depth belong to PS-2 well, and iii) 3 samples collected from 1665, 2100 and 2195 m depth belong to PS-2 well. Another water sample taken from PS-1 well-head was obtained in January 2021.

Figure 4.1. PS-1 well and well discharge through pipe in Akköy geothermal field

For Edremit geothermal field, drill cuttings from different levels of EDJ-12 well were provided by Assoc. Prof. Dr. Özgür Avşar who conducted his PhD studies in the Edremit geothermal field. A total of 70 samples collected in every two meters between 900-1038 m depth were obtained for this study.

Sample numbers of the drill cuttings with respect to their depths are marked in the stratigraphic columnar sections of the PS-1, PS-2 and EDJ-12 wells (except the last three samples from PS-2 well, Fig.3.5 and 3.6).

## 4.2 Analyses

### 4.2.1 Rock Analyses

Cuttings that were obtained from drill wells from Akköy and Edremit geothermal fields were geochemically investigated in the laboratories of Ankara University – YEBİM (Earth Sciences Application and Research Centre). Additional microscopic examinations were performed in the Tectonic Laboratory of METU Geological

Engineering Department. The geochemical analyses, each of which providing a different scale of information, performed on the rock samples are:

i. Examination of the samples under microscope to determine the mineralogical and petrographical characteristics,
ii. Selection of representative samples from reservoir rocks, and from the selected samples, execution of the analyses of Confocal Raman Spectroscopy (CRS) and X-Ray Diffraction (XRD) for detailed mineral identifications (especially for the secondary minerals that cannot be identified through thin section studies),
iii. EPMA (Electron Probe Microanalysis) for the determination of minerals of solid solution series,
iv. XRF (X-Ray Fluorescence) technique for whole rock analysis.

#### 4.2.1.1 Petrographic Techniques

All of the rock samples were initially examined macroscopically using Meiji Techno PKL-2+EMZ 5 TR reflected light microscope. Adequate amount of specimen placed on a small glass container with the addition of water was investigated in terms of colour, state of crystallinity and mineralogical composition. In order to distinguish carbonate minerals, 10% HCl solution was added to the studied sample.

Thin sections of drill cuttings were prepared for microscopic examinations. The rock and mineral compositions, the abundance of the fragments, grain sizes and textural features were determined by taking into account of the changes with depth. The instruments used in these studies were Zeiss Axio 100 (transmitted light) polarizing microscope in YEBİM and Leica Orthoplan-Pol (transmitted light) polarizing microscope in METU.

#### 4.2.1.2 Mineralogical Techniques

For the minerals that could not be distinguished solely by microscopic observations, X-Ray Diffraction (XRD), Confocal Raman Spectroscopy (CRS), Electron Probe Micro Analysis (EPMA) techniques were performed.

XRD analysis was carried out on 17 and 10 selected samples from Akköy and Edremit fields, respectively, by Inel Equinox 1000 diffractometer with Co cathode in the X-ray tube. Samples were prepared for the analysis with fine grinding procedure. Approximately 4 gr sample was put into the grinding jar with 10 balls and grinded for 40 seconds in Retsch’s Planetary Ball Mill PM 100 CM. Any remaining coarse grains were sorted out from the powdered sample before putting the sample into small plastic bag (Fig.4.2).

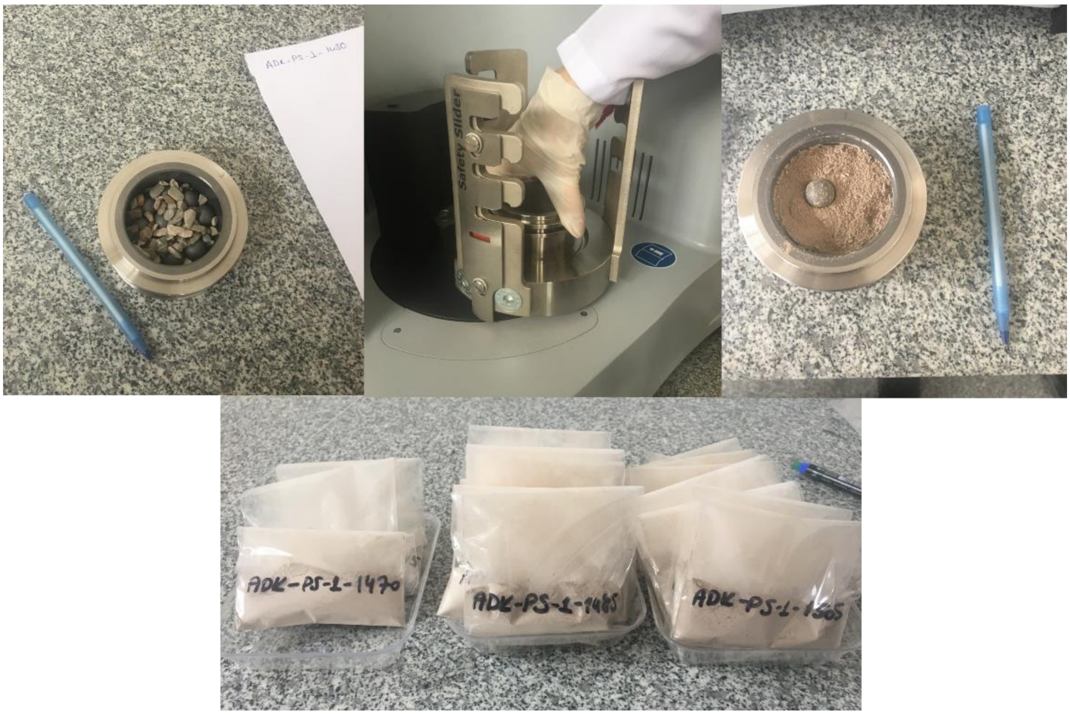

Figure 4.2. Fine grinding procedure for XRD and XRF analyses

Given the fact that drill cuttings are likely to be contaminated from overlying layers, the areas likely to represent reservoir rocks are marked on selected thin sections and CRS studies are performed on these areas with Thermo Scientific DXR Raman Microscopy equipped with 633 nm laser. For Akköy, 6 samples (2 samples from PS-1 and 4 samples from PS-2 well) were chosen, on which 62 points from 42 regions were analysed and for Edremit, on 6 selected samples, 110 different points from 41 regions were investigated. The Raman system included Olympus microscope, monochromator, filter and a charge coupled device (CCD) detector and the Raman measurements were excited at a resolution 2.4 $cm^{-1}$ in the range between 100-1200 $cm^{-1}$.

The fragments in the marked areas were also analysed using EPMA technique to determine the chemical compositions of minerals (especially the minerals from solid solution series). The studied thin sections were initially carbon coated with Quorum Q150T ES instrument and then, samples were analysed utilizing JEOL JXA 8230 Superprobe equipped with five Wavelength Dispersive Spectrometer (WDS) (Fig.4.3). The analyses were performed on a total of i) 183 spots from 11 samples (5 samples from PS-1 and 6 samples from PS-2 wells) of Akköy, ii) 284 spots from 6 samples of Edremit field. Compared to CRS analyses which was executed on randomly selected minerals, aside from similar results, different mineral compositions were also obtained in EPMA measurements for which fresh mineral grains were specifically selected.

Figure 4.3. a. Carbon coating procedure, b. EPMA system in YEBİM laboratories of Ankara University

#### 4.2.1.3 Whole Rock Geochemistry

Polarized Energy Dispersive (PED) XRF technique with Spectro X-Lab Pro instrument was used to determine the changes in major and trace element concentrations of all the samples. For this analysis, pellets were prepared using previously powdered samples. In the pellet preparation procedure, 4 gr powdered sample was weighed and 0.9 gr wax binder was added and mixed. The mixed powder was placed in a steel sleeve (die) and pressed using an XRF Pellet Press (Fig.4.4).

Figure 4.4. Pellet preparation procedure for XRF analyses

### 4.2.2 Fluid Analyses

Two water samples collected from PS-1 well of Akköy field (first sample in December 2018 and second one in January 2021) were analysed. Anion and cation contents of the water samples were determined via wet chemical methods (ion chromatography, colorimetric analysis, titration) while Al, Fe element values of the sample collected in 2018 were detected by using Inductively Coupled Plasma Mass Spectrometry (ICP-MS). These analyses were performed in the Laboratories of General Directorate of State Hydraulic Works Technical Research and Quality Control Department (DSİ TAKK). The isotopic composition ($\delta^{18}O$, $\delta D$, $\delta^{13}C$) of the water sample collected in 2021 was determined with Thermo Finnigan DeltaPlus XP Isotope Ratio Mass Spectrometer (IR-MS) in Middle East Technical University (METU) Central Laboratory using Gas Bench-Continuous Flow technique.

For the Edremit field, the results of fluid analyses are taken directly from Avşar et al. (2013) where it is reported that the element concentrations (major anion-cation, trace elements) were analysed by wet chemical methods and Inductively Coupled Plasma Atomic Emission Spectroscopy (ICP-AES) instrument while stable isotope concentrations were determined with Element Analyzer-Isotope Ratio Mass Spectrometer (EA-IRMS) in SRC Analytical and TUBITAK-MAM laboratories, respectively.

The calculations which are based on saturation index (SI) values, are performed at measured sampling temperature and pH by using the PHREEQC code (Parkhurst and Appelo, 2013).

## 4.3 Geochemical Modelling Setup

The assessment of Akköy and Edremit systems in the context of $CO_2$-water-rock interactions was realized through modelling studies performed with the software *PHREEQC* (version 3, Parkhurst and Appelo, 2013) which is extensively used in numerous geochemical modelling applications owing to its robust modelling of reactions. Equilibrium, kinetic and reactive transport modelling approaches were utilized in order to identify and interpret the potential reactions that govern the systems in the case of $CO_2$ addition and to predict the fate of $CO_2$. The necessary input parameters for these simulations were i) modal mineralogy of the reservoir rocks and ii) hydrogeochemistry of the reservoir fluid.

Given the relationship between the intensities of diffraction peaks of a known phase with its abundance in a mixture, the results from XRD analysis were used for the determination of modal mineralogy. The quantification calculations were performed using *Match!* software which implements “Reference Intensity Ratio - RIR” (de Woolf and Visser, 1988) method for a semi-quantitative analysis. The RIR method operates by scaling the diffraction data to a standard reference material. The intensity differences of reference and experimental peaks are minimized with a least-squares refinement in the calculations.

The thermodynamic database used in the simulations was *llnl.dat* (Lawrence Livermore National Laboratory database) due to the availability of more mineral phases and its wider range of temperatures for the equilibrium constants of reactions.

However, since llnl.dat uses the ideal gas law and the properties of real gases, including carbon dioxide, deviate from the ideal gas law at high pressures and low temperatures, $CO_2$ solubility correction was applied to the script. The correction was taken from phreeqc.dat in which the fugacity coefficient is calculated from the critical pressure and temperature with the Peng-Robinson equation of state (Peng and Robinson, 1976), better representing non-ideal gas behaviour and the dissolution in water (Klajmon et al., 2017). The thermodynamic parameters for minerals that were identified in the analyses but not present in the database, were also added (data for ankerite and plagioclase solid solution series, from Koenen et al., 2014 and from Arnorsson and Stefansson, 1999 in Zhang et al., 2019, respectively).

Assumptions made in the modelling were:

i) $CO_2$ as gas phase is assumed to be in equilibrium with the aqueous phase (Gaus et al., 2005; Klajmon et al., 2017; Ma et al., 2020; Fatah et al., 2022), in this regard, only partial pressure value of $CO_2$ for the relevant depth of the sample (calculated as the hydrostatic pressure) is defined,

ii) Pore space is assumed to be completely filled by 1 liter of solution and the weight fractions are scaled to the rock sample accordingly (e.g. if porosity equals 10% which corresponds to 1 liter of water, rock volume becomes 9 liters).

Molar values of minerals are calculated with the following equation:

$$n_i = \frac{m_i}{100} \, x \, \frac{(V \, x \, \rho)}{M_i} \tag{4.1}$$

where $n_i$ is the molar amount (mol), $m_i$ is the weight percentage (%), $M_i$ is the molecular weight (g $mol^{-1}$) of mineral i and V is the total rock volume ($m^3$), ρ is the rock density ($kg/m^3$).

The modelling studies were conducted on the “representative” samples which were differentiated according to:

i) mineral abundance (e.g. $SiO_2$ values of Akköy field are ≤ 50% from XRF analysis; samples which contain Quartz values that are above 50%, considering there are also other silicates in the mineral assemblage, are decided as not representative) and

ii) mineral assemblage (e.g. a sample containing only quartz and muscovite from Akköy and a sample with only quartz and orthoclase from Edremit are eliminated)

most likely for the relevant field.

Prior to the simulations, the secondary minerals that are likely to precipitate were determined with preliminary Saturation Index calculations for each sample and those minerals were also evaluated in the models. These calculations also revealed the $CO_2$ amount specific to each sample (since the abundance of minerals differs) to be used in the modelling, with the assumptions of i) abundant $CO_2$ is supplied to the aqueous system and ii) after the reactions, $CO_2$ does not remain as a free gas (i.e. becomes trapped either in mineral or in solution). Using the specified $CO_2$ amount added to the system, the percentages for mineral and/or solubility trapping were calculated from the changes in the mol values of carbonate species following the equilibrium modelling results.

Kinetic modelling studies were based on the equation (Eq.4.2) by Lasaga (1984) which describes the rate of dissolution and precipitation of minerals including several mechanisms (acid, neutral, base, carbonate) for the computation of pH dependence of the reaction rates (Palandri and Kharaka, 2004).

$$r_i = SSA_i M_i n_i \left(1 - \frac{Qi}{Ki}\right) \left(k_{i(acid)} + k_{i(neutral)} + k_{i(base)} + k_{i(carbonate)}\right) \qquad (4.2)$$

where for mineral i, $r_i$ is the reaction rate (mol $s^{-1}$), $SSA_i$ is the specific surface area ($m^2$ $g^{-1}$), $M_i$ is the molecular weight (g $mol^{-1}$), $n_i$ is the molar amount (mol), $Q_i$ is activity product and $K_i$ is equilibrium constant. The rate constant $k_i$ (mol $m^{-2}$ $s^{-1}$) is computed with Arrhenius equation (Eq.4.3) which describes the dependence on temperature.

$$k = A\, e^{\frac{-E_a}{RT}} \tag{4.3}$$

where A denotes Arrhenius pre-exponential factor, $E_a$ is activation energy of a reaction (kJ $mol^{-1}$), R is the universal gas constant (8.314 J $mol^{-1}$ $K^{-1}$) and T is temperature (K) (Palandri and Kharaka, 2004; Zhang et al., 2019). These equations are defined in PHREEQC via Basic language scripts inserted into the input file (Fig.4.5).

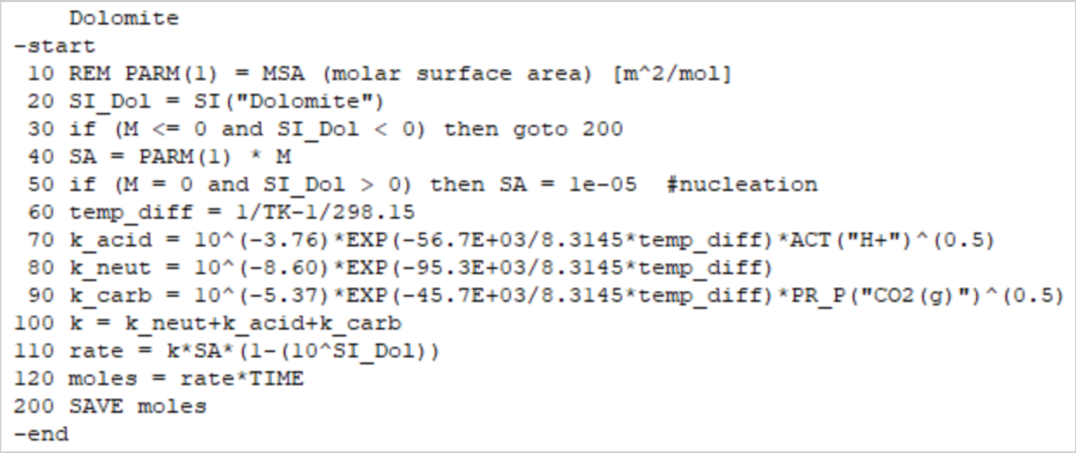

```
    Dolomite
-start
 10 REM PARM(1) = MSA (molar surface area) [m^2/mol]
 20 SI_Dol = SI("Dolomite")
 30 if (M <= 0 and SI_Dol < 0) then goto 200
 40 SA = PARM(1) * M
 50 if (M = 0 and SI_Dol > 0) then SA = 1e-05  #nucleation
 60 temp_diff = 1/TK-1/298.15
 70 k_acid = 10^(-3.76)*EXP(-56.7E+03/8.3145*temp_diff)*ACT("H+")^(0.5)
 80 k_neut = 10^(-8.60)*EXP(-95.3E+03/8.3145*temp_diff)
 90 k_carb = 10^(-5.37)*EXP(-45.7E+03/8.3145*temp_diff)*PR_P("CO2(g)")^(0.5)
100 k = k_neut+k_acid+k_carb
110 rate = k*SA*(1-(10^SI_Dol))
120 moles = rate*TIME
200 SAVE moles
-end
```

Figure 4.5. An example segment from the code in Rates data block of PHREEQC program written in Basic language representing the rate equations for the modelling. PARM(1) is the expression for $SSA_i$ (specific surface area) multiplied with $M_i$ (molecular weight)

Kinetic rate parameters were compiled from 2004 report of Palandri and Kharaka (except dawsonite and siderite, Table 4.1). Mineral specific surface areas applied in the calculations are given in Table 4.1. Considering the rapid reaction rates of calcite (Balashov et al., 2013; Hellevang et al., 2013; Haase et al., 2014; Ma et al., 2020), it was integrated into the models as an equilibrium phase. Simulation time of the reactions for kinetic modelling was defined as ten thousand years.

Table 4.1 Kinetic rate parameters used in the modelling. If not otherwise specified, all data are taken from Palandri & Kharaka (2004). Parameters of hornblende and montmorillonite in Palandri & Kharaka (2004) are used for amphibole and illite, respectively (Prg: Pargasite, Ann: Annite, Phl: Phlogopite)

| Mineral | Acid Mechanism | | | Neutral Mechanism | | Base Mechanism | | | Carbonate Mechanism | | | SSA |
|---|---|---|---|---|---|---|---|---|---|---|---|---|
| | log k (mol/m$^2$s) | E (kJ/mol) | n (H$^+$) | log k (mol/m$^2$ s) | E (kJ/mol) | log k (mol/m$^2$s) | E (kJ/mol) | n (H$^+$) | log k (mol/m$^2$s) | E (kJ/mol) | n P(CO$_2$) | (m$^2$/g) |
| Albite | -10.16 | 65.0 | 0.457 | -12.56 | 69.8 | -15.60 | 71.0 | -0.572 | - | - | - | 0.1[c] |
| Amphibole (Prg) | -7.00 | 75.5 | 0.600 | -10.30 | 94.4 | - | - | - | - | - | - | 0.6409[d] |
| Ankerite | -3.76 | 56.7 | 0.500 | -8.60 | 95.3 | - | - | - | -5.37 | 45.7 | 0.500 | 0.15[e] |
| Biotite (Ann) | -9.84 | 22.0 | 0.525 | -12.55 | 22.0 | - | - | - | - | - | - | 1.23[f] |
| Biotite (Phl) | - | - | - | -12.40 | 29.0 | - | - | - | - | - | - | 1.23[f] |
| Bytownite | -5.85 | 29.3 | 1.018 | -9.82 | 31.5 | - | - | - | - | - | - | 0.238[g] |
| Calcite | Equilibrium | | | | | | | | | | | |
| Chlorite | -11.11 | 88.0 | 0.500 | -12.52 | 88.0 | - | - | - | - | - | - | 1.14[h] |
| Dawsonite[a] | -4.48 | 49.43 | 0.982 | -6.89 | 63.82 | - | - | - | - | - | - | 9.8[i] |
| Dolomite | -3.76 | 56.7 | 0.500 | -8.60 | 95.3 | - | - | - | -5.37 | 45.7 | 0.500 | 0.18[e] |
| Illite | -12.71 | 48.0 | 0.220 | -14.41 | 48.0 | -14.41 | 48.0 | -0.130 | - | - | - | 0.468[j] |
| Kaolinite | -11.31 | 65.9 | 0.777 | -13.18 | 22.2 | -17.05 | 17.9 | -0.472 | - | - | - | 10[k] |
| Labradorite | -7.87 | 42.1 | 0.626 | -10.91 | 45.2 | - | - | - | - | - | - | 0.219[g] |
| Magnesite | -6.38 | 14.4 | 1.000 | -9.34 | 23.5 | | | | -5.22 | 62.8 | 1.000 | 0.13[l] |
| Muscovite | -11.85 | 22.0 | 0.370 | -13.55 | 22.0 | -14.55 | 22.0 | -0.220 | - | - | - | 0.68[m] |
| Orthoclase | -10.06 | 51.7 | 0.500 | -12.41 | 38.0 | -21.20 | 94.1 | -0.823 | - | - | - | 0.11[c] |
| Quartz | - | - | - | -13.40 | 90.9 | - | - | - | - | - | - | 0.02[i] |
| Siderite[b] | -8.00 | 65 | 0.750 | - | - | - | - | - | - | - | - | 0.18[i] |
| Smectite | -10.98 | 23.6 | 0.340 | -12.78 | 35.0 | -16.52 | 58.9 | -0.400 | - | - | - | 0.11[j] |

[a] Hellevang et al. (2010)
[b] Golubev et al. (2009)
[c] Brantley (2008)
[d] Diedrich et al. (2014)
[e] Klajmon et al. (2017)
[f] Taylor et al. (2000)
[g] Brantley & Mellott (2000)
[h] Jayasekara et al. (2020)
[i] Hellevang et al. (2013)
[j] Gaus et al. (2002)
[k] Yang & Steefel (2008)
[l] Pokrovsky et al. (2009)
[m] Oelkers et al. (2008)

Following the implementation of equilibrium and kinetic modelling, reactive transport simulations were conducted. In this simplified 1-D reactive transport modelling performed with PHREEQC, $CO_2$ was equilibrated with the “reinjected” reservoir fluid and representing the reservoir system, the minerals and the fluid were allowed to react kinetically throughout the simulation.

The mass of the transported chemical in a one dimentional column is calculated with the equation based on the Advection-Reaction-Dispersion Equation (ARD):

$$\frac{\partial C}{\partial t} = -\nu \frac{\partial C}{\partial t} + D_L \frac{\partial^2 C}{\partial x^2} - \frac{\partial q}{\partial t} \tag{4.4}$$

where C is the concentration in water (mol/kgw), t is the time (s), $\nu$ is the flow velocity in the pores (m/s), x is the distance (m), $D_L$ is the hydrodynamic dispersion coefficient [$m^2$/s, $D_L = D_e + \alpha_L \nu$, $D_e$ is the effective diffusion coefficient, $\alpha_L$ is the dispersivity (m)] and q is the concentration in the solid phase (mol/kgw in pore space) (Parkhurst and Appelo, 1999; Hemme and van Berk, 2017).

The flow velocity for the $CO_2$-charged solution was set as $10^{-7}$ m/s based on the reactive transport study in a hydrothermal setting by Yapparova et al. (2017). $10^{-9}$ $m^2$/s and 0.05 m were the values adopted as the diffusion coefficient and dispersivity, respectively, for aqueous phases in porous media (Parkhurst and Appelo, 2013 in Ma et al., 2020). A horizontal column of 100 m in length was simulated for a time period of 100 years with 100 cells of which each cell is 1 m long.

The geochemical models are based on the integration and/or derivation of algebraic equations. To evaluate the moles of reactions for a time subinterval in kinetic modelling, multiple rate expressions written in the Basic language are calculated with simultaneous integrations. 1-D advective-dispersive transport calculations are solved with an explicit finite difference algorithm. Since the calculations are iterative processes, computation time of the simulations directly depends on the physico-chemical properties of the system that is being modeled. Compared to equilibrium modelling, the calculation time for kinetic reactions is slower by a factor of six or more. Furthermore in transport modelling, the cell number and sizes affect the duration of the calculations. It is estimated that a 20-cell model takes 2.7 times, while a 200-cell model takes 600 times the CPU time of the 10-cell model since the increase in the grid size increases the solution calculations (e.g. doubling the grid size at least quadruples the number of calculations, Parkhurst and Appelo, 2013). Calculation of the chemical reactions take most of the computation time for the reactive transport modelling rather than the transport processes. The reasons include i) iterations performed in non-linear algebraic equations, ii) evaluation of thermodynamic properties at every iteration, such as activity coefficients, concentrations, activities and iii) the number of chemical species (Leal et al., 2017).

Calculation of very large molalities may also lead to convergence problems (Parkhurst and Appelo, 2013).

# CHAPTER 5

# LITHOGEOCHEMICAL CHARACTERIZATION

Drill cuttings obtained from Akköy and Edremit geothermal fields are investigated for the determination of mineralogical and petrographical features, mineral compositions and whole rock geochemistry. Variations in grain sizes and textural features with depth are additionally studied for Edremit samples.

The mineralogic-petrographic properties of rock samples are studied both macroscopically and microscopically. For detailed mineral identifications, Confocal Raman Spectroscopy (CRS), X-Ray Diffraction (XRD), Electron Probe Micro Analysis (EPMA) techniques and for the examination of elemental variations, X-Ray Fluorescence (XRF) analysis are conducted.

## 5.1 Petrographic Features

### 5.1.1 Akköy Field

Macroscopic and microscopic examinations are performed on all of the drill cuttings (46 samples from PS-1 and 63 samples from PS-2 wells). The photographs taken during these examinations are given in Figs. 5.1 to 5.3, and in Appendix A.

Abundant clay presence is observed on the spot for all the samples from both wells. Dominant rock fragments are identified as calcareous rocks (marble/limestone) in which marbles are generally micaceous (Figs.5.1a, 5.1b). Towards deeper levels (around 1375-1385 m, 1460-1465 m and >1500 m in PS-1 well, >1350 m in PS-2 well), schists composed mainly of calcschists (Figs.5.1c) and mica/chlorite schists (Figs.5.1b, 5.1d, 5.1e) start to increase in abundance.

Clay and clayey carbonate minerals (Figs.5.1f), quartz, calcite, micas (biotite and muscovite, Figs.5.1b, 5.1e) and hematite/limonite ± pyrite (Fig.5.1a) are the primary minerals observed in the cuttings from both PS-1 and PS-2 wells. Pyrite is generally present in PS-1 well at variable depths. In PS-2 well, although pyrite is observed at 1285, 1300, 1320, 1345 m depths, it is mainly abundant in the samples in depths shallower than 1000 m (755-875 m). The presence of Fe-bearing minerals (hematite/limonite ± pyrite) points to interaction of reservoir rocks with hydrothermal fluids.

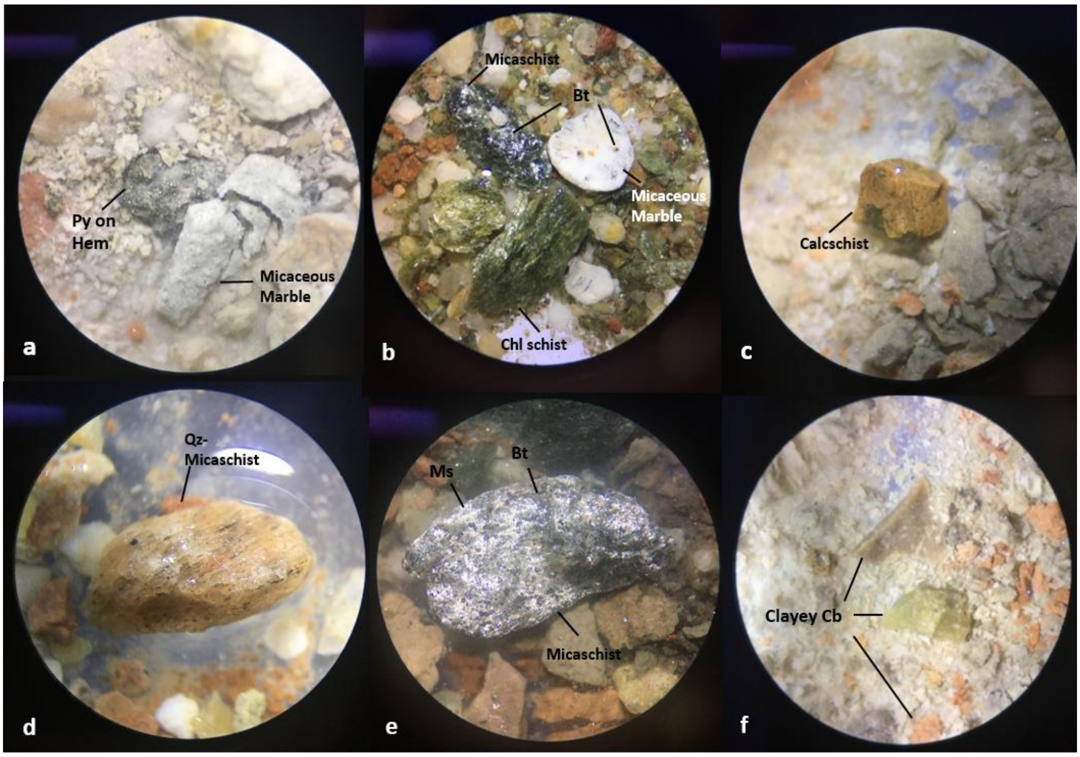

Figure 5.1. Macroscopic views of Akköy samples a. pyrite (Py) crystals on hematite (Hem) and argillized micaceous marble (sample no. ADK-PS-1-1330), b. micaschist, chlorite (Chl) schist and micaceous marble (sample no. ADK-PS-2-1380), c. calcschist (sample no. ADK-PS-1-1300), d. quartz (Qz) – micaschist (sample no. ADK-PS-2-1310), e. micaschist (sample no. ADK-PS-1-1525), f. clayey carbonate minerals (Cb) (sample no. ADK-PS-1-1300)

Microscopic examinations reveal the presence of sandstone, quartzite and chert fragments in the samples for both PS-1 and PS-2 wells, in addition to the macroscopically observed marble/limestone and schist (calcschist, micaschist, chlorite schist, amphibole schist) fragments (Figs.5.2a, 5.2b, 5.2c, 5.2d). Marble fragments are generally abundant at depths >1465 meters in PS-1 and >1295 meters in PS-2 well. As revealed by the macroscopic examinations, schist fragments are especially high in amount in deeper levels (e.g. >1485 m in PS-1, 1310-1330 m and 1345-1420 m in PS-2). In some levels (most of the samples in PS-1 well and between 1290-1305 m, 1360-1390 m and 1415 m in PS-2 well) serpentinite (Fig.5.2e) is found. These samples are likely to belong to the ophiolitic melange of the Lycian nappes of the region. These studies also confirm the abundance of clay minerals in all samples along with quartz and calcite (Figs.5.2a, 5.2b). Opaque minerals (Fig.5.2d) observed in the thin sections seem to be associated with the Fe-bearing minerals that are observed macroscopically. Further mineral observations lead to the identifications of feldspar, pyroxene, chlorite (Fig.5.2f) and amphibole minerals.

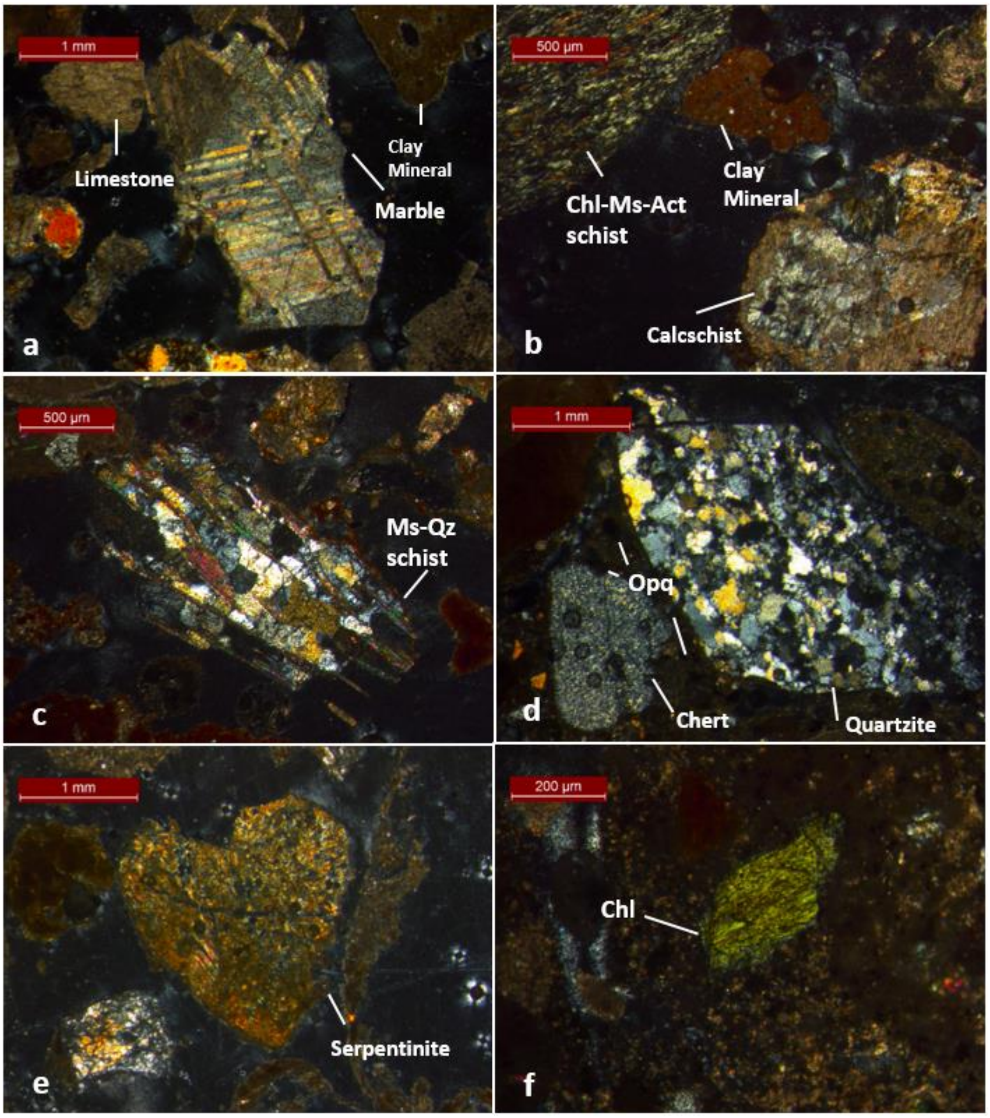

Figure 5.2. Microscopic views of Akköy samples a. marble with pressure twinning, limestone and clay mineral (sample no. ADK-PS-2-1410), b. chlorite (Chl)–muscovite (Ms)–actinolite (Act) schist, clay mineral and calschist (sample no. ADK-PS-1-1515), c. muscovite (Ms)-quartz (Qz) schist (sample no. ADK-PS-2-1315), d. quartzite, chert and opaque minerals (Opq) (sample no. ADK-PS-1-1385), e. serpentinite (sample no. ADK-PS-1-1320), f. chlorite (Chl) (sample no. ADK-PS-2-1265)

Petrographic studies also reveal pressure twinning on marbles (Figs.5.2a, 5.3a) and the indications for the effects of hydrothermal fluid on mineral grains (Fig.5.3b).

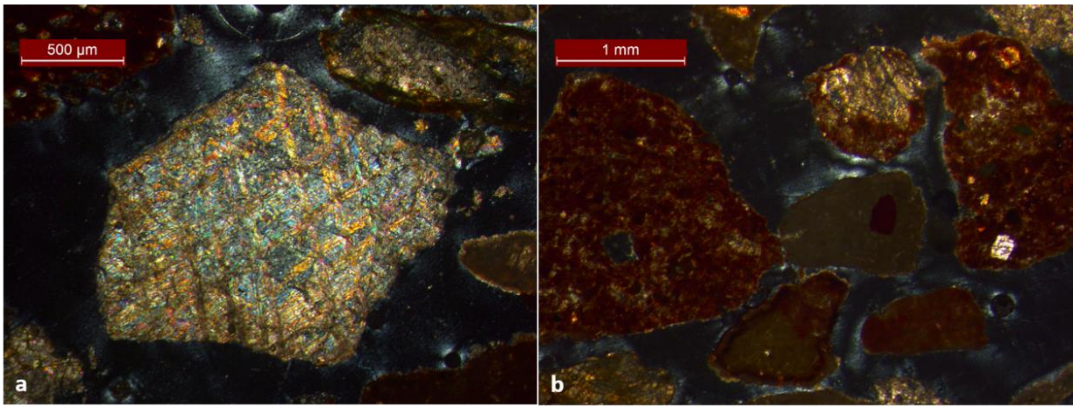

Figure 5.3. Microscopic views of a. marble with pressure twinning (sample no. ADK-PS-2-1390), b. effects of hydrothermal fluid (sample no. ADK-PS-2-1310)

### 5.1.2 Edremit Field

A total of 70 samples from the EDJ-12 well are studied macroscopically and microscopically. The photographs taken during these examinations are given in Figs. 5.4 to 5.7, and in Appendix A.

The macroscopic examinations display that rock fragments are dominated by granitic rocks (granite/granodiorite, Fig.5.4a). Metamorphic fragments (mainly marble, gneiss and calcschist) and fragments that belong to gabbroic (Fig.5.4b), volcanic and sedimentary rocks are also observed in some samples. The main minerals observed are quartz, biotite (Figs.5.4a, 5.4c), epidote (Fig.5.4d), calcite, amphibole, muscovite, chlorite, hematite/limonite (Fig.5.4e) and pyrite (Fig.5.4f). Although it is observed to be present in almost every sample, pyrite is found to be especially abundant in between 958-980 m levels. An apparent abundance of biotite is also noted in between 960-972 and 992-998 meters.

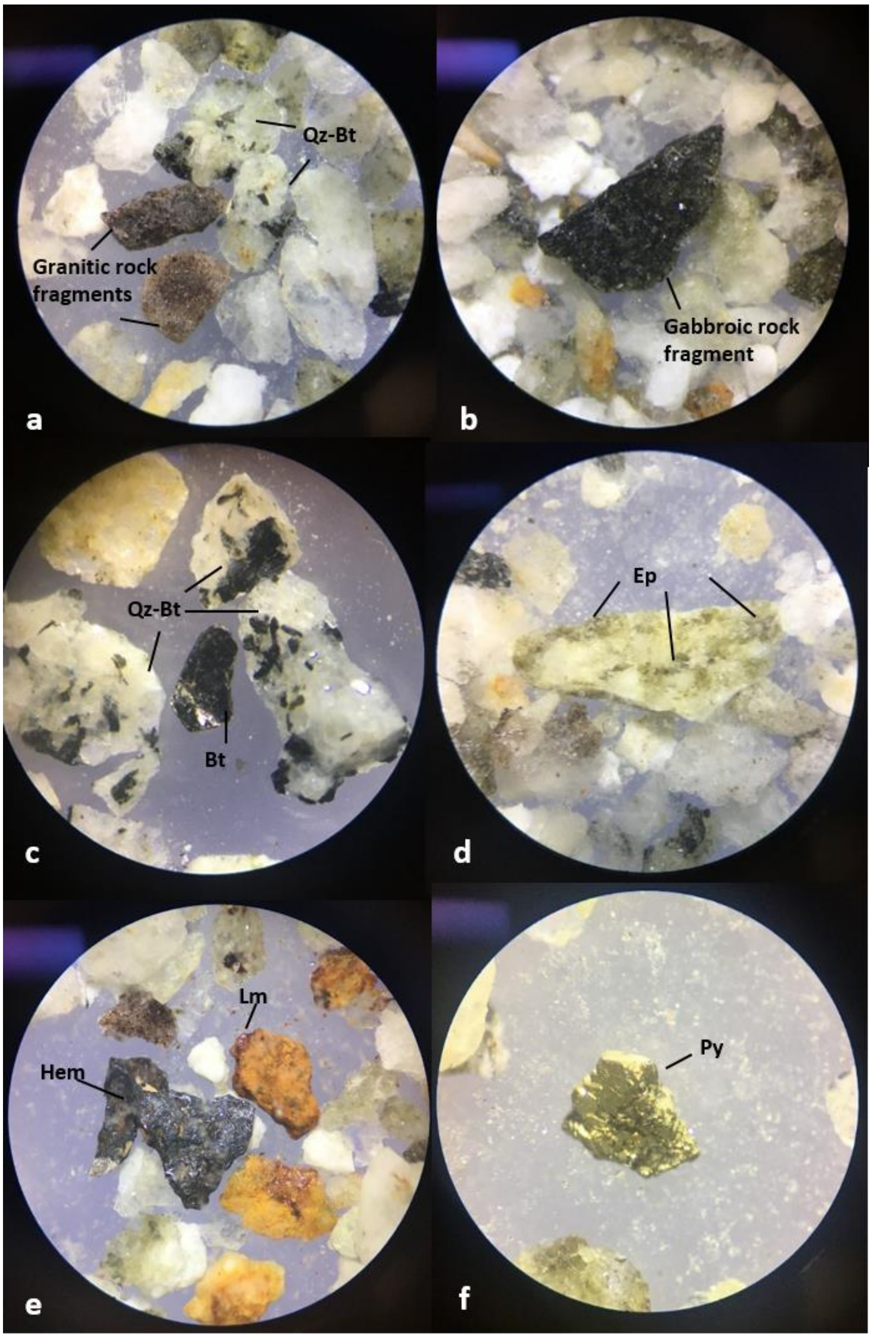

Figure 5.4. Macroscopic views of Edremit samples a. granitic rock fragments, quartz (Qz) and biotite (Bt) (sample no. EDR-912), b. gabbroic rock fragment (sample no. EDR-916), c. quartz (Qz) and biotite (Bt) (sample no. EDR-1026), d. epidotes (Ep) on a siliceous fragment (sample no. EDR-920), e. hematite (Hem) and limonite (Lm) (sample no. EDR-924), f. pyrite (Py) (sample no. EDR-968)

Cu-bearing minerals (chalcopyrite, azurite (Fig.5.5a), malachite), along with some grains containing native-Cu (Fig.5.5b) are recognized around 926-932, 942, 966, 984, 990-992, 1004 and 1024 m depths.

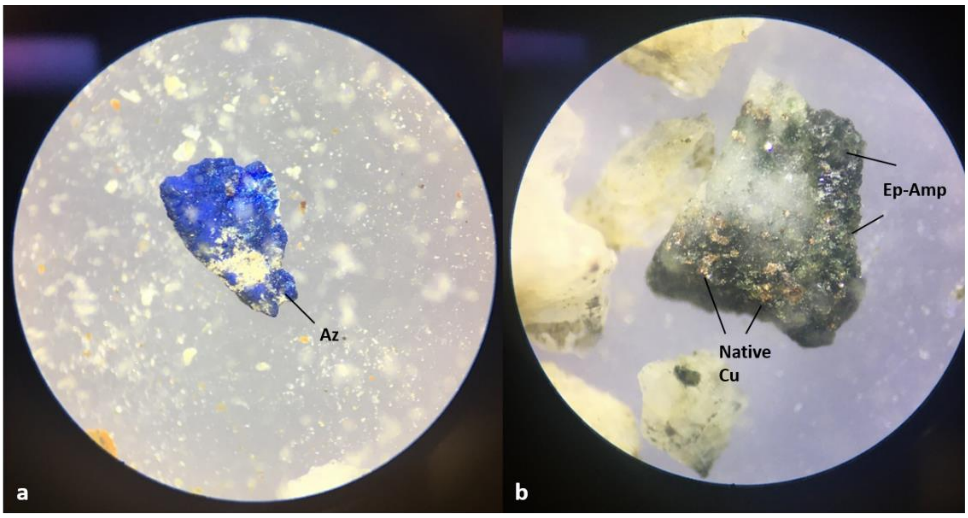

Figure 5.5. Macroscopic views of a. azurite (Az) (sample no. EDR-926), b. native Cu on a grain composed of epidote (Ep) and amphibole (Amp) (sample no. EDR-966)

The thin section examinations confirm the domination of granitic rocks (Fig.5.6a) with the average relative proportion of 80% followed by 17% for metamorphic, 2% for gabbroic (Fig.5.6b), 1% for sedimentary and 1% for volcanic rock fragments. Limestone (Fig.5.6a) is identified as a sedimentary rock fragment. Quartz, plagioclase (Fig.5.6c), calcite, biotite (Figs.5.6d, 5.6e, 5.6f), orthoclase, amphibole (Fig.5.6d), opaque minerals (Figs.5.6a, 5.6e, 5.6f), chlorite, pyroxene, epidote (Fig.5.6e) and muscovite (Fig.5.6f) are the minerals observed microscopically in the samples from Edremit field. The opaque minerals seem to be associated with the macroscopically observed Fe- and Cu-bearing minerals.

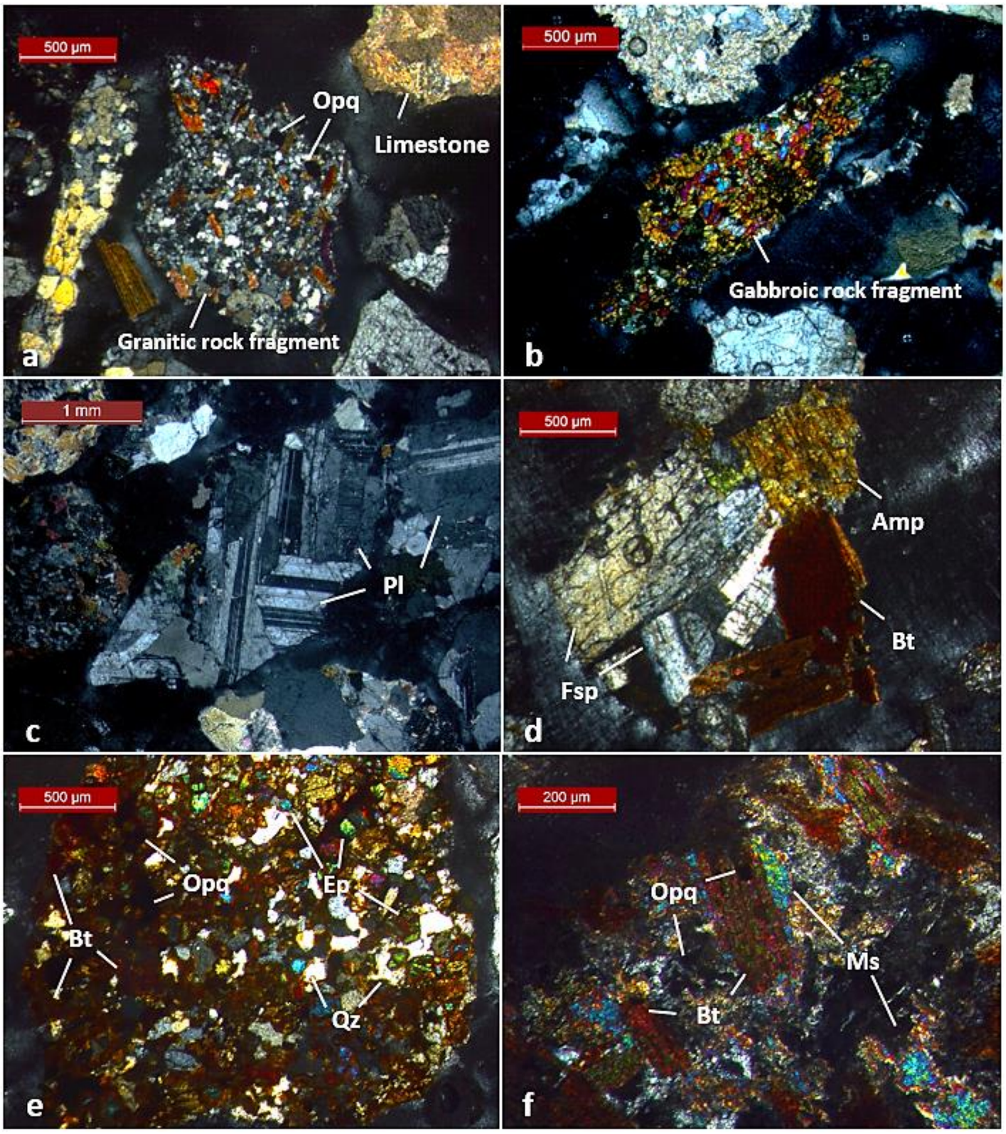

Figure 5.6. Microscopic views of Edremit samples a. granitic rock fragment, limestone and opaque minerals (Opq) (sample no. EDR-902), b. gabbroic rock fragment (sample no. EDR-944), c. plagioclase (Pl) minerals (sample no. EDR-986), d. biotite (Bt), amphibole (Amp) and feldspar (Fsp) minerals (sample no. EDR-998), e. biotite (Bt), epidote (Ep), quartz (Qz) and opaque minerals (Opq) (sample no. EDR-956), f. biotite (Bt), muscovite (Ms) and opaque minerals (Opq) (sample no. EDR-986)

The textures are heterogeneously distributed in each sample; there are holocrystalline fragments as well as the ones affected by cataclasis likely to be associated with a fault zone as revealed by the presence of cataclastic (Fig.5.7a), mylonitic (Fig.5.7b) and mortar (Fig.5.7c) textures. Furthermore, metasomatism (Fig.5.7d) and secondary uralitization (Figs.5.7e, 5.7f) are also observed in some fragments.

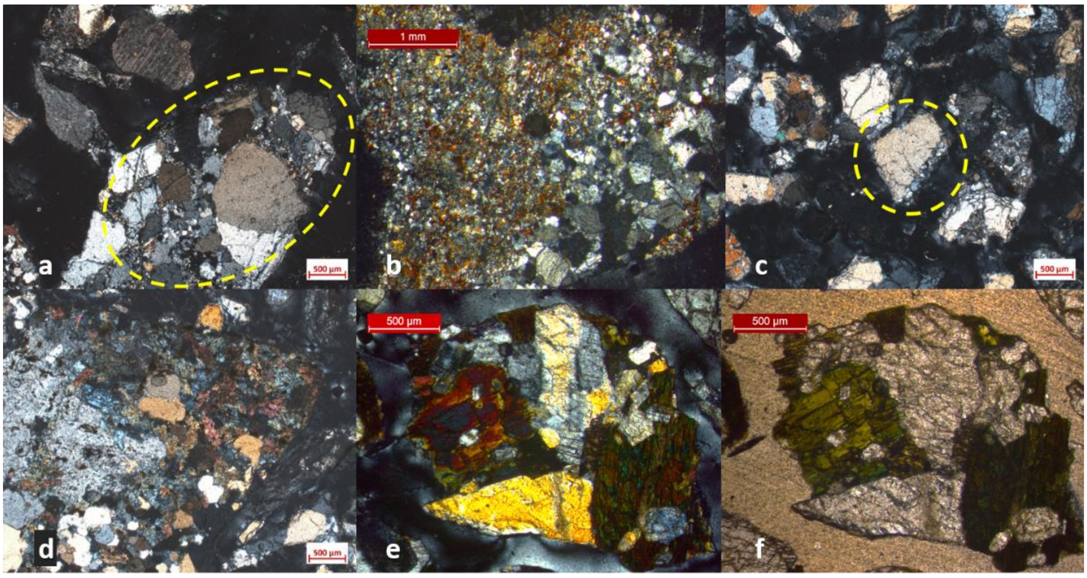

Figure 5.7. Microscopic views of textural features in Edremit samples a. cataclastic granite (shown in dashed line) with gneiss on top (sample no. EDR-912), b. mylonitic granite (sample no. EDR-966), c. mortar texture (shown in dashed line, sample no. EDR-932), d. metasomatism (sample no. EDR-954), e and f. gabbro rock fragment showing uralitization in cross-polarized light and plane-polarized light, respectively (sample no. EDR-1006)

The petrographic features of rock fragments from Edremit field are investigated in regard to the variations with depth along the wellbore (Fig.5.8). Grain sizes of granitic fragments change from coarse to fine at different depths: around the first 12 meters, the granitic fragments (mainly granite) are observed to be coarse grained and from 914 m to 984 m, the fragments become fine grained. After 986 meters to the deeper levels, relatively more granodiorite fragments are present, of which the grain sizes fluctuate from coarse to medium. The distribution of certain textural features also seem to apply to similar depth levels: cataclastic (904-912 m and 994-1014 m, Fig.5.7a), mylonitic (912-986 m, Fig.5.7b) and mortar (932 m, Fig.5.7c) textures reflect the effects of cataclasis which is likely to be associated with a fault zone. Metasomatism (e.g. 954 m, Fig.5.7d) and secondary uralitization (e.g. 1006 m, Figs.5.7e, 5.7f) observed in some fragments point to the effects of hot fluids circulating via the fault/fracture zone(s) at the relevant depth(s).

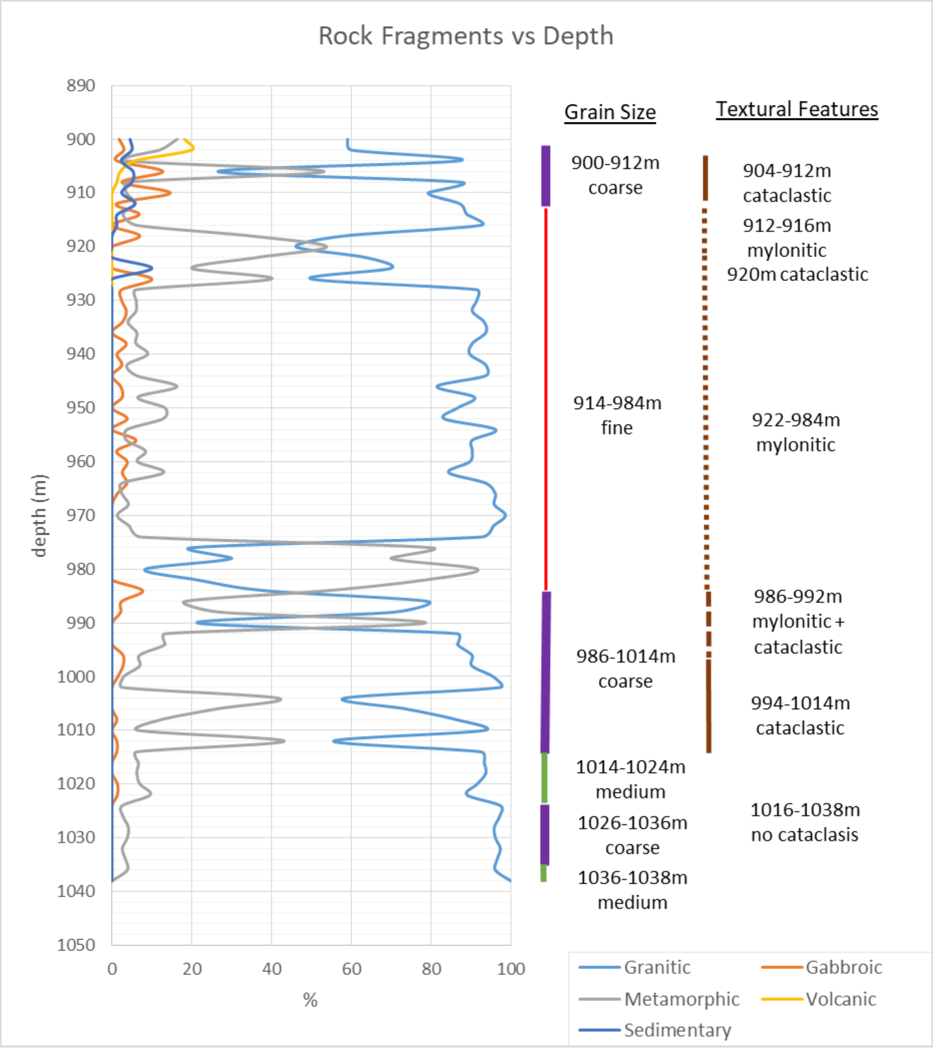

Figure 5.8. Analyses of rock fragments from Edremit field regarding their abundance, grain size and textural features with respect to depth

## 5.2 Identification of Mineral Phases

### 5.2.1 X-Ray Diffraction (XRD) Analysis Results

#### 5.2.1.1 Akköy Field

XRD analyses of the selected 8 samples from PS-1 and 9 samples from PS-2 wells (Appendix B) confirm quartz, calcite and clay minerals as the dominant mineral phases and reveal the presence of dolomite, ankerite, orthoclase, albite, labradorite and talc. Kaolinite, illite and smectite are the determined clay minerals. Based on the abundance of minerals, all analysed samples contain quartz, 76% of them contain calcite and muscovite, followed by 53% dolomite.

XRD diffractograms of the samples against depth are examined for the mineralogical composition and the effects of possible alteration (Fig.5.9). The argillization effect decreases in deeper levels in the samples of both PS-1 and PS-2 wells. In PS-1 samples, kaolinite, feldspar and carbonate mineral proportions increase while in PS-2 samples, the proportions of calcite and ankerite increase and clay mineral content decreases with increasing depth. The presence and increasing proportion of ankerite point to increasing degree of hydrothermal alteration with depth.

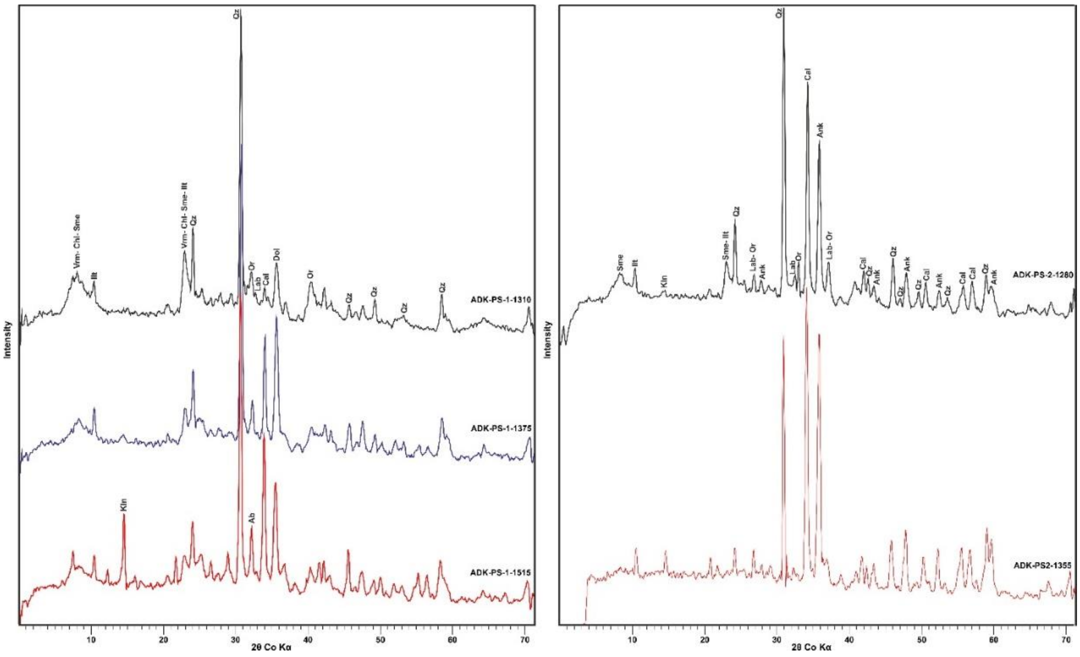

Figure 5.9. XRD patterns of the selected samples from different depths which belong to the PS-1 and PS-2 wells in Akköy field (Ab: Albite, Ank: Ankerite, Cal: Calcite, Chl: Chlorite, Ilt: Illite, Kln: Kaolinite, Lab: Labradorite, Or: Orthoclase, Sme: Smectite, Qz: Quartz, Vrm: Vermiculite)

#### 5.2.1.2 Edremit Field

XRD analyses of 10 selected samples from the EDJ-12 well (Appendix B) reveal the presence of dolomite and actinolite in addition to the microscopically identified quartz, orthoclase, plagioclase, calcite, biotite, muscovite and chlorite (Fig.5.10). Designated plagioclase minerals include albite, labradorite, andesine and bytownite. Quartz and orthoclase comprise 90% and 80% of the analysed samples, respectively. The determined clay minerals are illite, kaolinite, smectite and vermiculite. Feldspar, mica and illite abundances seem to increase towards deeper levels.

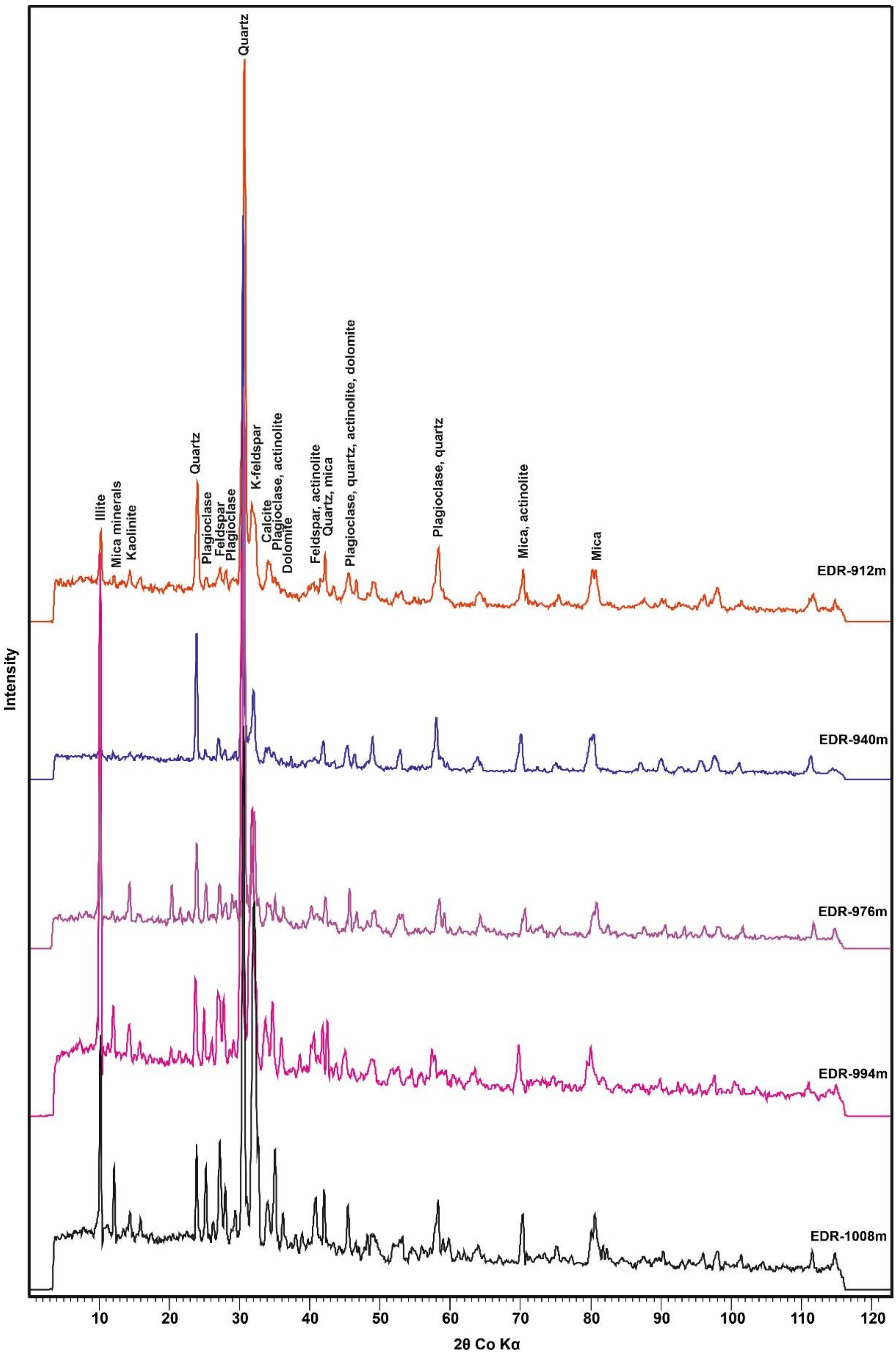

Figure 5.10. Example XRD patterns of Edremit samples from different depths

### 5.2.2 Confocal Raman Spectroscopy (CRS) Results

#### 5.2.2.1 Akköy Field

The results of CRS studies which are performed on 62 distinct points from the 6 selected samples that generally display the characteristics of reservoir lithology (2 samples from PS-1, 4 samples from PS-2 well), are tabulated in Table 5.1. Raman spectrums of some of the analysed minerals are displayed in Appendix C. The minerals detected in the samples are carbonate minerals (calcite, dolomite, ankerite), quartz, chalcedony, albite, muscovite, clinochlore, talc, actinolite, hematite and marcasite among which chalcedony, actinolite and marcasite are distinguished with these analyses.

Table 5.1 Results of the Confocal Raman Spectroscopy (CRS) analyses for Akköy samples

| **Sample No.** | **Minerals** | | | | | | | | | | | |
|---|---|---|---|---|---|---|---|---|---|---|---|---|
| | Calcite | Dolomite | Ankerite | Quartz | Chalcedony | Albite | Muscovite | Clinochlore | Talc | Actinolite | Hematite | Marcasite |
| ADK-PS-1-1495 | ● | ● | | ● | | ● | | | | | ● | |
| ADK-PS-1-1515 | ● | ● | ● | | ● | | | ● | | ● | ● | ● |
| ADK-PS-2-1310 | ● | ● | | | | | | | | | ● | |
| ADK-PS-2-1355 | ● | ● | | ● | | ● | | ● | | ● | ● | |
| ADK-PS-2-1380 | ● | | | | | | ● | | ● | | ● | |
| ADK-PS-2-1415 | ● | | | ● | | | | ● | | | | |

The results show that carbonate minerals are dominated by calcite. From all carbonate minerals that are analysed, 65.7% is recorded as calcite, 28.6% as dolomite and 5.7% as ankerite.

In order to investigate the changes in the physicochemical conditions of the reservoir lithology with depth, calcite which is the most abundant carbonate mineral in all samples, is selected for the comparison of the CRS results. The Raman spectrums of calcite of the analysed samples against depth are shown in Figure 5.11. Calcite has strong Raman shift around 1080 cm$^{-1}$ and weak peaks around 710, 270 and 150 cm$^{-1}$. The sharp Raman shift around 1080 cm$^{-1}$ is assigned to the $(CO_3)^{2-}$ symmetric stretching mode whereas the weak Raman shift around 710 cm$^{-1}$ is resulted from the symmetric $(CO_3)^{2-}$ deformation. The Raman peaks around 270 and 150 cm$^{-1}$, which are in the low wavenumber region of the Raman spectrum, are related with the external vibrations of the $(CO_3)^{2-}$ (Sun et al., 2014). The examination of the Raman spectrums reveals that there is a shifting in the peak positions of calcite with depth in both PS-1 and PS-2 wells (Fig.5.11). The shifting in all sharp and weak peaks of calcite is related to the pressure increase with the increasing depth. This is also supported by the increasing degree of metamorphism with depth in the region (e.g. the basement lithology). This shifting in the peaks is compatible with the empirical studies (Fong and Nicol, 1971). According to calcite Raman data from the literature (Fong and Nicol, 1971), calcite minerals of the samples from Akköy field may be formed under 1 bar pressure.

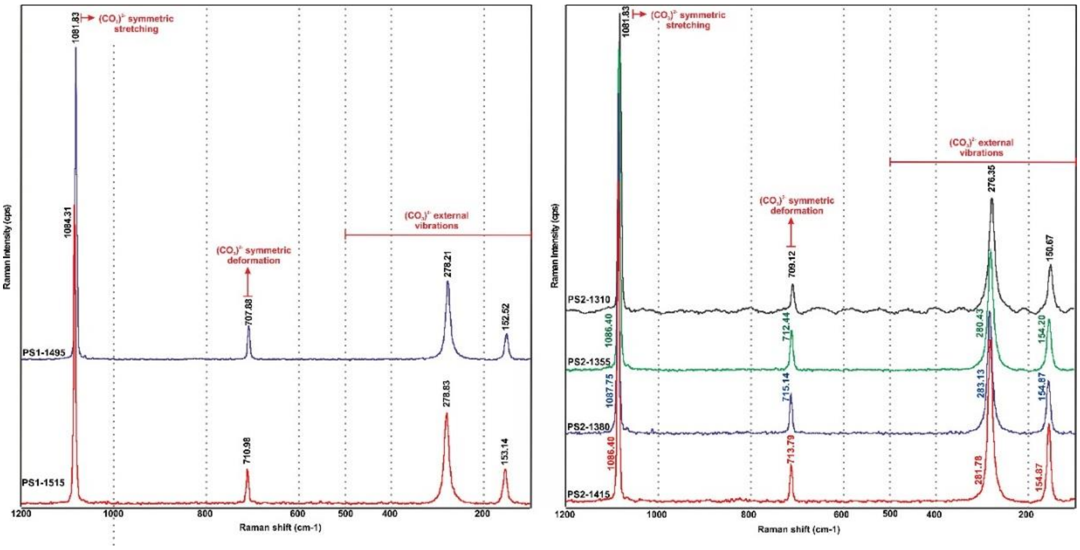

Figure 5.11. Calcite Raman spectrums of the analysed samples from PS-1 and PS-2 wells (Akköy field) against depth (The carbonate group minerals have characteristics with four distinct Raman shifts as the symmetric stretching, the asymmetric deformation, asymmetric stretching and symmetric deformation. The asymmetric stretching modes correspond to the 1700-1200 cm$^{-1}$ Raman shift interval which is beyond the range of our measurements. The 1200-600 cm$^{-1}$ region is due to the symmetric stretching whereas the 500-100 cm$^{-1}$ region is assigned to the external vibrations of the carbonate group minerals (Rutt and Nicola, 1974; Sun et al., 2014))

#### 5.2.2.2 Edremit Field

CRS analyses are performed for a total of 6 samples on 110 different points (Table 5.2). Raman spectrums of some of the analysed minerals are given in Appendix C. The results show that ankerite is also one of the carbonate mineral phases and calcite has the highest abundance. Plagioclase solid solution series are identified as bytownite (Ca-rich member), andesine and labradorite, with bytownite being the dominant mineral. Other minerals observed in the samples are phlogopite, clinochlore, richterite, pargasite and diopside. Magnetite, lepidocrocite and orpiment constitute the opaque minerals examined in the thin sections in addition to the ones identified microscopically. A notable observation for Edremit field is that plagioclase minerals seem to become more calcic towards deeper levels (Table 5.2). Yet another observation is that in the sample taken from 1032 m depth, plagioclase composition changes from andesine in the core to bytownite on the rims indicating reverse zoning.

Table 5.2 Results of the Confocal Raman Spectroscopy (CRS) analyses for Edremit samples

| **Sample No.** | **Minerals** | | | | | | | | | | | | | | | | | | | | | | |
|---|---|---|---|---|---|---|---|---|---|---|---|---|---|---|---|---|---|---|---|---|---|---|---|
| | Calcite | Dolomite | Ankerite | Quartz | Andesine | Labradorite | Bytownite | Orthoclase | Biotite | Phlogopite | Muscovite | Clinochlore | Actinolite | Richterite | Pargasite | Diopside | Epidote | Magnetite | Hematite | Limonite | Lepidocrocite | Pyrite | Orpiment |
| EDR-912 | ● | | | ● | ● | ● | | ● | ● | | ● | | ● | | | | | | | | | ● | |
| EDR-958 | ● | | | ● | ● | | | ● | | | | | | | | ● | ● | | ● | | | | |
| EDR-964 | ● | | ● | ● | ● | ● | ● | ● | | | | | ● | | | ● | | ● | | ● | ● | ● | ● |
| EDR-994 | | ● | | ● | | ● | ● | | ● | | | ● | | ● | ● | | | ● | | | | | |
| EDR-1008 | | ● | | ● | | ● | ● | | ● | ● | | | ● | ● | | | | ● | | | | | |
| EDR-1032 | | | | ● | | | ● | ● | ● | | | | ● | | | | | ● | | | | | |

The Raman spectrums of plagioclase minerals against depth are examined for the effects of possible deformation and/or alteration (Fig.5.12). Following the grouping proposed by Freeman et al. (2008), the spectrums are investigated in five spectral regions each of which corresponds to five different modes as can be seen in Fig.5.12. The peak position of the strongest peak draws near the 500 cm$^{-1}$ with increasing Ca content as observed at 958, 964 and 1032 m depths (Fig.5.12). This Ca increase is also reflected by the increase in the Group II and Group III features with depth from 912 to 1032 m levels. Furthermore, Group IV and V features of the plagioclases decrease towards deeper levels, with the loss of sharp bands in the spectral range from 700 to 1200 cm$^{-1}$ which might be related to the effects of an alteration pertinent to plagioclase minerals. It should also be noted that the width of the Raman peak in the 500-510 cm$^{-1}$ becomes slightly wider with increasing depth from 912 m to 1032 m. This band broadening is related with the increased Al-Si disorder due to pressure induced deformation (Freeman et al., 2008) as can be expected from increasing lithostatic pressure with depth.

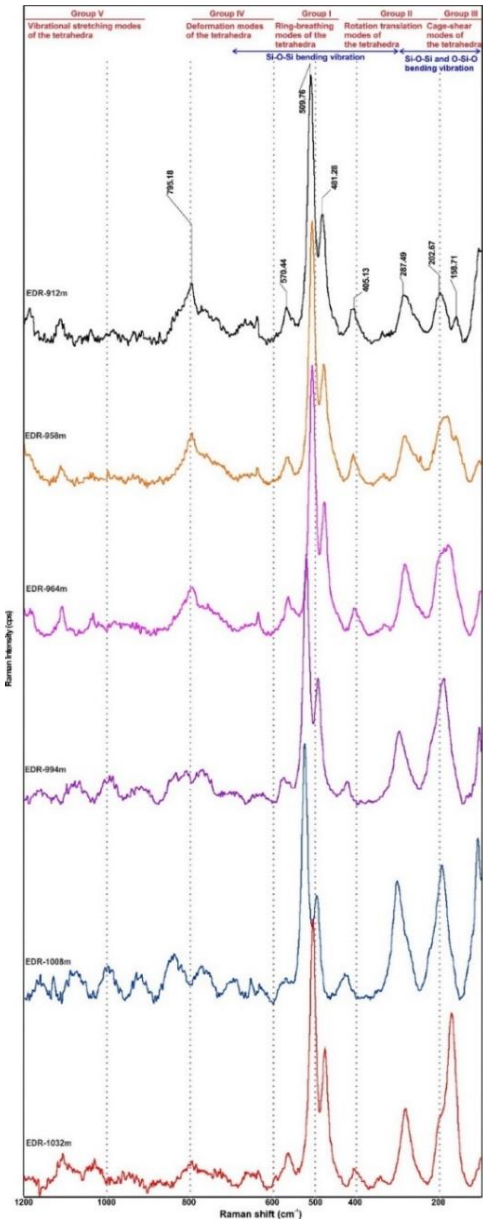

Figure 5.12. Raman spectrums of plagioclase minerals of the analysed samples from EDJ-12 well (Edremit field) against depth (Group I: Raman spectrums in the 450-520 cm$^{-1}$ related with the ring-breathing modes of the tetrahedral. Group II: Raman spectrums between 200-400 cm$^{-1}$ corresponding to rotation–translation modes of the tetrahedral. Group III: Raman peaks below the 200 cm$^{-1}$ representing the cage-shear modes of the tetrahedra. Group IV: Raman peaks in the 700-900 cm$^{-1}$ representative for the deformation modes of the tetrahedra. Group V: Raman peaks in the 900-1200 cm$^{-1}$ showing the vibrational stretching modes of the tetrahedra (Freeman et al., 2008). The Raman bands between 300-700 cm$^{-1}$ are also known as Si–O–Si bending vibration modes and the spectrums between 300-0 cm$^{-1}$ are a combination of Si–O–Si and O–Si–O bending vibrations (Lasaga and Gibbs, 1988))

## 5.3 Chemical Composition of Minerals

### 5.3.1 Akköy Field

Detailed characterization of minerals from solid solution series, feldspar, mica, amphibole and pyroxenes, is carried out utilizing EPMA technique. The results are tabulated in Appendix D and an example displaying the general view of the analysed sample is presented in Appendix E. Analyses are performed on a total of 183 points chosen from 11 thin sections (5 samples from PS-1, 6 samples from PS-2 well). The compositions of analysed feldspars resulted in 59% albite, 26% orthoclase and 15% oligoclase (Fig.5.13a). Regarding mica minerals, although the petrographic observations and XRD analyses point to biotite presence, results of selected samples which are deemed usable indicate muscovite composition (Fig.5.13b). Pyroxenes from the analysed spots are identified as augite (Fig.5.13c). Amphibole minerals, determined as Mg-hornblende, hastingsite and actinolite are calcic in composition (Fig.5.14). In addition to these observations, the presence of sulphur is detected in the compositions of feldspar and mica minerals pointing to hydrothermal fluid effect in the system (Appendix D).

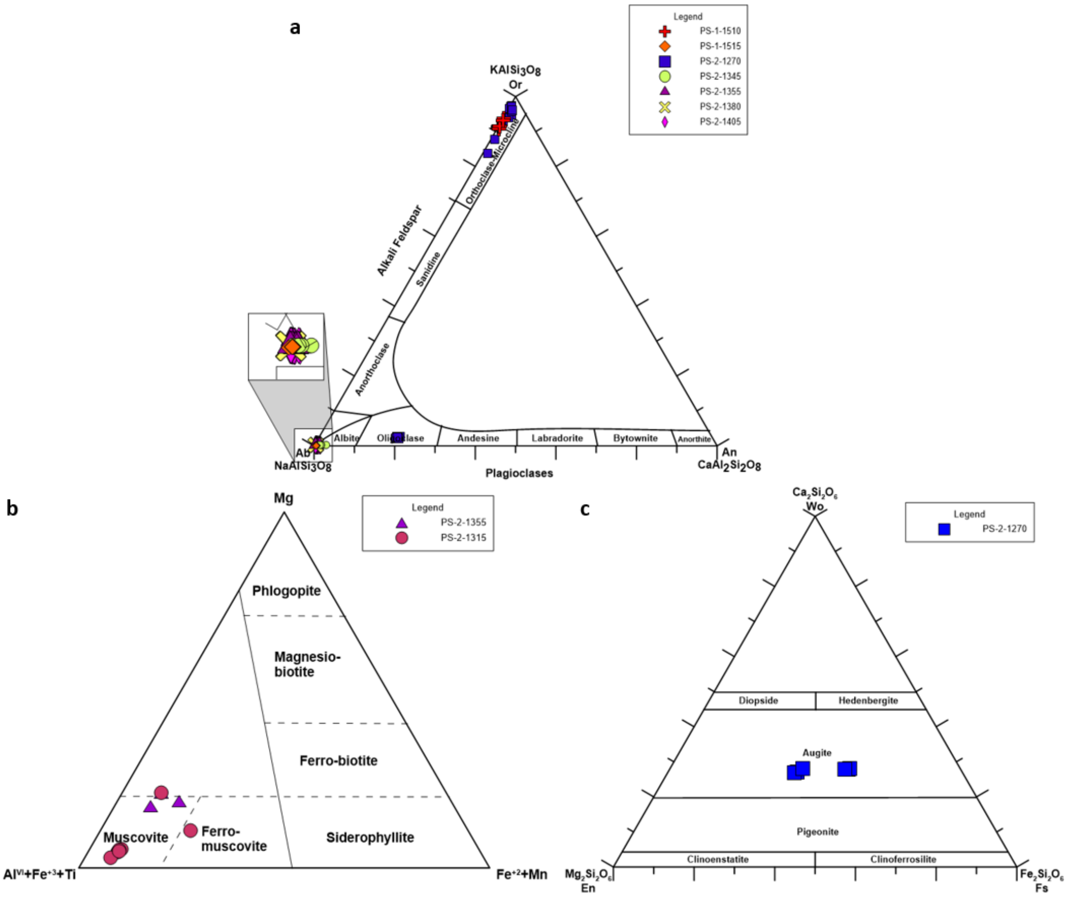

Figure 5.13. EPMA results of samples from Akköy field shown in ternary diagrams for a. feldspar minerals (Deer et al., 1992), b. mica minerals (Foster, 1960) and c. pyroxene minerals (Morimoto et al., 1988)

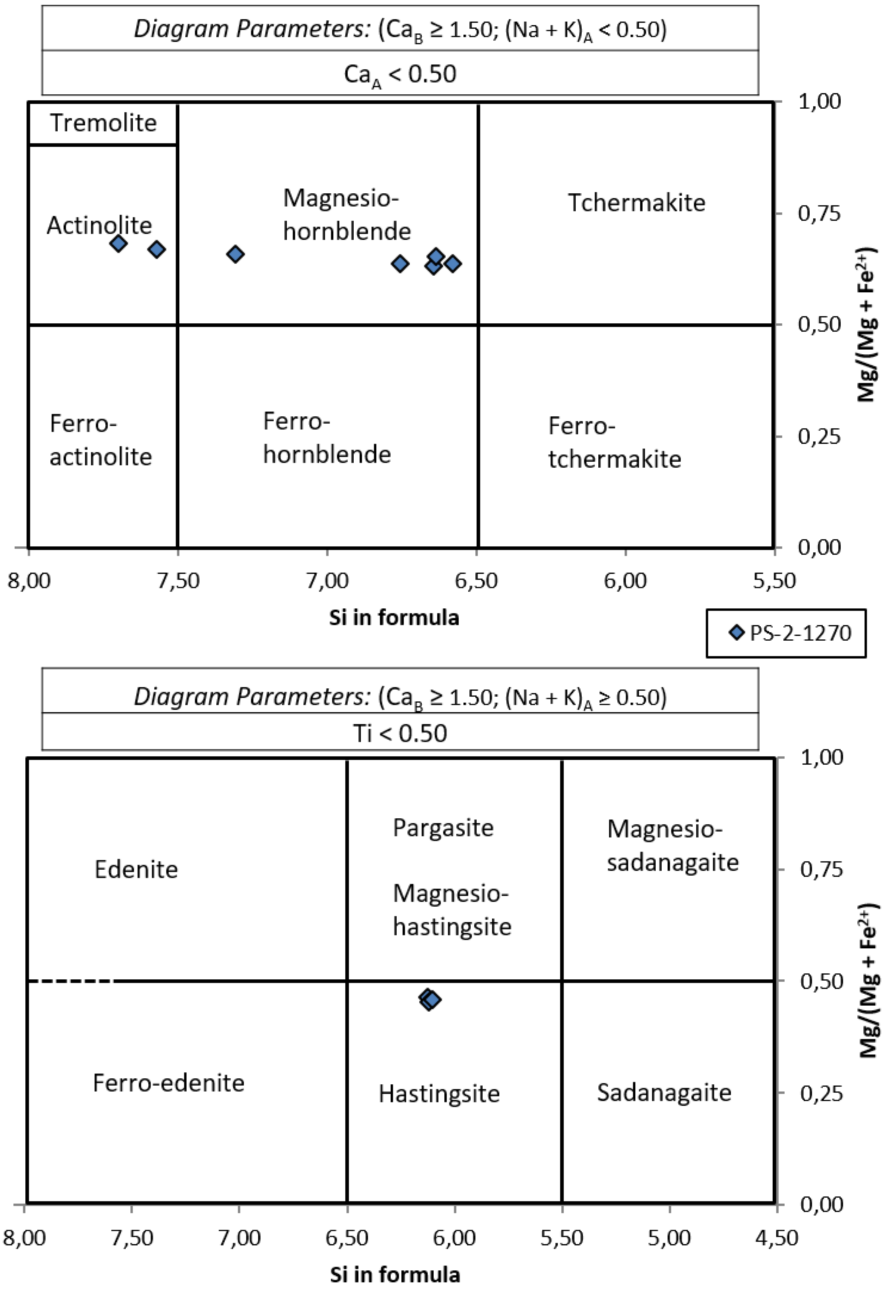

Figure 5.14. EPMA results of Akköy samples shown in classification diagrams of calcic amphiboles (Leake et al., 1997)

### 5.3.2 Edremit Field

EPMA studies are performed on a total of 284 spots for the 6 samples of EDJ-12 well (Appendix D). An example displaying the general view of the analysed sample is also presented in Appendix E. The results show that analyzed feldspars are 66% andesine, 19% orthoclase, 14% oligoclase and 1% sanidine in composition (Fig.5.15a). A detailed examination of sample from 1032 m depth reveals Na amount is relatively higher in the core whereas Ca has higher abundance in the rim (reverse zoning). The results of mica minerals point out Mg-Fe biotite composition (Fig.5.15b) and pyroxenes are found to be augite (Fig.5.15c). Some of the analyzed pyroxene grains are determined to be highly altered and they are not evaluated. Most of the amphibole minerals in the analyzed samples are calcic in composition and determined as Mg-hornblende, edenite and Mg-hastingsite (Figs.5.16a, 5.16b), while 3 points from two samples gave Fe-richterite composition (sodic-calcic, Fig.5.16c).

EPMA studies reveal the presence of sulphur in feldspar and mica minerals (Appendix D) pointing to hydrothermal fluid effect in the system, which may also stand for the $SO_4$-rich character of the geothermal waters (Avşar et al., 2013).

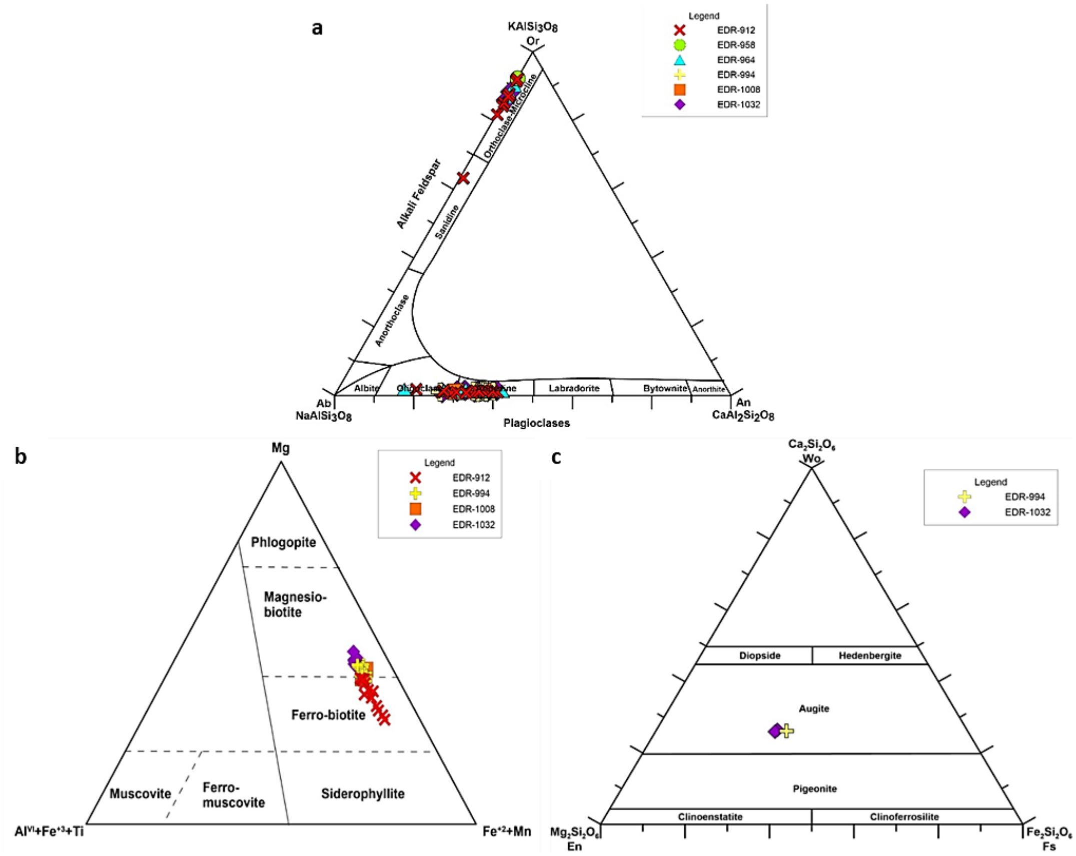

Figure 5.15. EPMA results of samples from Edremit field shown in ternary diagrams for a. feldspar minerals (Deer et al., 1992), b. mica minerals (Foster, 1960) and c. pyroxene minerals (Morimoto et al., 1988)

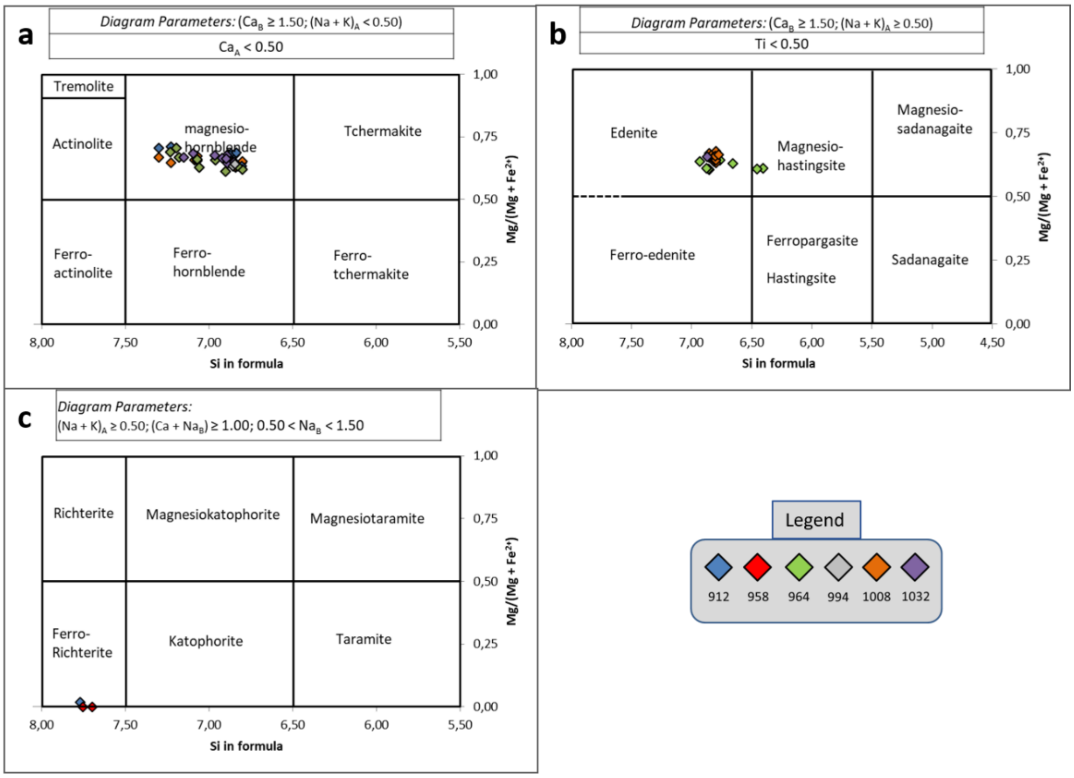

Figure 5.16. EPMA results of Edremit samples shown in classification diagrams of a, b. calcic and c. sodic-calcic amphiboles (Leake et al., 1997)

## 5.4 Whole Rock Geochemistry

### 5.4.1 Akköy Field

The XRF analysis results of both PS-1 and PS-2 wells of Akköy field are given as Appendix F. In both wells (PS-1 and PS-2), similar trends can be observed due to the lithological similarities (Figs.5.17 and 5.18). CaO values (although higher in PS-2) show increasing trends against depth for both of the wells (from ~5% to ~25% in PS-1 and from ~15% to ~60% in PS-2). On the other hand, $SiO_2$ values decrease towards the deeper levels in PS-2 (from ~40% to 10%), while in PS-1 there is no significant change (stays around 50%). The trends for CaO values imply the increasing abundance of Ca-bearing rocks such as marbles and calcschists (reservoir rocks) as also observed in the microscopic examinations (Figs.5.1a, 5.1b, 5.1c, 5.2a, 5.2b).

Changes in the abundances of minerals such as clays and mica (biotites) +/- chlorite +/- amphibole in schist fragments are reflected in the XRF results. Decreasing trend of $Al_2O_3$ values coupled with $K_2O$ values can be attributed to the decrease in clay mineral content from shallower to deeper levels in both wells. Enrichment displayed in the trends of $Fe_2O_3$ and MgO at depths around 1265-1275 m in PS-2 and ~1300 and ~1335 m in both wells, seem to be related to the abundance of schist fragments from these levels (Figs.5.1b, 5.1d, 5.1e). Given the similar geochemical behaviour as those of $Fe_2O_3$ and MgO, a correlative enrichment is observed for MnO, $Cr_2O_3$, $TiO_2$, Co and Ni values. The occurrence of relatively higher values of $SO_3$ coupled with $Fe_2O_3$, is in conformity with the observed pyrite (Fig.5.1a) and marcasite minerals in the samples. Increases in the concentrations of elements which are commonly associated with sulphide minerals (e.g. As, Cu, Pb, Zn) are also detected around 1310-1320 m depths. This observation can be attributed to sulphide mineralization in these levels.

Regarding the Loss on Ignition (LOI) contents, the values in PS-1 well are generally lower than the ones in PS-2 (<20% in PS-1, between 10% - 45% in PS-2). The PS-1 well LOI values are also relatively lower between 1375-1465 m depth compared to the shallower and deeper levels of the same well. On the other hand, for PS-2 well, there seems to be an increase in the LOI values starting at about 1375 m towards deeper levels. This increase in LOI values can be correlated with an increase in the carbonate content of the respective levels. It should be noted here that the well log of PS-1 and PS-2 wells reveals a transition from Miocene shale-marl to Paleozoic schist-marble levels of Menderes Massif metamorphics at about 1415 m and 1375 m depths, respectively (Fig.3.5). For PS-1 well, the decrease in the LOI value in between 1375-1465 m levels can be attributed to a relative decrease in the abundance of carbonate rocks.

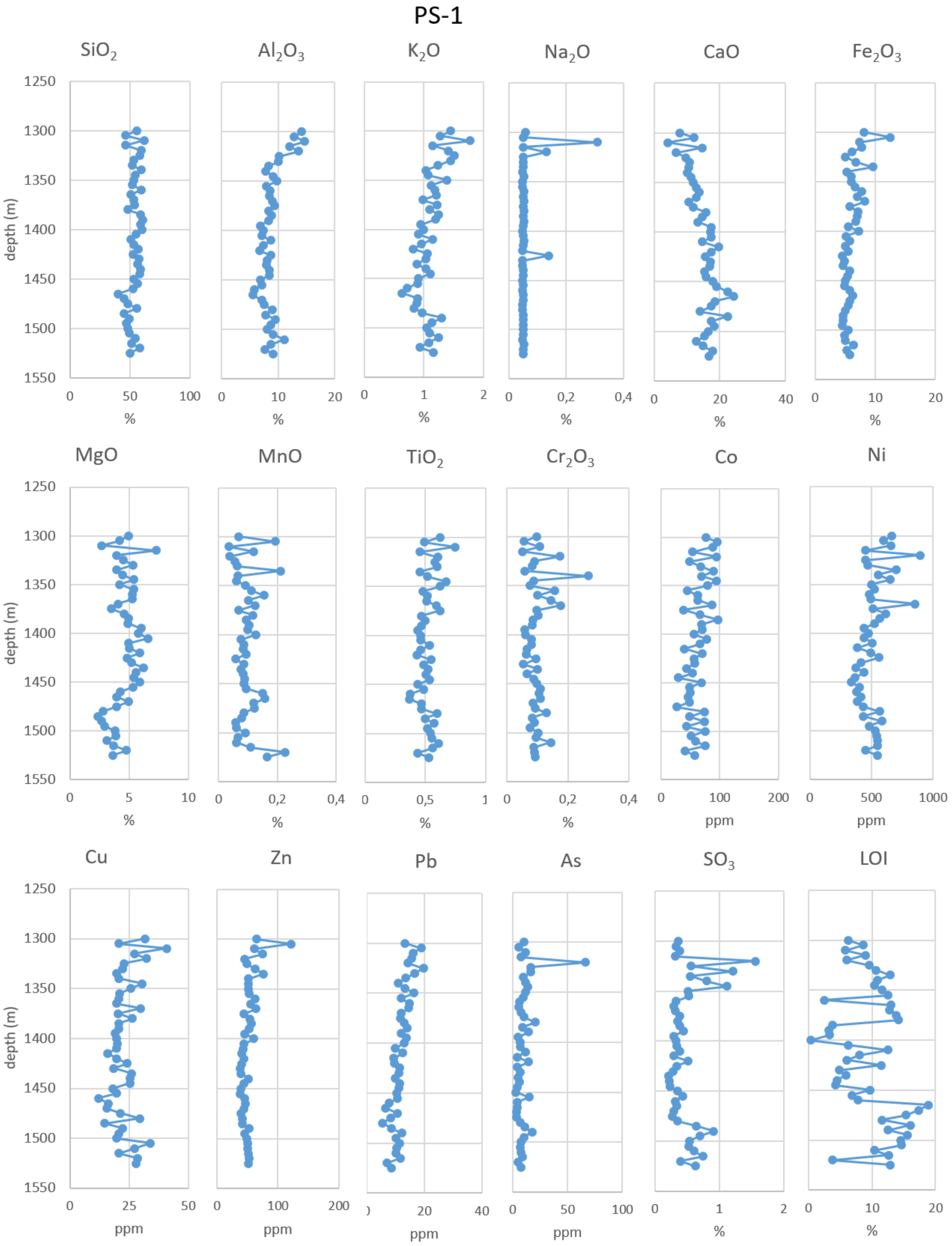

Figure 5.17. Major-minor oxide, trace element, loss on ignition (LOI) versus depth diagrams of the PS-1 well in Akköy field

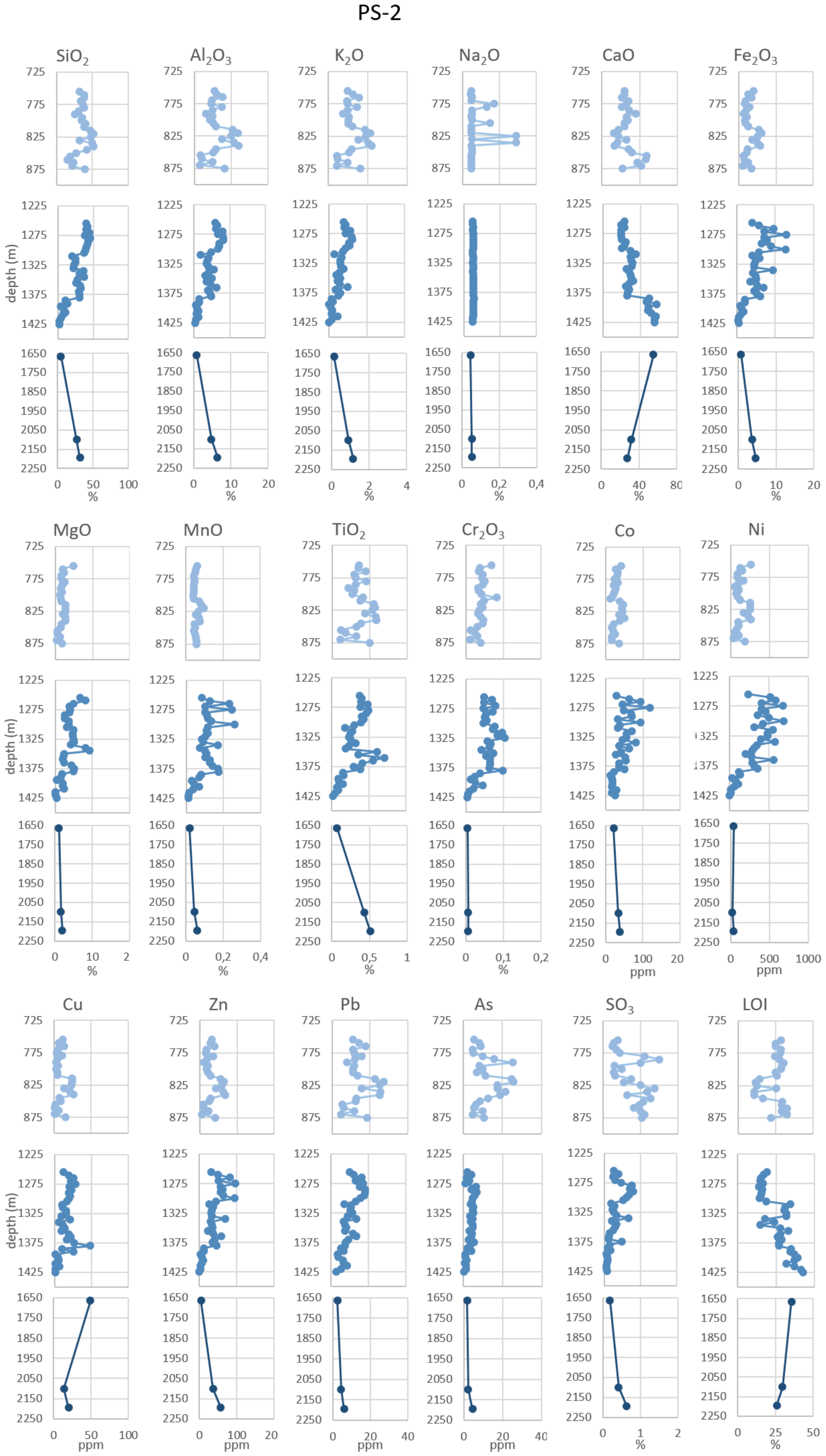

Figure 5.18. Major-minor oxide, trace element, loss on ignition (LOI) versus depth diagrams of the PS-2 well in Akköy field

### 5.4.2 Edremit Field

The XRF analysis results of EDJ-12 well of Edremit field are given in Appendix F. Three different concentration levels can be distinguished from the results of $SiO_2$, $Al_2O_3$, $Fe_2O_3$, MgO, MnO, $TiO_2$, Ni, Y, Zr, Pb, Th and $SO_3$ at depth intervals: 900-928 m, 930-974 m and 976-1038 m (Fig.5.19).

CaO values increase between 900-928 m, decrease between 930-984 m, start to increase again at 986 m. The increasing segments of the trend indicate the increasing abundance of Ca-bearing minerals (calcite and/or Ca-rich feldspar). On the other hand, $SiO_2$ and $Al_2O_3$ show inverse relation in terms of the trends they display against depth (e.g. results corresponding to 930-974 m depth interval yield relatively higher values for $SiO_2$ and lower values for $Al_2O_3$, with respect to the overlying and underlying levels). This observation might indicate the change in the relative abundances of quartz, feldspar and mica minerals.

MgO, $Fe_2O_3$, MnO, $TiO_2$ have higher values between 976-1038 m compared to the shallower levels. This increase can be attributed to the biotite abundance (coupled with $Al_2O_3$ content) observed in the samples, along with amphibole which is especially abundant between 990-1016 m, epidote and pyroxene (Figs.5.6d, 5.6e, 5.6f).

A conspicuous increase in $SO_3$ content at depths of ~966 and 980 m is also noted in XRF results which is coupled with an increase in the As content at 980 m (Fig.5.19). Given that the samples from these depths have highly fragmented appearance and abundant pyrite occurrence (Fig.5.4f), this increase points to sulphide mineralization possibly associated with hydrothermal brecciation.

A follow-up study for the paper (Elidemir et al., 2022) regarding the potential effect of alteration along the well bore in Edremit field is conducted with the CIA (Chemical Index of Alteration; Nesbitt and Young, 1982) and WIG (Weathering Index of Granite; Gong et al., 2013) indices which are used to describe the alteration and weathering intensities (Gong et al., 2016; Wu et al. 2021). The calculations are performed with the utilization of major oxide contents and the results are qualitatively described according to the degree of alteration/weathering as incipient for CIA<60 and WIG>60, intermediate for CIA = 60–80 and WIG = 20–60, extreme for CIA>80 and WIG<20 (Wu et al. 2021 and the references therein). The calculated CIA and WIG values of the samples point to incipient and slightly intermediate degree of alteration (Fig.5.19). As the sensitivity of WIG is higher than CIA (Gong et al., 2013), more variations can be detected in WIG values and relatively notable decreases are observed around levels 930 and 976 m suggesting a hydrothermal activity.

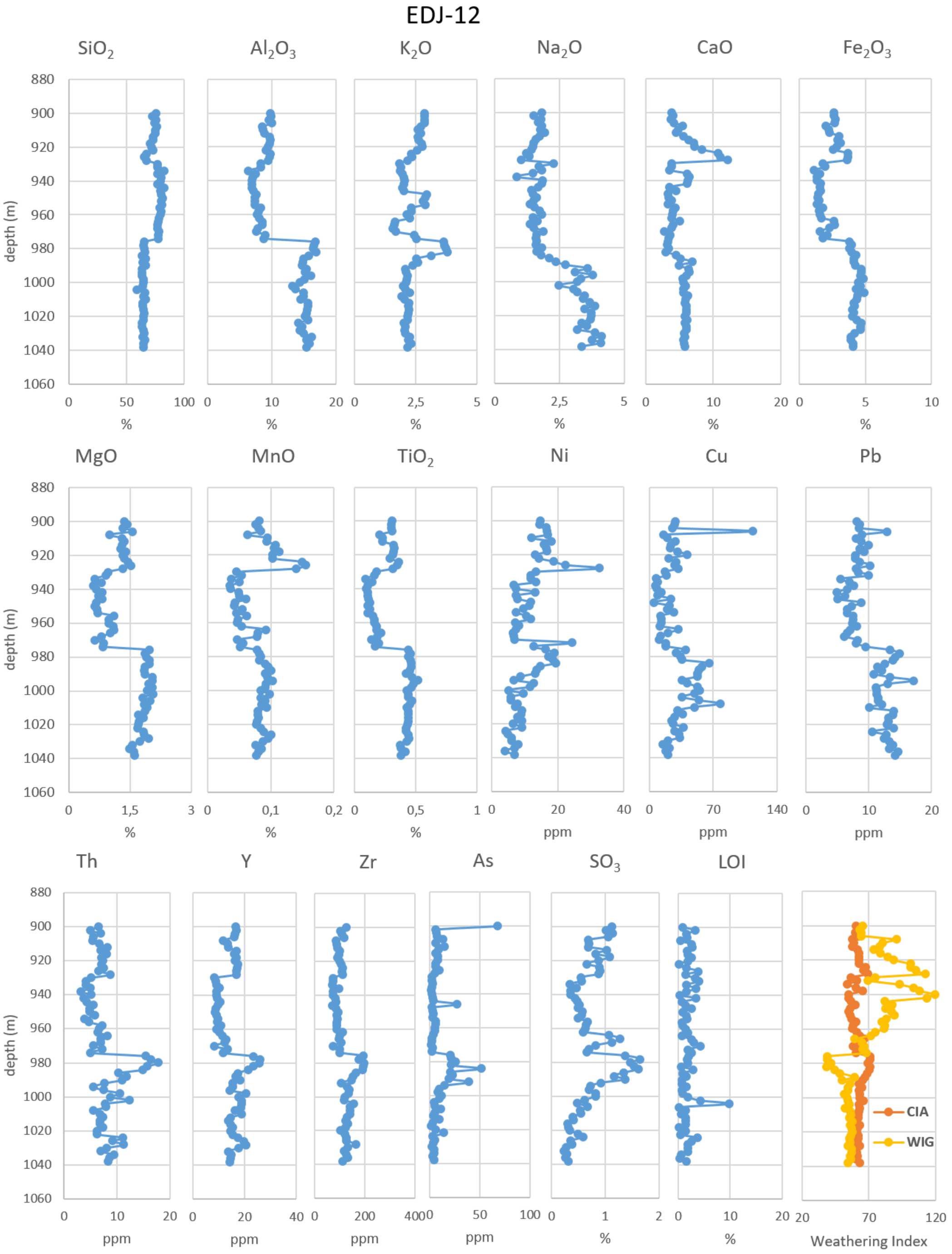

Figure 5.19. Major oxides, trace elements, loss on ignition (LOI) and the weathering indices of CIA and WIG variation diagrams with depth of the EDJ-12 well in Edremit field

## 5.5 Determination of the Modal Mineralogy

### 5.5.1 Akköy Field

Mineral percentages of the cutting samples from PS-1 and PS-2 wells are determined semi-quantitatively and selected results are visualised as pie charts (Figs.5.20, 5.21). The results indicate that silica and carbonate minerals are the main mineral phases in the rock samples. Mineral weight percentages of quartz and calcite are in the range of 27.6-52.9% and 0-26.6% in PS-1, 19.9-93.9% and 0-55.6% in PS-2, respectively. In average, clay minerals consist of approximately 16% in the samples of PS-1 while this ratio drops down to 8% in PS-2.

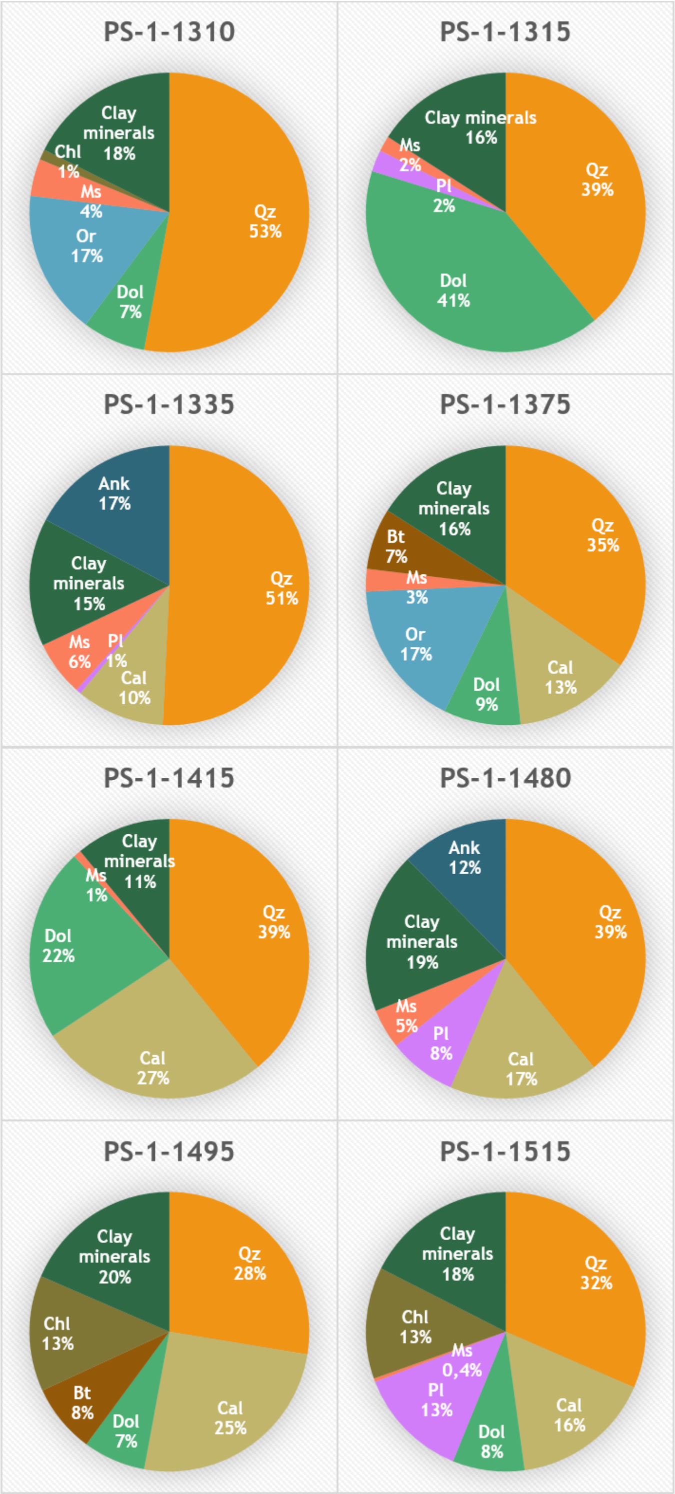

Figure 5.20. Mineral weight percentages of analysed samples from PS-1 well in Akköy field (Ank: ankerite, Bt: biotite, Cal: calcite, Chl: chlorite, Dol: dolomite, Ms: muscovite, Or: orthoclase, Pl: plagioclase, Qz: quartz)

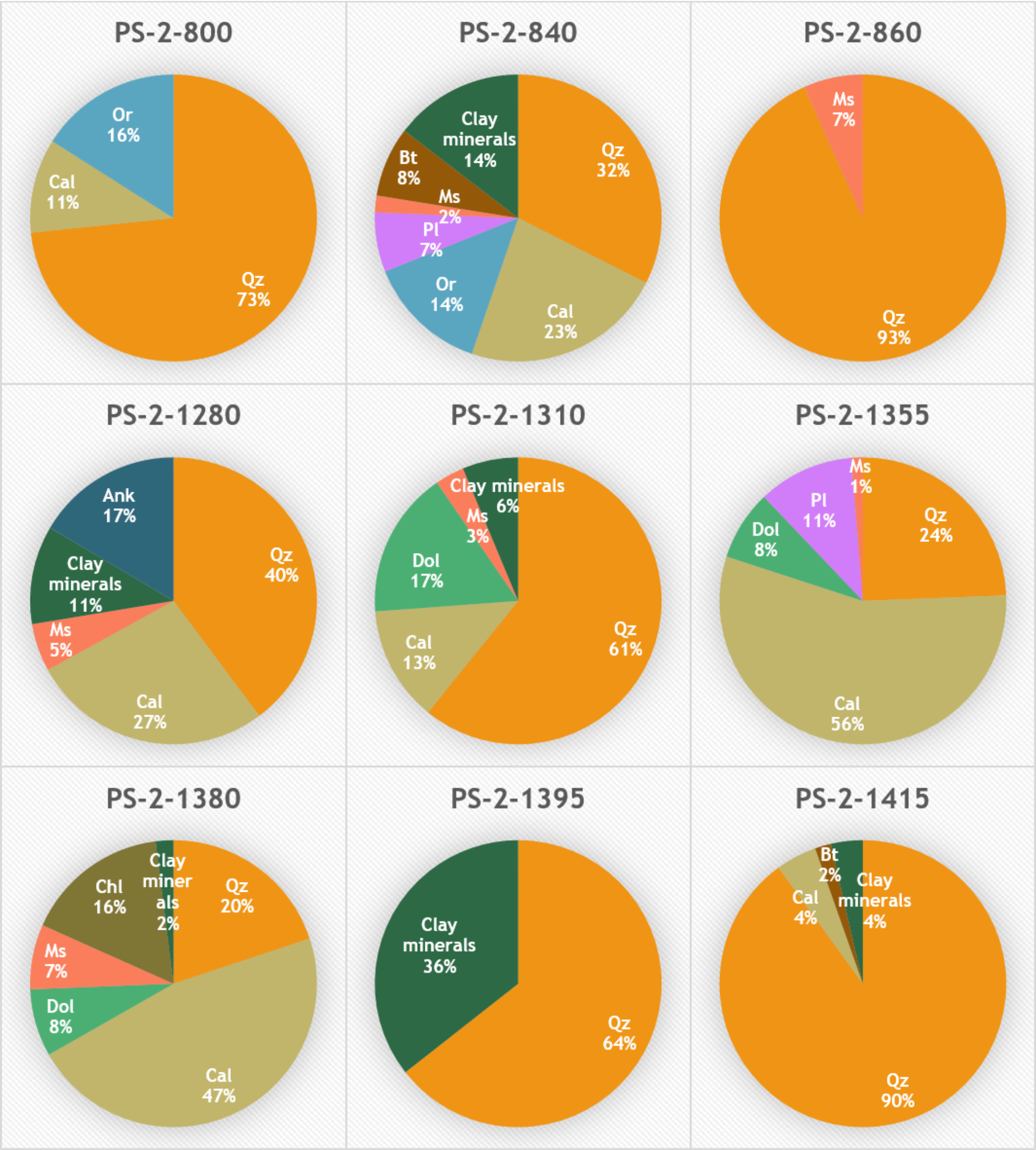

Figure 5.21. Mineral weight percentages of analysed samples from PS-2 well in Akköy field (Ank: ankerite, Bt: biotite, Cal: calcite, Chl: chlorite, Dol: dolomite, Ms: muscovite, Or: orthoclase, Pl: plagioclase, Qz: quartz)

### 5.5.2 Edremit Field

Pie charts depicting the weight percentages of minerals from EDJ-12 well samples determined from the XRD analyses' results are presented in Figure 5.22. The abundance of the primary minerals, quartz and orthoclase, ranges from 0-79.5% and 0-75.8%, respectively. Clay minerals constitute 8% of the samples in average.

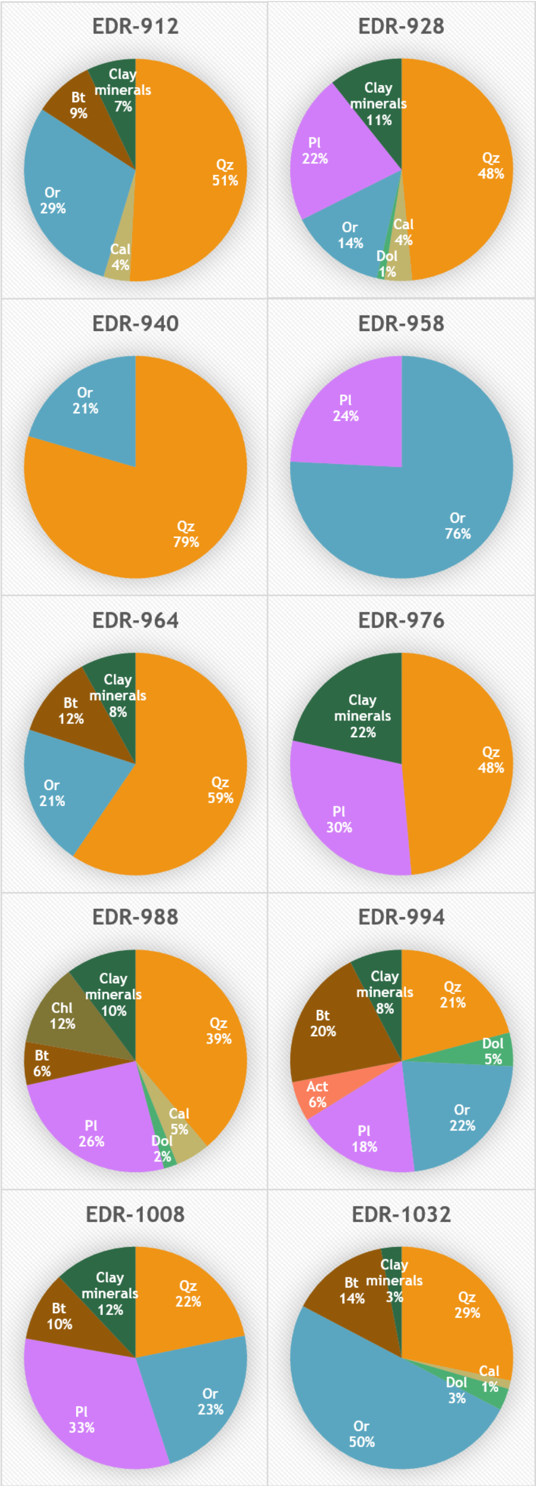

Figure 5.22. Mineral weight percentages of analysed samples from EDJ-12 well in Edremit field (Act: actinolite, Bt: biotite, Cal: calcite, Chl: chlorite, Dol: dolomite, Ms: muscovite, Or: orthoclase, Pl: plagioclase, Qz: quartz)

## 5.6 Comparison of the Lithogeochemical Results from Akköy & Edremit Fields

The investigations under microscope display that in the drill cuttings of Akköy field, dominant rock fragments are calcareous rocks (marble/limestone) and the main mineral phases include clayey carbonates and quartz. In Edremit samples, on the other hand, granitic rocks (granite/granodiorite) constitute the abundant fragments, while similar to Akköy field, quartz is the primary mineral. Fe-bearing minerals (hematite/limonite ± pyrite) present in both fields while pyrite is abundant in certain levels in both fields. XRD results are in favour of the previous findings regarding mineral species. CRS results of Edremit samples reveal more variety of silicate minerals (especially for feldspars and amphiboles) than in the samples of Akköy field. The feldspars of Akköy field seem to be more sodic in composition than the ones in Edremit.

Effects of the hydrothermal fluids on the samples and/or the indications for sulphide mineralization in Akköy and Edremit systems can be observed both in microscopic examinations and in the results of geochemical analyses (mainly EPMA and XRF).

In XRF results, $SiO_2$ values are higher in Edremit samples (>50%) while in Akköy, the amount is ≤50%. Edremit samples also have higher $Na_2O$ (~1-4%, in Akköy <0.4%) values, the relatively higher results of these two elements (Si and Na) may be attributed to the abundance of feldspar minerals. On the other hand, CaO content seems to be higher in Akköy samples (~20% to 50% in some samples), than in Edremit samples (<~10%), pointing to the dominant carbonate lithology in Akköy, as observed in the lithogeochemical investigations. Although there are some exceptions, As and $SO_3$ values are similar in both fields which may indicate a similar intensity of hydrothermal fluid activity in these systems.

The averages of the mineral weight percentages as generally classified into mineral groups are calculated for both fields and tabulated in Table 5.3. Average calculations are performed for 17 samples of Akköy and 10 samples of Edremit which are the samples studied for modal mineralogy.

Table 5.3 Comparison of the average modal mineralogy of the two fields

| **Field** | **Mineral Weight Percentage Averages (wt%)** | | | | | |
|---|---|---|---|---|---|---|
| | **Silica** | **Carbonates** | **Feldspars** | **Micas**[a] | **Clays** | **Other Minerals**[b] |
| **Akköy** | 47.84 | 27.23 | 6.18 | 4.22 | 11.95 | 2.58 |
| **Edremit** | 39.68 | 2.52 | 40.8 | 7.2 | 8.02 | 1.78 |

[a] micas: muscovite+biotite for Akköy, only biotite for Edremit

[b] other minerals: chlorite for Akköy, chlorite+actinolite for Edremit

Although quartz is the main mineral in both systems as also determined by previous studies, some differences in the modal mineralogies can be observed in Akköy and Edremit fields. In the samples of Akköy field, carbonate minerals have higher percentage than in Edremit samples, while in Edremit, feldspars are more abundant than in Akköy. The percentage of clay minerals is higher in the samples of Akköy field than the samples of Edremit.

These differences in mineralogy will potentially yield different modelling results in terms of $CO_2$-water-rock interactions.

## 5.7 Geochemical Implications for Possible Fault Zones of Edremit Field

Lithogeochemical characterization of Edremit geothermal field realized through the analyses of a total of 70 drill cuttings from EDJ-12 well in terms of their mineralogic-petrographic and geochemical properties against depth, has revealed three distinctive zones along the wellbore (Elidemir et al., 2022). The variations in rock fragments associated with chemical changes with increasing depth are visualized in Fig.5.23.

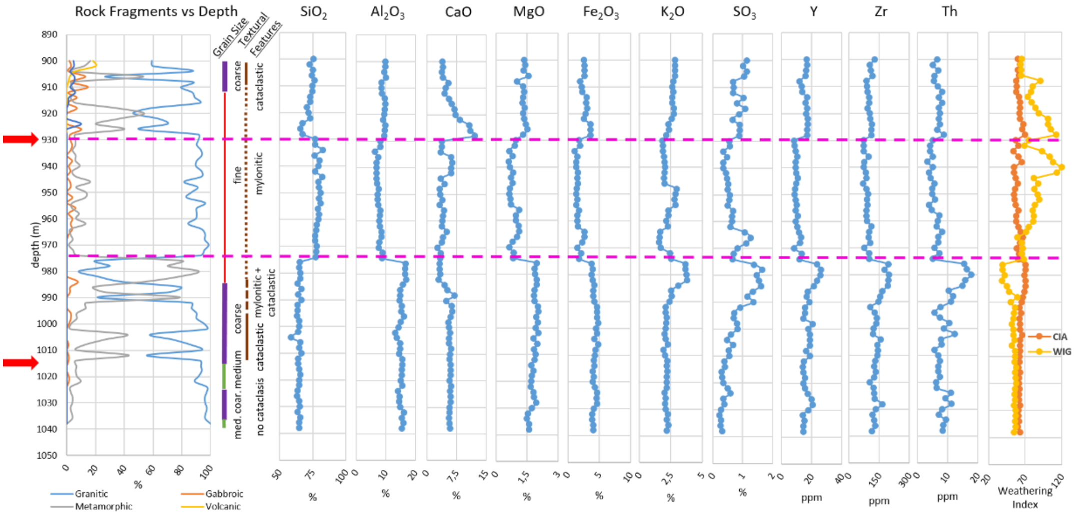

Figure 5.23. Correlation of variations in rock fragment percentages, grain sizes and element concentrations ($SiO_2$, $Al_2O_3$, CaO, MgO, $Fe_2O_3$, $K_2O$, $SO_3$, Y, Zr and Th) and the weathering indices of CIA and WIG of samples with depth in Edremit field (red arrows represent reported water leakage zones)

The effect of alteration which occurs as a result of fluid-rock interactions, changes proportionally with respect to the distance from the flow paths of hydrothermal fluid in a geothermal system (Warren et al., 2007). Variations in concentrations of both mobile and immobile elements with increasing depth, provide valuable information regarding fluid flow zones and lithologic correlations, respectively (Gifkins et al., 2005; Mauriohooho et al., 2016). The elements which are relatively mobile and can be easily transported in migrating fluids during hydrothermal activity are Si, Fe, Mg, Ca, Na, in addition to the large ion lithophile elements of Sr, K, Rb and Ba (and sometimes Th) due to their low ionic potential (Pearce, 1982; Gifkins et al., 2005; Franzson et al., 2008). Al and high field strength elements such as Ti, Zr and Y constitute the elements which remain relatively immobile and therefore, unlikely to undergo geochemical changes during hydrothermal alteration (Wagner and Jochum, 2002; Gifkins et al., 2005; Franzson et al., 2008; Mauriohooho et al., 2016). Consequently, whole rock geochemistry results which correlate well with the petrographical changes and bring out three distinctive zones (Fig.5.23), can be used to elaborate on the hydrothermal fluid pathways. Since the reported leakage is from 930 m depth, the part in between 928-976 meters is likely to belong to the fluid path of the system. Moreover, the results show inverse relationship of $SiO_2$ with other major elements (Figs.5.19, 5.23) which may indicate the presence of a Si-rich hydrothermal fluid. This can also explain the slightly silica-oversaturated nature of the geothermal waters in the field as reported by Avşar et al. (2013). Earlier alteration studies explain that as a result of Si-rich fluid input to a system, the precipitation of silica within the pore spaces leads to the loss of FeO, MgO, CaO, $K_2O$, MnO and other metals from the rocks (Gifkins et al., 2005 and the references therein). The chemical variations identified with whole rock geochemistry results are also supported by the textural features which imply metasomatism (Fig.5.7d) and secondary uralitization (Figs.5.7e, 5.7f).

Another indication of a flow path being present in the middle section of the downhole well plot, is the textural properties of the samples (Fig.5.23). The changes from cataclastic texture around the levels of 910 m to mylonitic texture towards 920 m, point to the proximity of the fault zone. From mortar texture to cataclastic texture, these features implicate areas that are at the edge of a fault. Mylonitic texture associated with fine grained rock fragments showing increased degree of deformation (Rankin, 1982) corresponds to the core of the fault zone. Therefore, textural features are in agreement with the geochemical observations regarding the location of hydrothermal fluid path and fault zone.

WIG calculations (Figs.5.19, 5.23) also point to the presence of a hydrothermal activity in various levels. A slightly increased degree of alteration is observed especially around 930 and 976 m depths. Although WIG values increase around 940 m (indicating decreasing alteration), this increase can be attributed to higher carbonate content (Gong et al., 2015) which is coupled with a small increase in CaO values in these levels (which is also the case in 928 m depth). After 942 m, the intensity of alteration starts increasing towards deeper levels. Moreover, the part from 976 to 1038 m displays an increased alteration effect in comparison with shallower levels.

The presence of fault zones and fluid paths inferred from this study are likely to correspond to the deep buried fault zones previously mentioned in Avşar (2011) and Avşar et al. (2013). The piezometric surface contour maps reported in these studies (and the references therein), point to two buried faults, the intersection of which shows a potentiometric (piezometric) high. The intersection is also revealed in the electrical resistivity surveys displaying low resistivity anomalies. It was reported that geothermal fluid ascends towards upper levels through this intersection of the buried faults.

A notable remark is that CRS and EPMA results suggest that towards deeper levels, the abundance of Ca-bearing minerals (feldspars and amphiboles) increases. This observation is in agreement with the remark of Avşar et al. (2013) that hydrogeochemistry of geothermal waters suggests increase in the calcite saturation index with increasing temperature (corresponding to increasing depth) in the field. Moreover, in the sample EDR-1032 from 1032 m depth, the plagioclase grains are characterized by reverse zoning, coupled with the increased Ca content as determined from the Raman spectrums of plagioclase minerals. Calculated WIG index values also suggest a change in the alteration degree towards deeper levels. These observations, combined with the information regarding a water leakage zone at 1015 m depth, might point to the presence of another fluid path around these levels.

# CHAPTER 6

# HYDROGEOCHEMICAL CHARACTERIZATION

Geochemical studies are performed on two water samples collected from PS-1 well-head in Akköy geothermal field. The results of the analyses lead up to i) the assessment of hydrogeochemical facies of the geothermal waters, ii) the estimation of possible reservoir temperature with geothermometry applications, iii) the evaluation of minerals for the potential of scaling with speciation–solubility calculations and iv) insight regarding the origin of fluids. While geochemical properties of Akköy water samples are personally investigated, for Edremit, the findings from the 2013 study of Avşar et al. are compiled in this chapter.

## 6.1 Geochemical Composition & Water Types

### 6.1.1 Akköy Field

The hydrochemical analyses results of the water samples collected in 2018 and 2021 from PS-1 well in Akköy field, are presented in Table 6.1 and major anion-cation concentrations are illustrated as Schoeller diagram in Figure 6.1. The waters are of alkaline-bicarbonate-sulphate (Na+K-$HCO_3$-$SO_4$) type and in three years although an increase in Ca and $SO_4$ contents is observed, there is no significant change in the hydrogeochemical facies of the thermal waters.

Table 6.1 Chemical analyses' results of the water samples from PS-1 well in Akköy field

| **PS-1** | **2018** | **2021** |
|---|---|---|
| T (°C)* | 81 | - |
| pH* | 7.6 | - |
| EC (µS/cm)* | 4371 | - |
| Na (mg/l) | 703 | 642 |
| $NH_4$ (mg/l) | 24 | <0.064 |
| K (mg/l) | 135 | 91 |
| Mg (mg/l) | 60 | 41 |
| Ca (mg/l) | 265 | 354 |
| $CO_3$ (mg/l) | 0 | 0 |
| $HCO_3$ (mg/l) | 1789 | 1679 |
| F (mg/l) | 3.3 | 4.1 |
| Cl (mg/l) | 73 | 72 |
| $NO_2$ (mg/l) | <0.05 | 0.55 |
| $NO_3$ (mg/l) | 6.9 | 10.6 |
| $PO_4$ (mg/l) | 295 | - |
| $SO_4$ (mg/l) | 894 | 1295 |
| Fe (µg/l) | 349 | - |
| Al (µg/l) | 20.11 | - |
| $SiO_2$ (mg/l) | 69 | 75 |
| CBE | 2.11 | -4.79 |

*Well-head measurements (on-site)

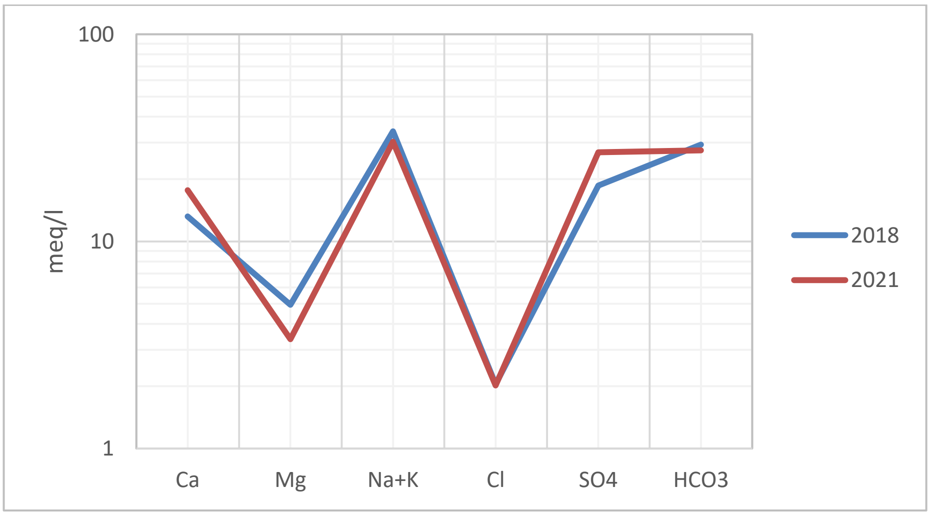

Figure 6.1. Schoeller diagram of waters from PS-1 well in Akköy field

The compositions of the waters are likely to be affected by water-rock interactions. Metamorphics (schist-calcschist-marble-quartzite) which comprise the reservoir rocks of the system provide the calcium, sodium and bicarbonate ions to the waters while S-bearing minerals are the potential source for $SO_4$ contents. High sodium values can also be attributed to the dissolution of Na-plagioclases (Fig.5.13a).

### 6.1.2 Edremit Field

There was no water data available for the studied EDJ-12 well and hence, previously published data of water samples from different wells in Edremit field (Avşar 2011; Avşar et al. 2013) are used in this study. As determined from major anion-cation contents of the waters of Edremit field (Avşar et al., 2013), hydrogeochemical facies are divided into three types according to the temperature ranges of the samples. The waters with measured temperature values are higher than 40°C are of $Na + K - SO_4$ type, the ones in between 30-40°C are of $Ca - SO_4$ type and relatively colder waters (<30°C) are of $Ca - HCO_3$ type (Fig.6.2). Possible processes that govern the system are identified as mixing and water-rock interactions.

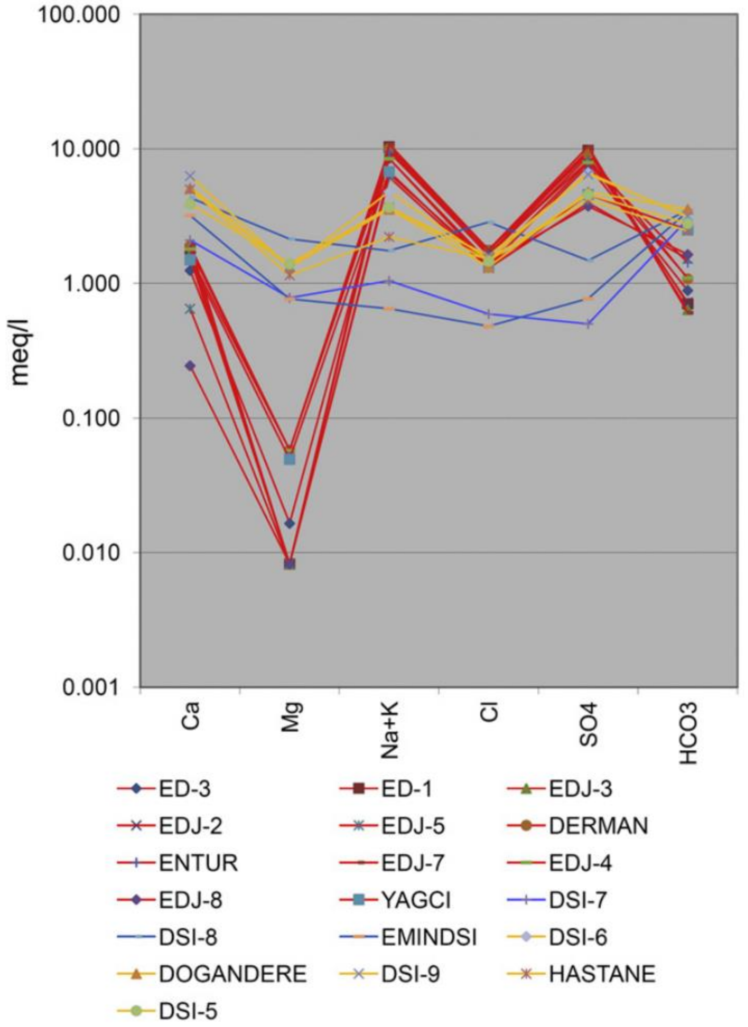

Figure 6.2. Schoeller diagram of waters from Edremit geothermal field (red: >40°C, orange: 30–40°C, blue: <30°C) (from Avşar et al., 2013)

## 6.2 Isotopic Compositions

### 6.2.1 Akköy Field

Stable isotope composition of the water sample collected in 2021 from PS-1 well is presented in Table 6.2 and plotted in $\delta^{18}O$-$\delta D$ diagram (Fig.6.3). The position of the sample with respect to the Global Meteoric Water Line (GMWL) points to a meteoric source. C-isotope composition indicates that carbon content of the water originates from the dissolution of carbonate rocks ($\delta^{13}C$ = 0‰; Sano and Marty, 1995). The determination of the original C-isotope composition of the system is of critical importance with regard to the monitoring of injected $CO_2$ in a possible carbon storage project.

Table 6.2 Stable isotope analysis results of the water sample from PS-1 well in Akköy field

| Sample | $\delta^{18}O$‰ (VSMOW) | $\delta^{2}H$‰ (VSMOW) | $\delta^{13}C$-DIC‰ (VPDB) |
|---|---|---|---|
| PS-1.2021 | -9.04 | -67.51 | 1.07 |

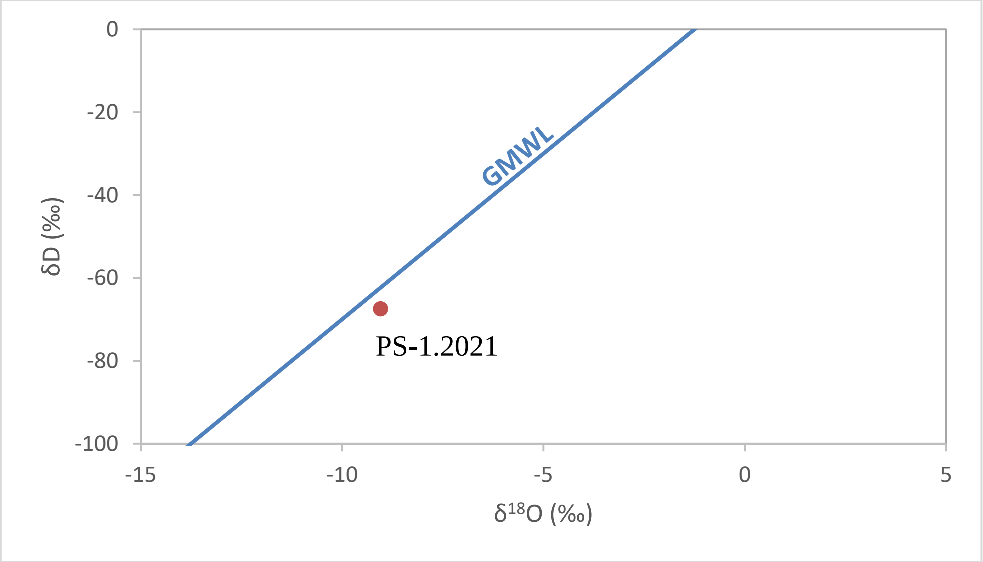

Figure 6.3. $\delta^{18}O$-δD diagram for the water sample from PS-1 well in Akköy field (GMWL: Global Meteoric Water Line ($\delta D = 8\ \delta^{18}O+10$) (Craig, 1961))

Since only one production well is present in the field, the estimation of recharge altitude with $\delta^{18}O$ and $\delta D$ isotopes is performed using the equations that are previously determined for Gölemezli and Pamukkale areas (Yıldırım and Güner, 2002; Alçiçek et al., 2019). The calculations result in between 1524 to 1543 m indicating that the possible recharge source of the waters is Babadağ Mountain (Fig.3.3). This implication is in accordance with the fluid circulation pathways depicted in conceptual models of the area (Şimşek, 1985; Alçiçek et al., 2019).

### 6.2.2 Edremit Field

Stable isotope compositions of Edremit waters display a range of -9.47‰ to -6.71‰ for $\delta^{18}O$, and -52.22‰ to -38.72‰ for $\delta D$ values (Avşar et al., 2013), indicating a meteoric source according to the Global Meteoric Water Line (GMWL) plot of the samples (Fig.6.4). It is reported in Avşar et al. (2013) that relatively hot waters have lower $\delta^{18}O$ and $\delta D$ values than colder waters, pointing to higher and lower recharge altitudes, respectively. The distribution of the waters also indicates mixing as a possible subsurface process. C-isotope values of the samples range between -14.4‰ to -9.1‰ (Avşar et al., 2013), indicating an organic source (Sano and Marty, 1995).

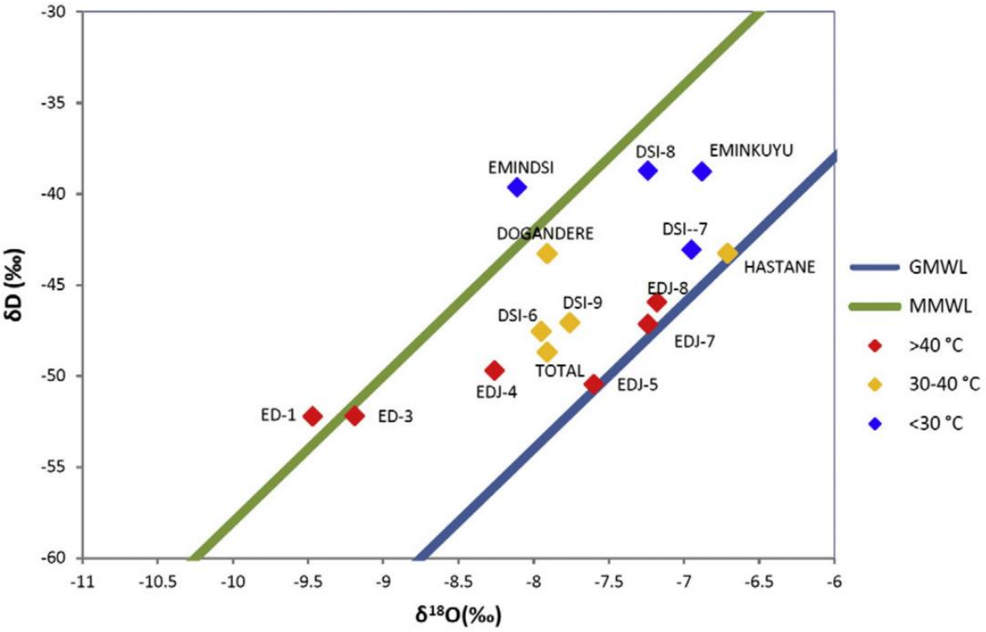

Figure 6.4. $\delta^{18}O$-$\delta D$ diagram for the water samples of Edremit field (MMWL: Mediterranean Meteoric Water Line (IAEA, 1981); GMWL: Global Meteoric Water Line ($\delta D = 8\ \delta^{18}O+10$) (Craig, 1961); red: >40°C, orange: 30–40°C, blue: <30°C) (from Avşar et al., 2013)

## 6.3 Geothermometry Applications

### 6.3.1 Akköy Field

Reservoir temperature estimations are carried out through the use of silica and cation geothermometers (Table 6.3). The maturity of the waters that reflects the physical-chemical balance between the fluid and the host rock is evaluated with Na-K-Mg ternary diagram developed by Giggenbach (1988) for the determination of the applicability of geothermometers (Fig.6.5). The samples plot into immature water zone indicating ongoing water-rock interactions.

Table 6.3 Chemical geothermometer results of Akköy samples (values in °C)

| **PS-1** | **Quartz**[a] | **Quartz-max. steam loss**[a] | **Chalcedony**[a] | **Na/K**[b] | **Na/K**[c] | **Na/K**[d] | **Na/K**[e] | **Na/K**[f] | **Na-K-Ca**[g] | **K-Mg**[e] |
|---|---|---|---|---|---|---|---|---|---|---|
| 2018 | 117 | 116 | 88 | 280 | 270 | 273 | 290 | 283 | 222 | 110 |
| 2021 | 122 | 120 | 94 | 249 | 228 | 233 | 262 | 238 | 198 | 104 |

[a] Fournier, 1977

[b] Fournier, 1979

[c] Truesdell, 1976

[d] Arnorsson et al., 1983

[e] Giggenbach, 1988

[f] Tonani, 1980

[g] Fournier & Truesdell, 1973

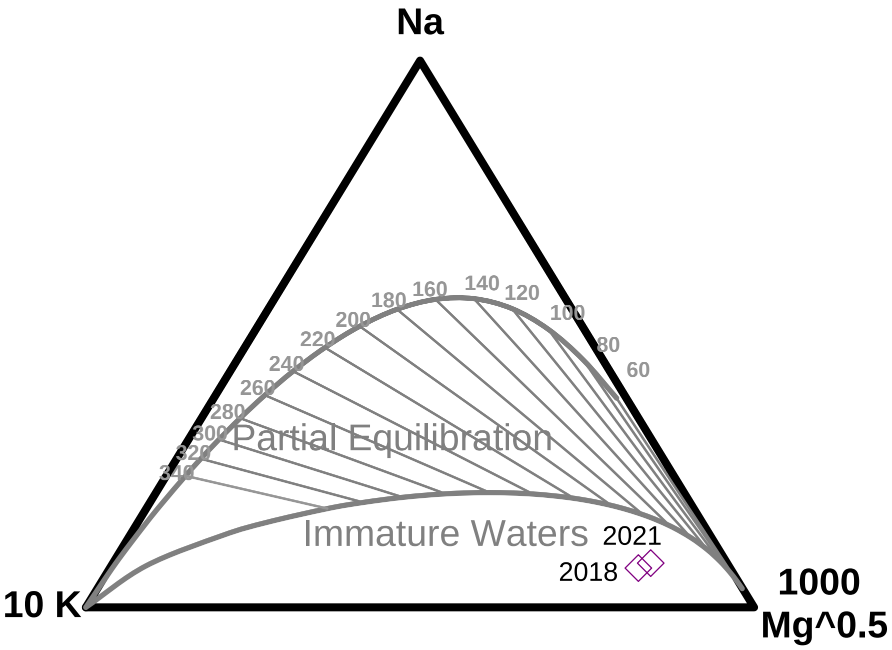

Figure 6.5. Na-K-Mg ternary diagram of Akköy water samples (Giggenbach, 1988)

Temperatures calculated with silica geothermometers vary between 88-122°C, while cation geothermometer estimations (except K-Mg) result in the range of 198-290°C. Given that the samples are classified as immature waters, silica geothermometers are considered to yield more reliable results and hence, the estimated reservoir temperature is in the 88-122°C range.

### 6.3.2 Edremit Field

Silica (quartz) and cation geothermometers (Na/K) are used for the calculation of the possible reservoir temperature in Edremit field (Avşar et al., 2013). The results produce a temperature range of 92-211°C.

## 6.4 Mineral Saturation States

### 6.4.1 Akköy Field

Saturation index (SI) calculations are performed for the minerals that are likely to be present in a carbonate dominated system at discharge temperature and pH conditions measured on-site (81°C and 7.6, respectively, Table 6.1). The Akköy water samples are undersaturated with anhydrite, dawsonite, gypsum, kaolinite and siderite, oversaturated with albite, aragonite, calcite, chalcedony, diopside, dolomite, illite, orthoclase, magnesite, quartz and smectite. The results point to the likely precipitation of most of the carbonate and silicate minerals in the system which is also in line with the travertine deposition observed extensively in the surrounding geothermal systems (e.g. Pamukkale, Karahayıt, Gölemezli and Yenice, Şimşek, 2003; Tarcan et al., 2016; Alçiçek et al., 2016, 2018, 2019; Brogi et al., 2021).

Given the assumption that minerals and fluid in the reservoir are in a temperature-dependent chemical equilibrium, the temperatures at which the mineral saturation indices equal to zero (i.e. SI = 0, the fluid and mineral are at chemical equilibrium) are considered to reflect the reservoir temperatures. In this regard, the saturation states of minerals are also investigated at different temperatures in the range of 60-150°C including the discharge temperature (T = 81°C) and temperature range obtained from silica geothermometers (88-122°C, Table 6.3). The results display that the SI values generally intersect with the equilibrium line in the range of 88-116°C (Fig.6.6). The comparison of the temperature estimations obtained from chemical geothermometers with the ones calculated by fluid mineral equilibria reveals a zone of overlap. Therefore, the most likely reservoir temperature for Akköy geothermal field is considered to be in the range of 88-116°C. In this range, the SI values of albite, chalcedony and illite minerals which point to oversaturation at discharge temperature, indicate undersaturation in the estimated reservoir conditions. Below 88°C the waters are undersaturated with anhydrite, dawsonite, gypsum, siderite, close to equilibrium and oversaturated with albite, aragonite, calcite, chalcedony, diopside, dolomite, illite, orthoclase, kaolinite, magnesite, quartz, smectite, while above 116°C the waters become undersaturated with albite, chalcedony, illite, orthoclase, kaolinite, quartz and close to equilibrium and oversaturated with anhydrite, siderite. On the other hand, at all temperatures the waters are oversaturated with carbonate minerals aragonite, calcite, dolomite and magnesite and the degree of oversaturation increases with increasing temperature.

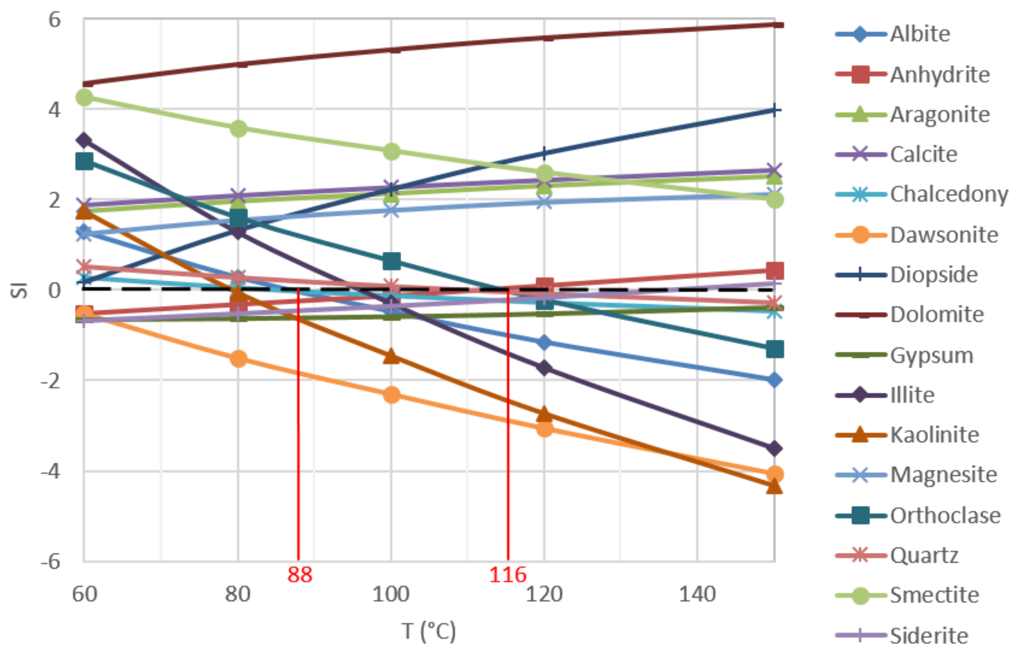

Figure 6.6. Changes in the saturation states of minerals at different temperatures of Akköy field

### 6.4.2 Edremit Field

Calculations for saturation indices of minerals (Avşar et al., 2013) indicate that over 110°C all waters are oversaturated with calcite, whereas below 90°C most of the samples are oversaturated with respect to quartz. Calcite oversaturation is not observed at the discharge temperatures of 42–62°C leading Avşar et al. (2013) to suggest that scaling is not a probable threat during production in the system.

Saturation index calculations conducted with predetermined alteration minerals are also utilized for the reservoir temperature estimations (Avşar et al., 2013). In this regard, the predicted temperature values are in the range of 60-150°C which show an overlap with the chemical geothermometer result of 92-211°C. Consequently, the range estimated for the reservoir temperature of Edremit field is in between 92-150°C.

## 6.5 Comparison of the Hydrogeochemical Results from Akköy & Edremit Fields

Hydrogeochemical facies of the fields indicate that in both geothermal fields, the waters are in alkaline character (except for the relatively cold waters in Edremit) and $SO_4$ is the major anion (coupled with $HCO_3$ in Akköy, given the abundance of carbonate minerals).

Water-rock interactions are the effective subsurface processes controlling the geochemical characteristics of both of the systems. In addition, Edremit waters seem to be affected by mixing as well. $\delta^{18}O$ and $\delta D$ isotope compositions of both fields suggest a meteoric origin. C-isotopes point to carbonate and organic sources for Akköy and Edremit fields, respectively.

Geothermometry calculations in parallel with fluid mineral equilibria, reveal the estimated reservoir temperatures are in the ranges of 88-116°C and 92-150°C for Akköy and Edremit fields, respectively, indicating a relatively higher temperature for Edremit system. Especially with increasing temperatures, likely carbonate oversaturation is observed in both fields according to the mineral saturations states.

# CHAPTER 7

# MODELLING OF $CO_2$-FLUID-ROCK INTERACTIONS

Geochemistry is an important tool in the determination of the fate of $CO_2$ in the subsurface during the implementation of a CCS project. The injection of $CO_2$ into a reservoir affects the chemistry of that system which may pose a risk for the wells, the reservoir and its surroundings. Therefore, the success of $CO_2$ injection and storage depends highly on understanding the subsurface behaviour of $CO_2$ and its interactions with the water and the rocks of the reservoir (Gaus et al., 2008). Experimental studies in laboratories may have limitations with respect to time, space and reservoir conditions, while thorough evaluation and prediction of the geochemical processes are possible with the geochemical modelling studies. In this regard, computer codes such as PHREEQC, TOUGHREACT and The Geochemist's Workbench are widely used for the geochemical simulations. Being an easily accessible and a prominent tool in geochemical studies for various applications, PHREEQC is especially endorsed by numerous literature work due to its competence of producing correct results (Hemme and van Berk, 2017 and the references therein).

The basis of geochemical models are comprised by three main processes: thermodynamics, reaction kinetics and flow and transport processes. The models in which the flow and transport processes are not taken into account, are named as “batch models”, whereas the models that couple geochemical reactions, flow and transport processes are called as “reactive transport models” (Gündoğan, 2011).

Thermodynamic Equilibrium Modelling (Speciation modelling): This is the most basic and common type of modelling. Distribution of species, their activities, saturation index values, redox state and the fugacities of the gases in the system can be calculated based on the assumption of thermodynamic equilibrium.

Kinetic Modelling: Thermodynamic equilibrium modelling approach does not take “time” into account and it is suitable for fast reactions. However, in a $CO_2$ storage scenario, it is important to know when the system reaches equilibrium again after the addition of $CO_2$ to the reservoir. This “time” variable for slow reactions (such as mineral dissolution and precipitation reactions) can be obtained through kinetic modelling.

Reactive Transport Modelling: With the injection of $CO_2$ into the reservoir, the balance of the system is disrupted and the equilibrium conditions are affected; flow and transport processes should be considered for the geochemical reactions. As a result, the static system (batch models) should be coupled with the flow and transport processes. In this modelling approach, the evolution of the geochemical reactions can be simulated temporally and spatially. PHREEQC software is capable of performing 1-D transport simulations coupling the equations of transport and chemical interaction with a sequential solution method (Addassi et al., 2021).

Batch models constitute a valuable tool for the establishment of the static system which includes the identification of the key reactions, aqueous species and minerals to be used as inputs for the reactive transport modelling. For the geochemical modelling of $CO_2$ storage, although being the most challenging technique, the reactive transport modelling is the most suitable and realistic approach due to its capabilities in the prediction of the distribution of the geochemical reactions in time and space and its ability to quantify the long-term fate of $CO_2$ (Gaus et al., 2008; Gündoğan, 2011).

In this study, potential fluid-rock interactions of Akköy and Edremit geothermal systems are investigated in the case of $CO_2$ addition with the utilization of PHREEQC software. Equilibrium, kinetic and reactive transport modelling studies are performed on the drill cutting and water samples of the relevant fields. Equilibrium modelling provides the assessment regarding the changes in fluid chemistry and mineral compositions. The dissolution/precipitation reactions that govern the systems are identified in this modelling step. Most likely trapping mechanisms for $CO_2$ storage are also deduced with equilibrium modelling results. In kinetic modelling, the reactions determined via equilibrium modelling are evaluated in terms of their temporal evolutions. Comprising the final stage of the geochemical modelling studies, the spatial distribution of the reactants (i.e. minerals) is simulated with reactive transport modelling. 3 samples from each field (ADK-PS-1-1515, ADK-PS-2-840, ADK-PS-2-1380 from Akköy and EDR-912, EDR-988, EDR-1008 from Edremit) are investigated extensively in this chapter, while the modelling results of remaining samples are presented in Appendices G and H.

## 7.1 Input Data for the Models

Amount of minerals in moles and composition of a water sample are the principal data required for the modelling. The data used in this study as inputs are, i) "representative" rock samples that were quantified by the weight proportions of the minerals (Akköy: 10 samples and Edremit: 8 samples) (Table 7.1, 7.2, Appendix G), ii) water sample collected in 2018 from PS-1 well for Akköy, iii) EDJ-7 well data from Avşar et al. (2013) for Edremit and iv) highest estimated temperatures calculated from the geothermometry applications (116°C and 150°C for Akköy and Edremit, respectively) (Table 7.3). Since Electrical Conductivity (EC) value is used as an indicator of the hydrogeochemical evolution of the system, among the water samples studied in Avşar et al. (2013) the one with the highest EC value is used in this study (EDJ-7).

Table 7.1 Reservoir rock mineralogy of the simulated samples from Akköy field used as input values in the modelling studies

| Mineral | Chemical Formula | Molecular Weight (g/mol) | PS-1-1515 | | PS-2-840 | | PS-2-1380 | |
|---|---|---|---|---|---|---|---|---|
| | | | Vol. (%) | Amount (mol) | Vol. (%) | Amount (mol) | Vol. (%) | Amount (mol) |
| Albite | $NaAlSi_3O_8$ | 263.02 | 13 | 37.27 | 6.7 | 19.21 | - | - |
| Ankerite | $CaMg_{0.3}Fe_{0.7}(CO_3)_2$ | 206.39 | - | - | - | - | - | - |
| Biotite | $KFe_3AlSi_3O_{10}(OH)_2$ | 511.88 | - | - | 7.9 | 11.64 | - | - |
| Calcite | $CaCO_3$ | 100.09 | 16.3 | 122.81 | 22.8 | 171.78 | 46.8 | 352.61 |
| Chlorite | $Fe_2Al_2SiO_5(OH)_4$ | 341.76 | 12.9 | 28 | - | - | 16.3 | 35.97 |
| Dolomite | $CaMg(CO_3)_2$ | 184.4 | 8.3 | 34 | - | - | 7.6 | 31.08 |
| Illite | $K_{0.6}Mg_{0.25}Al_{1.8}Al_{0.5}Si_{3.5}O_{10}(OH)_2$ | 383.9 | - | - | 12.4 | 24.36 | - | - |
| Kaolinite | $Al_2Si_2O_5(OH)_4$ | 258.16 | 17.5 | 51 | - | - | 2 | 5.84 |
| Muscovite | $KAl_3Si_3O_{10}(OH)_2$ | 398.71 | 0.4 | 0.76 | 1.9 | 3.59 | 7.3 | 13.81 |
| Orthoclase | $KAlSi_3O_8$ | 278.33 | - | - | 13.7 | 37.12 | - | - |
| Quartz | $SiO_2$ | 60.08 | 31.5 | 395.38 | 32.5 | 407.94 | 19.9 | 249.78 |
| Smectite | $Ca_{.02}Na_{.15}K_{.2}Fe_{.45}Mg_{.9}Al_{1.25}Si_{3.75}H_2O_{12}$ | 392.13 | - | - | 2.2 | 4.23 | - | - |

Table 7.2 Reservoir rock mineralogy of the simulated samples from Edremit field used as input values in the modelling studies

| **Mineral** | **Chemical Formula** | **Molecular Weight (g/mol)** | **EDR-912** | | **EDR-988** | | **EDR-1008** | |
|---|---|---|---|---|---|---|---|---|
| | | | **Vol. (%)** | **Amount (mol)** | **Vol. (%)** | **Amount (mol)** | **Vol. (%)** | **Amount (mol)** |
| Albite | $NaAlSi_3O_8$ | 263.02 | - | - | 25.6 | 50.86 | - | - |
| Amphibole | $NaCa_2Al_3Mg_4Si_6O_{22}(OH)_2$ | 835.83 | - | - | - | - | - | - |
| Biotite | $KAlMg_3Si_3O_{10}(OH)_2$ | 417.26 | 14.3 | 17.91 | 6.3 | 7.89 | 10.2 | 12.77 |
| Bytownite | $Na_{0.2}Ca_{0.8}Al_{1.8}Si_{2.2}O_8$ | 275.01 | - | - | - | - | - | - |
| Calcite | $CaCO_3$ | 100.09 | 1.2 | 6.26 | 5 | 26.1 | - | - |
| Chlorite | $Fe_2Al_2SiO_5(OH)_4$ | 341.76 | - | - | 12 | 18.35 | - | - |
| Dolomite | $CaMg(CO_3)_2$ | 184.4 | 3.2 | 9.07 | 2 | 5.67 | - | - |
| Illite | $K_{0.6}Mg_{0.25}Al_{1.8}Al_{0.5}Si_{3.5}O_{10}(OH)_2$ | 383.9 | - | - | - | - | 11.4 | 15.52 |
| Kaolinite | $Al_2Si_2O_5(OH)_4$ | 258.16 | 3 | 6.07 | 10.2 | 20.64 | 0.6 | 1.21 |
| Labradorite | $Na_{0.4}Ca_{0.6}Al_{1.6}Si_{2.4}O_8$ | 271.81 | - | - | - | - | 32.8 | 63.05 |
| Orthoclase | $KAlSi_3O_8$ | 278.33 | 50 | 93.86 | - | - | 23.2 | 43.55 |
| Quartz | $SiO_2$ | 60.08 | 28.3 | 246.12 | 38.9 | 338.3 | 21.8 | 189.59 |

Table 7.3 Hydrochemical data used in the modelling studies

| **PS-1** | **PS-1.2018** | **EDJ-7** |
|---|---|---|
| T (°C)* | 116 | 150 |
| pH | 7.6 | 7.61 |
| $SiO_2$ (mg/l) | 69 | 48 |
| Na (mg/l) | 703 | 246 |
| K (mg/l) | 135 | 5.7 |
| Mg (mg/l) | 60 | 0.1 |
| Ca (mg/l) | 265 | 39 |
| $HCO_3$ (mg/l) | 1789 | 37 |
| Cl (mg/l) | 73 | 63 |
| $NO_3$ (mg/l) | 6.9 | 0.22 |
| $SO_4$ (mg/l) | 894 | 500 |
| Fe (µg/l) | 349 | 79 |
| Al (µg/l) | 20.11 | 88 |

*highest estimated reservoir temperature
from the geothermometry calculations

Molar amounts of minerals are calculated with the equation 4.1, using the values of rock density and porosity (for the calculation of rock volume) assigned as 2630 kg/m$^3$ and 3.37% for Akköy (following the study of Janssen et al., 2023 in Kızıldere field), 2750 kg/m$^3$ and 5% for Edremit (Goodman, 1989 in Avşar, 2011).

In the models, particular minerals for biotite and amphibole groups are assigned according to the results from the analyses performed for the lithogeochemical characterization of the drill cuttings. For Akköy samples, annite which is the Fe-endmember of biotite group is used following the EPMA results which revealed Fe-rich nature for mica minerals. In the Edremit samples, since phlogopite and pargasite are already identified in CRS analyses (Table 5.2), these minerals are selected as biotite and amphibole, respectively for the simulations.

Ankerite, dawsonite, magnesite and siderite are the identified secondary phases in most of the samples.

## 7.2 Akköy Field

### 7.2.1 Simulated Sample: ADK-PS-1-1515

#### 7.2.1.1 Equilibrium Modelling

In the simulations of sample ADK-PS-1-1515, determined secondary mineral is ankerite and the calculated mol amount of $CO_2$ that can be completely used up is 50 moles following the preliminary Saturation Index calculations.

The equilibrium modelling results of sample ADK-PS-1-1515 are given in Tables 7.4 and 7.5. According to the results, with the addition of $CO_2$, pH drops down to 7.32, Al, Fe, Si contents increase and total C, Ca, K, Mg, Na, $SO_4$ values decrease in the water sample (Table 7.4).

Table 7.4 Equilibrium modelling results of the aqueous phase reacting with sample ADK-PS-1-1515 (Akköy field)

| **PS-1.2018** | **initial** | **final** |
|---|---|---|
| pH | 7.6 | 7.32 |
| Al (mol/L) | 7.48E-07 | 6.16E-06 |
| Total C (mol/L) | 0.02945 | 0.008101 |
| Ca (mol/L) | 0.006629 | 0.0001332 |
| Cl (mol/L) | 0.002052 | 0.002051 |
| Fe (mol/L) | 6.27E-06 | 0.002399 |
| K (mol/L) | 0.003457 | 2.91E-05 |
| Mg (mol/L) | 0.002483 | 1.72E-05 |
| Na (mol/L) | 0.03068 | 0.0292 |
| $SO_4$ (mol/L) | 0.009349 | 0.009346 |
| Si (mol/L) | 0.0005351 | 0.001209 |

The variations in the mineral assemblage point to the dissolution of calcite, chlorite, dolomite, quartz and the precipitation of ankerite and kaolinite (Table 7.5). The carbonate mineral that "traps" $CO_2$ is ankerite which is likely to form through the following reaction:

Calcite + Dolomite + Chlorite + Quartz -> Ankerite + Kaolinite

$7\,CaCO_3 + 3\,CaMg(CO_3)_2 + 3.5\,Fe_2Al_2SiO_5(OH)_4 + 3.5\,SiO_2 + 7\,CO_2 \rightarrow 10\,CaMg_{0.3}Fe_{0.7}(CO_3)_2 + 3.5\,Al_2Si_2O_5(OH)_4$

Table 7.5 Mineralogical changes with the equilibrium modelling for sample ADK-PS-1-1515 from Akköy field (values are as moles, blue colour indicates dissolution and red indicates precipitation, bold shows $CO_2$ trapping minerals)

| Mineral | ADK-PS-1-1515 | | |
|---|---|---|---|
| | Initial | Final | Delta |
| Albite | 37.27 | 37.27 | 0 |
| **Ankerite** | **0** | **71.45** | **71.45** |
| Biotite | 0 | 0 | 0 |
| Calcite | 122.81 | 72.8 | -50.01 |
| Chlorite | 28.46 | 3.453 | -25.01 |
| Dolomite | 33.94 | 12.51 | -21.43 |
| Illite | 0 | 0 | 0 |
| Kaolinite | 51.12 | 76.12 | 25.00 |
| Muscovite | 0.76 | 0.7634 | 0.01 |
| Orthoclase | 0 | 0 | 0 |
| Quartz | 395.38 | 370.4 | -24.98 |
| Smectite | 0 | 0 | 0 |
| Dawsonite | 0 | 0 | 0 |
| Magnesite | 0 | 0 | 0 |
| Siderite | 0 | 0 | 0 |

As a result of the reactions, 100% of the added $CO_2$ is trapped in minerals.

#### 7.2.1.2 Kinetic Modelling

Reactions for sample ADK-PS-1-1515 that are determined in equilibrium modelling are investigated in terms of time (Fig.7.1). Within the first 5 minutes of $CO_2$ addition, ankerite starts to precipitate (Fig.7.2a). $CO_2$ is totally consumed within one and a half years (i.e. the mol value of injected $CO_2$ becomes zero, Fig.7.2b). The system reaches equilibrium in approximately 15 years (Fig.7.1). The initial pH value of 7.6 drops to 4.97 with the addition of $CO_2$, it starts to increase in time and in approximately 15 years it reaches to the final value of 7.32 (Fig.7.2c).

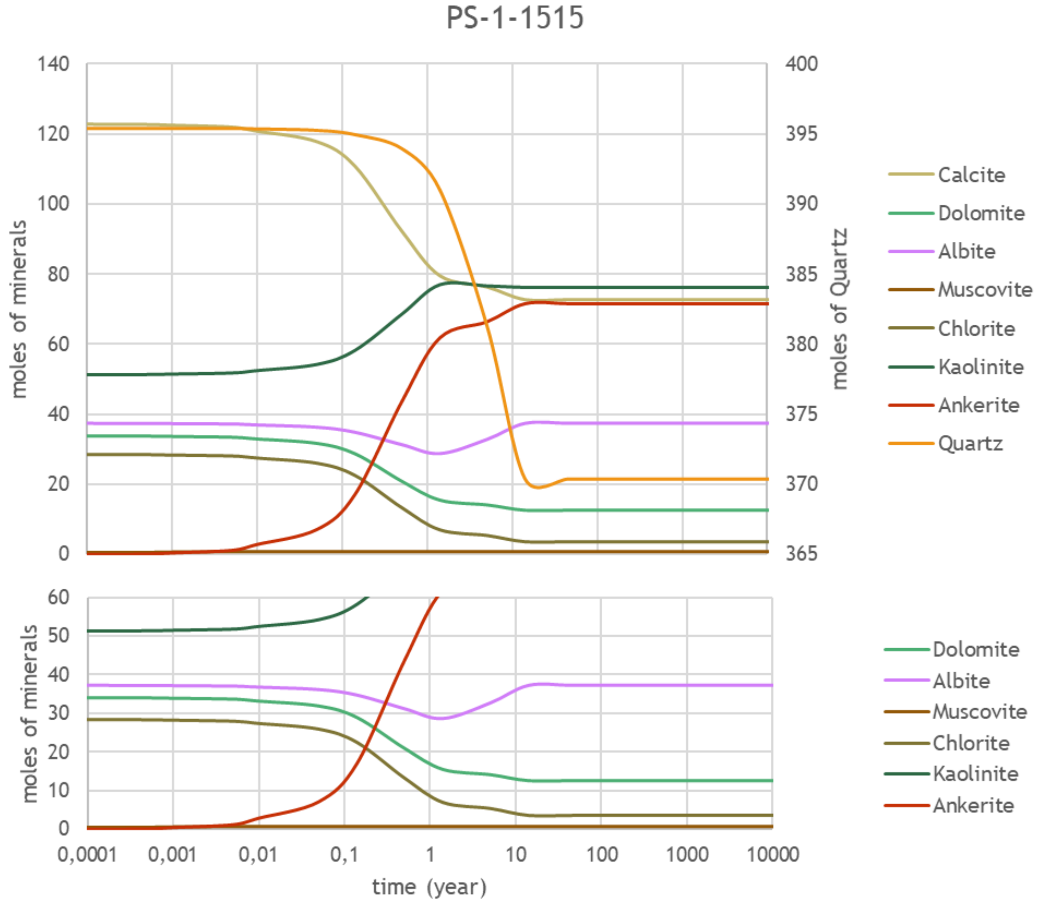

Figure 7.1. Temporal changes in the reservoir mineralogy (ADK-PS-1-1515, Akköy field) followed by $CO_2$ addition to the system

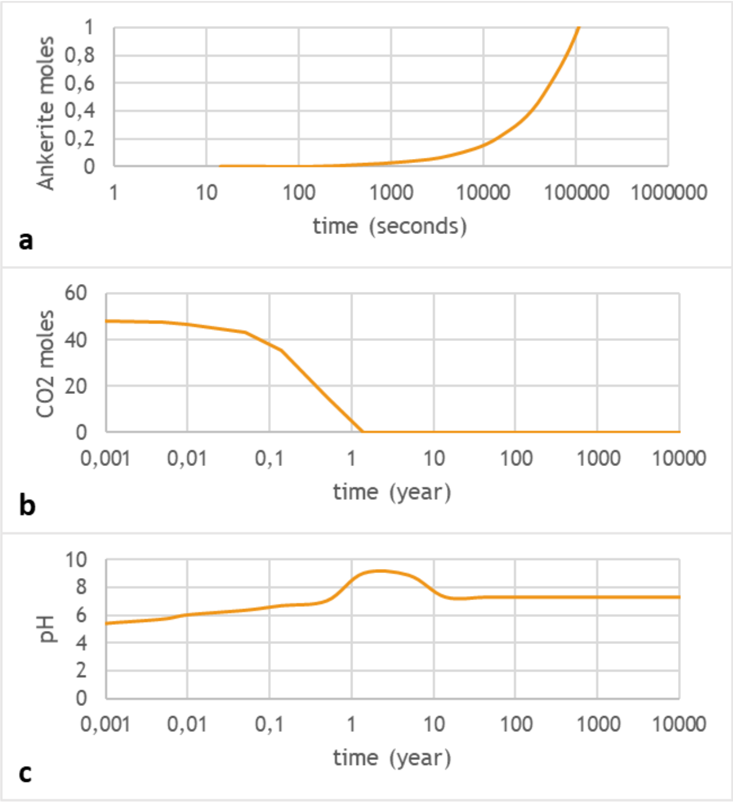

Figure 7.2. Changes that occur in time in a. the concentration of carbonate mineral reacting from the start, b. the amount of $CO_2$ and c. pH values of sample ADK-PS-1-1515 (Akköy field)

### 7.2.1.3 Reactive Transport Modelling

The changes in the mineral concentrations in 100 years along the reservoir which is simulated as a 100 m-long horizontal column for sample ADK-PS-1-1515 are illustrated in Figure 7.3 (100 m long column is zoomed in to 20 m for better inspection of results). According to the models, most of the reactions determined with equilibrium and kinetic modelling, take place in about 7-9 meters from the supposed $CO_2$ injection point and the effects of the reactions decrease gradually with distance. The reactions start to take place in the first year with lesser molar amounts in shorter distances (~1.5 m).

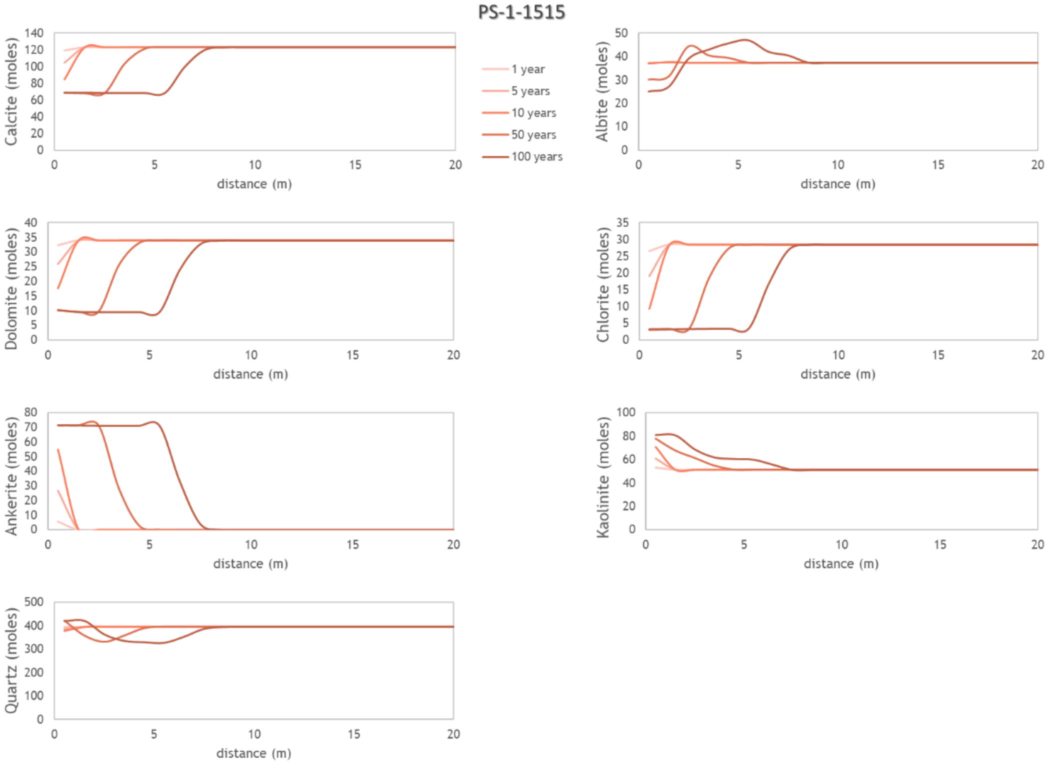

Figure 7.3. The changes in the mineral phases of sample ADK-PS-1-1515 (Akköy field) against distance in different times

### 7.2.2 Simulated Sample: ADK-PS-2-840

#### 7.2.2.1 Equilibrium Modelling

In the simulations of sample ADK-PS-2-840, determined secondary minerals are ankerite, dawsonite, dolomite, siderite and the calculated mol amount of $CO_2$ that can be completely used up is 67 moles following the preliminary Saturation Index calculations.

The equilibrium modelling results of sample ADK-PS-2-840 are given in Tables 7.6 and 7.7. According to the results, with the addition of $CO_2$, pH drops down to 6.53, total C, Cl, Fe, Na, $SO_4$, Si contents increase and Al, Ca, K, Mg values decrease in the water sample (Table 7.6).

Table 7.6 Equilibrium modelling results of the aqueous phase reacting with sample ADK-PS-2-840 (Akköy field)

| **PS-1.2018** | **initial** | **final** |
|---|---|---|
| pH | 7.6 | 6.53 |
| Al (mol/L) | 7.48E-07 | 4.17E-07 |
| Total C (mol/L) | 0.02945 | 0.8475 |
| Ca (mol/L) | 0.006629 | 8.57E-05 |
| Cl (mol/L) | 0.002052 | 0.002138 |
| Fe (mol/L) | 6.27E-06 | 5.92E-03 |
| K (mol/L) | 0.003457 | 9.95E-03 |
| Mg (mol/L) | 0.002483 | 2.03E-07 |
| Na (mol/L) | 0.03068 | 0.4872 |
| $SO_4$ (mol/L) | 0.009349 | 0.00974 |
| Si (mol/L) | 0.0005351 | 0.001194 |

The variations in the mineral assemblage point to the dissolution of albite, biotite, calcite, illite, smectite and the precipitation of ankerite, muscovite, orthoclase, quartz, dawsonite and siderite (Table 7.7). The carbonate minerals that "trap" $CO_2$ are ankerite, dawsonite and siderite. The likely series of reactions which lead up to the precipitation of these carbonate minerals are:

Calcite + Illite + Orthoclase -> Dolomite + Muscovite + Quartz

$$CaCO_3 + 4\ K_{0.6}Mg_{0.25}Al_{2.3}Si_{3.5}O_{10}(OH)_2 + KAlSi_3O_8 + CO_2 \rightarrow CaMg(CO_3)_2 + 3.4\ KAl_3Si_3O_{10}(OH)_2 + 6.8\ SiO_2 + 0.6\ H_2O$$

Calcite + Dolomite + Biotite -> Ankerite + Orthoclase

$2.1\ CaCO_3 + 0.9\ CaMg(CO_3)_2 + 0.7\ KFe_3AlSi_3O_{10}(OH)_2 + 2.1\ CO_2 \rightarrow 3\ CaMg_{0.3}Fe_{0.7}(CO_3)_2 + 0.7\ KAlSi_3O_8 + 0.7\ H_2O$

Biotite -> Siderite + Orthoclase

$KFe_3AlSi_3O_{10}(OH)_2 + 3CO_2 \rightarrow 3FeCO_3 + KAlSi_3O_8 + H_2O$

Albite -> Dawsonite + Quartz

$NaAlSi_3O_8 + CO_2 + H_2O \rightarrow NaAlCO_3(OH)_2 + 3\ SiO_2$

Table 7.7 Mineralogical changes with the equilibrium modelling for sample ADK-PS-2-840 from Akköy field (values are as moles, blue colour indicates dissolution and red indicates precipitation, bold shows $CO_2$ trapping minerals)

| Mineral | ADK-PS-2-840 | | |
|---|---|---|---|
| | Initial | Final | Delta |
| Albite | 19.21 | 0 | -19.21 |
| **Ankerite** | **0** | **33** | **33.00** |
| Biotite | 11.64 | 0 | -11.64 |
| Calcite | 171.78 | 138.9 | -32.88 |
| Chlorite | 0 | 0 | 0 |
| Dolomite | 0 | 0 | 0 |
| Illite | 24.36 | 0 | -24.36 |
| Kaolinite | 0 | 0 | 0 |
| Muscovite | 3.59 | 26.42 | 22.83 |
| Orthoclase | 37.12 | 41.38 | 4.26 |
| Quartz | 407.94 | 520.3 | 112.36 |
| Smectite | 4.23 | 0 | -4.23 |
| **Dawsonite** | **0** | **19.41** | **19.41** |
| Magnesite | 0 | 0 | 0 |
| **Siderite** | **0** | **13.72** | **13.72** |

As a result of the reactions, mineral trapping is estimated as 99% and solubility trapping as 1% for $CO_2$ added to the system.

#### 7.2.2.2 Kinetic Modelling

Reactions for sample ADK-PS-2-840 that are determined in equilibrium modelling are investigated in terms of time (Fig.7.4). With $CO_2$ addition, dolomite starts to precipitate (Fig.7.5a) and in 3 hours ankerite also precipitates (Fig.7.5b). Dolomite dissolves in 10 hours. Precipitation of siderite starts in one and a half days. $CO_2$ is totally consumed within 450 years (i.e. the mol value of injected $CO_2$ becomes zero, Fig.7.5c). The system reaches equilibrium in approximately 500 years (Fig.7.4). The initial pH value of 7.6 drops to 5.11 with the addition of $CO_2$, it starts to increase in time and in approximately 500 years it reaches to the final value of 6.53 (Fig.7.5d).

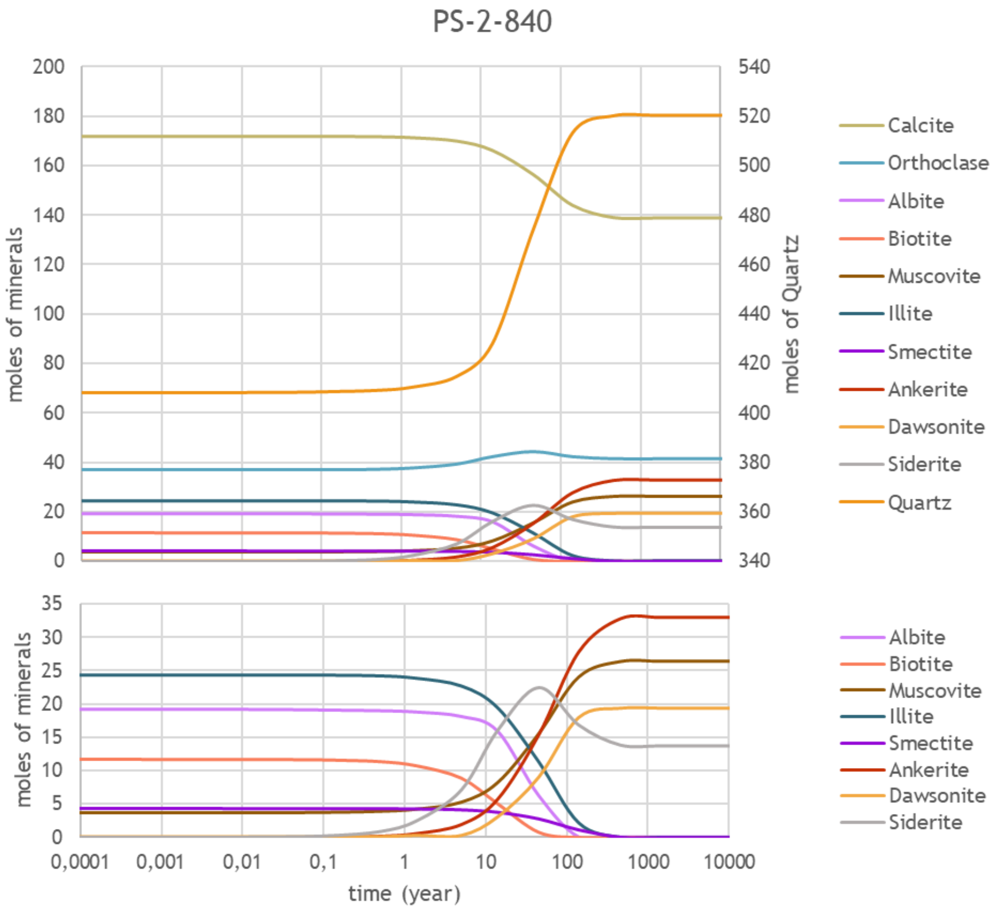

Figure 7.4. Temporal changes in the reservoir mineralogy (ADK-PS-2-840, Akköy field) followed by $CO_2$ addition to the system

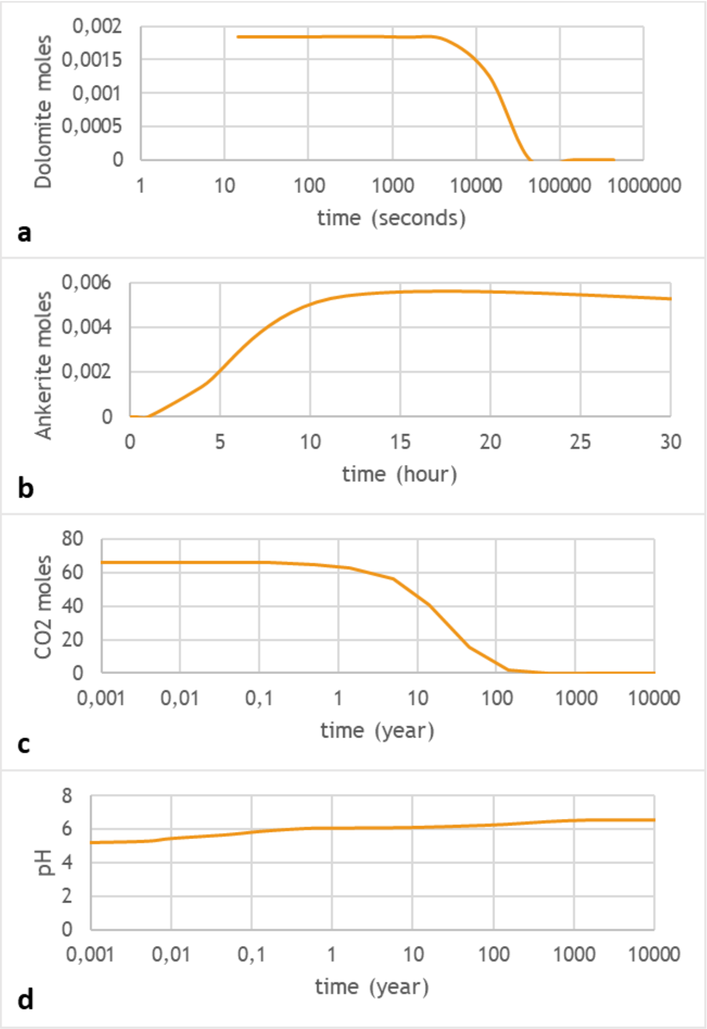

Figure 7.5. Changes that occur in time in a, b. the concentration of carbonate minerals reacting from the start, c. the amount of $CO_2$ and d. pH values of sample ADK-PS-2-840 (Akköy field)

### 7.2.2.3 Reactive Transport Modelling

The changes in the mineral concentrations in 100 years along the reservoir which is simulated as a 100 m-long horizontal column for sample ADK-PS-2-840 are illustrated in Figure 7.6 (100 m long column is zoomed in to 20 m for better inspection of results). According to the models, most of the reactions determined with equilibrium and kinetic modelling, take place in about 18 meters from the supposed $CO_2$ injection point and the effects of the reactions decrease gradually with distance. Dawsonite and siderite precipitations occur close to the inlet (3.5 meters). The reactions start to take place in the first year with lesser molar amounts in shorter distances (~1.5 m).

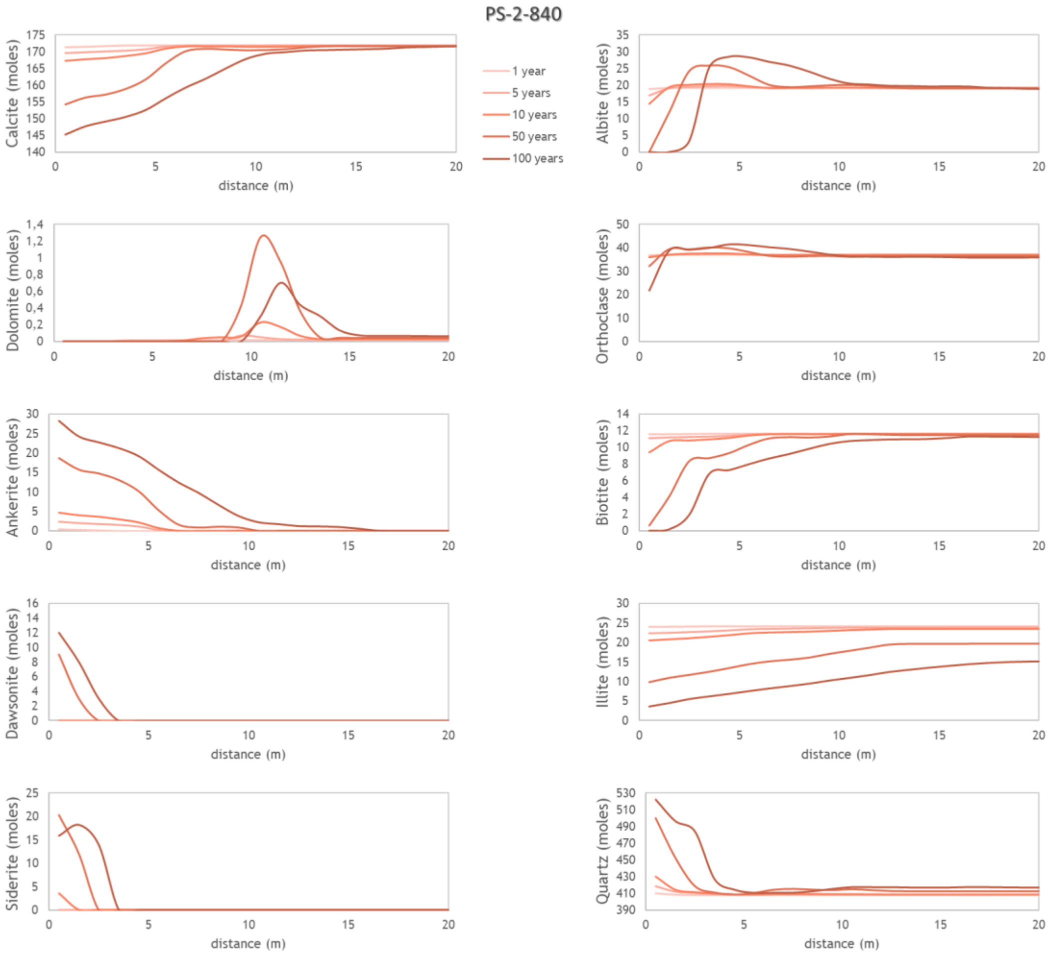

Figure 7.6. The changes in the mineral phases of sample ADK-PS-2-840 (Akköy field) against distance in different times

### 7.2.3 Simulated Sample: ADK-PS-2-1380

#### 7.2.3.1 Equilibrium Modelling

In the simulations of sample ADK-PS-2-1380, determined secondary mineral is ankerite and the calculated mol amount of $CO_2$ that can be completely used up is 73 moles following the preliminary Saturation Index calculations.

The equilibrium modelling results of sample ADK-PS-2-1380 are given in Tables 7.8 and 7.9. According to the results, with the addition of $CO_2$, pH drops down to 5.03, total C, Ca, Fe, K, Si contents increase and Al, Ca, Mg values decrease in the water sample (Table 7.8).

Table 7.8 Equilibrium modelling results of the aqueous phase reacting with sample ADK-PS-2-1380 (Akköy field)

| **PS-1.2018** | **initial** | **final** |
|---|---|---|
| pH | 7.6 | 5.03 |
| Al (mol/L) | 7.48E-07 | 8.28E-08 |
| Total C (mol/L) | 0.02945 | 1.089 |
| Ca (mol/L) | 0.006629 | 0.007127 |
| Cl (mol/L) | 0.002052 | 0.002052 |
| Fe (mol/L) | 6.27E-06 | 5.24E-04 |
| K (mol/L) | 0.003457 | 0.005558 |
| Mg (mol/L) | 0.002483 | 6.54E-04 |
| Na (mol/L) | 0.03068 | 0.03068 |
| $SO_4$ (mol/L) | 0.009349 | 0.00935 |
| Si (mol/L) | 0.0005351 | 0.001169 |

The variations in the mineral assemblage indicate the dissolution of calcite, chlorite, dolomite, quartz and the precipitation of ankerite and kaolinite (Table 7.9). The carbonate mineral that “traps” $CO_2$ is ankerite. The potential reaction for ankerite formation in this sample is:

Calcite + Dolomite + Chlorite + Quartz -> Ankerite + Kaolinite

$$7\ CaCO_3 + 3\ CaMg(CO_3)_2 + 3.5\ Fe_2Al_2SiO_5(OH)_4 + 3.5\ SiO_2 + 7\ CO_2 = 10\ CaMg_{0.3}Fe_{0.7}(CO_3)_2 + 3.5\ Al_2Si_2O_5(OH)_4$$

Table 7.9 Mineralogical changes with the equilibrium modelling for sample ADK-PS-2-1380 from Akköy field (values are as moles, blue colour indicates dissolution and red indicates precipitation, bold shows $CO_2$ trapping minerals)

| Mineral | ADK-PS-2-1380 | | |
|---|---|---|---|
| | Initial | Final | Delta |
| Albite | 0 | 0 | 0 |
| **Ankerite** | **0** | **102.8** | **102.8** |
| Biotite | 0 | 0 | 0 |
| Calcite | 352.61 | 280.7 | -71.91 |
| Chlorite | 35.97 | 0 | -35.97 |
| Dolomite | 31.08 | 0.2506 | -30.83 |
| Illite | 0 | 0 | 0 |
| Kaolinite | 5.84 | 41.81 | 35.97 |
| Muscovite | 13.81 | 13.81 | 0 |
| Orthoclase | 0 | 0 | 0 |
| Quartz | 249.78 | 213.8 | -35.98 |
| Smectite | 0 | 0 | 0 |
| Dawsonite | 0 | 0 | 0 |
| Magnesite | 0 | 0 | 0 |
| Siderite | 0 | 0 | 0 |

As a result of the reactions, 99% of the added $CO_2$ is trapped in minerals while 1% is held in the solution.

### 7.2.3.2 Kinetic Modelling

Reactions for sample ADK-PS-2-1380 that are determined in equilibrium modelling are investigated in terms of time (Fig.7.7). With $CO_2$ addition, ankerite starts to precipitate (Fig.7.8a). $CO_2$ is totally consumed within 45 years (i.e. the mol value of injected $CO_2$ becomes zero, Fig.7.8b). The system reaches equilibrium in approximately 45 years (Fig.7.7). The initial pH value of 7.6 drops to 4.99 with the addition of $CO_2$, it starts to increase in time and in approximately 45 years it reaches to the final value of 5.03 (Fig.7.8c).

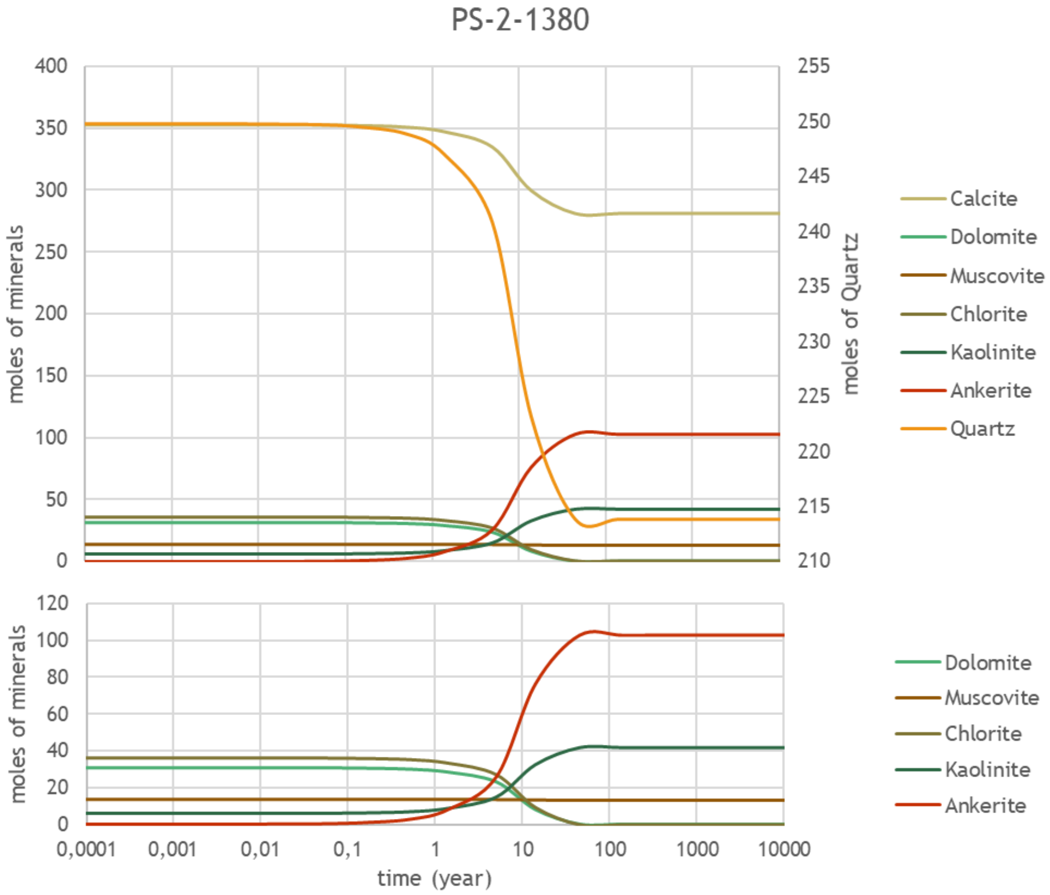

Figure 7.7. Temporal changes in the reservoir mineralogy (ADK-PS-2-1380, Akköy field) followed by $CO_2$ addition to the system

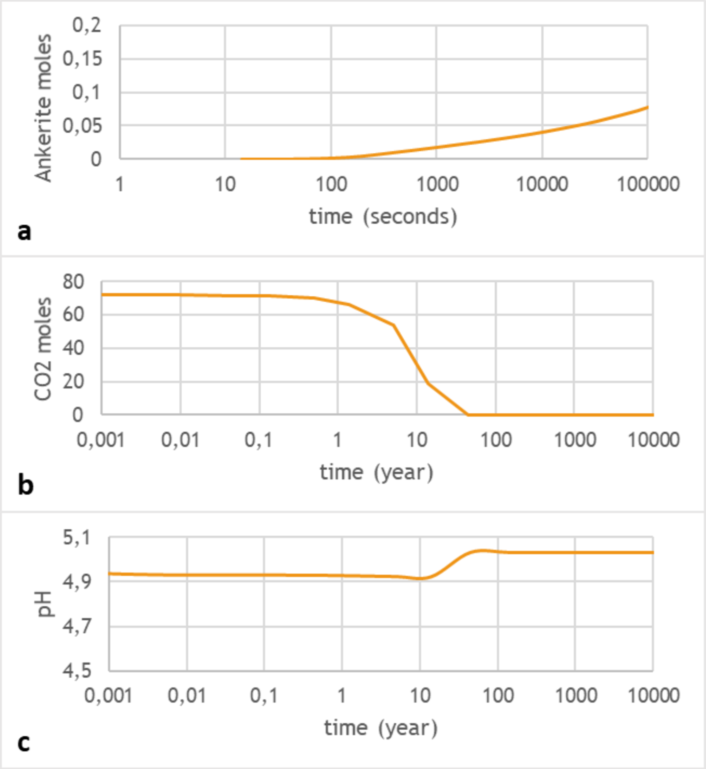

Figure 7.8. Changes that occur in time in a. the concentration of carbonate mineral reacting from the start, b. the amount of $CO_2$ and c. pH values of sample ADK-PS-2-1380 from Akköy field

### 7.2.3.3 Reactive Transport Modelling

The changes in the mineral concentrations in 100 years along the reservoir which is simulated as a 100 m-long horizontal column for sample ADK-PS-2-1380 are illustrated in Figure 7.9 (100 m-long column is zoomed in to 20 m for better inspection of results). According to the models, the reactions that are determined with equilibrium and kinetic modelling, take place in approximately 6.5 meters from the supposed $CO_2$ injection point and decrease gradually with distance. The results reveal that the evolution of the reactions from first year starts with lesser molar amounts in shorter distances (~1.5 m).

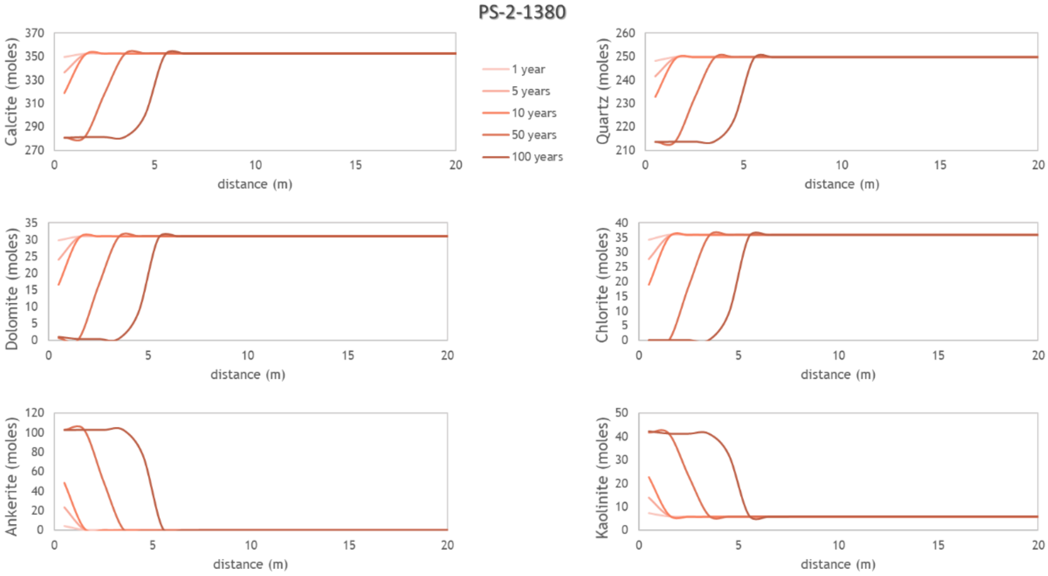

Figure 7.9. The changes in the mineral phases of sample ADK-PS-2-1380 (Akköy field) against distance in different times

## 7.3 Edremit Field

### 7.3.1 Simulated Sample: EDR-912

#### 7.3.1.1 Equilibrium Modelling

In the simulations of sample EDR-912, determined secondary mineral is ankerite and the calculated mol amount of $CO_2$ that can be completely used up is 33 moles following the preliminary Saturation Index calculations.

The equilibrium modelling results of sample EDR-912 are given in Tables 7.10 and 7.11. According to the equilibrium modelling results, with the addition of $CO_2$, pH drops down to 5.63, total C, K, Mg, Si contents increase and Al, Ca, Cl, Fe, Na, $SO_4$ values decrease in the water sample (Table 7.10).

Table 7.10 Equilibrium modelling results of the aqueous phase reacting with sample EDR-912 (Edremit field)

| **EDJ-7** | **initial** | **final** |
|---|---|---|
| pH | 7.61 | 5.63 |
| Al (mol/L) | 3.26E-06 | 7.43E-07 |
| Total C (mol/L) | 6.07E-04 | 0.2791 |
| Ca (mol/L) | 9.74E-04 | 8.79E-05 |
| Cl (mol/L) | 0.001779 | 0.001487 |
| Fe (mol/L) | 1.42E-06 | 1.18E-06 |
| K (mol/L) | 1.46E-04 | 1.12E-02 |
| Mg (mol/L) | 4.12E-06 | 1.69E-03 |
| Na (mol/L) | 0.01071 | 0.008956 |
| $SO_4$ (mol/L) | 0.005211 | 0.004357 |
| Si (mol/L) | 0.0003739 | 0.001949 |

The variations in the mineral assemblage display the dissolution of biotite, calcite and the precipitation of dolomite, orthoclase, quartz and magnesite (Table 7.11). The amount of quartz that precipitates is very little (0.01 mol). The carbonate minerals that “trap” $CO_2$ are dolomite and magnesite. These minerals are likely to form through the following reaction:

Biotite + Calcite -> Dolomite + Magnesite + Orthoclase

$KAlMg_3Si_3O_{10}(OH)_2 + CaCO_3 + 3\ CO_2 = CaMg(CO_3)_2 + 2\ MgCO_3 + KAlSi_3O_8 + H_2O$

Table 7.11 Mineralogical changes with the equilibrium modelling for sample EDR-912 from Edremit field (values are as moles, blue colour indicates dissolution and red indicates precipitation, bold shows $CO_2$ trapping minerals)

| Mineral | EDR-912 | | |
|---|---|---|---|
| | Initial | Final | Delta |
| Albite | 0 | 0 | 0 |
| Amphibole | 0 | 0 | 0 |
| Biotite | 10.89 | 0 | -10.89 |
| Bytownite | 0 | 0 | 0 |
| Calcite | 19.84 | 0 | -19.84 |
| Chlorite | 0 | 0 | 0 |
| **Dolomite** | **0** | **19.84** | **19.84** |
| Illite | 9.66 | 9.668 | 0 |
| Kaolinite | 0 | 0 | 0 |
| Labradorite | 0 | 0 | 0 |
| Orthoclase | 55.38 | 66.25 | 10.87 |
| Quartz | 441.79 | 441.8 | 0.01 |
| Ankerite | 0 | 0 | 0 |
| Dawsonite | 0 | 0 | 0 |
| **Magnesite** | **0** | **12.83** | **12.83** |
| Siderite | 0 | 0 | 0 |

As a result of the reactions, 99% of the added $CO_2$ is trapped in minerals and the remaining 1% is trapped in the solution.

#### 7.3.1.2 Kinetic Modelling

Reactions for sample EDR-912 that are determined in equilibrium modelling are investigated in terms of time (Fig.7.10). Within the first 3 hours of $CO_2$ addition, dolomite starts to precipitate (Fig.7.11a). Magnesite precipitates after 5 years. $CO_2$ is totally consumed within 40 years (i.e. the mol value of injected $CO_2$ becomes zero, Fig.7.11b). The system reaches equilibrium in approximately 40 years (Fig.7.10). The initial pH value of 7.61 drops to 5.05 with the addition of $CO_2$, it increases in time and in approximately 40 years it reaches to the final value of 5.63 (Fig.7.11c).

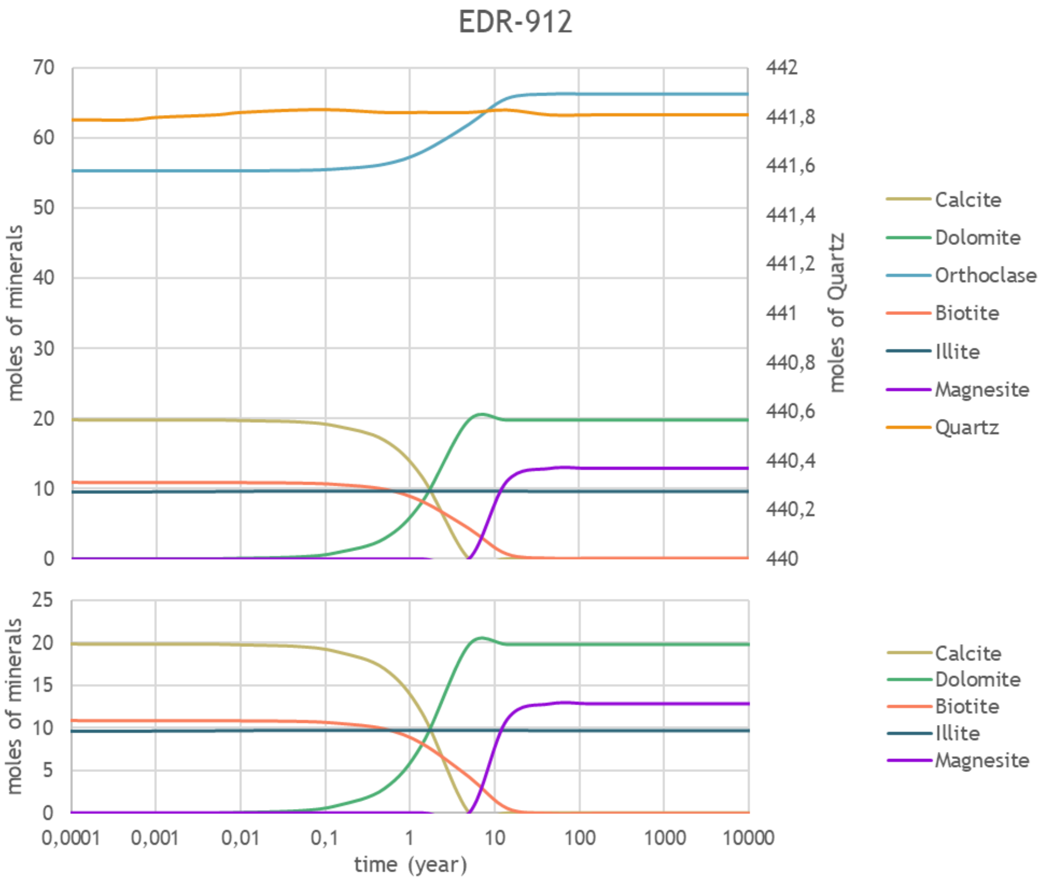

Figure 7.10. Temporal changes in the reservoir mineralogy (EDR-912, Edremit field) followed by $CO_2$ addition to the system

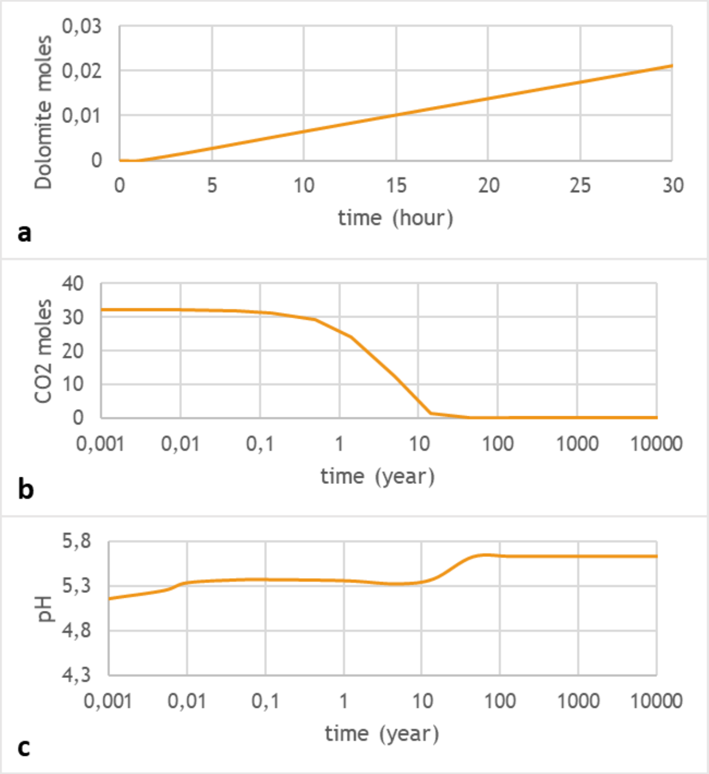

Figure 7.11. Changes that occur in time in a. the concentration of carbonate mineral reacting from the start, b. the amount of $CO_2$ and c. pH values of sample EDR-912 from Edremit field

#### 7.3.1.3 Reactive Transport Modelling

The changes in the mineral concentrations in 100 years along the reservoir which is simulated as a 100 m-long horizontal column for sample EDR-912 are illustrated in Figure 7.12 (100 m long column is zoomed in to 20 m for better inspection of results). According to the models, the reactions that are determined with equilibrium and kinetic modelling, take place in approximately 8.5 meters from the supposed $CO_2$ injection point and decrease gradually with distance. The results reveal that the evolution of the reactions from first year starts with lesser molar amounts in shorter distances (~1.5 m) displaying increase with time.

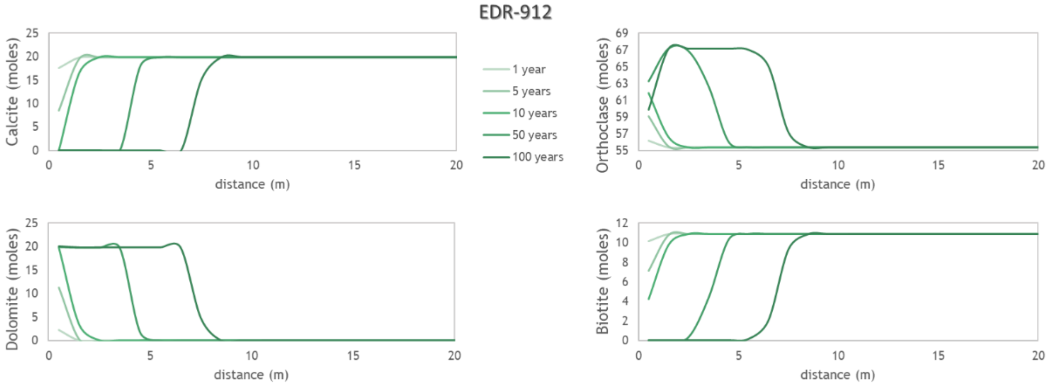

Figure 7.12. The changes in the mineral phases of sample EDR-912 (Edremit field) against distance in different times

### 7.3.2 Simulated Sample: EDR-988

#### 7.3.2.1 Equilibrium Modelling

In the simulations of sample EDR-988, determined secondary mineral is ankerite and the calculated mol amount of $CO_2$ that can be completely used up is 27 moles following the preliminary Saturation Index calculations.

The equilibrium modelling results of sample EDR-988 are given in Tables 7.12 and 7.13. According to the equilibrium modelling results, with the addition of $CO_2$, pH drops down to 6.23, total C, Fe, K, Mg, Na, Si contents increase and Al, Ca, Cl, $SO_4$ values decrease in the water sample (Table 7.10).

Table 7.12 Equilibrium modelling results of the aqueous phase reacting with sample EDR-988 (Edremit field)

| **EDJ-7** | **initial** | **final** |
|---|---|---|
| pH | 7.61 | 6.23 |
| Al (mol/L) | 3.26E-06 | 3.22E-06 |
| Total C (mol/L) | 6.07E-04 | 0.79 |
| Ca (mol/L) | 9.74E-04 | 1.70E-06 |
| Cl (mol/L) | 0.001779 | 0.001564 |
| Fe (mol/L) | 1.42E-06 | 1.37E-04 |
| K (mol/L) | 1.46E-04 | 0.003528 |
| Mg (mol/L) | 4.12E-06 | 3.59E-04 |
| Na (mol/L) | 0.01071 | 0.1564 |
| $SO_4$ (mol/L) | 0.005211 | 0.004581 |
| Si (mol/L) | 0.0003739 | 0.001961 |

The variations in the mineral assemblage indicate the dissolution of albite, biotite, calcite, chlorite, quartz and the precipitation of dolomite, kaolinite, orthoclase and ankerite (Table 7.13). The carbonate minerals that “trap” $CO_2$ are ankerite and dolomite which are likely to form through the following reactions:

Calcite + Biotite -> Dolomite + Orthoclase

$KAlMg_3Si_3O_{10}(OH)_2 + 3\ CaCO_3 + 3\ CO_2 \rightarrow 3\ CaMg(CO_3)_2 + KAlSi_3O_8 + H_2O$

Calcite + Chlorite + Dolomite + Quartz -> Ankerite + Kaolinite

$7\ CaCO_3 + 3.5\ Fe_2Al_2SiO_5(OH)_4 + 3\ CaMg(CO_3)_2 + 3.5\ SiO_2 + 7\ CO_2 \rightarrow 10\ CaMg_{0.3}Fe_{0.7}(CO_3)_2 + 3.5\ Al_2Si_2O_5(OH)_4$

Table 7.13 Mineralogical changes with the equilibrium modelling for sample EDR-988 from Edremit field (values are as moles, blue colour indicates dissolution and red indicates precipitation, bold shows $CO_2$ trapping minerals)

| Mineral | EDR-988 | | |
|---|---|---|---|
| | Initial | Final | Delta |
| Albite | 50.86 | 50.69 | -0.17 |
| Amphibole | 0 | 0 | 0 |
| Biotite | 7.89 | 0 | -7.89 |
| Bytownite | 0 | 0 | 0 |
| Calcite | 26.10 | 0 | -26.10 |
| Chlorite | 18.35 | 17.13 | -1.22 |
| **Dolomite** | **5.67** | **28.3** | **22.63** |
| Illite | 0 | 0 | 0 |
| Kaolinite | 20.64 | 21.94 | 1.30 |
| Labradorite | 0 | 0 | 0 |
| Orthoclase | 0 | 7.89 | 7.89 |
| Quartz | 338.30 | 337.4 | -0.90 |
| **Ankerite** | **0** | **3.47** | **3.47** |
| Dawsonite | 0 | 0 | 0 |
| Magnesite | 0 | 0 | 0 |
| Siderite | 0 | 0 | 0 |

As a result of the reactions, mineral trapping is estimated as 97% and solubility trapping as 3% for $CO_2$ added to the system.

### 7.3.2.2 Kinetic Modelling

Reactions for sample EDR-988 that are determined in equilibrium modelling are investigated in terms of time (Fig.7.13). With $CO_2$ addition, ankerite starts to precipitate (Fig.7.14a). Dolomite initially dissolves for the first 15 days, but in one and a half years it precipitates. $CO_2$ is totally consumed within one and a half years (i.e. the mol value of injected $CO_2$ becomes zero, Fig.7.14b). The system reaches equilibrium in approximately 140 years (Fig.7.13). The initial pH value of 7.61 drops to 5.05 with the addition of $CO_2$, it increases in time and in approximately one and a half years it reaches to the final value of 6.23 (Fig.7.14c).

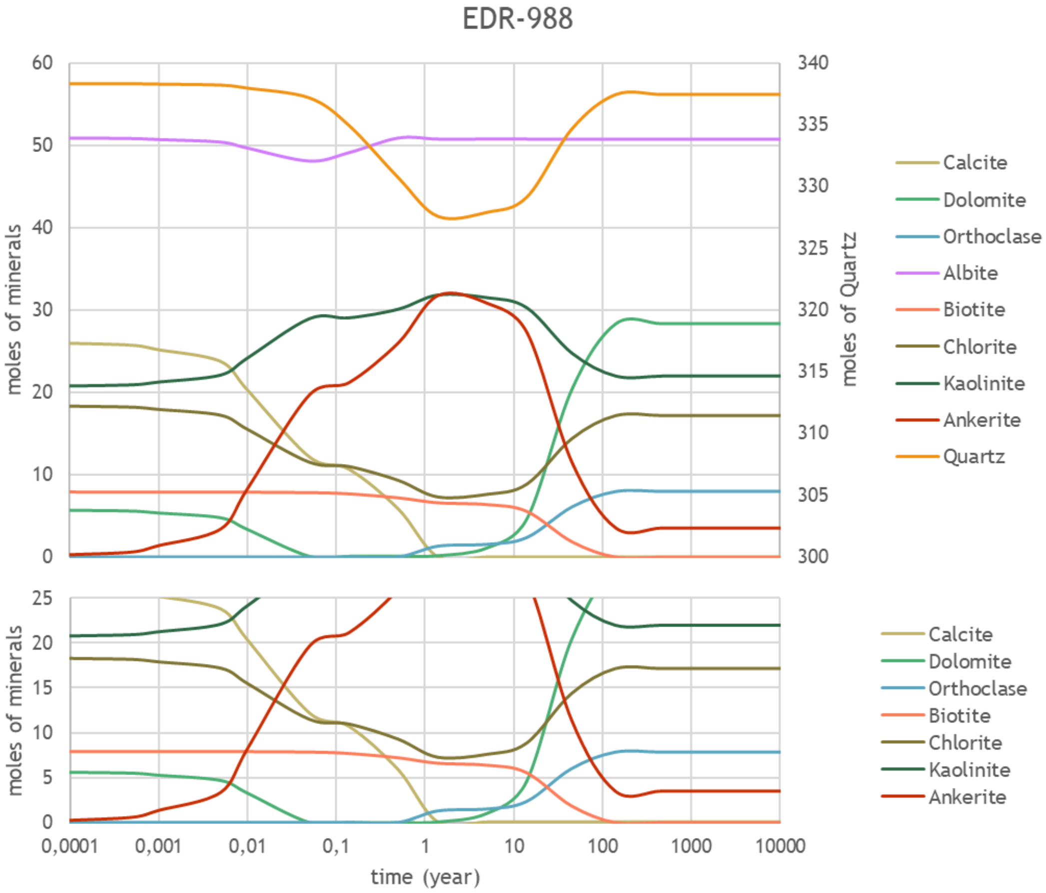

Figure 7.13. Temporal changes in the reservoir mineralogy (EDR-988, Edremit field) followed by $CO_2$ addition to the system

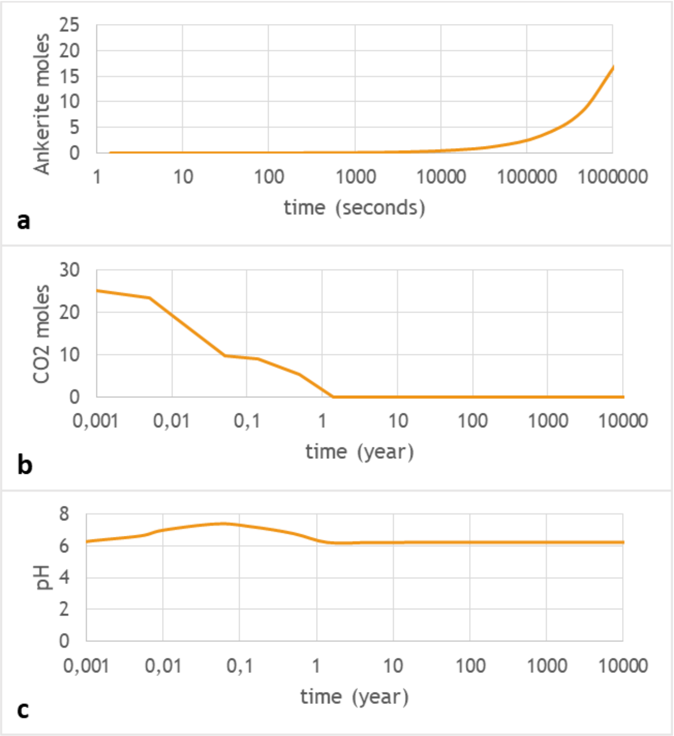

Figure 7.14. Changes that occur in time in a. the concentration of carbonate mineral reacting from the start, b. the amount of $CO_2$ and c. pH values for sample EDR-988 from Edremit field

#### 7.3.2.3 Reactive Transport Modelling

The changes in the mineral concentrations in 100 years along the reservoir which is simulated as a 100 m-long horizontal column for sample EDR-988 are illustrated in Figure 7.15 (100 m long column is zoomed in to 20 m for better inspection of results). According to the models, the reactions that are determined with equilibrium and kinetic modelling, take place in approximately 10.5 meters from the supposed $CO_2$ injection point. The results reveal that the evolution of the reactions from first year starts with lesser molar amounts in shorter distances (~2.5 m). The fluctuations observed in dolomite, ankerite, chlorite and kaolinite values indicate the complex reaction dynamics as determined from the equilibrium and kinetic modelling results.

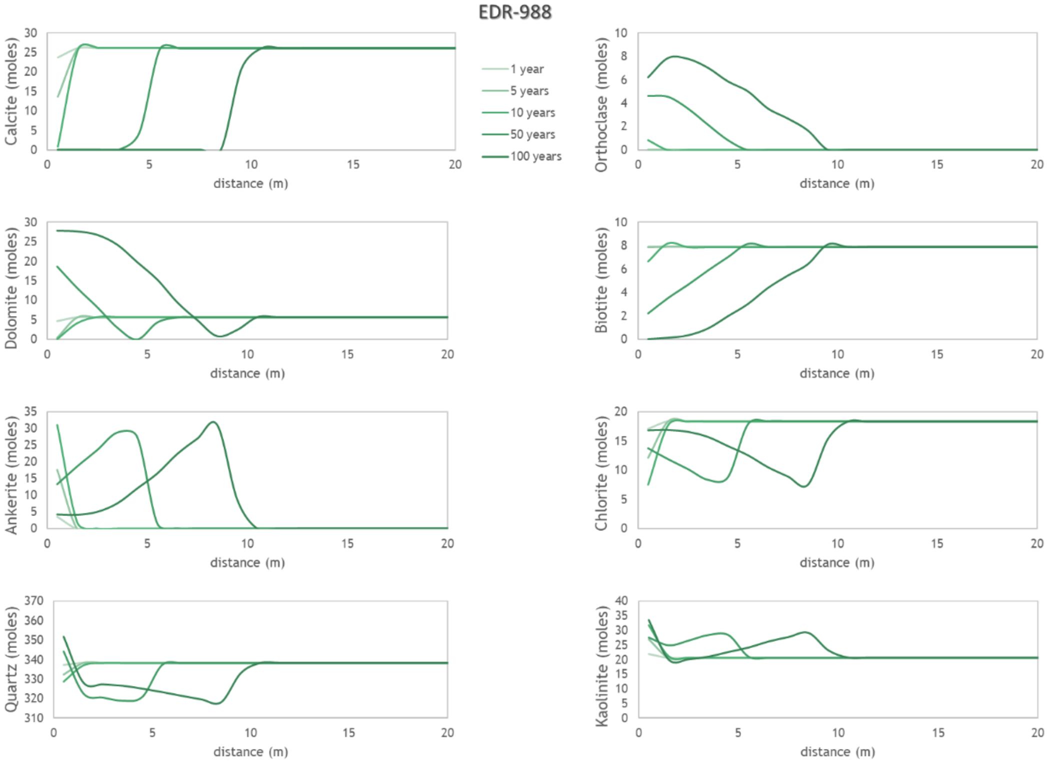

Figure 7.15. The changes in the mineral phases of sample EDR-988 (Edremit field) against distance in different times

## 7.3.3 Simulated Sample: EDR-1008

### 7.3.3.1 Equilibrium Modelling

In the simulations of sample EDR-1008, determined secondary minerals are calcite and dolomite and the calculated mol amount of $CO_2$ that can be completely used up is 60 moles following the preliminary Saturation Index calculations.

The equilibrium modelling results of sample EDR-1008 are given in Tables 7.14 and 7.15. According to the equilibrium modelling results, with the addition of $CO_2$, pH drops down to 6.89, Al, total C, Cl, Fe, K, Mg, Na, $SO_4$, Si contents increase and Ca values decrease in the water sample (Table 7.14).

Table 7.14 Equilibrium modelling results of the aqueous phase reacting with sample EDR-1008 (Edremit field)

| **EDJ-7** | **initial** | **final** |
|---|---|---|
| pH | 7.61 | 6.89 |
| Al (mol/L) | 3.26E-06 | 1.02E-05 |
| Total C (mol/L) | 6.07E-04 | 0.01367 |
| Ca (mol/L) | 9.74E-04 | 1.93E-04 |
| Cl (mol/L) | 0.001779 | 0.004252 |
| Fe (mol/L) | 1.42E-06 | 3.39E-06 |
| K (mol/L) | 1.46E-04 | 8.35E-04 |
| Mg (mol/L) | 4.12E-06 | 4.66E-05 |
| Na (mol/L) | 0.01071 | 0.03487 |
| $SO_4$ (mol/L) | 0.005211 | 0.01246 |
| Si (mol/L) | 0.0003739 | 0.001984 |

The variations in the mineral assemblage point to the dissolution of biotite, kaolinite, labradorite, orthoclase and the precipitation of albite, calcite, dolomite, illite and quartz (Table 7.15). The amount of quartz that precipitates is very little (0.01 mol). The carbonate minerals that “trap” $CO_2$ are calcite and dolomite. These minerals are likely to form through the following reactions:

Labradorite -> Calcite + Albite + Kaolinite

$2.5\ Na_{0.4}Ca_{0.6}Al_{1.6}Si_{2.4}O_8 + 1.5\ CO_2 + 3\ H_2O = 1.5\ CaCO_3 + NaAlSi_3O_8 + 1.5\ Al_2Si_2O_5(OH)_4$

Biotite + Calcite -> Dolomite + Orthoclase

$KAlMg_3Si_3O_{10}(OH)_2 + 3\ CaCO_3 + 3\ CO_2 = 3\ CaMg(CO_3)_2 + KAlSi_3O_8 + H_2O$

Dolomite + Labradorite + Orthoclase + Kaolinite -> Calcite + Illite + Albite

$1.5\ CaMg(CO_3)_2 + 3.5\ Na_{0.4}Ca_{0.6}Al_{1.6}Si_{2.4}O_8 + 3.6\ KAlSi_3O_8 + 3\ Al_2Si_2O_5(OH)_4 + 6\ CO_2 \rightarrow 3.6\ CaCO_3 + 6\ K_{0.6}Mg_{0.25}Al_{1.8}Al_{0.5}Si_{3.5}O_{10}(OH)_2 + 1.4\ NaAlSi_3O_8$

In these reactions, dissolution of calcite and dolomite as well as precipitation of kaolinite and orthoclase also take place as opposed to the equilibrium results. Kinetic modelling is referred to for detailed inspection of the reactions.

Table 7.15 Mineralogical changes with the equilibrium modelling for sample EDR-1008 from Edremit field (values are as moles, blue colour indicates dissolution and red indicates precipitation, bold shows $CO_2$ trapping minerals)

| Mineral | EDR-1008 | | |
|---|---|---|---|
| | Initial | Final | Delta |
| Albite | 0 | 25.22 | 25.22 |
| Actinolite | 0 | 0 | 0 |
| Biotite | 12.77 | 1.554 | -11.22 |
| Bytownite | 0 | 0 | 0 |
| **Calcite** | **0** | **15.67** | **15.67** |
| Chlorite | 0 | 0 | 0 |
| **Dolomite** | **0** | **22.16** | **22.16** |
| Illite | 15.52 | 61.45 | 45.93 |
| Kaolinite | 1.21 | 0 | -1.21 |
| Labradorite | 63.05 | 0 | -63.05 |
| Orthoclase | 43.55 | 27.21 | -16.34 |
| Quartz | 189.59 | 189.6 | 0.01 |
| Ankerite | 0 | 0 | 0 |
| Dawsonite | 0 | 0 | 0 |
| Magnesite | 0 | 0 | 0 |
| Siderite | 0 | 0 | 0 |

As a result of the reactions, 100% of the added $CO_2$ is trapped in minerals.

#### 7.3.3.2 Kinetic Modelling

Reactions for sample EDR-1008 that are determined in equilibrium modelling are investigated in terms of time (Fig.7.16). Within the first half an hour of $CO_2$ addition, calcite starts to precipitate (Fig.7.17a). Dolomite formation begins in 4 hours. Kaolinite also starts to precipitate within the first half an hour, it continues to form for 6 months and afterwards, it completely dissolves in 450 years (as determined by equilibrium modelling results, Fig.7.16). In the second year of the reactions, calcite dissolution (from 27.18 moles to 15.67 moles) is observed. $CO_2$ is totally consumed within 14 years (i.e. the mol value of injected $CO_2$ becomes zero, Fig.7.17b). The system reaches equilibrium in approximately 450 years (Fig.7.16). The initial pH value of 7.61 drops to 4.21 with the addition of $CO_2$, it increases in time and in approximately 450 years it reaches to the final value of 6.89 (Fig.7.17c).

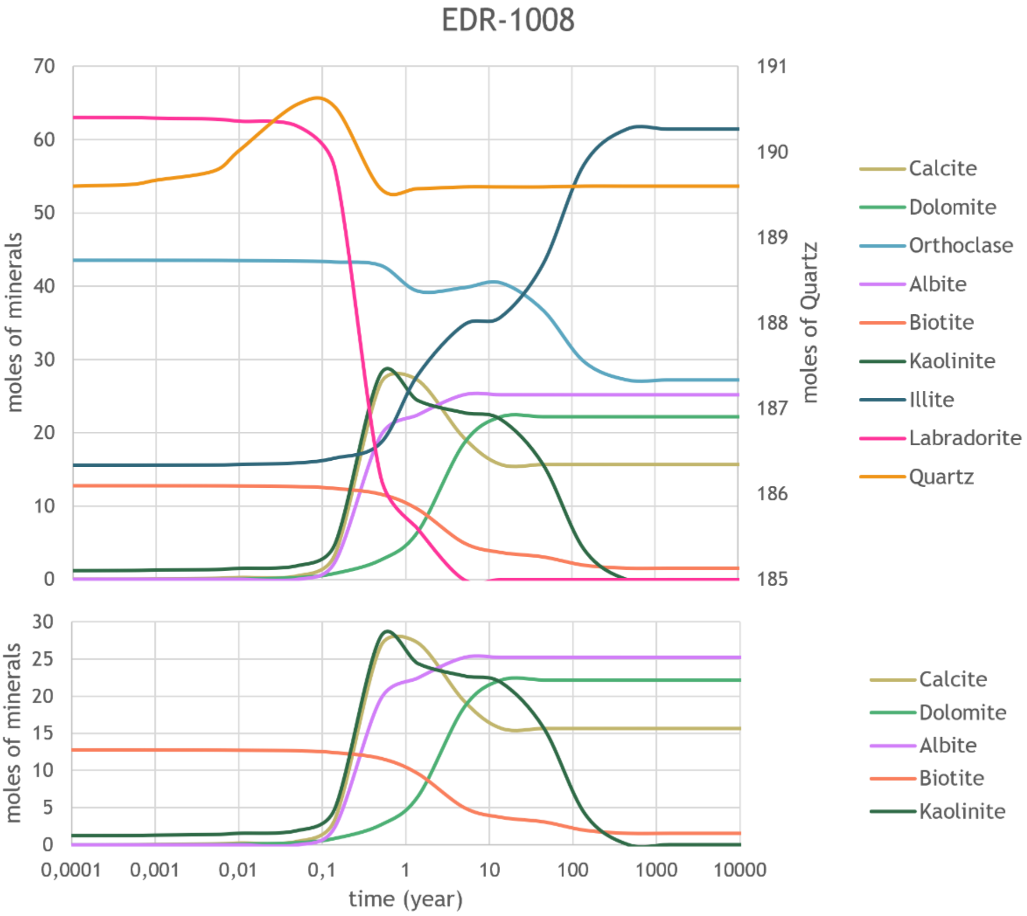

Figure 7.16. Temporal changes in the reservoir mineralogy (EDR-1008, Edremit field) followed by $CO_2$ addition to the system

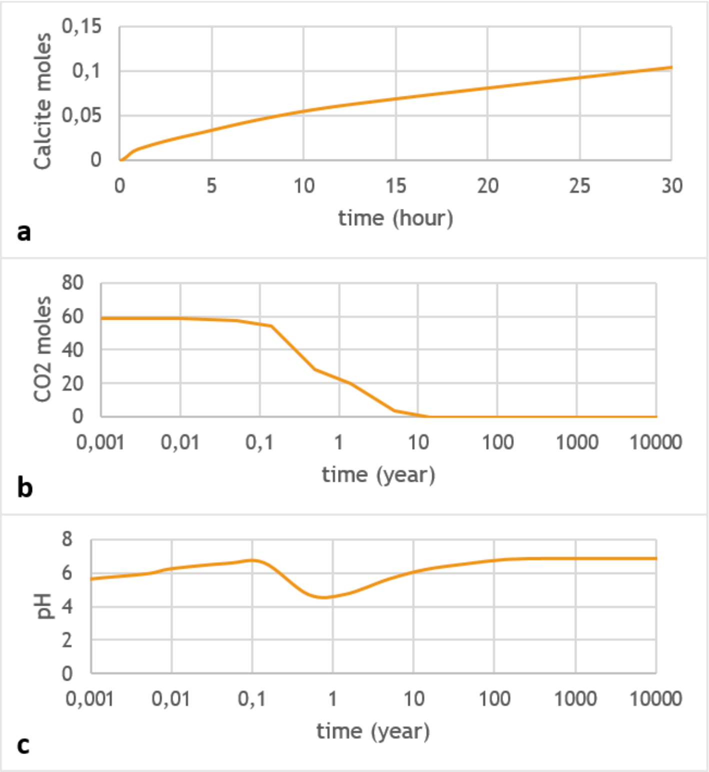

Figure 7.17. Changes that occur in time in a. the concentration of carbonate mineral reacting from the start, b. the amount of $CO_2$ and c. pH values of sample EDR-1008 from Edremit field

#### 7.3.3.3 Reactive Transport Modelling

The changes in the mineral concentrations in 100 years along the reservoir which is simulated as a 100 m-long horizontal column for sample EDR-1008 are illustrated in Figure 7.18 (100 m long column is zoomed in to 20 m for better inspection of results). According to the models, the reactions that are determined with equilibrium and kinetic modelling, take place in approximately 4.5 meters from the supposed $CO_2$ injection point and decrease gradually with distance. The reactions start to take place in the first year with lesser molar amounts in shorter distances (~1.5 m). The likely reason for the fluctuations observed in calcite, albite and illite values is the complex reaction dynamics that govern the system as determined from the equilibrium and kinetic modelling results.

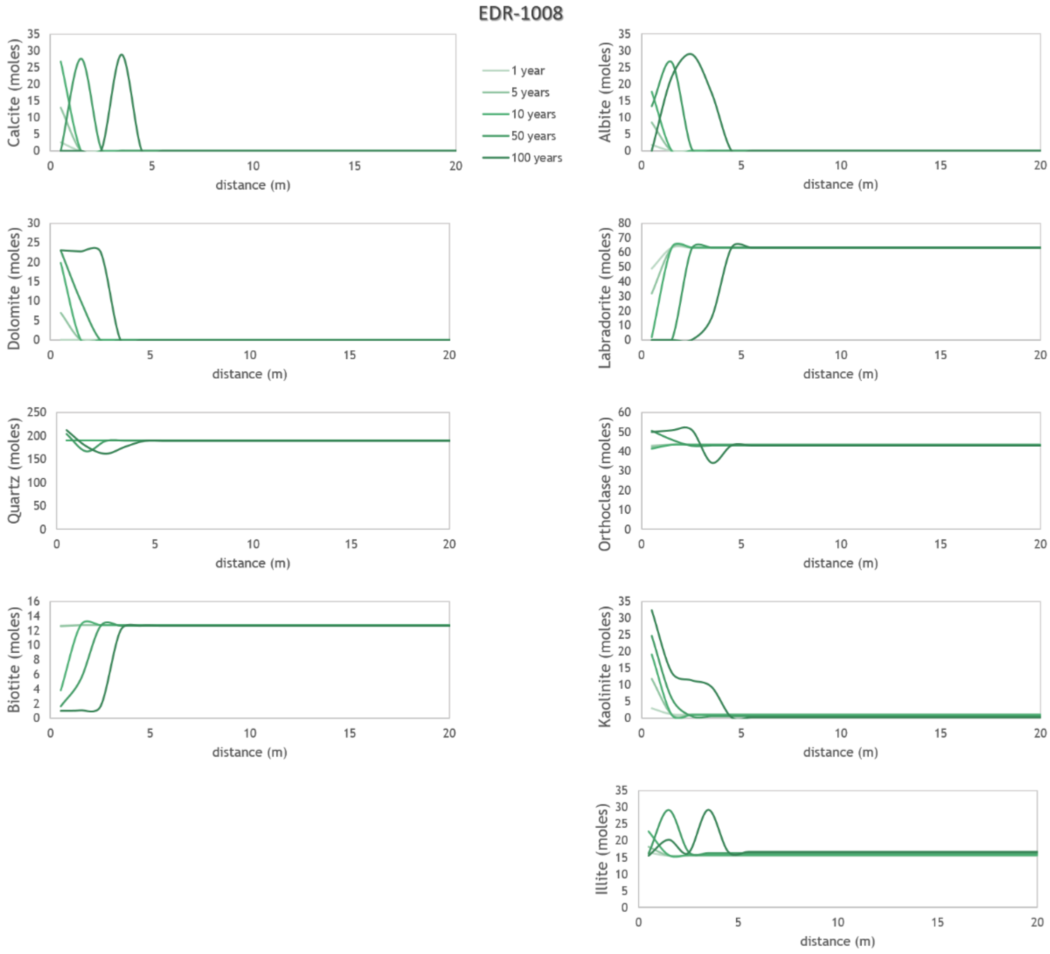

Figure 7.18. The changes in the mineral phases of sample EDR-1008 (Edremit field) against distance in different times

# CHAPTER 8

# DISCUSSIONS & IMPLICATIONS FOR $CO_2$ STORAGE

## 8.1 Akköy Field

In Akköy field, modelling results show that ankerite precipitates in most of the samples and it is the main carbonate phase to act as a trap for $CO_2$. Dawsonite, dolomite and siderite are the other carbonates which precipitate as secondary minerals and hold the added $CO_2$.

Alumino-silicate minerals that donate the required cations for secondary carbonate precipitation are mainly clay minerals (illite and smectite) which are followed by albite, chlorite and biotite. Calcite, being the main carbonate mineral in most of the samples, dissolves in the majority of the reactions and acts as a donor for $Ca^{2+}$. In the presence of clay minerals, both ankerite and dolomite show precipitation in most of the samples while chlorite or biotite generally seem to promote ankerite precipitation coupled with dolomite dissolution (PS-1-1375, PS-1-1495, PS-1-1515, PS-2-1380). The dissolution of albite seems to be directly related to the formation of dawsonite (PS-1-1315, PS-1-1480, PS-2-840, PS-2-1355), however, albite is not the only source for dawsonite precipitation. Smectite dissolution also leads to dawsonite precipitation in the absence of albite (PS-1-1415, PS-2-1280).

Towards deeper levels in the samples of both PS-1 and PS-2 wells (PS-1-1495, PS-1-1515, PS-2-1380), it is observed that the effective reaction is calcite, dolomite, chlorite dissolution resulting in the precipitation of ankerite.

All reactions seem to start very quickly (either immediately or one and a half days); however, the time to reach equilibrium for these reactions changes from 10 years to 500 years (Table 8.1). It is observed that if a reaction involves the dissolution of a clay mineral (i.e. clays being a “cation donor” for the secondary carbonate formation), that reaction’s time to reach equilibrium increases significantly compared to the reactions that do not indicate clay dissolution.

Table 8.1 Timings of the kinetic reactions of Akköy field samples

| Sample No. | | Timing | | Maximum distance in 100 years (m) | Main reactions |
|---|---|---|---|---|---|
| | | Rxns start | Equilibrium reached | | |
| **PS-1** | **1315** | one and a half days | 14 yrs | 42.5 | Alb -> Daws + Qtz |
| **PS-1** | **1375** | 3 hrs | 500 yrs | 13.5 | Cal + Dol + Bio -> Ank + Orth<br>Cal + Ill + Bio + Orth -> Ank + Musc + Qtz |
| **PS-1** | **1415** | one day | 500 yrs | 71.5 | Cal + Ill -> Dol + Musc + Kaol + Qtz<br>Cal + Ill + Sme -> Dol + Ank + Daws |
| **PS-1** | **1480** | instantly | 500 yrs | 57.5 | Alb -> Daws + Qtz<br>Cal + Sme -> Ank + Dol |
| **PS-1** | **1495** | 5 mins | 500 yrs | 2 | Cal + Ill + Chl + Qtz -> Dol + Bio + Kaol<br>Cal + Dol + Chl + Qtz -> Ank + Kaol |
| **PS-1** | **1515** | 5 mins | 10 yrs | 8 | Cal + Dol + Chl + Qtz -> Ank + Kaol |
| **PS-2** | **840** | instantly | 500 yrs | 18 | Cal + Ill + Orth -> Dol + Musc + Qtz<br>Cal + Dol + Bio -> Ank + Orth<br>Bio -> Sid + Orth, Alb -> Daws + Qtz |
| **PS-2** | **1280** | instantly | 450 yrs | 81.5 | Cal + Sme -> Ank + Dol + Daws |
| **PS-2** | **1355** | one and a half days | 140 yrs | 23.5 | Alb -> Daws + Qtz |
| **PS-2** | **1380** | instantly | 45 yrs | 6.5 | Cal + Dol + Chl + Qtz -> Ank + Kaol |

The spatial evolution of the samples ranges from 2 m to 81.5 m from the point that $CO_2$ added to the system (Table 8.1). A notable observation is that all the reactions in which smectite is one of the reactants (PS-1-1415, PS-1-1480, PS-2-1280), propagate longer distances (>50 m).

## 8.2 Edremit Field

Modelling studies of Edremit reveal that dolomite precipitates in most of the samples constituting the principal carbonate phase that restrains $CO_2$. Magnesite, calcite and ankerite are the additional secondary carbonates.

Biotite is the main cation donor of the system followed by the plagioclase minerals (albite, labradorite and bytownite), actinolite, chlorite and illite. In the samples in which calcite dissolves, calcite donates the necessary $Ca^{2+}$ ion for the formation of dolomite and ankerite, except for the reactions where Ca-plagioclase (labradorite and bytownite) minerals are present. In fact, only cases of calcite precipitation take place coupled with the dissolution of Ca-bearing plagioclase feldspars towards relatively deeper levels (EDR-976, EDR-994, EDR-1008).

All reactions start very quickly (under 6 hours) and most of the samples reach equilibrium relatively faster (under 150 years, Table 8.2). In the samples which take longer time to attain equilibrium, it is observed that clay minerals participate in the dissolution reactions (illite and kaolinite).

Table 8.2 Timings of the kinetic reactions of Edremit field samples

| **Sample No.** | | **Timing** | | **Maximum distance in 100 years (m)** | **Main reactions** |
|---|---|---|---|---|---|
| | | **Rxns start** | **Equilibrium reached** | | |
| **EDR** | **912** | 3 hrs | 40 yrs | 8.5 | Bio + Cal -> Dol + Mag + Orth |
| **EDR** | **928** | instantly | 450 yrs | 3.5 | Cal + Ill -> Dol + Orth + Kaol |
| **EDR** | **964** | 5 hrs | 45 yrs | 5.5 | Bio -> Mag + Orth |
| **EDR** | **976** | half an hour | 6 mos | 8.5 | Labr -> Cal + Alb + Kaol |
| **EDR** | **988** | instantly | 140 yrs | 10.5 | Cal + Bio -> Dol + Orth<br>Cal + Chl + Dol + Qtz -> Ank + Kaol |
| **EDR** | **994** | instantly | 200 yrs | 2.5 | Act + Orth -> Dol + Ill + Alb + Bio<br>Dol + Orth + Byt + Kaol -> Cal + Alb + Ill<br>Cal + Bio -> Dol + Orth |
| **EDR** | **1008** | half an hour | 450 yrs | 4.5 | Labr -> Cal + Alb + Kaol<br>Bio + Cal -> Dol+Orth<br>Dol + Lab + Orth + Kaol -> Cal + Ill + Alb |
| **EDR** | **1032** | half an hour | 45 yrs | 7.5 | Bio + Cal -> Dol + Mag + Orth |

The reactions take place in the distances from 2.5 m to 10.5 m from the inlet (Table 8.2). Shorter distances might indicate relatively faster reactions (as determined by kinetic modelling) resulting in the inhibition regarding the progress of $CO_2$-induced fluid further into the system.

## 8.3 Comparison of the Results

Main processes that are effective in Akköy and Edremit fields following a $CO_2$ addition to the systems determined as a result of modelling are summarized in Tables 8.3 and 8.4.

Table 8.3 Summary of modelling results of the samples from Akköy field

| **Sample No.** | | **Silica** | **Carbonate** | | | **Feldspar** | | **Mica** | | **Chlorite** | **Clay** | | | **Secondary Carbonates** | | **Trapping Mechanism** | | **$CO_2$** |
|---|---|---|---|---|---|---|---|---|---|---|---|---|---|---|---|---|---|---|
| | | **Quartz** | **Calcite** | **Dolomite** | **Ankerite** | **Orthoclase** | **Albite** | **Muscovite** | **Biotite** | | **Kaolinite** | **Illite** | **Smectite** | **Dawsonite** | **Siderite** | **Mineral** | **Solubility** | **moles** |
| **PS-1** | **1315** | 🟥 | | 🟪 | | | 🟦 | 🟥 | | | | 🟦 | | 🟪 | | **89** | **11** | **8** |
| **PS-1** | **1375** | 🟥 | 🟦 | 🟦 | 🟪 | 🟥 | | 🟥 | 🟦 | | | 🟦 | 🟦 | | | **97** | **3** | **46** |
| **PS-1** | **1415** | 🟥 | 🟦 | 🟪 | 🟪 | | | 🟥 | | | 🟥 | 🟦 | 🟦 | 🟪 | | **91** | **9** | **13** |
| **PS-1** | **1480** | 🟥 | 🟦 | 🟪 | 🟪 | | 🟦 | 🟥 | | | 🟥 | | 🟦 | 🟪 | | **97** | **3** | **31** |
| **PS-1** | **1495** | 🟦 | 🟦 | 🟦 | 🟪 | | | | 🟥 | 🟦 | 🟥 | 🟦 | 🟥 | | | **100** | **0** | **20** |
| **PS-1** | **1515** | 🟦 | 🟦 | 🟦 | 🟪 | | | 🟥 | | 🟦 | 🟥 | | | | | **100** | **0** | **50** |
| **PS-2** | **840** | 🟥 | 🟦 | 🟪 | 🟪 | 🟦 | 🟦 | 🟥 | 🟦 | | | 🟦 | 🟥 | 🟪 | 🟪 | **99** | **1** | **67** |
| **PS-2** | **1280** | 🟥 | 🟦 | 🟪 | 🟪 | | | 🟦 | | | | 🟥 | 🟦 | 🟪 | | **92** | **8** | **8** |
| **PS-2** | **1355** | 🟥 | | | | | 🟦 | | | | | | | 🟪 | | **100** | **0** | **31** |
| **PS-2** | **1380** | 🟦 | 🟦 | 🟦 | 🟪 | | | | | 🟦 | 🟥 | | | | | **99** | **1** | **73** |

🟦 **Dissolution**
🟥 **Precipitation**
🟪 **$CO_2$ Trap**

Table 8.4 Summary of modelling results of the samples from Edremit field

| Sample No. | | Silica | Carbonate | | Feldspar | | | | Mica | Amphibole | Chlorite | Clay | | Secondary Carbonates | | Trapping Mechanism | | CO$_2$ |
|---|---|---|---|---|---|---|---|---|---|---|---|---|---|---|---|---|---|---|
| | | Quartz | Calcite | Dolomite | Orthoclase | Albite | Labradorite | Bytownite | Biotite | Actinolite | | Kaolinite | Illite | Ankerite | Magnesite | Mineral | Solubility | moles |
| EDR | 912 | 🟥 | 🟦 | 🟪 | 🟥 | | | | 🟦 | | | | | | 🟪 | 99 | 1 | 33 |
| EDR | 928 | 🟥 | 🟦 | 🟪 | 🟥 | 🟦 | | | | | | 🟥 | 🟦 | | | 90 | 10 | 4 |
| EDR | 964 | 🟥 | | | 🟥 | | | | 🟦 | | | | 🟥 | | 🟪 | 98 | 2 | 46 |
| EDR | 976 | 🟦 | 🟪 | | | 🟥 | 🟦 | | | | | 🟥 | | | | 100 | 0 | 27 |
| EDR | 988 | 🟦 | 🟦 | 🟪 | 🟥 | 🟦 | | | 🟦 | | 🟦 | 🟥 | | 🟪 | | 97 | 3 | 27 |
| EDR | 994 | 🟥 | 🟪 | 🟪 | 🟦 | 🟥 | | 🟦 | 🟦 | 🟦 | | 🟦 | 🟥 | | | 100 | 0 | 69 |
| EDR | 1008 | 🟥 | 🟪 | | 🟦 | 🟥 | 🟦 | | 🟦 | | | 🟦 | 🟥 | | | 100 | 0 | 60 |
| EDR | 1032 | 🟦 | 🟦 | 🟪 | 🟥 | | | | 🟦 | | | | | | 🟪 | 100 | 0 | 54 |

🟦 Dissolution
🟥 Precipitation
🟪 CO$_2$ Trap

Calcareous rocks and minerals dominate Akköy geothermal system and modelling results show that calcite (which is the main carbonate mineral) dissolves in all samples where it is present. In Edremit, on the other hand, carbonates are not as dominant as in Akköy field and calcite precipitation is observed in some samples (unlike calcite dissolution in majority of samples of Akköy).

Ankerite is the main carbonate phase that can trap the injected $CO_2$ in Akköy, whereas dolomite is the mineral that can sequester $CO_2$ in Edremit field. The formation of ankerite may point to the availability of $Fe^{2+}$ ion due to the mineralogical composition of rocks in Akköy field. This also results in siderite precipitation in one of the samples from Akköy (PS-2-840). These findings of carbon mineralization seem to be in conformity with the results of large-scale demonstration projects that revealed ankerite and siderite as the main minerals trapping $CO_2$ in Wallula Basalt-USA and in Otway-Australia, respectively (Romanov et al., 2015 and the references therein; McGrail et al., 2017; White et al., 2020).

Principal “cation donors” in the reactions of Akköy and Edremit fields are clay minerals (illite, smectite) and biotite, respectively. Calcite also acts as the supplier for calcium ions in both fields. The lithological differences most likely determine the “role” of a mineral that donate its divalent cations to the system to be used in the formation of a secondary carbonate mineral.

The amount of feldspars in the samples from Edremit is almost seven times more than the samples from Akköy according to the modal mineralogy results (Table 5.3). If a feldspar (especially plagioclase) is present as a primary mineral, it dissolves in most of the samples in both fields forming a secondary carbonate mineral. One of the main reactions in Akköy field is the formation of dawsonite from the dissolution of albite. Although albite is also present in some of the Edremit samples, this reaction does not occur. The reasons might be that as the result of the reactions i) the amount of dissolved albite is very small (EDR-928 – Appendix H, EDR-988 – Table 7.13) and ii) the water sample is undersaturated with respect to dawsonite. Qu et al. (2022) and Forray et al. (2021 and the references therein) state that Al and (especially) Na source for dawsonite formation is generally the formation water. Therefore, due to the unavailability of the required cations, dawsonite does not form in those samples.

In the samples of both fields in which clay minerals dissolve in the reactions and supply cations for secondary carbonate formation, equilibrium seems to be reached in a very long time (especially in Akköy samples in which clay minerals constitute one of the abundant phases in the mineral assemblage). Each sample in which the equilibrium is reached in longer than 150 years, a clay mineral (illite/smectite/kaolinite) dissolution is observed (PS-1-1375, PS-1-1415, PS-1-1480, PS-1-1495, PS-2-840, PS-2-1280, EDR-928, EDR-994, EDR-1008, Tables 8.1, 8.2). Time scale for the dissolution of clay minerals is described to be long-term (Rathnaweera et al., 2016 in Fatah et al., 2022), in fact, it is emphasized in Balashov et al. (2013) that equilibrations of especially clay mineral reactions take the longest time. Contrary to these slow reacting minerals, some of the relatively fast reactions of both fields contain chlorite which is reported as a very reactive mineral, rapidly engaging in reactions (Balashov et al., 2013; Higgs et al., 2015).

Most of the Edremit samples reach equilibrium faster than Akköy samples (Tables 8.1, 8.2). The clay mineral dominance as well as the relatively higher molar values of minerals in Akköy samples (e.g. determined porosity values are 3.37% and 5% in Akköy and Edremit, respectively) appear to affect the reaction times.

Although presence of clay minerals in the reactions as “cation donors” prolongs the time to reach equilibrium in those samples, there seems to be no simple relation on the distance. Relatively distal regions (>50 m) are attained especially for the reactions with smectite. Aside from the complexity of structural formula of smectite group minerals which may prolong the time and the distance of the reactions, another potential reason might be the larger surface area and hence, the higher adsorption capacity of these minerals. Due to greater adsorption capacity of smectites (Zhang et al., 2012 in Gueu et al., 2019; Kumari and Mohan, 2021), these minerals can adsorb $CO_2$ molecules on its interlayer domain increasing the inner spacing (Chouikhi et al., 2019 and the references therein). This may result in the adsorption of some of the added $CO_2$ in smectite structure (to be used later) while the remaining $CO_2$ in the fluid travels further in the system (as opposed to being quickly consumed in the reactions close to inlet) increasing the time and the distance for these reactions.

The average maximum distances in 100 years that reactions take place from the presumed point of $CO_2$ injection are approximately 30 m for Akköy field and 6 m for Edremit field. The longest distance in Akköy field reaches up to 81.5 m in sample PS-2-1280 (Appendix H). Most notable difference of these two systems is the lithology. Known as the complex silicates, clay minerals have distinctive properties due to their layered structures, chemical compositions and adsorption capacities (Kumari and Mohan, 2021). The complex nature of these minerals is the likely cause for the slow-moving reactions which lead to transportation of aqueous species for longer distances resulting in the precipitation of secondary minerals around more distal parts of the reservoir. On the contrary, the "straightforward" chemical reactions due to the relatively simple structured minerals in Edremit field limit the spatial scale of the reactions. Higher mass fractions of minerals such as calcite, dolomite, biotite, chlorite dissolved close to the inlet and gradually decreased with distance. Fast kinetic reaction rates of carbonate minerals also speed up these processes. Precipitation of carbonates restricts the fluids to become oversaturated with bicarbonate species and reduces the transportation distances for these constituents which as a result, paves the way for a small-scaled or in-situ precipitations of secondary carbonate minerals such as dolomite and ankerite (Ma et al., 2020). It is also important to note that Kampman et al. (2014) stated that the existence of multiple mineral phases in a system complicates the approach to equilibrium due to the reaction rate differences of each mineral having a diverse effect on the solution chemistry.

Regarding the amount of $CO_2$ that can be added to the system, the range is between 8-73 moles for Akköy (Table 8.3) and 4-69 moles for Edremit field (Table 8.4). To give a general idea to the reader, these mol amounts can roughly be converted to volume by using the $PV = nRT$ relationship. In the calculations, the temperature and pressure values are taken as those utilized in the models (i.e. T = highest estimated reservoir temperature, P = hydrostatic pressure at the relevant depth). The results of calculations yield a range of 2-26 liters for Akköy, and 1.5-24 liters for Edremit field. It should be noted here that a more realistic approach would require 3-D modelling of the reservoir.

A striking comparison is that, the reactions take place in the mainly metamorphic/sedimentary rocks of Akköy in longer times and distances while in the dominantly igneous reservoir of Edremit, the time and the distance of the reactions are relatively quicker and shorter. Recent studies regarding suitability and feasibility of rock formations for effective $CO_2$ storage highlight that igneous rocks constitute more favourable settings in terms of carbon mineralization, especially as opposed to sedimentary formations in which the reactivity of $CO_2$ may be low due to higher quartz content and as a result, mobile $CO_2$ may remain in the reservoir for centuries (Luhmann et al., 2017; Kelemen et al., 2019; Snaebjörnsdóttir et al., 2020; Ratouis, 2022; Raza et al., 2022; Kim et al., 2023). Although the simulations performed in this study have shown that both fields reach the desired outcome of $CO_2$ confinement through mineral trapping, an injection into the ignous rocks of Edremit field may yield better results. The quicker times and shorter distances of resulted reactions may also limit the potentially negative changes induced by $CO_2$ addition to the overall properties of the reservoir (such as porosity, permeability, integrity and rock strength).

## 8.4 Effect of $CO_2$ Amount

The simulations are performed with the assumption of abundant $CO_2$ is supplied into the system. The mol amount is calculated specific to each sample which differs due to the mineralogical differences. In order to investigate the effect of $CO_2$ amount on the reaction kinetics, among the simulated samples one from each field are chosen (PS-2-840 and EDR-988) and modelled with 10 moles of $CO_2$.

PS-2-840 was initially modelled with 67 moles of $CO_2$, the reactions resulted in the precipitation of 33 moles of ankerite, 19.41 moles of dawsonite and 13.72 moles of siderite (Table 7.7). An insignificant amount of dolomite was also precipitated, but it dissolved in a short time at the beginning of reactions. The reactions initiated with $CO_2$ addition and equilibrated in approximately 500 years. $CO_2$ was completely consumed within 450 years. At the end of the reactions, the initial pH value 7.6 dropped down to 6.53. The reactions of the model in which 10 moles of $CO_2$ is added, started with $CO_2$ addition and lasted for 500 years (similar results with previous modelling). $CO_2$ consumption is realised in 45 years and pH value is reduced to 7.51. The decreased amount of $CO_2$ resulted in the reduced degree of mineral interactions (i.e. minerals are dissolved/precipitated in lesser molar amounts). As a result of the reactions with 10 moles of $CO_2$, 5.55 moles of ankerite and 4.41 moles of dolomite precipitated.

The modelling of the sample EDR-988 was initially performed with 27 moles of $CO_2$. As a result, 22.63 moles of dolomite and 3.47 moles of ankerite were precipitated (Table 7.13). The reactions started immediately and continued for approximately 140 years. $CO_2$ was consumed within one and a half years. The initial value of pH (7.61) dropped to 6.23. In the model with 10 moles of $CO_2$, the reactions similarly start with $CO_2$ addition; however, the equilibration of the system takes place within 6 months and pH value becomes 7.00. $CO_2$ is also used up relatively quickly, in half a month. While dolomite dissolved in this scenario, ankerite precipitated for 14.25 moles.

The increase in the $CO_2$ amount has caused i) lower pH values, ii) the prolonged time of $CO_2$ consumption and iii) the raise in the molar values of minerals resulted from the reactions for both samples. The reactions of Edremit sample have also reached equilibrium in longer time with higher amount of $CO_2$. Moreover in both samples, increased $CO_2$ has resulted in the precipitation of additional secondary minerals. It can be deduced that mineralogical differences are also reflected in the changes induced by various $CO_2$ quantities.

## 8.5 Limitations & Uncertainties

In this thesis study, the major limitations and uncertainties are those related to i) the type of samples (drill cuttings) and ii) the assumptions, as well as the parameters used in modelling.

Drill cutting samples may result in geochemical bias due to i) loss of less resistant minerals during sample collection, ii) mixing of collapsed material from shallower levels, iii) contamination related to the drilling processes (drilling mud, equipment, fractures etc.) (Fowler and Zierenberg, 2016 and the references therein; Sanei et al., 2020). Textural, lithologic, paragenetic relationships of mineral phases as well as the potential alteration products may not be well-preserved and easily assessed in fine-grained particles of drill cuttings. In this regard, drill core samples yield better conserved properties and geochemical studies performed on such samples offer more credible results. Despite these limitations, however, drill cuttings are widely used in various geothermal studies (Nasution et al., 2003; Hebert et al., 2011; Libbey and Williams-Jones, 2016a; Libbey and Williams-Jones, 2016b; Mauriohooho et al., 2016; Kölbel et al., 2020; Elidemir et al., 2022; Galeczka et al., 2022). One potential advantage of cuttings is even mentioned in the study of Libbey and Williams-Jones (2016a): in lithogeochemical investigations, the fine-grained, randomized nature of cutting samples provides unbiased insight compared to the core samples in which the small scale heterogeneities (e.g. veins) may contradict the larger scale geochemical signature of a system. Moreover, drill cuttings are not as costly as core samples and they are easily accessible in a drilling operation. In this study, the variety of the geochemical analyses performed on the cutting samples may minimize the potential errors. It should also be noted that all the minerals which are regarded as less-resistant and prone to be lost during sample collection (e.g. chlorite, actinolite, clay minerals - Fowler and Zierenberg, 2016) are observed in the studied samples which may indicate the relatively better quality of these samples.

Uncertainties regarding geochemical modelling are mainly the assumptions made in the setup and the associated kinetic parameters. In the setup stage, the scaling of rock volume to 1 liter of water filling the pore space (leading to the simulations of smaller scaled rock samples) and the limited availability of well log data from the studied fields, may cause a biased representation of the whole reservoir lithology. Furthermore, the major sources of uncertainties regarding kinetic parameters which may affect the accuracy of modelling, include those relevant to reactive surface areas, reaction rate constants and heterogeneities/impurities in the minerals and/or reservoir (Gaus et al., 2005; Gündoğan, 2011; Pham et al., 2012; Balashov et al., 2013; Hellevang et al., 2013; Fatah et al., 2022; Galeczka et al., 2022; Luo et al., 2022). For example, reactive surface area of minerals is calculated for ideal mineral phases, in other words, it may not reflect the reservoir conditions in which the area of minerals may be affected from various geochemical interactions that take place in the system (Fatah et al., 2022). Compared to batch modelling, even higher levels of uncertainty is present in reactive transport models. Large set of parameters is required to be used in reactive transport modelling studies and lengthy computation time is needed to solve the complete geochemical reactions (e.g. increasing the cell number with smaller cell lengths for detailed simulation) that can accurately represent the system for large-scale reservoir simulations (Gündoğan, 2011; Hellevang et al., 2013). Nevertheless, geochemical models are useful tools to make predictions and have an insight regarding the geochemical mechanisms in a system since natural systems are complex and continuously change over time.

# CHAPTER 9

# CONCLUSIONS & RECOMMENDATIONS

The lithogeochemical and hydrogeochemical properties of Akköy and Edremit geothermal fields are investigated, as potential sites for $CO_2$ storage, for the modelling of $CO_2$-fluid-rock interactions.

Petrographic examinations of the cuttings from Akköy field have revealed that the majority of rock fragments are comprised of calcareous rocks (marble/limestone) and quartz, calcite and clay minerals are determined as the primary mineral phases. For Edremit field, the dominant grains are identified as granitic rocks while quartz, feldspars, micas, carbonates and amphiboles are the main minerals. XRD, CRS and EPMA studies have provided additional insight regarding detailed characterization of mineral phases. The effects of hydrothermal fluid in the system (e.g. notable sulphur presence, sulphide mineralization) are also reflected in the results of these analyses as well as in the whole rock geochemistry results for both fields. Modal mineralogy evaluations indicate that carbonate and clay minerals are more abundant in Akköy samples than in Edremit whereas percentages of feldspars are distinctly higher in Edremit.

The waters are characterized as $Na + K – HCO_3 – SO_4$ type and $Na + K – SO_4$ type for Akköy and Edremit fields, respectively. Geothermometry and fluid mineral equilibria calculations of Akköy samples reveal 88-116°C as the estimated range for the reservoir temperature, slightly lower than the range of 92-150°C for Edremit field.

Utilizing the geochemical data of the studied rock and water samples, $CO_2$-fluid-rock interactions of Akköy and Edremit fields are simulated with equilibrium, kinetic and reactive transport modelling. The results have shown that:

1) The principal carbonate phases which precipitate as secondary minerals acting as traps for $CO_2$ are ankerite, followed by dawsonite and dolomite for Akköy field. Clay minerals (illite/smectite) and calcite constitute the main “cation donors” for ankerite and dolomite, while albite seems to be the main source for dawsonite. In deeper levels of Akköy field, chlorite dissolution (accompanied by calcite and dolomite) appears to be the effective reaction supplying the cations for ankerite.
2) In Edremit field, the main minerals that trap $CO_2$ are dolomite, followed by magnesite and calcite. Biotite seems to be the major $Mg^{2+}$ supplier for dolomite and/or magnesite, while the source of $Ca^{2+}$ ion is most likely calcite or Ca-plagioclase, depending on the mineralogical assemblage.
3) Dissolution of clay minerals has been observed to increase the time for reactions to reach equilibrium (longer than 150 years). Moreover for the reactions that include smectite, the reactions seem to propagate longer distances (>50 m) which may be due to i) complex mineralogical structure and ii) greater adsorption capacity of smectite than other clays.
4) When both fields are compared, the time and the distance of the reactions are observed to be longer in Akköy field where clay minerals are present in higher abundances and the reservoir rocks are dominantly metamorphic/sedimentary. Given that the reservoir of Edremit field is composed mainly of igneous rocks, coupled with the shorter time and distance for the reactions, makes Edremit field a more favourable site for $CO_2$ storage.
5) Increased $CO_2$ amount have also resulted in lower pH values, the increase of the time that $CO_2$ is consumed in the system and the increase in the amounts of the produced minerals, even causing the precipitation of an additional secondary trapping mineral.

The modelling results point to the importance of the lithological/mineralogical characteristics of a reservoir in $CO_2$-fluid-rock interactions. The “role” of the mineral (i.e. donor, trap) seems to be closely interrelated with the mineral composition and assemblage of the rock sample which as a result, directly affects the fate of $CO_2$ in a possible injection scenario. Thorough geochemical investigation also has a significant importance on the characterization of a reservoir to be as accurate as possible. Lithogeochemical studies, in this regard, complement the hydrogeochemical data providing useful insight from an additional viewpoint for a deep geothermal system that may otherwise have plenty of unknowns.

For a better assessment of the reservoir rock in a possible $CO_2$ storage scenario, the utilization of core samples instead of cuttings is recommended, especially for detailed and depth-related investigations. Potential reactions and geochemical mechanisms that may affect the system should then be evaluated since the lithologic and/or mineralogic differences have critical importance in $CO_2$-fluid-rock interactions. 3-D reactive transport simulations should also be incorporated into such studies, as 1-D models are limited and the evolution of a natural system where $CO_2$ is injected, can be more realistically evaluated as a multidimensional process. It must also be noted here that, although relatively simple, 1-D geochemical models provide key points of understanding for the fundamental predictions regarding the fate of $CO_2$ in the underground storage studies.

Geochemical approaches are an essential part of any CCS study. From geochemical analyses to modelling, each step provides distinctive knowledge on various aspects of the studied system. This thesis study underlines the importance of lithogeochemical characterization especially accompanied by hydrogeochemical investigations in a multiphase system such as geothermal fields. Furthermore, the modelling studies constitute remarkably helpful tools in evaluation of the evolution of these systems, notably in the case of $CO_2$ storage. Following the geochemical analyses and simulations performed within the scope of this thesis work, the studied fields, Akköy and Edremit, are revealed to be suitable candidates for a possible CCS project.

# REFERENCES

Addassi, M., Omar, A., Ghorayeb, K., & Hoteit, H. (2021). Comparison of various reactive transport simulators for geological carbon sequestration. *International Journal of Greenhouse Gas Control, 110*. doi:10.1016/j.ijggc.2021.103419

Alçiçek, H., Bülbül, A., & Alçiçek, M. (2016). Hydrogeochemistry of the thermal waters from the Yenice Geothermal Field (Denizli Basin, Southwestern Anatolia, Turkey). *Journal of Volcanology and Geothermal Research, 309*, 118-138. doi:10.1016/j.jvolgeores.2015.10.025

Alçiçek, H., Bülbül, A., Brogi, A., Liotta, D., Ruggieri, G., Capezzuoli, E., . . . Alçiçek, M. C. (2018). Origin, evolution and geothermometry of the thermal waters in the Gölemezli Geothermal Field, Denizli Basin (SW Anatolia, Turkey). *Journal of Volcanology and Geothermal Research, 349*, 1-30. doi:https://doi.org/10.1016/j.jvolgeores.2017.07.021

Alçiçek, H., Bülbül, A., Yavuzer, İ., & Alçiçek, M. C. (2019). Origin and evolution of the thermal waters from the Pamukkale Geothermal Field (Denizli Basin, SW Anatolia, Turkey): Insights from hydrogeochemistry and geothermometry. *Journal of Volcanology and Geothermal Research, 372*, 48-70. doi:https://doi.org/10.1016/j.jvolgeores.2018.09.011

Alçiçek, H., Varol, B., & Özkul, M. (2007). Sedimentary facies, depositional environments and palaeogeographic evolution of the Neogene Denizli Basin, SW Anatolia, Turkey. *Sedimentary Geology, 202*, 596–637.

Al-Khdheeawi, E. A., Mahdi, D. S., Ali, M., Iglauer, S., & Barifcani, A. (2021). Reservoir Scale Porosity-Permeability Evolution in Sandstone due to CO2 Geological Storage. *15th International Conference on Greenhouse Gas Control Technologies, GHGT-15.* Abu Dhabi, UAE.

Anthonsen, K., & Christensen, N. (2021). *EU Geological $CO_2$ storage summary.* Geological Survey of Denmark and Greenland for Clean Air Task Force. doi:10.22008/gpub/34594

Arnorsson, S., & Stefansson, A. (1999). Assessment of feldspar solubility constants in water in the range of 0 degrees to 350 degrees C at vapor saturation pressures. *American Journal of Science, 299*, 173-209.

Arnorsson, S., Gunnlaugsson, E., & Svavarsson, H. (1983). The chemistry of geothermal waters in Iceland-II. Mineral equilibria and independent variables controlling water compositions. *Geochimica et Cosmochimica Acta, 47*, 547-566.

Assayag, N., Matter, J., Ader, M., Goldberg, D., & Agrinier, P. (2009). Water–rock interactions during a CO2 injection field-test: Implications on host rock dissolution and alteration effects. *Chemical Geology, 265*, 227–235. doi:10.1016/j.chemgeo.2009.02.007

Avanthi Isaka, B., Ranjith, P., & Rathnaweera, T. (2019). The use of super-critical carbon dioxide as the working fluid in enhanced geothermal systems (EGSs): A review study. *Sustainable Energy Technologies and Assessments, 36*. doi:10.1016/j.seta.2019.100547

Avşar, Ö. (2011). Geochemical evaluation and conceptual modeling of Edremit geothermal field. *thesis*. Ankara: Middle East Technical University.

Avşar, Ö., Güleç, N., & Parlaktuna, M. (2013). Hydrogeochemical characterization and conceptual modeling of the Edremit geothermal field (NW Turkey). *Journal of Volcanology and Geothermal Research, 262*, 68-79.

Avşar, Ö., Güleç, N., & Parlaktuna, M. (2015). Geothermal Potential Assessment of Edremit Geothermal Field (NW Turkey). *Proceedings World Geothermal Congress 2015.* Melbourne, Australia.

Baba, A., & Sözbilir, H. (2012). Source of arsenic based on geological and hydrogeochemical properties of geothermal systems in Western Turkey. *Chemical Geology, 334*, 364-377. doi:https://doi.org/10.1016/j.chemgeo.2012.06.006

Bachu, S. (2015). Review of CO2 storage efficiency in deep saline aquifers. *International Journal of Greenhouse Gas Control, 40*, 188-202. doi:10.1016/j.ijggc.2015.01.007

Balashov, V., Guthrie, G., Hakala, J., Lopano, C., Rimstidt, J., & Brantley, S. (2013). Predictive modeling of CO2 sequestration in deep saline sandstone reservoirs: Impacts of geochemical kinetics. *Applied Geochemistry, 30*, 41-56. doi:10.1016/j.apgeochem.2012.08.016

Bensinger, J., & Beckingham, L. E. (2020). CO2 storage in the Paluxy formation at the Kemper County CO2 storage complex: Pore network properties and simulated reactive permeability evolution. *International Journal of Greenhouse Gas Control, 93*. doi:10.1016/j.ijggc.2019.102887

Bingöl, E. (1969). Geology of the central and southeastern sections of the Kazdag Massif. *Mineral Exploration Institute of Turkey Bulletin, 72*, 102-123.

Bingöl, E., Akyürek, B., & Korkmazer, B. (1973). Biga yarımadası'nın jeolojisi ve karakaya formasyonunun bazı özellikleri. *MTA, cumhuriyetin 50.yılı yer bilimleri kongresi, tebliğler*, (s. 70-76). Ankara.

Bozkurt, E., & Mittwede, S. (2001). Introduction to the geology of Turkey – a synthesis. *International Geology Review*, 578-594.

Bozkurt, E., & Rojay, B. (2005). Episodic, two-stage Neogene extension and short-term intervening compression in Western Turkey: field evidence from the Kiraz Basin and Bozdağ Horst. *Geodinamica Acta, 18,* 299-316.

Brantley, S. (2008). Kinetics of mineral dissolution. In S. Brantley, J. Kubicki, & A. White (Eds.), *Kinetics of Water–Rock Interaction* (pp. 151–210). Springer.

Brantley, S., & Mellott, N. (2000). Surface area and porosity of primary silicate minerals. *American Mineralogist, 85,* 1767–1783.

Brogi, A., Alçiçek, M. C., Liotta, D., Capezzuoli, E., Zucchi, M., & Matera, P. F. (2021). Step-over fault zones controlling geothermal fluid-flow and travertine formation (Denizli Basin, Turkey). *Geothermics, 89,* 1-17. doi:https://doi.org/10.1016/j.geothermics.2020.101941

Busch, A., Kampman, N., Hangx, S., Snippe, J., Bickle, M., Bertier, P., . . . Schaller, M. (2014). The Green River natural analogue as a field laboratory to study the long-term fate of CO2 in the subsurface. *Energy Procedia, 63,* 2821 – 2830.

Chouikhi, N., Cecilia, J., Vilarrasa-Garcia, E., Besghaier, S., Chlendi, M., Duro, F., . . . Bagane, M. (2019). CO2 Adsorption of Materials Synthesized from Clay Minerals: A Review. *Minerals, 9*. doi:10.3390/min9090514

Clark, D., Oelkers, E., Gunnarsson, I., Sigfusson, B., Snæbjörnsdottir, S., Aradottir, E., & Gislason, S. (2020). CarbFix2: CO2 and H2S mineralization during 3.5 years of continuous injection into basaltic rocks at more than 250 C. *Geochimica et Cosmochimica Acta, 279,* 45-66. doi:10.1016/j.gca.2020.03.039

CO2 Storage Research Group. (2024). *Research on CCS Safety Assessment*. Retrieved from The Research Institute of Innovative Technology for the Earth (RITE): https://www.rite.or.jp/co2storage/en/safety/

CO2GeoNet. (2024). *What does CO2 geological storage really mean?* Retrieved from The European Network of Excellence on the Geological Storage of CO2: https://co2geonet.com/resources/#1392

Craig, H. (1961). Isotopic variations in meteoric waters. *Science, 133,* 1833-1834.

de Leeuw, G., Hilton, D., Güleç, N., & Mutlu, H. (2010). Regional and temporal variations in CO2/3He, 3He/4He and d13C along the North Anatolian Fault Zone, Turkey. *Applied Geochemistry, 25,* 524–539.

de Woolf, P., & Visser, J. (1988). Absolute Intensities - Outline of a Recommended Practice *Reprinted from TPD Technical Report 641-109 (May 29, 1964. *Powder Diffraction, 3*(4), 202 - 204. doi:https://doi.org/10.1017/S0885715600013488

Deer, W., Howie, A., & Zussman, J. (1992). *An Introduction to rock-forming minerals.* Longman Ltd.

Delerce, S., Marieni, C., & Oelkers, E. (2021). *Carbonate geochemistry and its role in geologic carbon storage.* Retrieved from https://hal.science/hal-03433164/document

Diedrich, T., Schott, J., & Oelkers, E. (2014). An experimental study of tremolite dissolution rates as a function of pH and temperature: Implications for tremolite toxicity and its use in carbon storage. *Mineralogical Magazine, 78,* 1449–1464. doi:10.1180/minmag.2014.078.6.12

Dürr, S. (1975). *Über Alter und geotektonische Stellung des Menderes-Kristallins/SW-Anatolien und seine Äequivalente in der mittleren Ägäis.* Habilitation Thesis, University of Marburg/Lahn.

Edremit Geothermal Inc. (2018). *Edremit Geothermal Project Document.* Retrieved October 12, 2021, from http://edremitjeotermal.com.tr/gold_1.pdf

Elidemir, S., & Güleç, N. (2018). Geochemical characterization of geothermal systems in western Anatolia (Turkey): implications for CO2 trapping mechanisms in prospective CO2-EGS sites. *Greenhouse Gases: Science and Technology, 8,* 63-76. doi:10.1002/ghg.1747

Elidemir, S., Güleç, N., Deniz, K., & Kadıoğlu, Y. (2022). Reservoir rock characterization in Edremit geothermal field: Geochemical implications for possible fault zones. *Applied Geochemistry, 143.* doi:10.1016/j.apgeochem.2022.105388

Esteves, A., Santos, F., & Pires, J. (2019). Carbon dioxide as geothermal working fluid: An overview. *Renewable and Sustainable Energy Reviews, 114*. doi:10.1016/j.rser.2019.109331

Fatah, A., Mahmud, H., Bennour, Z., Gholami, R., & Hossain, M. (2022). Geochemical modelling of CO2 interactions with shale: Kinetics of mineral dissolution and precipitation on geological time scales. *Chemical Geology, 592*. doi:10.1016/j.chemgeo.2022.120742

Fong, M., & Nicol, M. (1971). Raman Spectrum of Calcium Carbonate at High Pressures. *The Journal of Chemical Physics, 54*(2), 579-585.

Forray, V., Király, C., Demény, A., Cseresznyés, D., Szabó, C., & Falus, G. (2021). Mineralogical and geochemical changes in conglomerate reservoir rocks induced by CO2 influx at Mihályi-Répcelak natural analogue, NW-Hungary. *Environmental Earth Sciences, 80*. doi:10.1007/s12665-021-10050-9

Foster, M. (1960). Interpretation of composition of trioctaheral micas. *U. S. Geol. Surv. Prof. Pap., 354B,* 1–49.

Fournier, R. (1977). Chemical geothermometers and mixing models for geothermal systems. *Geothermics, 5,* 41-50.

Fournier, R. (1979). A revised equation for the Na-K geothermometer. *Geothermal Resource Council Transections, 3*, 221-224.

Fournier, R., & Truesdell, A. (1973). An Emprical Na-K-Ca Geothermometer for Natural Waters. *Geochimica et Cosmochimica Acta, 37*, 1255-1275.

Fowler, A., & Zierenberg, R. (2016). Geochemical bias in drill cutting samples versus drill core samples returned from the Reykjanes Geothermal System, Iceland. *Geothermics, 62,* 48-60. doi:10.1016/j.geothermics.2016.02.007

Franzson, H., Zierenberg, R., & Schiffman, P. (2008). Chemical transport in geothermal systems in Iceland: Evidence from hydrothermal alteration. *Journal of Volcanology and Geothermal Research, 173*(3-4), 217-229. doi:https://doi.org/10.1016/j.jvolgeores.2008.01.027

Freeman, J., Wang, A., Kuebler, K., Jolliff, B., & Haskin, L. (2008). Characterization of natural feldspars by Raman spectroscopy for future planetary exploration. *The Canadian Mineralogist, 46*, 1477-1500. doi:https://doi.org/10.3749/canmin.46.6.1477

Galeczka, I., Stefansson, A., Kleine, B., Gunnarsson-Robin, J., Snæbjörnsdottir, S., Sigfusson, B., . . . Oelkers, E. (2022). A pre-injection assessment of CO2 and

H2S mineralization reactions at the Nesjavellir (Iceland) geothermal storage site. *International Journal of Greenhouse Gas Control, 115*. doi:10.1016/j.ijggc.2022.103610

Gao, B., Li, Y., Pang, Z., Huang, T., Kong, Y., Li, B., & Zhang, F. (2024). Geochemical mechanisms of water/CO2-rock interactions in EGS and its impacts on reservoir properties: A review. *Geothermics, 118*. doi:10.1016/j.geothermics.2024.102923

Gaus, I. (2010). Role and impact of CO2–rock interactions during CO2 storage in sedimentary rocks. *International Journal of Greenhouse Gas Control, 4*, 73-89. doi:10.1016/j.ijggc.2009.09.015

Gaus, I., Audigane, P., Andre, L., Lions, J., Jacquemet, N., Durst, P., . . . Azaroual, M. (2008). Geochemical and solute transport modelling for CO2 storage, what to expect from it? *International Journal of Greenhouse Gas Control, 2*, 605-625. doi:10.1016/j.ijggc.2008.02.011

Gaus, I., Azaroual, M., & Czernichowski-Lauriol, I. (2002). *Preliminary modelling of the geochemical impact of CO2-injection on the cap rock at Sleipner.* BRGM Report BRGM/RP-52081-FR.

Gaus, I., Azaroual, M., & Czernichowski-Lauriol, I. (2005). Reactive transport modelling of the impact of CO2 injection on the clayey cap rock at Sleipner (North Sea). *Chemical Geology, 217*, 319 – 337. doi:10.1016/j.chemgeo.2004.12.016

Gifkins, C., Herrmann, W., & Large, R. (2005). *Altered Volcanic Rocks: A Guide to Description and Interpretation.* Centre for Ore Deposit Research: University of Tasmania, Australia.

Giggenbach, W. F. (1988). Geothermal solute equilibria. Derivation of Na-K-Mg-Ca geoindicators. *Geochimica et Cosmochimica Acta, 52*, 2749-2765. doi:https://doi.org/10.1016/0016-7037(88)90143-3

Global CCS Institute. (2016). *The Global Status of CCS: 2016.* Summary Report, Australia.

Global CCS Institute. (2023). *CCS in Europe - Regional Overview.* Retrieved March 2024, from https://www.globalccsinstitute.com/resources/publications-reports-research/ccs-in-europe-regional-overview/

Golubev, S., Benezeth, P., Schott, J., Dandurand, J., & Castillo, A. (2009). Siderite dissolution kinetics in acidic aqueous solutions from 25 to 100 °C and 0 to

50 atm pCO2. *Chemical Geology, 265,* 13-19. doi:10.1016/j.chemgeo.2008.12.031

Gong, Q., Deng, J., Jia, Y., Tong, Y., & Liu, N. (2015). Empirical equations to describe trace element behaviors due to rock weathering in China. *Journal of Geochemical Exploration, 152,* 110-117. doi:https://doi.org/10.1016/j.gexplo.2015.02.004

Gong, Q., Deng, J., Wang, C., Wang, Z., & Zhou, L. (2013). Element behaviors due to rock weathering and its implication to geochemical anomaly recognition: A case study on Linglong biotite granite in Jiaodong peninsula, China. *Journal of Geochemical Exploration, 128,* 14-24. doi:https://doi.org/10.1016/j.gexplo.2013.01.004

Gong, Q., Yan, T., Li, J., Zhang, M., & Liu, N. (2016). Experimental simulation of element mass transfer and primary halo zone on water-rock interaction. *Applied Geochemistry, 69,* 1-11. doi:https://doi.org/10.1016/j.apgeochem.2016.04.001

Goodman, R. (1989). *Introduction to rock mechanics.* New York: John Wiley and Sons.

Grove, B. (2021). *Geologic storage of carbon dioxide in Europe: FAQ*. Retrieved from Clean Air Task Force: https://www.catf.us/2021/12/carbon-dioxide-storage-europe/

Gueu, S., Finqueneisel, G., Zimny, T., Bartier, D., & Yao, B. (2019). Physicochemical characterization of three natural clays used as adsorbent for the humic acid removal from aqueous solution. *Adsorption Science and Technology, 37,* 77-94. doi:10.1177/0263617418811469

Gunnarsson, I., Aradottir, E., Oelkers, E., Clark, D., Arnarson, M., Sigfusson, B., . . . Gislason, S. (2018). The rapid and cost-effective capture and subsurface mineral storage of carbon and sulfur at the CarbFix2 site. *International Journal of Greenhouse Gas Control, 79,* 117-126. doi:10.1016/j.ijggc.2018.08.014

Güleç, N., & Hilton, D. R. (2006). Helium and Heat Distribution in Western Anatolia, Turkey: Relationship to Active Extension and Volcanism. In Y. a. Dilek (Ed.), *Post-Collisional Tectonics and Magmatism in the Eastern Mediterranean Region* (Vol. 409, pp. 305-319). Colorado: Geological Society of America. doi:10.1130/2006.2409(16)

Güleç, N., & Hilton, D. R. (2016). Turkish geothermal fields as natural analogues of CO2 storage sites: Gas geochemistry and implications for CO2 trapping mechanisms. *Geothermics, 64*, 96-110. doi:10.1016/j.geothermics.2016.04.008

Gündoğan, Ö. (2011). Geochemical Modelling of CO2 Storage. Heriot-Watt University.

Haase, C., Dahmke, A., Ebert, M., Schafer, D., & Dethlefsen, F. (2014). Suitability of Existing Numerical Model Codes and Thermodynamic Databases for the Prognosis of Calcite Dissolution Processes in Near-Surface Sediments Due to a CO2 Leakage Investigated by Column Experiments. *Aquatic Geochemistry, 20*, 639–661. doi:10.1007/s10498-014-9240-0

Hebert, R., Ledesert, B., Genter, A., Bartier, D., & Dezayes, C. (2011). Mineral precipitation in geothermal reservoir: the study case of calcite in the Soultz-sous-Forêts enhanced geothermal system. *36rd Workshop on Geothermal Reservoir Engineering.* Stanford, California, United States.

Hellevang, H., Declercq, J., Kvamme, B., & Aagaard, P. (2010). The dissolution rates of dawsonite at pH 0.9 to 5 and temperatures of 22, 60 and 77 C. *Applied Geochemistry, 25*, 1575–1586. doi:10.1016/j.apgeochem.2010.08.007

Hellevang, H., Pham, V., & Aagaard, P. (2013). Kinetic modelling of CO2–water–rock interactions. *International Journal of Greenhouse Gas Control, 15*, 3-15. doi:10.1016/j.ijggc.2013.01.027

Hemme, C., & van Berk, W. (2017). Change in cap rock porosity triggered by pressure and temperature dependent CO2-water-rock interactions in CO2 storage systems. *Petroleum, 3*, 96-108. doi:10.1016/j.petlm.2016.11.010

Herece, E. (1990). The fault trace of 1953 Yenice-Gonen earthquake and the westernmost known extension of the NAF system in the Biga Peninsula. *Mineral Research and Exploration Bulletin, 111*, 31-42.

Higgs, K., Haese, R., Golding, S., Schacht, U., & Watson, M. (2015). The Pretty Hill Formation as a natural analogue for CO2 storage: An investigation of mineralogical and isotopic changes associated with sandstones exposed to low, intermediate and high CO2 concentrations over geological time. *Chemical Geology, 399*, 36-64. doi:10.1016/j.chemgeo.2014.10.019

IAEA. (1981). *Stable isotope hydrology. Deuterium and oxygen-18 in water cycle. Gat, J.R.; Gonfiantini, R. (eds.).* Vienna: International Atomic Energy Agency Technical Report No.210. Retrieved November 2023, from https://inis.iaea.org/collection/NCLCollectionStore/_Public/13/677/13677657.pdf

IEAGHG. (2008). Geologic Storage of Carbon Dioxide – Staying Safely Underground. Retrieved March 2024, from https://www.ieaghg.org/docs/general_publications/geostoragesafe-web.pdf

IPCC. (2005). *Carbon Dioxide Capture and Storage: Special Report of the Intergovernmental Panel on Climate Change.* New York: Cambridge University Press.

IPCC. (2018). *Global warming of 1.5°C.* Cambridge University Press, Cambridge, UK and New York, NY, USA: [V. Masson-Delmotte, P. Zhai, H. O. Pörtner, D. Roberts, J. Skea, P.R. Shukla, A. Pirani, W. Moufouma-Okia, C. Péan, R. Pidcock, S. Connors, J. B. R. Matthews, Y. Chen, X. Zhou, M. I. Gomis, E. Lonnoy, T. Maycock, M. Tignor, T. Waterfield (eds.)] . doi: 10.1017/9781009157940

Janssen, M., Draganov, D., Barnhoorn, A., & Wolf, K. (2023). Storing CO2 in geothermal reservoir rocks from the Kizildere field, Turkey: Combined stress, temperature, and pore fluid dependence of seismic properties. *Geothermics, 108*. doi:10.1016/j.geothermics.2022.102615

Jayasekara, D., Ranjith, P., Wanniarachchi, W., Rathnaweera, T., & Van Gent, D. (2020). CO2-brine-caprock interaction: Reactivity experiments on mudstone caprock of South-west Hub geo-sequestration project. *Journal of Petroleum Science and Engineering, 189*. doi:10.1016/j.petrol.2020.107011

Kalam, S., Olayiwola, T., Al-Rubaii, M., Amaechi, B., Jamal, M., & Awotunde, A. (2021). Carbon dioxide sequestration in underground formations: review of experimental, modeling, and feld studies. *Journal of Petroleum Exploration and Production Technology, 11*, 303–325. doi:10.1007/s13202-020-01028-7

Kampman, N., Bertier, P., Busch, A., Snippe, J., Harrington, J., Pipich, V., . . . Bickle, M. (2017). Validating reactive transport models of CO2-brine-rock reactions in caprocks using observations from a natural CO2 reservoir. *Energy Procedia, 114*, 4902 – 4916.

Kampman, N., Bickle, M., Wigley, M., & Dubacq, B. (2014). Fluid flow and CO2–fluid–mineral interactions during CO2-storage in sedimentary basins. *Chemical Geology, 369*, 22-50. doi:10.1016/j.chemgeo.2013.11.012

Karakuş, H., & Şimşek, Ş. (2013). Tracing deep thermal water circulation systems in the E–W trending Büyük Menderes Graben, western Turkey. *Journal of*

*Volcanology and Geothermal Research, 252,* 38-52. doi:10.1016/j.jvolgeores.2012.11.006

Karakuş, H., Ergüler, Z., Özkul, C., Yanık, G., & Kibici, Y. (2019). Geochemical and isotopic characteristics of geothermal discharges in the Emet Basin, Western Anatolia, Turkey. *Applied Geochemistry, 107,* 105-119. doi:https://doi.org/10.1016/j.apgeochem.2019.06.002

Kaszuba, J., Yardley, B., & Andreani, M. (2013). Experimental perspectives of mineral dissolution and precipitation due to carbon dioxide-water-rock interactions. *Reviews in Mineralogy and Geochemistry, 77,* 153-188. doi:10.2138/rmg.2013.77.5

Kelemen, P., Benson, S., Pilorge, H., Psarras, P., & Wilcox, J. (2019). An Overview of the Status and Challenges of CO2 Storage in Minerals and Geological Formations. *Frontiers in Climate, 1*. doi:10.3389/fclim.2019.00009

Kim, K., Kim, D., Na, Y., Song, Y., & Wang, J. (2023). A review of carbon mineralization mechanism during geological CO2 storage. *Heliyon, 9*. doi:10.1016/j.heliyon.2023.e23135

Klajmon, M., Havlova, V., Cervinka, R., Mendoza, A., Francu, J., Berenblyum, R., & Arild, O. (2017). REPP-CO2: Equilibrium Modelling of CO2-Rock-Brine Systems. *Energy Procedia, 114,* 3364 – 3373. doi:10.1016/j.egypro.2017.03.1468

Koenen, M., ter Heege, J., & Peeters, R. (2014). *Transport properties of intact caprocks and effects of CO2-water-rock interaction: CO2-induced mineral reactions in sandstone reservoirs (CATO2-WP3.03-D12).* CATO-2 project public report.

Kölbel, L., Kölbel, T., Sauter, M., Schafer, T., Siefert, D., & Wiegand, B. (2020). Identification of fracture zones in geothermal reservoirs in sedimentary basins: A radionuclide-based approach. *Geothermics, 85*. doi:10.1016/j.geothermics.2019.101764

Kumari, N., & Mohan, C. (2021). Basics of Clay Minerals and Their Characteristic Properties. In G. M. Nascimento (Ed.), *Clay and Clay Minerals.* doi:10.5772/intechopen.97672

Lamy-Chappuis, B., Angus, D., Fisher, Q., Grattoni, C., & Yardley, B. W. (2014). Rapid porosity and permeability changes of calcareous sandstone due to CO2-enriched brine injection. *Geophysical Research Letters, 41,* 399-406. doi:10.1002/2013GL058534

Lasaga, A. (1984). Chemical kinetics of water–rock interactions. *Journal of Geophysical Research Solid Earth, 89*, 4009–4025.

Lasaga, A., & Gibbs, G. (1988). Quantum mechanical potential surfaces and calculations on minerals and molecular clusters. *Phys Chem Minerals, 16*, 29-41. doi:10.1007/BF00201327

Leake, B., Woolley, A., Arps, C., Birch, W., Gilbert, M., Grice, J., & .... Youzhi, G. (1997). Nomenclature of Amphiboles; Report of the Subcommittee on Amphiboles of the International Mineralogical Association Commission on New Minerals and Mineral Names. *Mineralogical Magazine, 61*(405), 295-310. doi:10.1180/minmag.1997.061.405.13

Leal, A., Kulik, D., & Saar, M. (2017). *Ultra-Fast Reactive Transport Simulations When Chemical Reactions Meet Machine Learning: Chemical Equilibrium.* doi:10.48550/arXiv.1708.04825

Lee, H., Seo, J., Lee, Y., Jung, W., & Sung, W. (2016). Regional CO2 solubility trapping potential of a deep saline aquifer in Pohang basin, Korea. *Geosciences Journal, 20*(4), 561-568.

Libbey, R., & Williams-Jones, A. (2016a). Lithogeochemical approaches in geothermal system characterization: An application to the Reykjanes geothermal field, Iceland. *Geothermics, 64*, 61-80. doi:10.1016/j.geothermics.2016.05.001

Libbey, R., & Williams-Jones, A. (2016b). Compositions of hydrothermal silicates and carbonates as indicators of physicochemical conditions in the Reykjanes geothermal system, Iceland. *Geothermics, 64*, 15-27. doi:10.1016/j.geothermics.2016.04.007

Liu, R., Heinemann, N., Liu, J., Zhu, W., Wilkinson, M., Xie, Y., . . . Haszeldine, R. (2019). CO2 sequestration by mineral trapping in natural analogues in the Yinggehai Basin, South China Sea. *Marine and Petroleum Geology, 104*, 190-199. doi:10.1016/j.marpetgeo.2019.03.018

Luhmann, A., Tutolo, B., Tan, C., Moskowitz, B., Saar, M., & Seyfried Jr., W. (2017). Whole rock basalt alteration from CO2-rich brine during flow-through experiments at 150 °C and 150 bar. *Chemical Geology, 453*, 92-110. doi:10.1016/j.chemgeo.2017.02.002

Luo, A., Li, Y., Chen, X., Zhu, Z., & Peng, Y. (2022). Review of CO2 sequestration mechanism in saline aquifers. *Natural Gas Industry B, 9*, 383-393. doi:10.1016/j.ngib.2022.07.002

Ma, B., Cao, Y., Zhang, Y., & Eriksson, K. (2020). Role of CO2-water-rock interactions and implications for CO2 sequestration in Eocene deeply buried sandstones in the Bonan Sag, eastern Bohai Bay Basin, China. *Chemical Geology, 541*. doi:10.1016/j.chemgeo.2020.119585

Maskell, A., Scott, P., Buisman, I., & Bickle, M. (2018). A siltstone reaction front related to CO2- and sulfur-bearing fluids: Integrating quantitative elemental mapping with reactive transport modeling. *American Mineralogist, 103*, 314–323.

Matter, J., & Kelemen, P. (2009). Permanent storage of carbon dioxide in geological reservoirs by mineral carbonation. *Nature Geoscience, 2,* 837-841. doi:10.1038/ngeo683

Mauriohooho, K., Barker, S., & Rae, A. (2016). Mapping lithology and hydrothermal alteration in geothermalsystems using portable X-ray fluorescence (pXRF): A case study fromthe Tauhara geothermal system, Taupo Volcanic Zone. *Geothermics, 64*, 125-134.

McGrail, B., Schaef, H., Spane, F., Cliff, J., Qafoku, O., Horner, J., . . . Sullivan, C. (2017). Field Validation of Supercritical CO2 Reactivity with Basalts. *Environmental Science & Technology Letters, 4,* 6-10. doi:10.1021/acs.estlett.6b00387

Mishra, A., Chaudhuri, A., & Haese, R. R. (2021). Conditions and processes controlling carbon mineral trapping in intraformational baffles. *International Journal of Greenhouse Gas Control, 106*. doi:10.1016/j.ijggc.2021.103264

MIT. (2016). *Cranfield Fact Sheet: Carbon Dioxide Capture and Storage Project*. Retrieved May 2024, from Carbon Capture and Sequestration Technologies: https://sequestration.mit.edu/tools/projects/cranfield.html

Morimoto, N., Fabries, J., Ferguson, A., Ginzburg, I., Ross, M., Seifert, F., . . . Gottardi, G. (1988). Nomenclature of pyroxenes. *American Mineralogist, 73*(9-10), 1123–1133.

Nasution, A., Taniguchi, M., Kikuchi, T., & Muraoka, H. (2003). A lithostatically pressurized clay cap of the vapordominated reservoir deduced from hydrothermal alterations of borehole cuttings in the Mataloko geothermal field, Flores Island, eastern Indonesia. *Journal of the Geothermal Research Society of Japan, 25,* 193-210.

Nesbitt, H., & Young, G. (1982). Early Proterozoic climates and plate motions inferred from major element chemistry of lutites. *Nature, 299*, 715-717. doi:https://doi.org/10.1038/299715a0

Oelkers, E., Schott, J., Gauthier, J., & Herrero-Roncal, T. (2008). An experimental study of the dissolution mechanism and rates of muscovite. *Geochimica et Cosmochimica Acta, 72*, 4948–4961. doi:10.1016/j.gca.2008.01.040

Okay, A. (1989). Geology of the Menderes Massif and the Lycian Nappes South of Denizli, Western Taurides. *Bulletin of The Mineral Research and Exploration, 109*, 37-51.

Özgür, N., & Çalışkan, T. (2014). Reservoirs and Reinjection of the Thermal Waters of Kızıldere, Western Anatolia, Turkey. *Thirty-Ninth Workshop on Geothermal Reservoir Engineering*. Stanford University, Stanford, California.

Palandri, J., & Kharaka, Y. (2004). *A compilation of rate parameters of water-mineral interaction kinetics for application to geochemical modelling.* Menlo Park, California: U.S. Geological Survey. November 2023 tarihinde https://pubs.usgs.gov/of/2004/1068/ adresinden alındı

Parkhurst, D. L., & Appelo, C. (1999). *User's guide to PHREEQC (Version 2): A computer program for speciation, batch-reaction, one-dimensional transport, and inverse geochemical calculations.* U.S. Geological Survey. doi:10.3133/wri994259

Parkhurst, D., & Appelo, C. (2013). Description of input and examples for PHREEQC version 3—A computer program for speciation, batch-reaction, one-dimensional transport, and inverse geochemical calculations. In *U.S. Geological Survey Techniques and Methods book 6, chap. A43* (p. 497). U.S. Geological Survey. Retrieved from http://pubs.usgs.gov/tm/06/a43/

Parlaktuna, M., & Avşar, Ö. (2019). *Edremit Jeotermal A.Ş. Edremit Jeotermal Sahası Değerlendirme Raporu*. unpublished.

Pearce, J. (1982). Trace element characteristics of lavas from destructive plate boundaries. R. Thorpe (Dü.) içinde, *Andesites: Orogenic Andesites and Related Rocks* (s. 525-548). Chichester: Wiley.

Peng, D., & Robinson, D. (1976). A new two-constant equation of state. *Ind. Eng. Chem. Fundam., 15*, 59-64.

Pham, T., Aagaard, P., & Hellevang, H. (2012). On the potential for CO2 mineral storage in continental flood basalts – PHREEQC batch- and 1D diffusion–reaction simulations. *Geochemical Transactions, 13*. doi:10.1186/1467-4866-13-5

Pham, V., Lu, P., Aagaard, P., Zhu, C., & Hellevang, H. (2011). On the potential of CO2–water–rock interactions for CO2 storage using a modified kinetic model. *International Journal of Greenhouse Gas Control, 5*, 1002-1015. doi:10.1016/j.ijggc.2010.12.002

Pogge von Strandmann, P., Burton, K., Snæbjörnsdóttir, S., Sigfusson, B., Aradottir, E., Gunnarsson, I., . . . Gislason, S. (2019). Rapid CO2 mineralisation into calcite at the CarbFix storage site quantified using calcium isotopes. *Nature Communications, 10*. doi:10.1038/s41467-019-10003-8

Pokrovsky, O., Golubev, S., Schott, J., & Castillo, A. (2009). Calcite, dolomite and magnesite dissolution kinetics in aqueous solutions at acid to circumneutral pH, 25 to 150 °C and 1 to 55 atm pCO2: New constraints on CO2 sequestration in sedimentary basins. *Chemical Geology, 265*, 20-32. doi:10.1016/j.chemgeo.2009.01.013

Qu, X., Zhang, Y., Li, Q., Du, T., & Li, Y. (2022). Geological features and occurrence conditions of dawsonite as a main Carbon-Fixing mineral. *Alexandria Engineering Journal, 61*, 2997–3011. doi:10.1016/j.aej.2021.08.022

Rackley, S. A. (2010). *Carbon Capture and Storage*. Oxford, UK: Elsevier. doi:10.1016/C2009-0-19306-6

Randolph, J., & Saar, M. (2011). Combining geothermal energy capture with geologic carbon dioxide sequestration. *Geophysical Research Letters, 38*. doi:10.1029/2011GL047265

Rankin, P. (1982). Mylonitic fabric development through the east flank of the Bitterroot dome Montana. *thesis*. The University of Montana.

Rathnaweera, T., Ranjith, P., & Perera, M. (2016). Experimental investigation of geochemical and mineralogical effects of CO2 sequestration on flow characteristics of reservoir rock in deep saline aquifers. *Scientific Reports, 6*. doi:10.1038/srep19362

Ratouis, T. (2022). *Permanent and Secure Geological Storage of CO2 by In-Situ Carbon Mineralization*. Iceland: Carbfix.

Raza, A., Glatz, G., Gholami, R., Mahmoud, M., & Alafnan, S. (2022). Carbon mineralization and geological storage of CO2 in basalt: Mechanisms and technical challenges. *Earth-Science Reviews, 229*. doi:10.1016/j.earscirev.2022.104036

Romanov, V., Soong, Y., Carney, C., Rush, G., Nielsen, B., & O'Connor, W. (2015). Mineralization of Carbon Dioxide: A Literature Review. *ChemBioEng Reviews, 2*, 231-256. doi:10.1002/cben.201500002

Rutt, H., & Nicola, J. (1974). Raman spectra of carbonates of calcite structure. *J. Phys. C: Solid State Phys., 7*, 4522-4528.

Rütters, H., Möller, I., May, F., Flornes, K., Hladik, V., Arvanitis, A., . . . Georgiev, G. (2013). *State-of-the-art of monitoring methods to evaluate CO2 storage site performance.* CGS Europe report No. D3.3.

Saar, M., Buscheck, T., Jenny, P., Garapati, N., Randolph, J., Karvounis, D., . . . Bielicki, J. (2015). Numerical Study of Multi-Fluid and Multi-Level Geothermal System Performance. *Proceedings World Geothermal Congress 2015* . Melbourne, Australia.

Sanei, H., Ardakani, O., Akai, T., Akihisa, K., Jiang, C., & Wood, J. (2020). Core versus cuttings samples for geochemical and petrophysical analysis of unconventional reservoir rocks. *Scientific Reports, 10*. doi:10.1038/s41598-020-64936-y

Sano, Y., & Marty, B. (1995). Origin of carbon in fumarolic gas from island arcs. *Chemical Geology, 119,* 264-274. doi:https://doi.org/10.1016/0009-2541(94)00097-R

Scripps Institution of Oceanography. (2024, March). *The Keeling Curve.* Retrieved from Scripps CO2 Program - Mauna Loa Record: https://scrippsco2.ucsd.edu/graphics_gallery/mauna_loa_record/mauna_loa_record.html

Shukla, R., Ranjith, P., Haque, A., & Choi, X. (2010). A review of studies on CO2 sequestration and caprock integrity. *Fuel, 89*, 2651–2664.

Siegenthaler, U. (1984). 19th Century Measurements of Atmospheric CO2 - A Comment. *Climatic Change, 6*, 409-411.

Snaebjörnsdóttir, S., Sigfússon, B., Marieni, C., Goldberg, D., Gíslason, S., & Oelkers, E. (2020). Carbon dioxide storage through mineral carbonation.

*Nature Reviews Earth & Environment, 1,* 90-102. doi:10.1038/s43017-019-0011-8

Sun, J., Wu, Z., Cheng, H., Zhang, Z., & Frost, R. (2014). A Raman spectroscopic comparison of calcite and dolomite. *Spectrochimica Acta Part A: Molecular and Biomolecular Spectroscopy, 117,* 158–162.

Şengör, A. (1984). Structural classification of the tectonic history of Turkey. *Proceedings of Ketin Symposium,* (s. 37-61). Ankara.

Şengör, A., & Yılmaz, Y. (1981). Tethyan evolution of Turkey: A plate tectonic approach. *Tectonophysics, 75,* 181-241.

Şengör, A., Görür, N., & Şaroğlu, F. (1985). Strike-slip faulting and related basin formation in zones of tectonic escape: Turkey as a case study. In K. Biddle, & N. Christie-Blick, *Strike-Slip Deformation, Basin Formation, and Sedimentation* (Vol. 37, pp. 227-264). Society of Economic Paleontologists and Mineralogists.

Şengör, A., Satır, M., & Akkök, R. (1984). Timing of the tectonic events in the Menderes Massif, western Turkey: implications for tectonic evolution and evidence for Pan-African basement in Turkey. *Tectonics, 3,* 693-707.

Şimşek, Ş. (1984). *Denizli-Kızıldere-Tekkehamam-Tosunlar-Buldan-Yenice alanının jeolojisi ve jeotermal enerji olanakları.* Mineral Res. Expl. Direct. Turkey (MTA), Scientific Report, 7846, 85.

Şimşek, Ş. (1985). Geothermal model of Denizli, Sarayköy-Buldan area. *Geothermics, 14,* 393-417. doi:10.1016/0375-6505(85)90078-1

Şimşek, Ş. (2003). Hydrogeological and isotopic survey of geothermal fields in the Buyuk Menderes graben, Turkey. *Geothermics, 32,* 669-678. doi:10.1016/S0375-6505(03)00072-5

Şimşek, Ş., Yıldırım, N., & Gülgör, A. (2005). Developmental and environmental effects of the Kızıldere geothermal power project, Turkey. *Geothermics, 34,* 239–256.

Tarcan, G. (2005). Mineral saturation and scaling tendencies of waters discharged from wells (>150 C) in geothermal areas of Turkey. *Journal of Volcanology and Geothermal Research, 142,* 263-283.

Tarcan, G., Özen, T., Gemici, Ü., Çolak, M., & Karamanderesi, İ. H. (2016). Geochemical assessment of mineral scaling in Kızıldere geothermal field, Turkey. *Environmental Earth Sciences, 75*. doi:https://doi.org/10.1007/s12665-016-6112-5

Taylor, A., Blum, J., Lasaga, A., & MacInnis, I. (2000). Kinetics of dissolution and Sr release during biotite and phlogopite weathering. *Geochimica et Cosmochimica Acta, 64*, 1191–1208.

Taymaz, T., Tan, O., & Yolsal Çevikbilen, S. (2004). Active Tectonics of Turkey and Surroundings Seismic Risk in the Marmara Sea Region. *The Proceedings of 1st International Workshop on Active Monitoring in the Solid Earth Geophysics*, (pp. 110-115). Gifu, Japan.

Tonani, F. (1980). Some Remarks on the Application of Geochemical Techniques in Geothermal Exploration. *Proceedings, Adv. Eur. Geoth. Res. Second Symp.*, (s. 428-443). Strasbourg.

Truesdell, A. (1976). Summary of Section III - Geochemical Techniques in Exploration. *Proceedings, Second United Nations Symposium on the Development and Use of Geothermal Resources, 1*, s. 1iii-1xiii. San Francisco,CA.

Tutolo, B., Kong, X., Seyfried Jr., W., & Saar, M. (2015). High performance reactive transport simulations examining the effects of thermal, hydraulic, and chemical (THC) gradients on fluid injectivity at carbonate CCUS reservoir scales. *International Journal of Greenhouse Gas Control, 39*, 285-301. doi:10.1016/j.ijggc.2015.05.026

Vengosh, A., Helvacı, C., & Karamanderesi, İ. (2002). Geochemical constraints for the origin of thermal waters from western Turkey. *Applied Geochemistry, 17*, 163-183. doi:https://doi.org/10.1016/S0883-2927(01)00062-2

Voigt, M., Marieni, C., Baldermann, A., Galeczka, I., Wolff-Boenisch, D., Oelkers, E., & Gislason, S. (2021). An experimental study of basalt–seawater–CO2 interaction at 130 C. *Geochimica et Cosmochimica Acta, 308*, 21-41. doi:10.1016/j.gca.2021.05.056

Wagner, T., & Jochum, J. (2002). Fluid–rock interaction processes related to hydrothermal vein-type mineralization in the Siegerland district, Germany: implications from inorganic and organic alteration patterns. *Applied Geochemistry, 17*(3), 225-243. doi:https://doi.org/10.1016/S0883-2927(01)00067-1

Wang, H., Alvarado, V., Bagdonas, D. A., McLaughlin, J., Kaszuba, J. P., Grana, D., . . . Ng, K. (2021). Effect of CO2-brine-rock reactions on pore architecture and permeability in dolostone: Implications for CO2 storage and EOR. *International Journal of Greenhouse Gas Control, 107*. doi:10.1016/j.ijggc.2021.103283

Warren, I., Simmons, S., & Mauk, J. (2007). Whole-Rock Geochemical Techniques for Evaluating Hydrothermal Alteration, Mass Changes, and Compositional Gradients Associated with Epithermal Au-Ag Mineralization. *Economic Geology, 102*, 923-948.

White, S., Spane, F., Schaef, H., Miller, Q., White, M., Horner, J., & McGrail, B. (2020). Quantification of CO2 Mineralization at the Wallula Basalt Pilot Project. *Environmental Science & Technology, 54*. doi:10.1021/acs.est.0c05142

Wright, C. (2022, June). *What Happens to Carbon Stored Underground?* Retrieved November 2023, from AZoCleantech: https://www.azocleantech.com/article.aspx?ArticleID=1582

Wu, Y., Li, X., Gong, Q., Wu, X., Yao, N., Peng, C., . . . Pu, X. (2021). Test and application of the geochemical lithogene on weathering profiles developed over granitic and basaltic rocks in China. *Applied Geochemistry, 128*, 1-8. doi:https://doi.org/10.1016/j.apgeochem.2021.104958

Yang, L., & Steefel, C. (2008). Kaolinite dissolution and precipitation kinetics at 22 °C and pH 4. *Geochimica et Cosmochimica Acta, 72*, 99-116. doi:10.1016/j.gca.2007.10.011

Yapparova, A., Gabellone, T., Whitaker, F., Kulik, D., & Matthai, S. (2017). Reactive transport modelling of hydrothermal dolomitisation using the CSMP++GEM coupled code: Effects of temperature and geological heterogeneity. *Chemical Geology, 466*, 562-574. doi:10.1016/j.chemgeo.2017.07.005

Yıldırım, N., & Güner, İ. N. (2002). Büyük Menderes Grabeninin Doğusunda Yeralan Jeotermal Sahalarda Bulunan Suların İzotopik ve Hidrojeokimyasal Özellikleri. *Hidrojeolojide İzotop Tekniklerinin Kullanılması Sempozyumu*, (s. 79-97). Adana, Turkiye (in Turkish).

Zhang, L., Luo, L., & Zhang, S. (2012). Integrated investigations on the adsorption mechanisms of fulvic and humic acids on three clay minerals. *Colloids and Surfaces A: Physicochemical and Engineering Aspects, 406*, 84-90. doi:10.1016/j.colsurfa.2012.05.003

Zhang, S., & DePaolo, D. (2017). Rates of CO2 Mineralization in Geological Carbon Storage. *Accounts of Chemical Research*, *50*, 2075−2084. doi:10.1021/acs.accounts.7b00334

Zhang, Y., Hu, B., Teng, Y., Tu, K., & Zhu, C. (2019). A library of BASIC scripts of reaction rates for geochemical modeling using PHREEQC. *Computers and Geosciences*, *133*. doi:10.1016/j.cageo.2019.104316

Zhang, Y., Jackson, C., & Krevor, S. (2022). An Estimate of the Amount of Geological CO2 Storage over the Period of 1996–2020. *Environmental Science & Technology Letters, 9*, 693-698. doi:10.1021/acs.estlett.2c00296

Zhang, Z., & Huisingh, D. (2017). Carbon dioxide storage schemes: Technology, assessment and deployment. *Journal of Cleaner Production, 142*, 1055-1064. doi:10.1016/j.jclepro.2016.06.199

# APPENDICES

## A. Views from Microscopic Examinations of Samples from Akköy and Edremit Fields

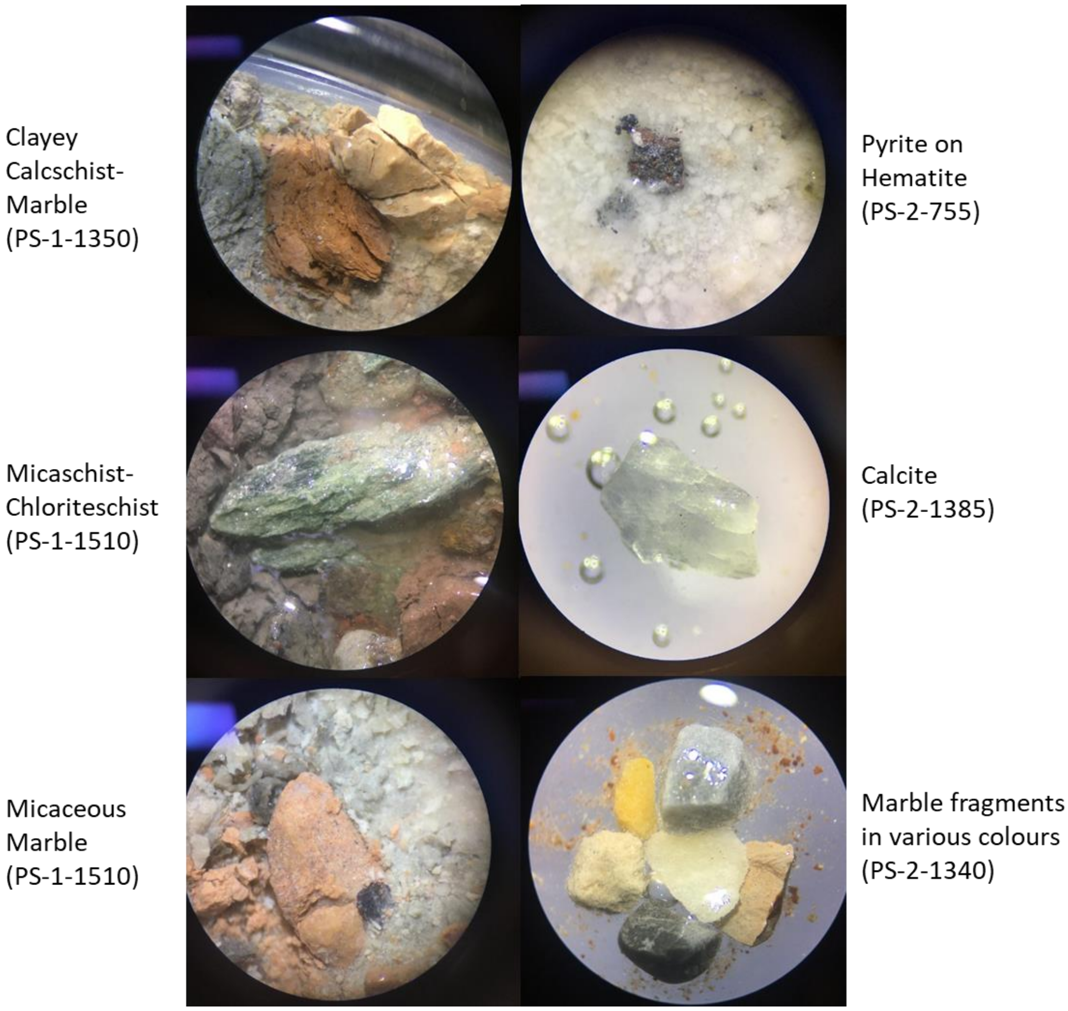

Figure A.1. Macroscopic views of Akköy samples

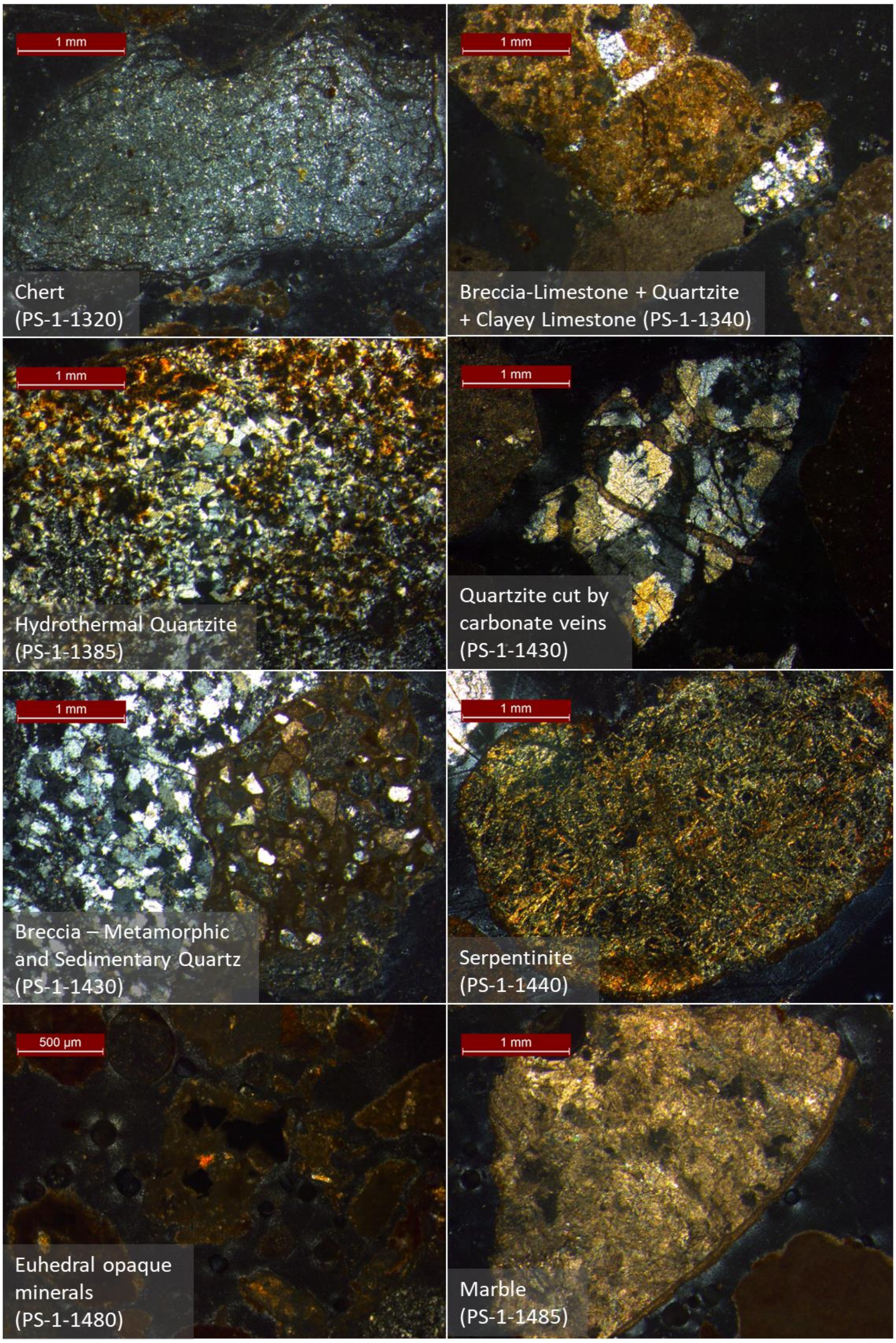

Figure A.2. Microscopic views of Akköy samples

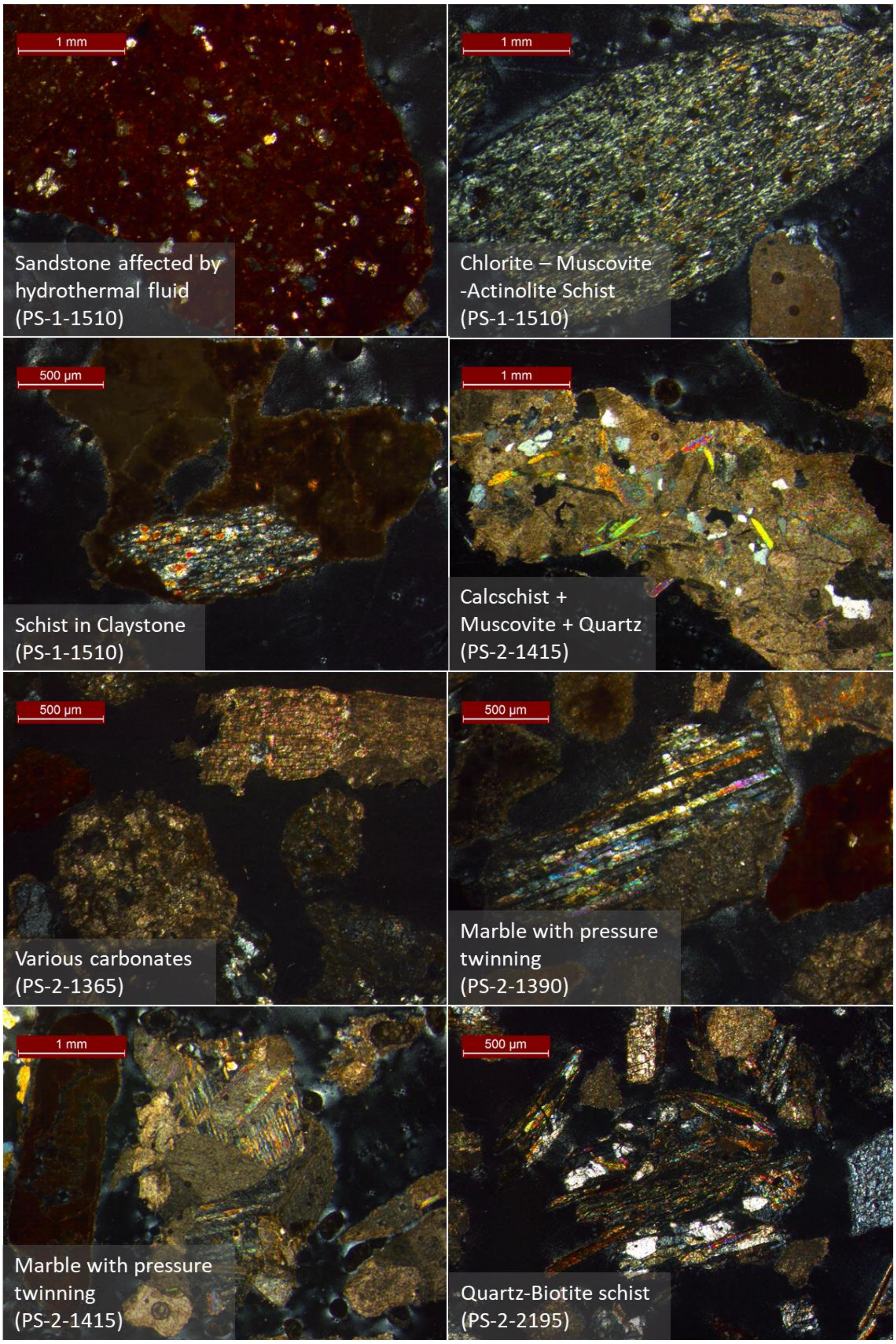

Figure A.3. Microscopic views of Akköy samples

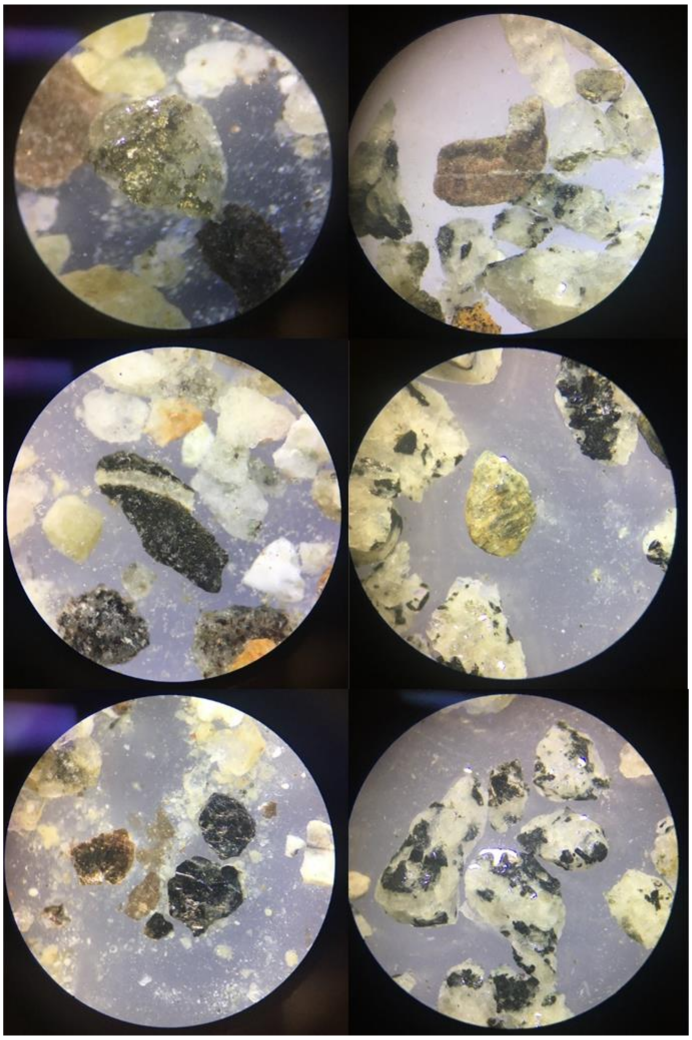

Quartz grain with pyrite and biotite (EDR-900)

Pyrite + granite fragment cut by quartz vein (EDR-1010)

Gabbroic fragment cut by quartz vein (EDR-924)

Schist + quartz with biotite (EDR-1024)

Muscovite + biotite (EDR-932)

Quartz with biotite (EDR-1024)

Figure A.4. Macroscopic views of Edremit samples

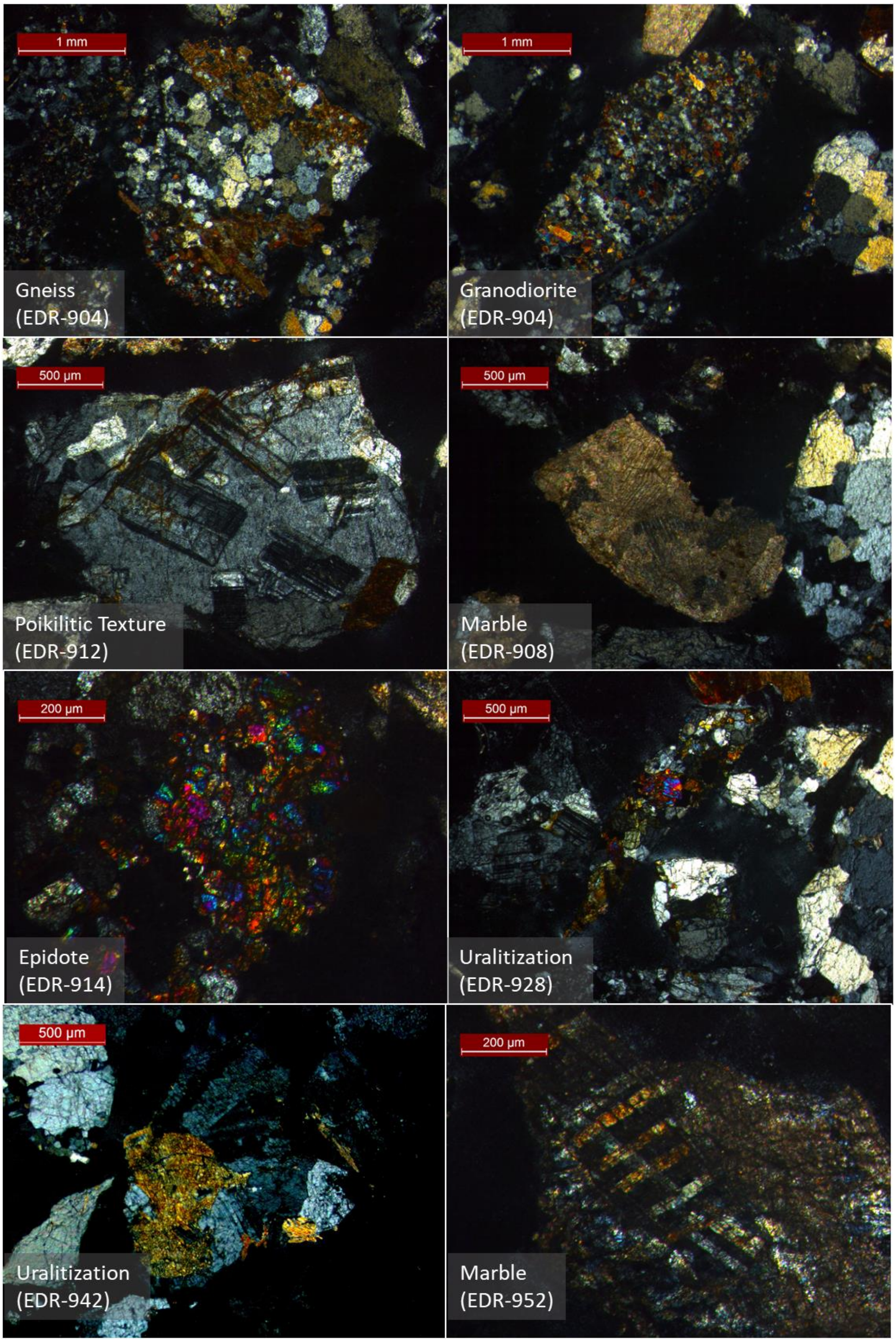

Figure A.5. Microscopic views of Edremit samples

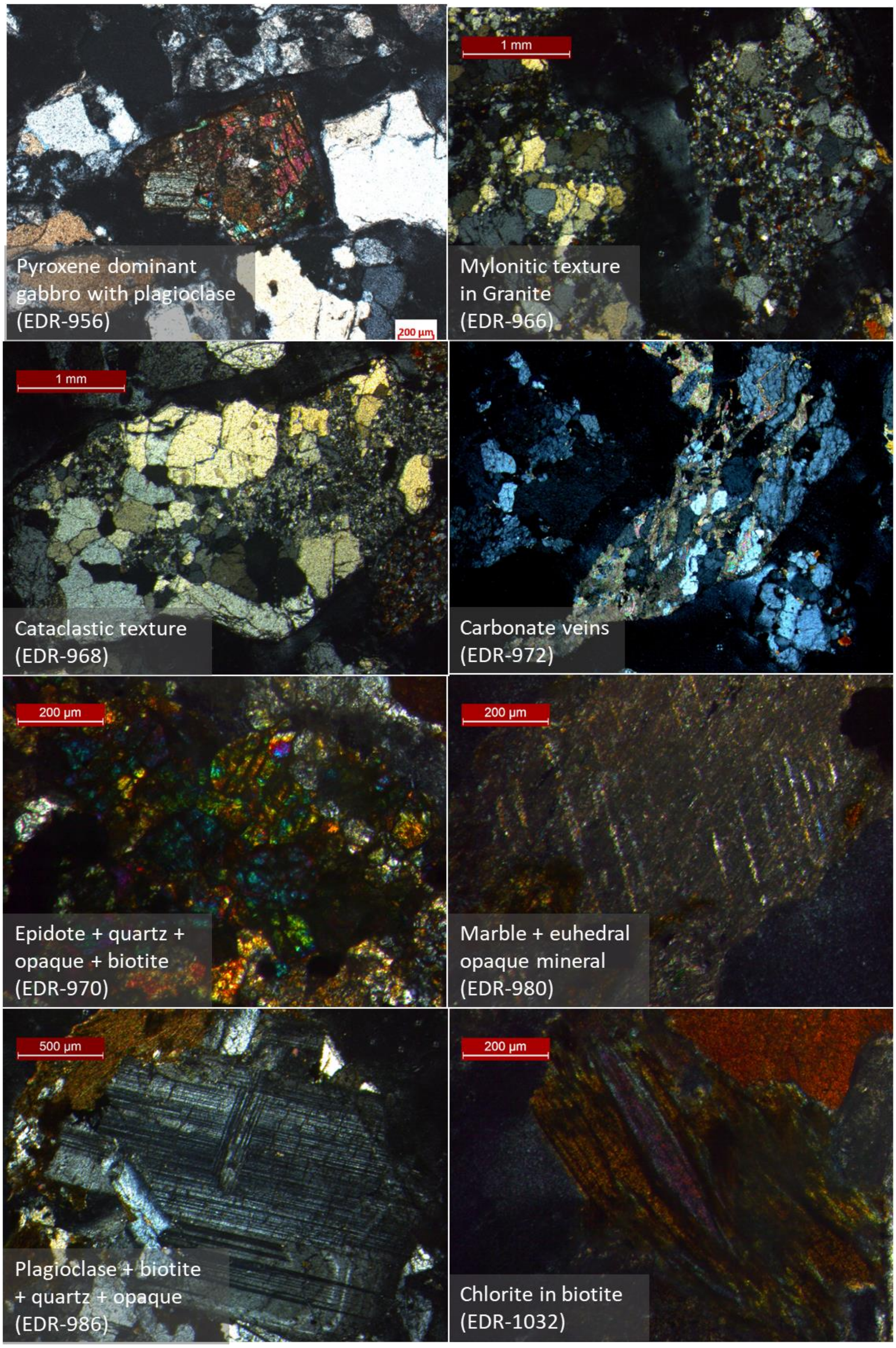

Figure A.6. Microscopic views of Edremit samples

# B. XRD Patterns of Samples from Akköy and Edremit Fields

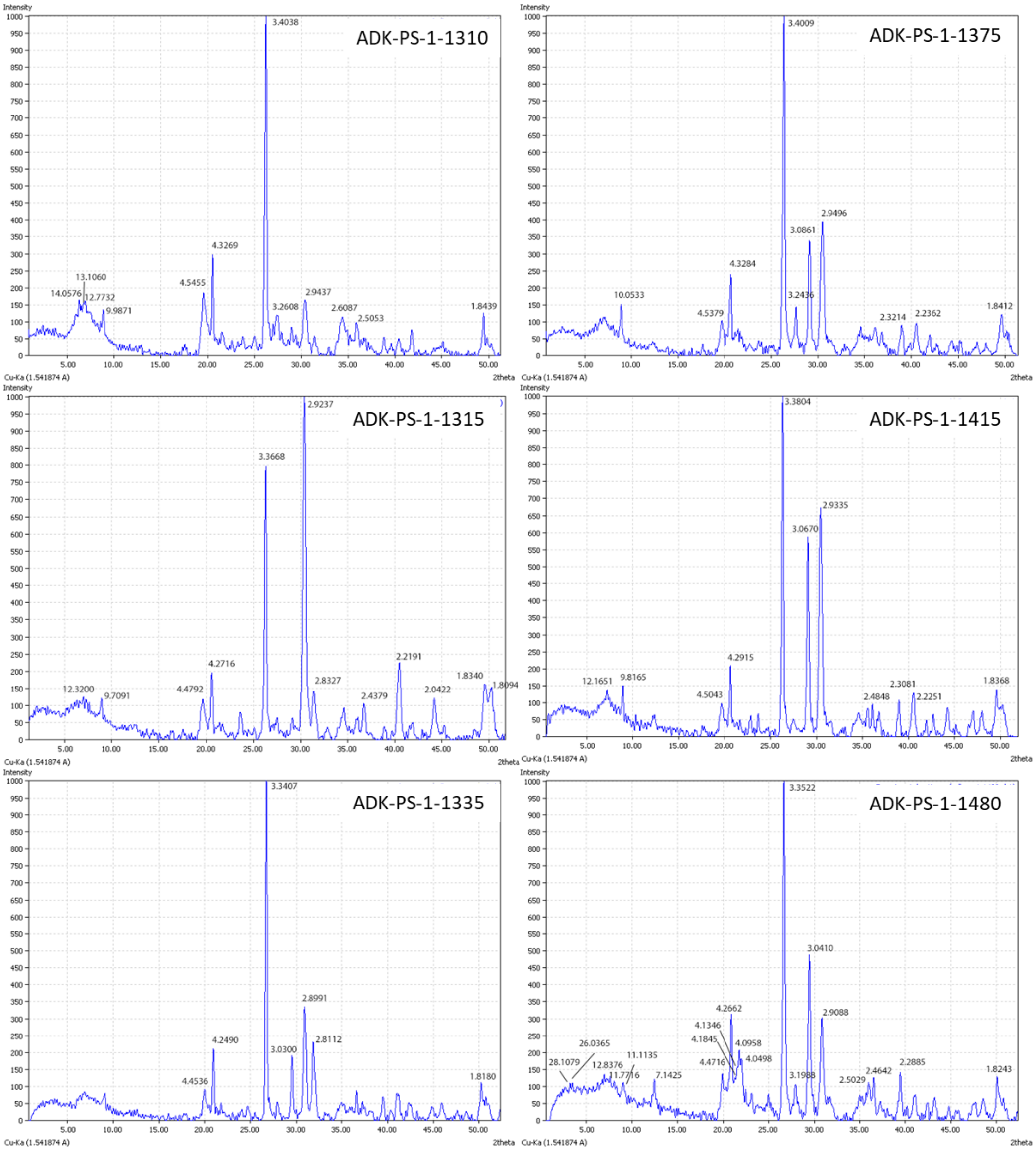

Figure B.1. XRD patterns of Akköy samples

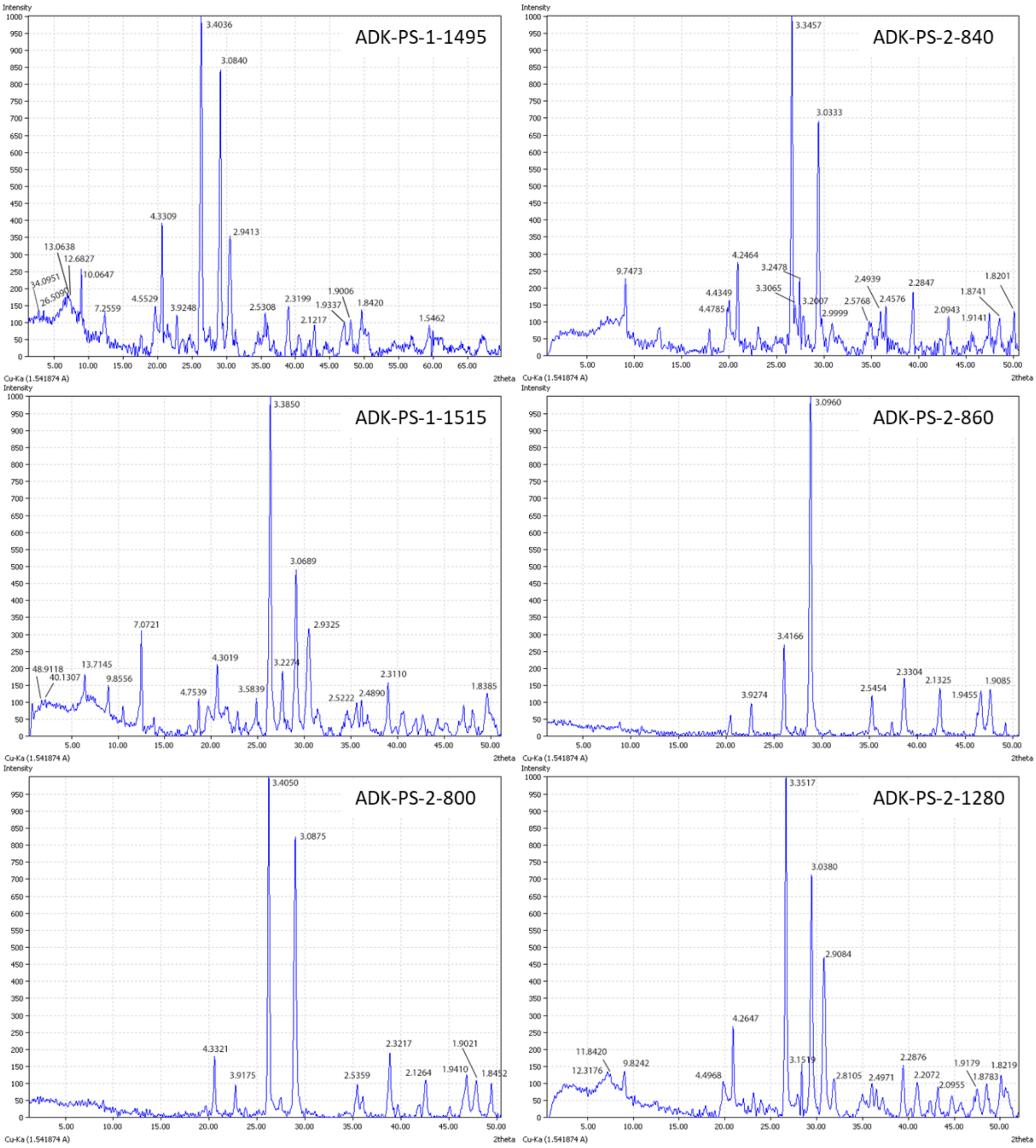

Figure B.2. XRD patterns of Akköy samples

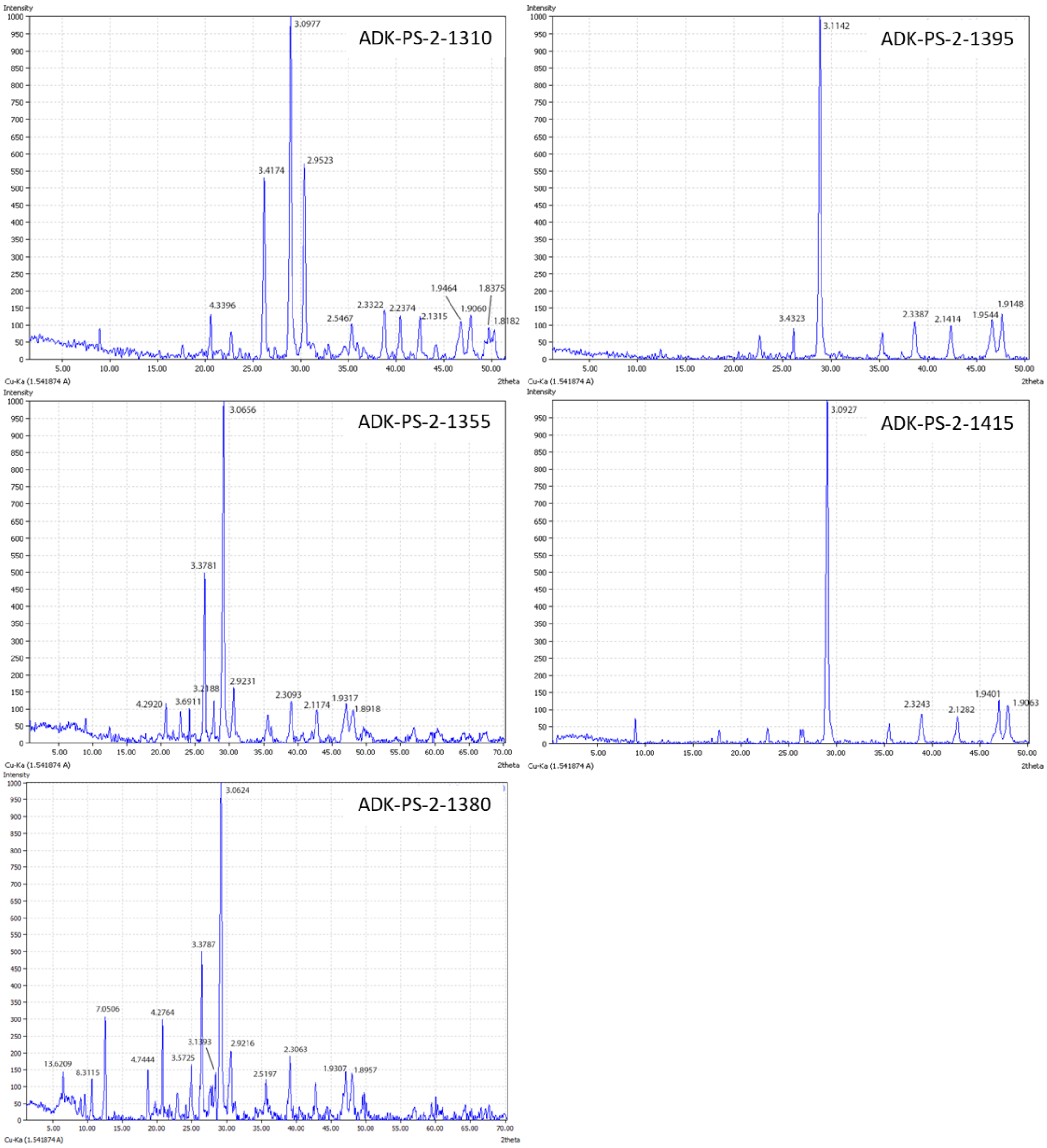

Figure B.3. XRD patterns of Akköy samples

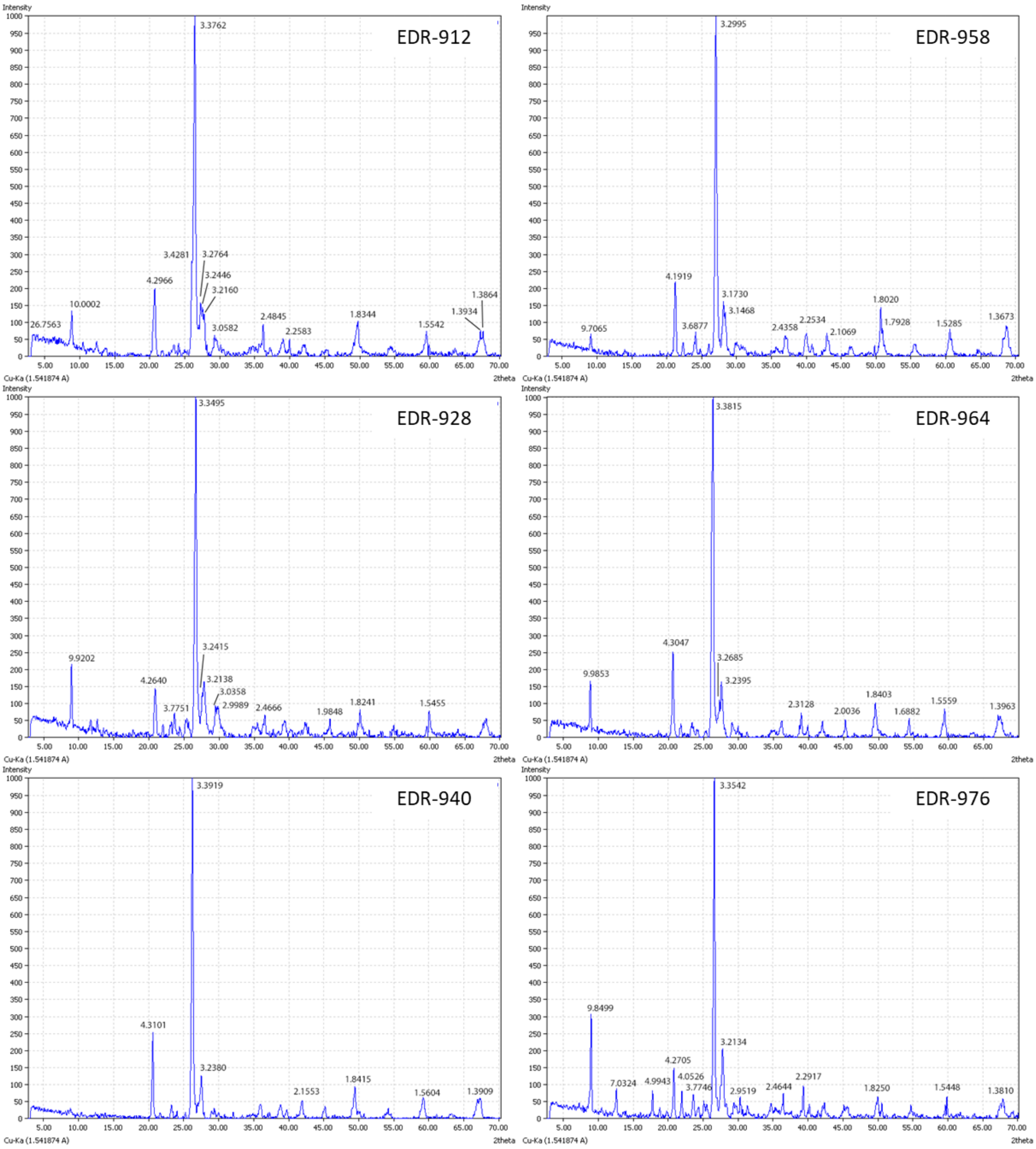

Figure B.4. XRD patterns of Edremit samples

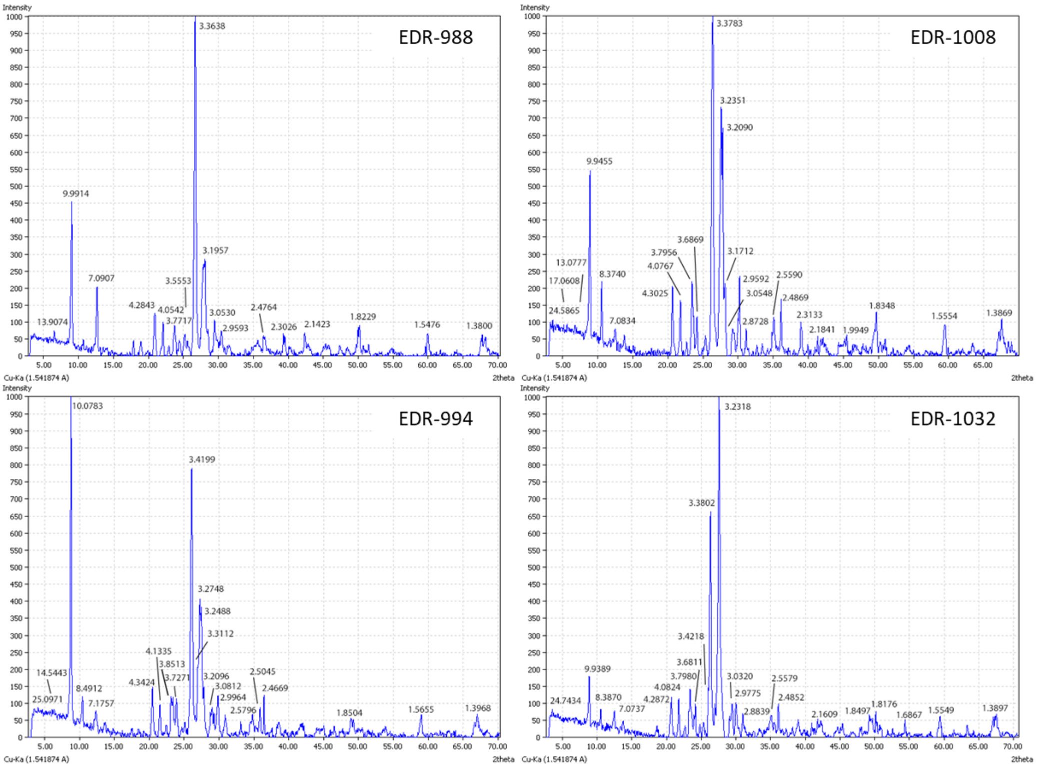

Figure B.5. XRD patterns of Edremit samples

## C. Raman Spectrums of Various Minerals from Akköy and Edremit Fields

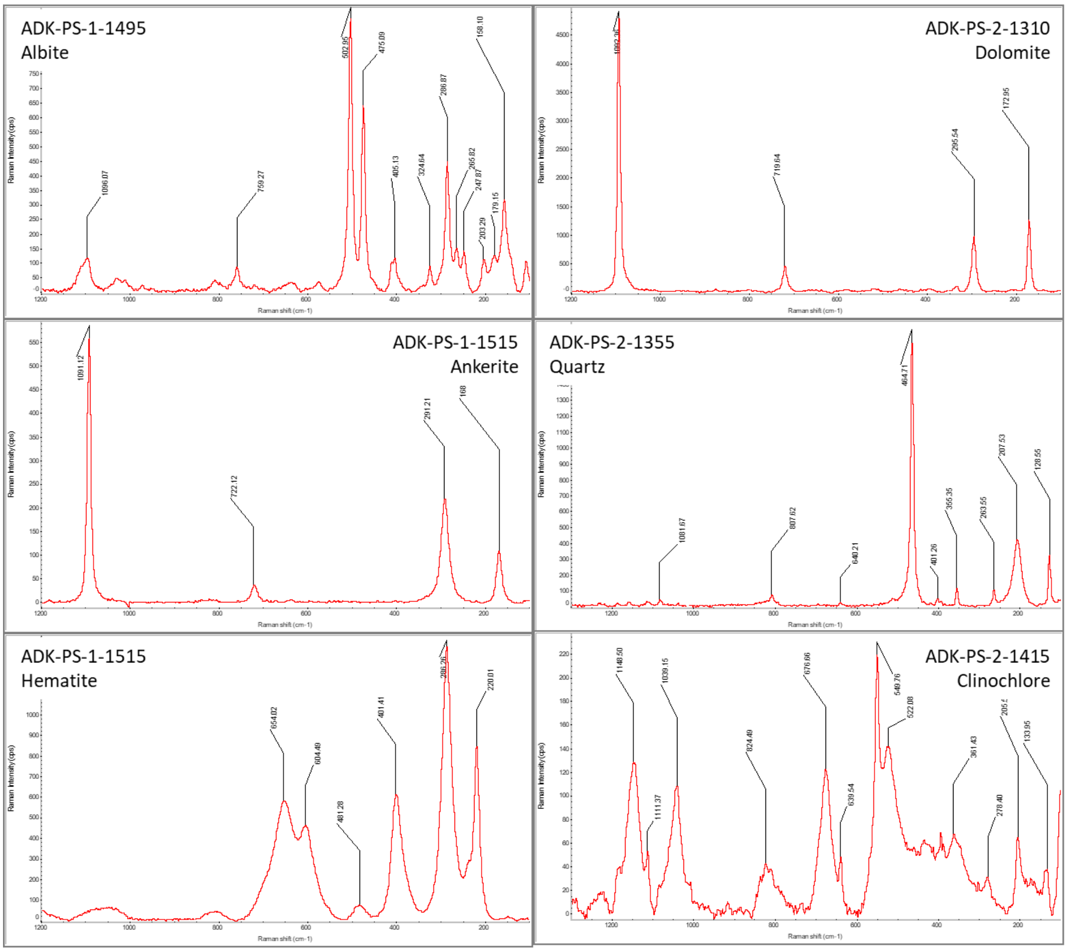

Figure C.1. Raman spectrums of various minerals from Akköy field

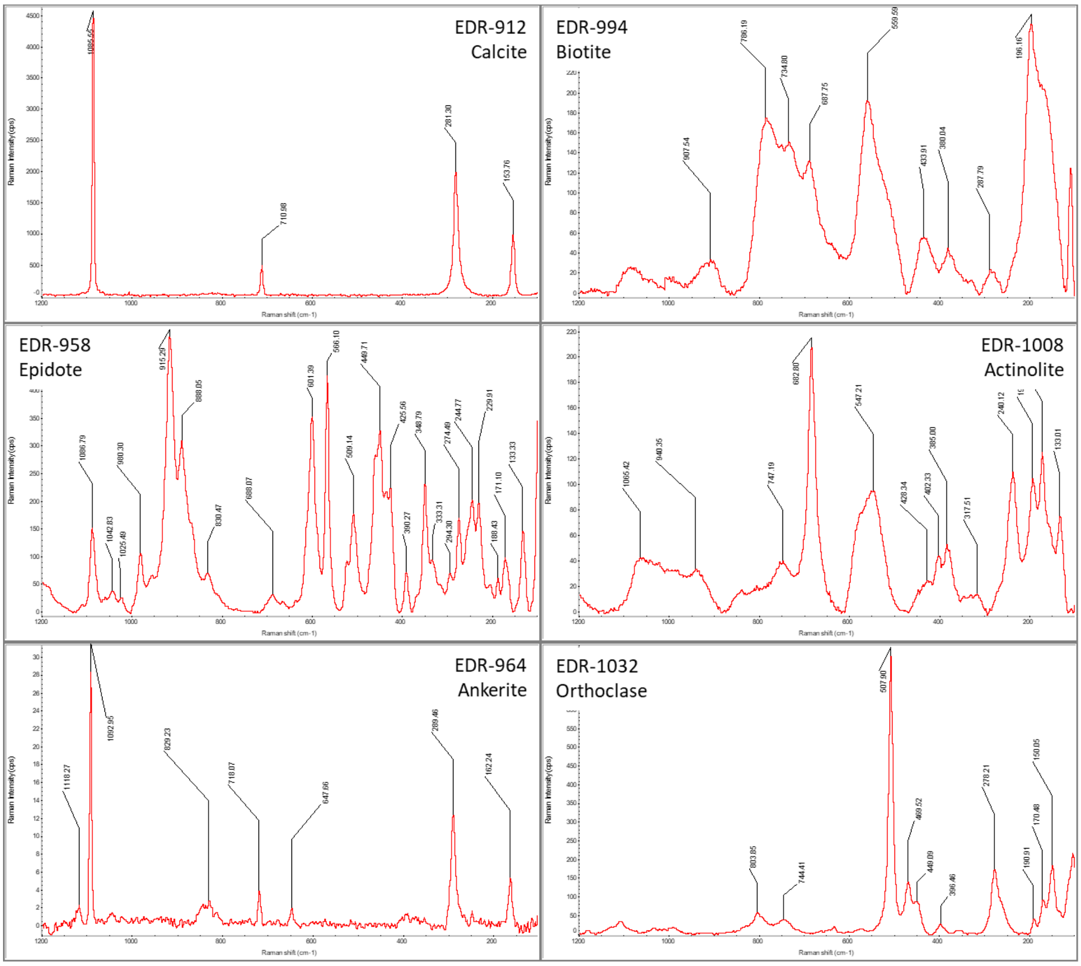

Figure C.2. Raman spectrums of various minerals from Edremit field

# D. EPMA Results of Samples from Akköy and Edremit Fields

Table D.1 EPMA results of feldspar minerals from Akköy field

| Feldspar | **Sample No.** | **PS-1-1510** | | | | | | **PS-1-1515** | | | | | | | | **PS-2-1270** | | | | | **PS-2-1270** |
|---|---|---|---|---|---|---|---|---|---|---|---|---|---|---|---|---|---|---|---|---|---|
| | Region/Mineral | 1/1 | | | | | | 1/1 | | | 1/2 | 1/3 | | | | 1/1 | | | | | 1/2 |
| | Spot No. | 1 | 2 | 3 | 5 | 6 | 7 | 1 | 3 | 5 | 2 | 1 | 2 | 3 | 4 | 2 | 3 | 4 | 5 | 6 | 1 |
| | $SiO_2$ | 61,96 | 61,56 | 62,11 | 62,71 | 62,42 | 62,74 | 68,10 | 67,78 | 67,40 | 66,54 | 66,51 | 65,91 | 66,16 | 67,46 | 61,41 | 61,69 | 62,02 | 63,51 | 62,69 | 60,16 |
| | $TiO_2$ | 0,00 | 0,00 | 0,00 | 0,00 | 0,00 | 0,00 | 0,04 | 0,01 | 0,00 | 0,00 | 0,02 | 0,01 | 0,00 | 0,00 | 0,00 | 0,00 | 0,00 | 0,00 | 0,00 | 0,00 |
| | $Al_2O_3$ | 19,54 | 19,33 | 19,66 | 19,99 | 19,56 | 19,87 | 20,85 | 20,91 | 20,88 | 20,45 | 20,53 | 20,29 | 22,02 | 20,86 | 19,47 | 19,62 | 19,57 | 19,95 | 19,89 | 24,02 |
| | FeO | 0,03 | 0,02 | 0,02 | 0,02 | 0,02 | 0,02 | 0,03 | 0,01 | 0,02 | 0,01 | 0,10 | 0,04 | 0,00 | 0,02 | 0,03 | 0,03 | 0,02 | 0,03 | 0,05 | 0,14 |
| | MnO | 0,00 | 0,00 | 0,00 | 0,00 | 0,00 | 0,00 | 0,00 | 0,00 | 0,00 | 0,00 | 0,00 | 0,00 | 0,00 | 0,00 | 0,00 | 0,00 | 0,00 | 0,00 | 0,00 | 0,00 |
| | MgO | 0,01 | 0,00 | 0,02 | 0,01 | 0,00 | 0,01 | 0,00 | 0,01 | 0,02 | 0,01 | 0,02 | 0,00 | 0,04 | 0,02 | 0,00 | 0,00 | 0,01 | 0,01 | 0,00 | 0,00 |
| | CaO | 0,01 | 0,04 | 0,10 | 0,05 | 0,04 | 0,07 | 0,16 | 0,15 | 0,11 | 0,03 | 0,12 | 0,13 | 0,10 | 0,12 | 0,21 | 0,26 | 0,14 | 0,14 | 0,29 | 4,33 |
| | $Na_2O$ | 1,01 | 0,98 | 1,05 | 0,98 | 0,71 | 0,77 | 12,41 | 12,88 | 12,41 | 12,77 | 12,48 | 12,02 | 11,74 | 12,84 | 1,32 | 1,81 | 0,87 | 0,78 | 0,54 | 9,19 |
| | $K_2O$ | 16,46 | 16,49 | 16,46 | 16,51 | 16,74 | 16,58 | 0,02 | 0,03 | 0,03 | 0,01 | 0,03 | 0,02 | 0,02 | 0,02 | 15,69 | 15,27 | 16,35 | 16,39 | 16,54 | 0,46 |
| | $SO_3$ | 0,01 | 0,01 | 0,02 | 0,01 | 0,00 | 0,01 | 0,03 | 0,05 | 0,03 | 0,02 | 0,00 | 0,01 | 0,03 | 0,02 | 0,02 | 0,01 | 0,01 | 0,04 | 0,04 | 0,02 |
| | *Total* | *99,04* | *98,43* | *99,44* | *100,28* | *99,50* | *100,05* | *101,63* | *101,81* | *100,90* | *99,85* | *99,80* | *98,42* | *100,11* | *101,35* | *98,15* | *98,70* | *98,99* | *100,84* | *100,02* | *98,32* |
| | ***Formula*** | | | | | | | | | | | | | | | | | | | | |
| | Si | 11,66 | 11,67 | 11,65 | 11,65 | 11,69 | 11,67 | 11,76 | 11,71 | 11,73 | 11,72 | 11,71 | 11,75 | 11,58 | 11,70 | 11,64 | 11,62 | 11,67 | 11,70 | 11,67 | 10,89 |
| | Al | 4,34 | 4,32 | 4,35 | 4,37 | 4,32 | 4,36 | 4,24 | 4,26 | 4,28 | 4,25 | 4,26 | 4,26 | 4,54 | 4,27 | 4,35 | 4,36 | 4,34 | 4,33 | 4,36 | 5,13 |
| | Ti | 0,00 | 0,00 | 0,00 | 0,00 | 0,00 | 0,00 | 0,005 | 0,002 | 0,00 | 0,00 | 0,002 | 0,001 | 0,00 | 0,00 | 0,00 | 0,00 | 0,00 | 0,00 | 0,00 | 0,00 |
| | Fe | 0,004 | 0,003 | 0,003 | 0,002 | 0,003 | 0,003 | 0,004 | 0,001 | 0,003 | 0,002 | 0,015 | 0,005 | 0,00 | 0,002 | 0,004 | 0,004 | 0,003 | 0,005 | 0,007 | 0,021 |
| | Mn | 0,00 | 0,00 | 0,00 | 0,00 | 0,00 | 0,00 | 0,00 | 0,00 | 0,00 | 0,00 | 0,00 | 0,00 | 0,00 | 0,00 | 0,00 | 0,00 | 0,00 | 0,00 | 0,00 | 0,00 |
| | Mg | 0,003 | 0,001 | 0,004 | 0,001 | 0,001 | 0,002 | 0,000 | 0,003 | 0,006 | 0,003 | 0,004 | 0,00 | 0,010 | 0,004 | 0,001 | 0,001 | 0,003 | 0,002 | 0,00 | 0,00 |
| | Ca | 0,00 | 0,01 | 0,02 | 0,01 | 0,01 | 0,01 | 0,03 | 0,03 | 0,02 | 0,01 | 0,02 | 0,02 | 0,02 | 0,02 | 0,04 | 0,05 | 0,03 | 0,03 | 0,06 | 0,84 |
| | Na | 0,37 | 0,36 | 0,38 | 0,35 | 0,26 | 0,28 | 4,15 | 4,31 | 4,18 | 4,36 | 4,26 | 4,15 | 3,98 | 4,32 | 0,49 | 0,66 | 0,32 | 0,28 | 0,19 | 3,23 |
| | K | 3,95 | 3,99 | 3,94 | 3,91 | 4,00 | 3,93 | 0,00 | 0,01 | 0,01 | 0,00 | 0,01 | 0,00 | 0,00 | 0,00 | 3,79 | 3,67 | 3,92 | 3,85 | 3,93 | 0,11 |
| | *Total* | *20,33* | *20,35* | *20,34* | *20,30* | *20,28* | *20,26* | *20,20* | *20,32* | *20,23* | *20,34* | *20,29* | *20,20* | *20,14* | *20,32* | *20,32* | *20,37* | *20,28* | *20,20* | *20,21* | *20,21* |
| | ***End Members*** | | | | | | | | | | | | | | | | | | | | |
| | Or | 91,39 | 91,54 | 90,75 | 91,48 | 93,76 | 93,08 | 0,12 | 0,13 | 0,14 | 0,05 | 0,15 | 0,11 | 0,09 | 0,10 | 87,77 | 83,71 | 91,89 | 92,68 | 94,00 | 2,55 |
| | Ab | 8,54 | 8,29 | 8,78 | 8,27 | 6,04 | 6,59 | 99,19 | 99,24 | 99,37 | 99,81 | 99,32 | 99,29 | 99,45 | 99,38 | 11,25 | 15,08 | 7,46 | 6,66 | 4,63 | 77,33 |
| | An | 0,07 | 0,17 | 0,47 | 0,25 | 0,21 | 0,33 | 0,69 | 0,63 | 0,49 | 0,14 | 0,54 | 0,59 | 0,45 | 0,52 | 0,98 | 1,21 | 0,65 | 0,66 | 1,37 | 20,12 |
| | *Total* | *100* | *100* | *100* | *100* | *100* | *100* | *100* | *100* | *100* | *100* | *100* | *100* | *100* | *100* | *100* | *100* | *100* | *100* | *100* | *100* |

Table D.1 EPMA results of feldspar minerals from Akköy field (cont'd)

| | **Sample No.** | **PS-2-1270** | | | | | | | | | | | | | | | | | | | | |
|---|---|---|---|---|---|---|---|---|---|---|---|---|---|---|---|---|---|---|---|---|---|---|
| | Region/Mineral | 1/2 | | | | | | | | | | 1/3 | 2/1 | | | | | | 2/2 | | | |
| | Spot No. | 2 | 3 | 4 | 5 | 6 | 7 | 8 | 9 | 10 | 11 | 1 | 1 | 2 | 3 | 4 | 5 | 6 | 2 | 3 | 4 | 5 |
| Feldspar | $SiO_2$ | 62,43 | 61,65 | 61,82 | 60,87 | 61,25 | 60,79 | 60,88 | 60,38 | 61,29 | 59,99 | 61,95 | 63,36 | 62,39 | 62,90 | 63,35 | 63,07 | 63,49 | 62,91 | 63,60 | 63,99 | 62,77 |
| | $TiO_2$ | 0,00 | 0,00 | 0,01 | 0,00 | 0,00 | 0,01 | 0,02 | 0,00 | 0,01 | 0,01 | 0,00 | 0,00 | 0,00 | 0,00 | 0,00 | 0,00 | 0,00 | 0,00 | 0,01 | 0,01 | 0,04 |
| | $Al_2O_3$ | 24,54 | 24,39 | 24,60 | 24,48 | 24,42 | 24,39 | 24,41 | 24,37 | 24,57 | 24,39 | 24,07 | 19,45 | 19,11 | 19,54 | 19,60 | 19,34 | 19,36 | 19,68 | 19,71 | 20,02 | 19,67 |
| | FeO | 0,15 | 0,16 | 0,16 | 0,11 | 0,14 | 0,13 | 0,17 | 0,16 | 0,14 | 0,15 | 0,15 | 0,06 | 0,03 | 0,02 | 0,03 | 0,04 | 0,07 | 0,70 | 0,20 | 0,20 | 1,40 |
| | MnO | 0,00 | 0,00 | 0,00 | 0,00 | 0,00 | 0,00 | 0,00 | 0,00 | 0,00 | 0,00 | 0,00 | 0,00 | 0,00 | 0,00 | 0,00 | 0,00 | 0,00 | 0,00 | 0,00 | 0,00 | 0,00 |
| | MgO | 0,00 | 0,00 | 0,00 | 0,02 | 0,00 | 0,01 | 0,00 | 0,00 | 0,00 | 0,02 | 0,00 | 0,00 | 0,01 | 0,00 | 0,01 | 0,01 | 0,02 | 0,39 | 0,07 | 0,06 | 0,53 |
| | CaO | 4,30 | 4,27 | 4,36 | 4,28 | 4,25 | 4,32 | 4,20 | 4,23 | 4,22 | 4,38 | 4,30 | 0,28 | 0,07 | 0,06 | 0,10 | 0,23 | 0,24 | 0,06 | 0,10 | 0,06 | 0,33 |
| | $Na_2O$ | 9,82 | 9,64 | 9,85 | 9,50 | 9,61 | 9,42 | 9,23 | 9,47 | 9,59 | 9,44 | 9,49 | 0,33 | 0,37 | 0,28 | 0,28 | 0,37 | 0,32 | 0,29 | 0,30 | 0,40 | 0,42 |
| | $K_2O$ | 0,40 | 0,48 | 0,42 | 0,47 | 0,43 | 0,41 | 0,44 | 0,44 | 0,43 | 0,38 | 0,45 | 17,08 | 17,03 | 17,22 | 17,38 | 17,29 | 17,25 | 16,60 | 17,02 | 17,03 | 16,46 |
| | $SO_3$ | 0,02 | 0,00 | 0,02 | 0,02 | 0,02 | 0,00 | 0,02 | 0,04 | 0,05 | 0,04 | 0,04 | 0,02 | 0,00 | 0,02 | 0,02 | 0,01 | 0,01 | 0,00 | 0,00 | 0,00 | 0,00 |
| | *Total* | *101,67* | *100,58* | *101,24* | *99,73* | *100,14* | *99,46* | *99,37* | *99,09* | *100,29* | *98,78* | *100,44* | *100,58* | *99,00* | *100,04* | *100,77* | *100,36* | *100,75* | *100,64* | *101,01* | *101,77* | *101,62* |
| | ***Formula*** | | | | | | | | | | | | | | | | | | | | | |
| | Si | 10,93 | 10,91 | 10,88 | 10,87 | 10,89 | 10,88 | 10,89 | 10,86 | 10,88 | 10,83 | 10,97 | 11,74 | 11,75 | 11,72 | 11,73 | 11,73 | 11,75 | 11,66 | 11,72 | 11,70 | 11,57 |
| | Al | 5,06 | 5,09 | 5,10 | 5,15 | 5,12 | 5,14 | 5,15 | 5,17 | 5,14 | 5,19 | 5,03 | 4,25 | 4,24 | 4,29 | 4,28 | 4,24 | 4,22 | 4,30 | 4,28 | 4,32 | 4,27 |
| | Ti | 0,00 | 0,00 | 0,001 | 0,000 | 0,000 | 0,001 | 0,002 | 0,000 | 0,001 | 0,001 | 0,00 | 0,00 | 0,00 | 0,00 | 0,00 | 0,00 | 0,00 | 0,00 | 0,001 | 0,001 | 0,006 |
| | Fe | 0,022 | 0,023 | 0,024 | 0,016 | 0,021 | 0,019 | 0,025 | 0,025 | 0,020 | 0,022 | 0,022 | 0,009 | 0,004 | 0,003 | 0,005 | 0,006 | 0,011 | 0,108 | 0,031 | 0,031 | 0,216 |
| | Mn | 0,00 | 0,00 | 0,00 | 0,00 | 0,00 | 0,00 | 0,00 | 0,00 | 0,00 | 0,00 | 0,00 | 0,00 | 0,00 | 0,00 | 0,00 | 0,00 | 0,00 | 0,00 | 0,00 | 0,00 | 0,00 |
| | Mg | 0,001 | 0,000 | 0,000 | 0,005 | 0,00 | 0,002 | 0,000 | 0,000 | 0,001 | 0,005 | 0,00 | 0,001 | 0,002 | 0,00 | 0,001 | 0,002 | 0,006 | 0,11 | 0,02 | 0,02 | 0,15 |
| | Ca | 0,81 | 0,81 | 0,82 | 0,82 | 0,81 | 0,83 | 0,80 | 0,81 | 0,80 | 0,85 | 0,82 | 0,05 | 0,01 | 0,01 | 0,02 | 0,05 | 0,05 | 0,01 | 0,02 | 0,01 | 0,06 |
| | Na | 3,33 | 3,31 | 3,36 | 3,29 | 3,31 | 3,27 | 3,20 | 3,30 | 3,30 | 3,30 | 3,26 | 0,12 | 0,14 | 0,10 | 0,10 | 0,13 | 0,11 | 0,10 | 0,11 | 0,14 | 0,15 |
| | K | 0,09 | 0,11 | 0,09 | 0,11 | 0,10 | 0,09 | 0,10 | 0,10 | 0,10 | 0,09 | 0,10 | 4,04 | 4,09 | 4,09 | 4,10 | 4,10 | 4,07 | 3,92 | 4,00 | 3,97 | 3,87 |
| | *Total* | *20,25* | *20,25* | *20,29* | *20,25* | *20,25* | *20,23* | *20,18* | *20,26* | *20,25* | *20,27* | *20,19* | *20,21* | *20,24* | *20,23* | *20,23* | *20,27* | *20,23* | *20,21* | *20,19* | *20,20* | *20,30* |
| | ***End Members*** | | | | | | | | | | | | | | | | | | | | | |
| | Or | 2,13 | 2,56 | 2,22 | 2,51 | 2,33 | 2,21 | 2,47 | 2,37 | 2,31 | 2,04 | 2,43 | 95,85 | 96,48 | 97,30 | 97,16 | 95,79 | 96,18 | 97,10 | 96,94 | 96,27 | 94,74 |
| | Ab | 78,80 | 78,28 | 78,59 | 78,05 | 78,50 | 78,02 | 77,95 | 78,31 | 78,57 | 77,97 | 78,03 | 2,85 | 3,19 | 2,40 | 2,36 | 3,13 | 2,70 | 2,59 | 2,56 | 3,45 | 3,67 |
| | An | 19,07 | 19,15 | 19,19 | 19,44 | 19,18 | 19,77 | 19,58 | 19,32 | 19,11 | 19,99 | 19,55 | 1,30 | 0,33 | 0,30 | 0,47 | 1,08 | 1,13 | 0,31 | 0,49 | 0,28 | 1,59 |
| | *Total* | *100* | *100* | *100* | *100* | *100* | *100* | *100* | *100* | *100* | *100* | *100* | *100* | *100* | *100* | *100* | *100* | *100* | *100* | *100* | *100* | *100* |

# Table D.1 EPMA results of feldspar minerals from Akköy field (cont'd)

| Feldspar | **Sample No.** | **PS-2-1345** | | | | **PS-2-1355** | | | | | | | | | | | **PS-2-1380** | | | | | |
|---|---|---|---|---|---|---|---|---|---|---|---|---|---|---|---|---|---|---|---|---|---|---|
| | Region/Mineral | 1/1 | | | | 2/1 | | | | | | | | | | | 2/1 | | | | | |
| | Spot No. | 5 | 7 | 9 | 10 | 1 | 2 | 3 | 4 | 5 | 6 | 7 | 8 | 9 | 10 | 11 | 1 | 2 | 3 | 4 | 5 | 6 |
| | $SiO_2$ | 67,23 | 67,70 | 67,94 | 66,92 | 66,74 | 67,17 | 66,84 | 67,41 | 66,63 | 67,23 | 66,61 | 66,89 | 67,39 | 67,52 | 67,33 | 65,84 | 67,57 | 68,70 | 66,25 | 66,11 | 66,54 |
| | $TiO_2$ | 0,01 | 0,01 | 0,01 | 0,09 | 0,00 | 0,00 | 0,00 | 0,02 | 0,00 | 0,00 | 0,00 | 0,00 | 0,00 | 0,00 | 0,00 | 0,00 | 0,00 | 0,02 | 0,01 | 0,03 | 0,00 |
| | $Al_2O_3$ | 21,00 | 19,63 | 20,66 | 20,33 | 20,38 | 20,55 | 20,53 | 20,73 | 20,26 | 20,62 | 20,42 | 20,35 | 20,78 | 20,82 | 20,53 | 20,32 | 20,56 | 20,61 | 20,48 | 20,66 | 20,53 |
| | FeO | 0,09 | 0,26 | 0,07 | 0,08 | 0,02 | 0,04 | 0,01 | 0,04 | 0,00 | 0,03 | 0,04 | 0,02 | 0,02 | 0,04 | 0,03 | 0,03 | 0,03 | 0,03 | 0,02 | 0,03 | 0,04 |
| | MnO | 0,00 | 0,00 | 0,00 | 0,00 | 0,00 | 0,00 | 0,00 | 0,00 | 0,00 | 0,00 | 0,00 | 0,00 | 0,00 | 0,00 | 0,00 | 0,00 | 0,00 | 0,00 | 0,00 | 0,00 | 0,00 |
| | MgO | 0,01 | 0,06 | 0,00 | 0,00 | 0,02 | 0,00 | 0,01 | 0,01 | 0,00 | 0,00 | 0,00 | 0,00 | 0,01 | 0,02 | 0,01 | 0,01 | 0,00 | 0,02 | 0,01 | 0,02 | 0,01 |
| | CaO | 0,66 | 0,36 | 0,14 | 0,29 | 0,04 | 0,18 | 0,12 | 0,08 | 0,04 | 0,11 | 0,21 | 0,04 | 0,30 | 0,28 | 0,04 | 0,06 | 0,05 | 0,08 | 0,05 | 0,09 | 0,07 |
| | $Na_2O$ | 12,70 | 12,42 | 13,01 | 12,49 | 12,60 | 12,84 | 12,75 | 13,02 | 12,56 | 12,79 | 12,87 | 12,55 | 12,91 | 12,85 | 12,60 | 12,65 | 12,80 | 11,84 | 12,69 | 12,67 | 12,79 |
| | $K_2O$ | 0,06 | 0,06 | 0,06 | 0,06 | 0,06 | 0,06 | 0,05 | 0,06 | 0,06 | 0,05 | 0,05 | 0,06 | 0,06 | 0,06 | 0,06 | 0,05 | 0,04 | 0,05 | 0,05 | 0,04 | 0,04 |
| | $SO_3$ | 0,01 | 0,01 | 0,00 | 0,01 | 0,01 | 0,01 | 0,00 | 0,01 | 0,01 | 0,02 | 0,02 | 0,00 | 0,02 | 0,03 | 0,01 | 0,02 | 0,02 | 0,00 | 0,01 | 0,02 | 0,01 |
| | *Total* | *101,77* | *100,50* | *101,89* | *100,26* | *99,87* | *100,84* | *100,31* | *101,37* | *99,57* | *100,85* | *100,23* | *99,91* | *101,47* | *101,61* | *100,60* | *98,97* | *101,07* | *101,35* | *99,58* | *99,66* | *100,03* |
| | ***Formula*** | | | | | | | | | | | | | | | | | | | | | |
| | Si | 11,64 | 11,85 | 11,73 | 11,74 | 11,74 | 11,72 | 11,72 | 11,71 | 11,76 | 11,72 | 11,71 | 11,76 | 11,69 | 11,70 | 11,76 | 11,71 | 11,75 | 11,85 | 11,70 | 11,67 | 11,70 |
| | Al | 4,29 | 4,05 | 4,21 | 4,20 | 4,23 | 4,23 | 4,24 | 4,24 | 4,21 | 4,24 | 4,23 | 4,22 | 4,25 | 4,25 | 4,22 | 4,26 | 4,21 | 4,19 | 4,26 | 4,30 | 4,26 |
| | Ti | 0,001 | 0,002 | 0,001 | 0,011 | 0,000 | 0,000 | 0,000 | 0,002 | 0,00 | 0,00 | 0,00 | 0,00 | 0,00 | 0,00 | 0,00 | 0,00 | 0,00 | 0,002 | 0,001 | 0,004 | 0,00 |
| | Fe | 0,012 | 0,038 | 0,010 | 0,012 | 0,003 | 0,006 | 0,001 | 0,006 | 0,000 | 0,005 | 0,006 | 0,002 | 0,003 | 0,005 | 0,004 | 0,004 | 0,004 | 0,005 | 0,003 | 0,005 | 0,006 |
| | Mn | 0,00 | 0,00 | 0,00 | 0,00 | 0,00 | 0,00 | 0,00 | 0,00 | 0,00 | 0,00 | 0,00 | 0,00 | 0,00 | 0,00 | 0,00 | 0,00 | 0,00 | 0,00 | 0,00 | 0,00 | 0,00 |
| | Mg | 0,003 | 0,02 | 0,000 | 0,000 | 0,004 | 0,00 | 0,002 | 0,002 | 0,00 | 0,00 | 0,00 | 0,00 | 0,002 | 0,006 | 0,002 | 0,002 | 0,001 | 0,006 | 0,002 | 0,004 | 0,004 |
| | Ca | 0,12 | 0,07 | 0,03 | 0,05 | 0,01 | 0,03 | 0,02 | 0,01 | 0,01 | 0,02 | 0,04 | 0,01 | 0,05 | 0,05 | 0,01 | 0,01 | 0,01 | 0,01 | 0,01 | 0,02 | 0,01 |
| | Na | 4,27 | 4,21 | 4,36 | 4,25 | 4,30 | 4,34 | 4,34 | 4,38 | 4,30 | 4,33 | 4,39 | 4,28 | 4,34 | 4,32 | 4,27 | 4,36 | 4,32 | 3,96 | 4,35 | 4,34 | 4,36 |
| | K | 0,01 | 0,01 | 0,01 | 0,01 | 0,01 | 0,01 | 0,01 | 0,01 | 0,01 | 0,01 | 0,01 | 0,01 | 0,01 | 0,01 | 0,01 | 0,01 | 0,01 | 0,01 | 0,01 | 0,01 | 0,01 |
| | *Total* | *20,35* | *20,24* | *20,35* | *20,28* | *20,30* | *20,34* | *20,33* | *20,37* | *20,29* | *20,33* | *20,38* | *20,28* | *20,36* | *20,34* | *20,27* | *20,35* | *20,30* | *20,04* | *20,34* | *20,35* | *20,35* |
| | ***End Members*** | | | | | | | | | | | | | | | | | | | | | |
| | Or | 0,32 | 0,31 | 0,29 | 0,30 | 0,30 | 0,29 | 0,27 | 0,29 | 0,30 | 0,28 | 0,24 | 0,29 | 0,28 | 0,28 | 0,29 | 0,27 | 0,21 | 0,25 | 0,25 | 0,22 | 0,20 |
| | Ab | 96,90 | 98,13 | 99,13 | 98,45 | 99,52 | 98,92 | 99,20 | 99,39 | 99,53 | 99,25 | 98,85 | 99,52 | 98,48 | 98,53 | 99,54 | 99,48 | 99,60 | 99,39 | 99,52 | 99,41 | 99,48 |
| | An | 2,79 | 1,55 | 0,58 | 1,26 | 0,18 | 0,78 | 0,53 | 0,32 | 0,17 | 0,48 | 0,91 | 0,19 | 1,24 | 1,19 | 0,17 | 0,25 | 0,19 | 0,35 | 0,23 | 0,37 | 0,31 |
| | *Total* | *100* | *100* | *100* | *100* | *100* | *100* | *100* | *100* | *100* | *100* | *100* | *100* | *100* | *100* | *100* | *100* | *100* | *100* | *100* | *100* | *100* |

Table D.1 EPMA results of feldspar minerals from Akköy field (cont’d)

| | **Sample No.** | **PS-2-1405** | | | | | | | | | | | | | | | | | |
|---|---|---|---|---|---|---|---|---|---|---|---|---|---|---|---|---|---|---|---|
| | Region/Mineral | 1/1 | | | | | 1/2 | | | | | | | | | | 1/3 | | |
| | Spot No. | 2 | 3 | 4 | 5 | 6 | 1 | 2 | 3 | 4 | 6 | 7 | 8 | 9 | 10 | 11 | 1 | 2 | 3 |
| Feldspar | $SiO_2$ | 66,78 | 68,17 | 67,39 | 66,46 | 66,82 | 66,36 | 67,25 | 67,40 | 67,42 | 67,39 | 67,16 | 66,92 | 68,13 | 67,17 | 67,66 | 66,29 | 66,87 | 67,58 |
| | $TiO_2$ | 0,00 | 0,00 | 0,00 | 0,00 | 0,00 | 0,00 | 0,00 | 0,00 | 0,02 | 0,00 | 0,00 | 0,02 | 0,00 | 0,00 | 0,02 | 0,00 | 0,01 | 0,00 |
| | $Al_2O_3$ | 20,30 | 20,54 | 20,66 | 20,23 | 20,49 | 20,25 | 20,48 | 20,56 | 20,50 | 20,55 | 20,52 | 20,51 | 20,44 | 20,22 | 20,51 | 20,43 | 20,80 | 20,76 |
| | FeO | 0,01 | 0,02 | 0,01 | 0,01 | 0,02 | 0,06 | 0,04 | 0,01 | 0,05 | 0,03 | 0,02 | 0,04 | 0,04 | 0,02 | 0,03 | 0,03 | 0,03 | 0,05 |
| | MnO | 0,00 | 0,00 | 0,00 | 0,00 | 0,00 | 0,00 | 0,00 | 0,00 | 0,00 | 0,00 | 0,00 | 0,00 | 0,00 | 0,00 | 0,00 | 0,00 | 0,00 | 0,00 |
| | MgO | 0,00 | 0,01 | 0,00 | 0,05 | 0,00 | 0,00 | 0,00 | 0,01 | 0,02 | 0,00 | 0,00 | 0,01 | 0,00 | 0,00 | 0,00 | 0,00 | 0,00 | 0,01 |
| | CaO | 0,04 | 0,05 | 0,12 | 0,07 | 0,08 | 0,34 | 0,08 | 0,06 | 0,17 | 0,20 | 0,12 | 0,12 | 0,08 | 0,15 | 0,09 | 0,05 | 0,28 | 0,06 |
| | $Na_2O$ | 12,40 | 12,94 | 12,95 | 12,36 | 12,62 | 12,68 | 12,70 | 13,09 | 12,73 | 12,99 | 12,71 | 12,84 | 12,69 | 12,52 | 12,82 | 12,57 | 12,32 | 12,89 |
| | $K_2O$ | 0,06 | 0,06 | 0,06 | 0,06 | 0,06 | 0,05 | 0,06 | 0,05 | 0,05 | 0,05 | 0,06 | 0,05 | 0,06 | 0,05 | 0,06 | 0,05 | 0,05 | 0,06 |
| | $SO_3$ | 0,00 | 0,00 | 0,12 | 0,03 | 0,02 | 0,01 | 0,00 | 0,02 | 0,00 | 0,01 | 0,00 | 0,02 | 0,02 | 0,00 | 0,01 | 0,01 | 0,01 | 0,00 |
| | *Total* | *99,59* | *101,79* | *101,30* | *99,27* | *100,11* | *99,75* | *100,61* | *101,20* | *100,95* | *101,21* | *100,59* | *100,52* | *101,45* | *100,14* | *101,19* | *99,44* | *100,37* | *101,39* |
| | ***Formula*** | | | | | | | | | | | | | | | | | | |
| | Si | 11,77 | 11,77 | 11,72 | 11,76 | 11,73 | 11,71 | 11,75 | 11,72 | 11,74 | 11,72 | 11,74 | 11,72 | 11,79 | 11,78 | 11,76 | 11,72 | 11,70 | 11,72 |
| | Al | 4,22 | 4,18 | 4,23 | 4,22 | 4,24 | 4,21 | 4,22 | 4,22 | 4,21 | 4,21 | 4,23 | 4,23 | 4,17 | 4,18 | 4,20 | 4,26 | 4,29 | 4,24 |
| | Ti | 0,00 | 0,00 | 0,00 | 0,00 | 0,00 | 0,00 | 0,00 | 0,00 | 0,002 | 0,00 | 0,00 | 0,002 | 0,00 | 0,00 | 0,002 | 0,001 | 0,002 | 0,000 |
| | Fe | 0,002 | 0,002 | 0,001 | 0,001 | 0,003 | 0,009 | 0,005 | 0,002 | 0,007 | 0,005 | 0,003 | 0,006 | 0,005 | 0,003 | 0,005 | 0,005 | 0,004 | 0,007 |
| | Mn | 0,00 | 0,00 | 0,00 | 0,00 | 0,00 | 0,00 | 0,00 | 0,00 | 0,00 | 0,00 | 0,00 | 0,00 | 0,00 | 0,00 | 0,00 | 0,00 | 0,00 | 0,00 |
| | Mg | 0,000 | 0,002 | 0,000 | 0,014 | 0,00 | 0,00 | 0,00 | 0,002 | 0,004 | 0,001 | 0,00 | 0,003 | 0,00 | 0,00 | 0,00 | 0,000 | 0,000 | 0,002 |
| | Ca | 0,01 | 0,01 | 0,02 | 0,01 | 0,02 | 0,06 | 0,02 | 0,01 | 0,03 | 0,04 | 0,02 | 0,02 | 0,01 | 0,03 | 0,02 | 0,01 | 0,05 | 0,01 |
| | Na | 4,24 | 4,33 | 4,37 | 4,24 | 4,30 | 4,34 | 4,30 | 4,41 | 4,30 | 4,38 | 4,31 | 4,36 | 4,26 | 4,26 | 4,32 | 4,31 | 4,18 | 4,33 |
| | K | 0,01 | 0,01 | 0,01 | 0,01 | 0,01 | 0,01 | 0,01 | 0,01 | 0,01 | 0,01 | 0,01 | 0,01 | 0,01 | 0,01 | 0,01 | 0,01 | 0,01 | 0,01 |
| | *Total* | *20,25* | *20,31* | *20,36* | *20,26* | *20,30* | *20,35* | *20,30* | *20,38* | *20,31* | *20,37* | *20,31* | *20,35* | *20,26* | *20,26* | *20,31* | *20,31* | *20,24* | *20,33* |
| | ***End Members*** | | | | | | | | | | | | | | | | | | |
| | Or | 0,33 | 0,32 | 0,32 | 0,31 | 0,31 | 0,25 | 0,30 | 0,27 | 0,26 | 0,25 | 0,30 | 0,25 | 0,28 | 0,25 | 0,28 | 0,28 | 0,28 | 0,28 |
| | Ab | 99,48 | 99,48 | 99,19 | 99,40 | 99,33 | 98,28 | 99,35 | 99,47 | 99,02 | 98,91 | 99,18 | 99,25 | 99,38 | 99,08 | 99,35 | 99,52 | 98,47 | 99,47 |
| | An | 0,19 | 0,20 | 0,49 | 0,30 | 0,36 | 1,47 | 0,35 | 0,26 | 0,73 | 0,84 | 0,52 | 0,49 | 0,33 | 0,67 | 0,37 | 0,20 | 1,25 | 0,25 |
| | *Total* | *100* | *100* | *100* | *100* | *100* | *100* | *100* | *100* | *100* | *100* | *100* | *100* | *100* | *100* | *100* | *100* | *100* | *100* |

## Table D.2 EPMA results of amphibole minerals from Akköy field

| Amphibole | **Sample No.** | **PS-2-1270** | | | | | | | | | |
|---|---|---|---|---|---|---|---|---|---|---|---|
| | Region/Mineral | 1/1 | | | | 2/1 | | | 2/2 | 2/3 | |
| | Spot No. | 2 | 4 | 5 | 6 | 1 | 3 | 4 | 1 | 1 | 3 |
| | $SiO_2$ | 45,73 | 44,00 | 45,41 | 43,91 | 40,27 | 40,00 | 39,96 | 53,36 | 51,38 | 50,01 |
| | $TiO_2$ | 0,37 | 0,45 | 0,41 | 0,45 | 1,58 | 1,56 | 1,61 | 0,03 | 0,03 | 0,05 |
| | $Al_2O_3$ | 8,13 | 8,40 | 8,92 | 8,81 | 11,07 | 11,09 | 11,13 | 2,17 | 2,35 | 4,08 |
| | $Cr_2O_3$ | 0,14 | 0,16 | 0,18 | 0,19 | 0,03 | 0,01 | 0,03 | 0,02 | 0,02 | 0,00 |
| | FeO | 17,47 | 17,64 | 17,64 | 17,91 | 22,88 | 23,01 | 23,09 | 14,38 | 15,01 | 16,84 |
| | MnO | 0,00 | 0,00 | 0,00 | 0,00 | 0,00 | 0,00 | 0,00 | 0,00 | 0,00 | 0,00 |
| | MgO | 12,21 | 11,68 | 12,38 | 11,73 | 8,16 | 8,01 | 8,02 | 15,17 | 14,72 | 13,82 |
| | CaO | 11,60 | 11,53 | 11,49 | 11,50 | 11,56 | 11,41 | 11,37 | 12,04 | 12,47 | 12,06 |
| | $Na_2O$ | 1,36 | 1,40 | 1,49 | 1,44 | 1,55 | 1,75 | 1,64 | 0,36 | 0,35 | 0,56 |
| | $K_2O$ | 0,71 | 0,76 | 0,77 | 0,82 | 1,51 | 1,58 | 1,59 | 0,19 | 0,12 | 0,28 |
| | *Total* | *97,72* | *96,00* | *98,70* | *96,76* | *98,61* | *98,42* | *98,44* | *97,71* | *96,45* | *97,72* |
| | O | 23 | 23 | 23 | 23 | 23 | 23 | 23 | 23 | 23 | 23 |
| | Cation | 15 | 15 | 15 | 15 | 15 | 15 | 15 | 15 | 15 | 15 |
| | ***Formula*** | | | | | | | | | | |
| | Si | 6,76 | 6,64 | 6,64 | 6,58 | 6,12 | 6,12 | 6,10 | 7,70 | 7,57 | 7,31 |
| | Ti | 0,04 | 0,05 | 0,05 | 0,05 | 0,18 | 0,18 | 0,18 | 0,00 | 0,00 | 0,01 |
| | Al-iv | 1,24 | 1,36 | 1,36 | 1,42 | 1,88 | 1,88 | 1,90 | 0,30 | 0,43 | 0,69 |
| | Al-vi | 0,17 | 0,14 | 0,17 | 0,13 | 0,11 | 0,11 | 0,10 | 0,07 | 0,00 | 0,01 |
| | Cr | 0,02 | 0,02 | 0,02 | 0,02 | 0,00 | 0,00 | 0,00 | 0,00 | 0,00 | 0,00 |
| | $Fe^{3+}$ | 0,63 | 0,69 | 0,73 | 0,75 | 0,77 | 0,73 | 0,78 | 0,22 | 0,24 | 0,50 |
| | $Fe^{2+}$ | 1,53 | 1,54 | 1,43 | 1,49 | 2,14 | 2,22 | 2,17 | 1,51 | 1,61 | 1,56 |
| | Mn | 0,00 | 0,00 | 0,00 | 0,00 | 0,00 | 0,00 | 0,00 | 0,00 | 0,00 | 0,00 |
| | Mg | 2,69 | 2,63 | 2,70 | 2,62 | 1,85 | 1,83 | 1,83 | 3,26 | 3,23 | 3,01 |
| | Ca | 1,84 | 1,86 | 1,80 | 1,85 | 1,88 | 1,87 | 1,86 | 1,86 | 1,97 | 1,89 |
| | Na | 0,39 | 0,41 | 0,42 | 0,42 | 0,46 | 0,52 | 0,48 | 0,10 | 0,10 | 0,16 |
| | K | 0,13 | 0,15 | 0,14 | 0,16 | 0,29 | 0,31 | 0,31 | 0,04 | 0,02 | 0,05 |
| | *Total* | *15,44* | *15,48* | *15,46* | *15,49* | *15,69* | *15,76* | *15,72* | *15,07* | *15,16* | *15,19* |
| | CaB | 1,84 | 1,86 | 1,80 | 1,85 | 1,88 | 1,87 | 1,86 | 1,86 | 1,97 | 1,89 |
| | NaB | 0,09 | 0,07 | 0,11 | 0,08 | 0,06 | 0,07 | 0,07 | 0,07 | 0,00 | 0,02 |
| | NaA | 0,30 | 0,34 | 0,31 | 0,33 | 0,39 | 0,45 | 0,41 | 0,03 | 0,14 | 0,14 |
| | KA | 0,13 | 0,15 | 0,14 | 0,16 | 0,29 | 0,31 | 0,31 | 0,04 | 0,02 | 0,05 |

Table D.3 EPMA results of mica minerals from Akköy field

| | **Sample No.** | **PS-2-1315** | | | | | | | **PS-2-1355** | | |
|---|---|---|---|---|---|---|---|---|---|---|---|
| | Region/Mineral | 1/1 | 2/1 | | | 2/2 | | | 1/1 | | |
| | Spot No. | 5 | 2 | 3 | 5 | 1 | 2 | 3 | 3 | 4 | 5 |
| Mica | $SiO_2$ | 49,27 | 45,02 | 42,77 | 45,78 | 44,96 | 44,74 | 42,01 | 51,68 | 49,77 | 50,44 |
| | $TiO_2$ | 0,74 | 0,29 | 0,33 | 0,32 | 0,31 | 0,23 | 0,29 | 0,14 | 0,20 | 0,19 |
| | $Al_2O_3$ | 26,45 | 32,99 | 29,71 | 32,07 | 32,91 | 34,78 | 30,19 | 24,33 | 26,79 | 25,21 |
| | FeO | 8,24 | 2,62 | 2,31 | 2,72 | 2,56 | 2,22 | 2,46 | 3,40 | 3,15 | 5,63 |
| | MnO | 0,00 | 0,00 | 0,00 | 0,00 | 0,00 | 0,00 | 0,00 | 0,00 | 0,00 | 0,00 |
| | MgO | 2,24 | 0,92 | 0,81 | 1,05 | 1,00 | 0,59 | 0,86 | 4,26 | 3,47 | 3,92 |
| | CaO | 0,07 | 0,05 | 0,03 | 0,06 | 0,03 | 0,05 | 0,07 | 0,06 | 0,09 | 0,09 |
| | $Na_2O$ | 0,26 | 0,61 | 0,52 | 0,63 | 0,58 | 0,63 | 0,54 | 0,23 | 0,53 | 0,45 |
| | $K_2O$ | 11,33 | 10,58 | 10,56 | 10,59 | 10,94 | 10,90 | 9,77 | 10,97 | 10,73 | 10,28 |
| | $Cr_2O_3$ | 0,01 | 0,02 | 0,01 | 0,00 | 0,02 | 0,03 | 0,02 | 0,73 | 0,68 | 0,60 |
| | $SO_3$ | 0,03 | 0,04 | 0,02 | 0,04 | 0,03 | 0,01 | 0,03 | 0,00 | 0,01 | 0,01 |
| | *Total* | *98,62* | *93,14* | *87,08* | *93,26* | *93,34* | *94,15* | *86,23* | *95,79* | *95,42* | *96,82* |
| | ***Formula*** | | | | | | | | | | |
| | Si | 6,60 | 6,20 | 6,32 | 6,29 | 6,19 | 6,09 | 6,24 | 6,94 | 6,71 | 6,76 |
| | Al-iv | 1,40 | 1,80 | 1,68 | 1,71 | 1,81 | 1,91 | 1,76 | 1,06 | 1,29 | 1,24 |
| | Al-vi | 2,78 | 3,55 | 3,49 | 3,49 | 3,53 | 3,67 | 3,53 | 2,78 | 2,96 | 2,75 |
| | Ti | 0,07 | 0,03 | 0,04 | 0,03 | 0,03 | 0,02 | 0,03 | 0,01 | 0,02 | 0,02 |
| | Cr | 0,00 | 0,00 | 0,00 | 0,00 | 0,00 | 0,00 | 0,00 | 0,08 | 0,07 | 0,06 |
| | $Fe^{+2}$ | 0,92 | 0,30 | 0,29 | 0,31 | 0,29 | 0,25 | 0,31 | 0,38 | 0,35 | 0,63 |
| | Mn | 0,00 | 0,00 | 0,00 | 0,00 | 0,00 | 0,00 | 0,00 | 0,00 | 0,00 | 0,00 |
| | Mg | 0,45 | 0,19 | 0,18 | 0,22 | 0,20 | 0,12 | 0,19 | 0,85 | 0,70 | 0,78 |
| | Ca | 0,01 | 0,01 | 0,00 | 0,01 | 0,00 | 0,01 | 0,01 | 0,01 | 0,01 | 0,01 |
| | Na | 0,07 | 0,16 | 0,15 | 0,17 | 0,16 | 0,17 | 0,16 | 0,06 | 0,14 | 0,12 |
| | K | 1,94 | 1,86 | 1,99 | 1,86 | 1,92 | 1,89 | 1,85 | 1,88 | 1,84 | 1,76 |
| | *Total* | *14,24* | *14,10* | *14,13* | *14,09* | *14,14* | *14,13* | *14,08* | *14,06* | *14,10* | *14,13* |
| | Fe/Fe+Mg | 0,67 | 0,62 | 0,62 | 0,59 | 0,59 | 0,68 | 0,62 | 0,31 | 0,34 | 0,45 |
| | Fe+Mn+Ti | 1,00 | 0,33 | 0,32 | 0,35 | 0,33 | 0,28 | 0,34 | 0,40 | 0,38 | 0,65 |
| | Mg-Li | 0,45 | 0,19 | 0,18 | 0,22 | 0,20 | 0,12 | 0,19 | 0,85 | 0,70 | 0,78 |

Table D.4 EPMA results of pyroxene minerals from Akköy field

|  | **Sample No.** | **PS-2-1270** |  |  |  |  |  |  |  |
|---|---|---|---|---|---|---|---|---|---|
|  | Region/Mineral | 1/1 |  | 2/1 |  |  |  |  | 2/2 |
|  | Spot No. | 1 | 3 | 2 | 5 | 6 | 7 | 8 | 2 |
| Pyroxene | $SiO_2$ | 46,52 | 47,13 | 40,67 | 40,49 | 40,18 | 39,91 | 41,59 | 47,52 |
|  | $TiO_2$ | 0,39 | 0,41 | 1,53 | 1,61 | 1,60 | 1,65 | 1,55 | 0,17 |
|  | $Al_2O_3$ | 8,10 | 8,55 | 11,21 | 11,60 | 11,50 | 11,50 | 11,19 | 6,89 |
|  | $Cr_2O_3$ | 0,16 | 0,15 | 0,02 | 0,04 | 0,03 | 0,03 | 0,04 | 0,00 |
|  | FeO | 17,57 | 17,41 | 22,87 | 23,12 | 23,16 | 23,22 | 22,85 | 18,42 |
|  | MnO | 0,00 | 0,00 | 0,00 | 0,00 | 0,00 | 0,00 | 0,00 | 0,00 |
|  | MgO | 12,63 | 12,98 | 8,30 | 8,20 | 8,17 | 8,00 | 8,48 | 12,28 |
|  | CaO | 11,59 | 11,63 | 11,38 | 11,34 | 11,37 | 11,37 | 11,43 | 12,32 |
|  | $Na_2O$ | 1,36 | 1,32 | 1,73 | 1,78 | 1,79 | 1,75 | 1,62 | 0,99 |
|  | $K_2O$ | 0,69 | 0,68 | 1,56 | 1,62 | 1,64 | 1,63 | 1,56 | 0,29 |
|  | *Total* | *99,00* | *100,26* | *99,25* | *99,80* | *99,43* | *99,06* | *100,30* | *98,88* |
|  | O | 6 | 6 | 6 | 6 | 6 | 6 | 6 | 6 |
|  | Cation | 4 | 4 | 4 | 4 | 4 | 4 | 4 | 4 |
|  | ***Formula*** |  |  |  |  |  |  |  |  |
|  | Si | 1,79 | 1,79 | 1,63 | 1,62 | 1,61 | 1,61 | 1,64 | 1,83 |
|  | Ti | 0,01 | 0,01 | 0,05 | 0,05 | 0,05 | 0,05 | 0,05 | 0,00 |
|  | Al | 0,37 | 0,38 | 0,53 | 0,55 | 0,54 | 0,55 | 0,52 | 0,31 |
|  | Cr | 0,005 | 0,005 | 0,001 | 0,001 | 0,001 | 0,001 | 0,001 | 0,00 |
|  | Fe | 0,57 | 0,55 | 0,77 | 0,77 | 0,78 | 0,78 | 0,75 | 0,59 |
|  | Mn | 0,00 | 0,00 | 0,00 | 0,00 | 0,00 | 0,00 | 0,00 | 0,00 |
|  | Mg | 0,73 | 0,73 | 0,50 | 0,49 | 0,49 | 0,48 | 0,50 | 0,71 |
|  | Ca | 0,48 | 0,47 | 0,49 | 0,48 | 0,49 | 0,49 | 0,48 | 0,51 |
|  | Na | 0,10 | 0,10 | 0,13 | 0,14 | 0,14 | 0,14 | 0,12 | 0,07 |
|  | K | 0,03 | 0,03 | 0,08 | 0,08 | 0,08 | 0,08 | 0,08 | 0,01 |
|  | ***End Members*** |  |  |  |  |  |  |  |  |
|  | Es | 41,00 | 41,74 | 28,32 | 27,97 | 27,86 | 27,41 | 28,75 | 39,02 |
|  | Wo | 27,02 | 26,87 | 27,91 | 27,79 | 27,86 | 27,99 | 27,84 | 28,14 |
|  | Fs | 31,98 | 31,39 | 43,77 | 44,24 | 44,28 | 44,60 | 43,41 | 32,84 |
|  | *Total* | *100* | *100* | *100* | *100* | *100* | *100* | *100* | *100* |

# Table D.5 EPMA results of feldspar minerals from Edremit field

| Feldspar | **Sample No.** | **EDR-912** | | | | | | | | | | | | | | | | | | | |
|---|---|---|---|---|---|---|---|---|---|---|---|---|---|---|---|---|---|---|---|---|---|
| | Region/Mineral | 2/1 | | | | 2/2 | | | 2/3 | | | 4/1 | | | | | 4/2 | | | | |
| | Spot No. | 1 | 2 | 4 | 5 | 2 | 3 | 4 | 1 | 2 | 5 | 1 | 2 | 3 | 4 | 5 | 2 | 3 | 5 | 6 | 8 |
| | $SiO_2$ | 61,83 | 62,97 | 63,41 | 62,56 | 58,40 | 56,14 | 57,86 | 57,15 | 55,01 | 55,84 | 62,26 | 62,20 | 63,39 | 56,30 | 55,20 | 60,43 | 54,07 | 54,38 | 57,71 | 55,20 |
| | $TiO_2$ | 0,00 | 0,00 | 0,00 | 0,01 | 0,00 | 0,03 | 0,00 | 0,01 | 0,00 | 0,00 | 0,00 | 0,00 | 0,01 | 0,00 | 0,00 | 0,02 | 0,00 | 0,00 | 0,00 | 0,00 |
| | $Al_2O_3$ | 19,33 | 20,21 | 19,36 | 19,18 | 26,03 | 27,96 | 26,30 | 26,76 | 28,37 | 28,33 | 19,48 | 19,48 | 19,66 | 27,20 | 27,77 | 24,08 | 28,70 | 28,62 | 26,12 | 27,90 |
| | FeO | 0,11 | 0,11 | 0,08 | 0,10 | 0,23 | 0,20 | 0,19 | 0,24 | 0,27 | 0,23 | 0,10 | 0,12 | 0,12 | 0,23 | 0,23 | 0,13 | 0,23 | 0,23 | 0,23 | 0,26 |
| | MnO | 0,00 | 0,00 | 0,00 | 0,00 | 0,00 | 0,00 | 0,00 | 0,00 | 0,00 | 0,00 | 0,00 | 0,00 | 0,00 | 0,00 | 0,00 | 0,00 | 0,00 | 0,00 | 0,00 | 0,00 |
| | MgO | 0,01 | 0,03 | 0,00 | 0,01 | 0,01 | 0,02 | 0,02 | 0,02 | 0,00 | 0,01 | 0,00 | 0,01 | 0,01 | 0,01 | 0,00 | 0,00 | 0,00 | 0,01 | 0,00 | 0,01 |
| | CaO | 0,03 | 0,06 | 0,03 | 0,05 | 5,60 | 7,32 | 5,76 | 6,20 | 7,80 | 7,41 | 0,06 | 0,06 | 0,04 | 6,92 | 7,31 | 4,36 | 8,59 | 8,10 | 5,79 | 7,41 |
| | $Na_2O$ | 1,42 | 1,81 | 0,99 | 1,72 | 8,43 | 7,64 | 8,45 | 8,26 | 6,99 | 6,94 | 1,42 | 1,50 | 2,18 | 7,77 | 7,32 | 9,58 | 6,81 | 6,77 | 8,57 | 7,19 |
| | $K_2O$ | 15,39 | 14,97 | 16,29 | 15,32 | 0,18 | 0,15 | 0,18 | 0,13 | 0,22 | 0,25 | 15,74 | 15,61 | 14,98 | 0,22 | 0,23 | 0,33 | 0,18 | 0,20 | 0,26 | 0,21 |
| | $SO_3$ | 0,01 | 0,003 | 0,00 | 0,004 | 0,01 | 0,00 | 0,01 | 0,01 | 0,00 | 0,01 | 0,00 | 0,00 | 0,00 | 0,01 | 0,01 | 0,003 | 0,01 | 0,01 | 0,02 | 0,002 |
| | *Total* | *98,12* | *100,16* | *100,17* | *98,95* | *98,89* | *99,45* | *98,77* | *98,77* | *98,67* | *99,02* | *99,06* | *98,98* | *100,39* | *98,65* | *98,07* | *98,93* | *98,57* | *98,32* | *98,69* | *98,17* |
| | ***Formula*** | | | | | | | | | | | | | | | | | | | | |
| | Si | 11,70 | 11,64 | 11,76 | 11,73 | 10,54 | 10,13 | 10,47 | 10,36 | 10,02 | 10,11 | 11,68 | 11,68 | 11,70 | 10,24 | 10,11 | 10,88 | 9,89 | 9,95 | 10,46 | 10,09 |
| | Al | 4,31 | 4,40 | 4,23 | 4,24 | 5,54 | 5,95 | 5,61 | 5,72 | 6,09 | 6,04 | 4,31 | 4,31 | 4,28 | 5,83 | 5,99 | 5,11 | 6,19 | 6,17 | 5,58 | 6,01 |
| | Ti | 0,00 | 0,00 | 0,00 | 0,00 | 0,00 | 0,00 | 0,00 | 0,00 | 0,00 | 0,00 | 0,00 | 0,00 | 0,00 | 0,00 | 0,00 | 0,00 | 0,00 | 0,00 | 0,00 | 0,00 |
| | Fe | 0,02 | 0,02 | 0,01 | 0,02 | 0,03 | 0,03 | 0,03 | 0,04 | 0,04 | 0,03 | 0,02 | 0,02 | 0,02 | 0,04 | 0,04 | 0,02 | 0,03 | 0,04 | 0,03 | 0,04 |
| | Mn | 0,00 | 0,00 | 0,00 | 0,00 | 0,00 | 0,00 | 0,00 | 0,00 | 0,00 | 0,00 | 0,00 | 0,00 | 0,00 | 0,00 | 0,00 | 0,00 | 0,00 | 0,00 | 0,00 | 0,00 |
| | Mg | 0,00 | 0,01 | 0,00 | 0,00 | 0,00 | 0,00 | 0,00 | 0,01 | 0,00 | 0,00 | 0,00 | 0,00 | 0,00 | 0,00 | 0,00 | 0,00 | 0,00 | 0,00 | 0,00 | 0,00 |
| | Ca | 0,01 | 0,01 | 0,01 | 0,01 | 1,08 | 1,42 | 1,12 | 1,20 | 1,52 | 1,44 | 0,01 | 0,01 | 0,01 | 1,35 | 1,43 | 0,84 | 1,68 | 1,59 | 1,12 | 1,45 |
| | Na | 0,52 | 0,65 | 0,36 | 0,63 | 2,95 | 2,67 | 2,96 | 2,90 | 2,47 | 2,44 | 0,51 | 0,55 | 0,78 | 2,74 | 2,60 | 3,34 | 2,42 | 2,40 | 3,01 | 2,55 |
| | K | 3,71 | 3,53 | 3,85 | 3,66 | 0,04 | 0,03 | 0,04 | 0,03 | 0,05 | 0,06 | 3,77 | 3,74 | 3,53 | 0,05 | 0,05 | 0,08 | 0,04 | 0,05 | 0,06 | 0,05 |
| | *Total* | *20,26* | *20,25* | *20,23* | *20,29* | *20,19* | *20,24* | *20,23* | *20,25* | *20,20* | *20,12* | *20,30* | *20,31* | *20,31* | *20,24* | *20,22* | *20,27* | *20,25* | *20,19* | *20,28* | *20,20* |
| | ***End Members*** | | | | | | | | | | | | | | | | | | | | |
| | Or | 87,60 | 84,26 | 91,43 | 85,24 | 1,00 | 0,82 | 1,02 | 0,72 | 1,26 | 1,48 | 87,75 | 86,98 | 81,74 | 1,24 | 1,33 | 1,79 | 1,00 | 1,17 | 1,43 | 1,20 |
| | Ab | 12,25 | 15,45 | 8,44 | 14,55 | 72,42 | 64,86 | 71,89 | 70,18 | 61,07 | 61,97 | 11,99 | 12,73 | 18,06 | 66,20 | 63,59 | 78,45 | 58,35 | 59,47 | 71,77 | 62,93 |
| | An | 0,15 | 0,29 | 0,14 | 0,21 | 26,58 | 34,33 | 27,09 | 29,10 | 37,67 | 36,55 | 0,26 | 0,29 | 0,20 | 32,56 | 35,09 | 19,75 | 40,65 | 39,36 | 26,79 | 35,87 |
| | *Total* | *100* | *100* | *100* | *100* | *100* | *100* | *100* | *100* | *100* | *100* | *100* | *100* | *100* | *100* | *100* | *100* | *100* | *100* | *100* | *100* |

Table D.5 EPMA results of feldspar minerals from Edremit field (cont'd)

| | **Sample No.** | **EDR-912** | | | | **EDR-958** | **EDR-964** | | | | | | | | | | | | | |
|---|---|---|---|---|---|---|---|---|---|---|---|---|---|---|---|---|---|---|---|---|
| | Region/Mineral | 4/2 | | 4/3 | | 1/1 | 1/1 | | | | | 1/2 | | | 1/3 | 2/1 | | | 2/3 | 2/4 |
| | Spot No. | 9 | 10 | 5 | 6 | 3 | 1 | 2 | 3 | 4 | 5 | 1 | 2 | 3 | 3 | 1 | 2 | 3 | 1 | 4 |
| Feldspar | $SiO_2$ | 56,73 | 62,34 | 55,74 | 62,00 | 64,44 | 58,42 | 55,27 | 54,56 | 54,90 | 55,21 | 56,79 | 53,39 | 55,06 | 60,64 | 55,92 | 55,86 | 57,69 | 56,67 | 55,79 |
| | $TiO_2$ | 0,00 | 0,00 | 0,02 | 0,00 | 0,00 | 0,01 | 0,01 | 0,01 | 0,00 | 0,00 | 0,00 | 0,00 | 0,00 | 0,00 | 0,00 | 0,00 | 0,00 | 0,00 | 0,00 |
| | $Al_2O_3$ | 26,74 | 19,40 | 27,55 | 19,26 | 19,38 | 25,83 | 27,39 | 27,97 | 28,24 | 28,25 | 26,60 | 28,17 | 28,27 | 23,58 | 27,57 | 27,45 | 26,53 | 27,24 | 27,43 |
| | FeO | 0,22 | 0,04 | 0,19 | 0,10 | 0,02 | 0,14 | 0,16 | 0,21 | 0,22 | 0,20 | 0,18 | 0,23 | 0,23 | 0,19 | 0,20 | 0,20 | 0,16 | 0,20 | 0,21 |
| | MnO | 0,00 | 0,00 | 0,00 | 0,00 | 0,00 | 0,00 | 0,00 | 0,00 | 0,00 | 0,00 | 0,00 | 0,00 | 0,00 | 0,00 | 0,00 | 0,00 | 0,00 | 0,00 | 0,00 |
| | MgO | 0,00 | 0,01 | 0,01 | 0,00 | 0,00 | 0,01 | 0,00 | 0,00 | 0,00 | 0,00 | 0,01 | 0,00 | 0,01 | 0,01 | 0,02 | 0,00 | 0,00 | 0,01 | 0,00 |
| | CaO | 6,45 | 0,19 | 6,84 | 0,02 | 0,01 | 5,90 | 7,79 | 8,15 | 8,05 | 7,91 | 6,60 | 8,52 | 7,80 | 3,75 | 6,80 | 7,16 | 5,94 | 6,77 | 6,98 |
| | $Na_2O$ | 8,07 | 4,46 | 7,66 | 0,93 | 0,90 | 8,67 | 7,23 | 7,04 | 6,91 | 7,26 | 7,84 | 6,46 | 7,06 | 10,07 | 7,68 | 7,62 | 8,38 | 7,95 | 7,47 |
| | $K_2O$ | 0,17 | 11,93 | 0,13 | 16,73 | 16,35 | 0,25 | 0,21 | 0,18 | 0,19 | 0,17 | 0,22 | 0,21 | 0,21 | 0,34 | 0,31 | 0,17 | 0,26 | 0,20 | 0,20 |
| | $SO_3$ | 0,01 | 0,001 | 0,002 | 0,01 | 0,02 | 0,01 | 0,00 | 0,00 | 0,004 | 0,01 | 0,01 | 0,01 | 0,00 | 0,02 | 0,01 | 0,01 | 0,01 | 0,01 | 0,02 |
| | *Total* | *98,41* | *98,37* | *98,13* | *99,06* | *101,11* | *99,25* | *98,06* | *98,10* | *98,51* | *99,01* | *98,25* | *96,98* | *98,64* | *98,59* | *98,50* | *98,47* | *98,96* | *99,04* | *98,10* |
| | ***Formula*** | | | | | | | | | | | | | | | | | | | |
| | Si | 10,33 | 11,66 | 10,18 | 11,69 | 11,82 | 10,53 | 10,13 | 10,01 | 10,02 | 10,03 | 10,35 | 9,92 | 10,03 | 10,95 | 10,18 | 10,18 | 10,43 | 10,26 | 10,20 |
| | Al | 5,74 | 4,28 | 5,93 | 4,28 | 4,19 | 5,49 | 5,92 | 6,05 | 6,07 | 6,05 | 5,71 | 6,17 | 6,07 | 5,02 | 5,92 | 5,90 | 5,65 | 5,81 | 5,91 |
| | Ti | 0,00 | 0,00 | 0,00 | 0,00 | 0,00 | 0,00 | 0,00 | 0,00 | 0,00 | 0,00 | 0,00 | 0,00 | 0,00 | 0,00 | 0,00 | 0,00 | 0,00 | 0,00 | 0,00 |
| | Fe | 0,03 | 0,01 | 0,03 | 0,02 | 0,00 | 0,02 | 0,02 | 0,03 | 0,03 | 0,03 | 0,03 | 0,04 | 0,03 | 0,03 | 0,03 | 0,03 | 0,02 | 0,03 | 0,03 |
| | Mn | 0,00 | 0,00 | 0,00 | 0,00 | 0,00 | 0,00 | 0,00 | 0,00 | 0,00 | 0,00 | 0,00 | 0,00 | 0,00 | 0,00 | 0,00 | 0,00 | 0,00 | 0,00 | 0,00 |
| | Mg | 0,00 | 0,00 | 0,00 | 0,00 | 0,00 | 0,00 | 0,00 | 0,00 | 0,00 | 0,00 | 0,00 | 0,00 | 0,00 | 0,00 | 0,00 | 0,00 | 0,00 | 0,00 | 0,00 |
| | Ca | 1,26 | 0,04 | 1,34 | 0,00 | 0,00 | 1,14 | 1,53 | 1,60 | 1,57 | 1,54 | 1,29 | 1,70 | 1,52 | 0,73 | 1,33 | 1,40 | 1,15 | 1,31 | 1,37 |
| | Na | 2,85 | 1,62 | 2,71 | 0,34 | 0,32 | 3,03 | 2,57 | 2,50 | 2,45 | 2,56 | 2,77 | 2,33 | 2,49 | 3,53 | 2,71 | 2,69 | 2,94 | 2,79 | 2,65 |
| | K | 0,04 | 2,85 | 0,03 | 4,02 | 3,83 | 0,06 | 0,05 | 0,04 | 0,05 | 0,04 | 0,05 | 0,05 | 0,05 | 0,08 | 0,07 | 0,04 | 0,06 | 0,05 | 0,05 |
| | *Total* | *20,25* | *20,44* | *20,22* | *20,35* | *20,16* | *20,27* | *20,22* | *20,24* | *20,19* | *20,25* | *20,20* | *20,19* | *20,20* | *20,34* | *20,25* | *20,24* | *20,25* | *20,25* | *20,20* |
| | ***End Members*** | | | | | | | | | | | | | | | | | | | |
| | Or | 0,94 | 63,24 | 0,74 | 92,10 | 92,25 | 1,34 | 1,20 | 1,02 | 1,11 | 0,96 | 1,25 | 1,20 | 1,19 | 1,78 | 1,74 | 0,96 | 1,47 | 1,12 | 1,16 |
| | Ab | 68,70 | 35,93 | 66,45 | 7,81 | 7,69 | 71,68 | 61,93 | 60,36 | 60,18 | 61,85 | 67,42 | 57,12 | 61,34 | 81,45 | 65,99 | 65,19 | 70,80 | 67,26 | 65,18 |
| | An | 30,36 | 0,83 | 32,82 | 0,10 | 0,06 | 26,98 | 36,87 | 38,62 | 38,71 | 37,19 | 31,33 | 41,68 | 37,47 | 16,77 | 32,27 | 33,85 | 27,74 | 31,62 | 33,66 |
| | *Total* | *100* | *100* | *100* | *100* | *100* | *100* | *100* | *100* | *100* | *100* | *100* | *100* | *100* | *100* | *100* | *100* | *100* | *100* | *100* |

Table D.5 EPMA results of feldspar minerals from Edremit field (cont'd)

| | **Sample No.** | **EDR-964** | | | **EDR-994** | | | | | | | | | | | | | | **EDR-1008** | | |
|---|---|---|---|---|---|---|---|---|---|---|---|---|---|---|---|---|---|---|---|---|---|
| Feldspar | Region/Mineral | 2/5 | | | 1/1 | | | | 2/1 | | | | | | | 2/2 | | | 3/1 | | 3/2 |
| | Spot No. | 1 | 2 | 3 | 1 | 2 | 3 | 4 | 1 | 2 | 3 | 4 | 5 | 6 | 7 | 2 | 3 | 4 | 2 | 3 | 5 |
| | $SiO_2$ | 62,71 | 62,60 | 62,38 | 57,15 | 56,62 | 56,97 | 56,99 | 55,86 | 55,86 | 55,10 | 56,16 | 55,44 | 55,86 | 55,76 | 58,79 | 55,69 | 56,24 | 54,98 | 58,07 | 54,74 |
| | $TiO_2$ | 0,00 | 0,00 | 0,00 | 0,00 | 0,00 | 0,01 | 0,00 | 0,00 | 0,00 | 0,01 | 0,01 | 0,02 | 0,00 | 0,02 | 0,00 | 0,02 | 0,00 | 0,00 | 0,00 | 0,00 |
| | $Al_2O_3$ | 19,34 | 19,19 | 19,27 | 27,15 | 26,97 | 27,71 | 27,69 | 27,47 | 27,60 | 28,03 | 27,85 | 27,60 | 27,88 | 27,83 | 25,47 | 28,06 | 27,02 | 28,23 | 26,66 | 28,31 |
| | FeO | 0,11 | 0,11 | 0,06 | 0,21 | 0,21 | 0,14 | 0,16 | 0,17 | 0,22 | 0,24 | 0,25 | 0,26 | 0,25 | 0,25 | 0,08 | 0,20 | 0,19 | 0,25 | 0,16 | 0,25 |
| | MnO | 0,00 | 0,00 | 0,00 | 0,00 | 0,00 | 0,00 | 0,00 | 0,00 | 0,00 | 0,00 | 0,00 | 0,00 | 0,00 | 0,00 | 0,00 | 0,00 | 0,00 | 0,00 | 0,00 | 0,00 |
| | MgO | 0,00 | 0,00 | 0,01 | 0,01 | 0,00 | 0,00 | 0,01 | 0,00 | 0,01 | 0,00 | 0,01 | 0,01 | 0,02 | 0,03 | 0,00 | 0,03 | 0,00 | 0,01 | 0,00 | 0,00 |
| | CaO | 0,06 | 0,05 | 0,03 | 7,53 | 7,67 | 7,72 | 7,55 | 7,87 | 7,85 | 8,19 | 7,69 | 7,78 | 7,58 | 7,78 | 5,55 | 7,80 | 7,15 | 7,91 | 6,50 | 7,88 |
| | $Na_2O$ | 1,11 | 1,51 | 1,39 | 7,57 | 7,48 | 7,41 | 7,40 | 7,35 | 7,22 | 6,80 | 7,11 | 7,04 | 7,09 | 7,15 | 8,52 | 7,01 | 7,39 | 6,87 | 8,22 | 6,88 |
| | $K_2O$ | 15,97 | 15,48 | 15,62 | 0,22 | 0,22 | 0,18 | 0,16 | 0,20 | 0,25 | 0,22 | 0,30 | 0,29 | 0,28 | 0,24 | 0,19 | 0,17 | 0,22 | 0,18 | 0,21 | 0,21 |
| | $SO_3$ | 0,001 | 0,00 | 0,02 | 0,01 | 0,00 | 0,003 | 0,01 | 0,02 | 0,02 | 0,01 | 0,00 | 0,001 | 0,01 | 0,001 | 0,002 | 0,01 | 0,00 | 0,02 | 0,01 | 0,01 |
| | *Total* | *99,30* | *98,94* | *98,76* | *99,85* | *99,16* | *100,13* | *99,97* | *98,93* | *99,03* | *98,60* | *99,37* | *98,43* | *98,95* | *99,07* | *98,59* | *98,99* | *98,21* | *98,45* | *99,83* | *98,28* |
| | ***Formula*** | | | | | | | | | | | | | | | | | | | | |
| | Si | 11,73 | 11,74 | 11,73 | 10,27 | 10,25 | 10,21 | 10,22 | 10,15 | 10,14 | 10,05 | 10,15 | 10,12 | 10,13 | 10,11 | 10,63 | 10,10 | 10,26 | 10,03 | 10,41 | 10,01 |
| | Al | 4,27 | 4,24 | 4,27 | 5,75 | 5,76 | 5,85 | 5,85 | 5,88 | 5,90 | 6,02 | 5,93 | 5,94 | 5,96 | 5,95 | 5,43 | 6,00 | 5,81 | 6,07 | 5,63 | 6,10 |
| | Ti | 0,00 | 0,00 | 0,00 | 0,00 | 0,00 | 0,00 | 0,00 | 0,00 | 0,00 | 0,00 | 0,00 | 0,00 | 0,00 | 0,00 | 0,00 | 0,00 | 0,00 | 0,00 | 0,00 | 0,00 |
| | Fe | 0,02 | 0,02 | 0,01 | 0,03 | 0,03 | 0,02 | 0,02 | 0,03 | 0,03 | 0,04 | 0,04 | 0,04 | 0,04 | 0,04 | 0,01 | 0,03 | 0,03 | 0,04 | 0,02 | 0,04 |
| | Mn | 0,00 | 0,00 | 0,00 | 0,00 | 0,00 | 0,00 | 0,00 | 0,00 | 0,00 | 0,00 | 0,00 | 0,00 | 0,00 | 0,00 | 0,00 | 0,00 | 0,00 | 0,00 | 0,00 | 0,00 |
| | Mg | 0,00 | 0,00 | 0,00 | 0,00 | 0,00 | 0,00 | 0,00 | 0,00 | 0,00 | 0,00 | 0,00 | 0,00 | 0,01 | 0,01 | 0,00 | 0,01 | 0,00 | 0,00 | 0,00 | 0,00 |
| | Ca | 0,01 | 0,01 | 0,01 | 1,45 | 1,49 | 1,48 | 1,45 | 1,53 | 1,53 | 1,60 | 1,49 | 1,52 | 1,47 | 1,51 | 1,07 | 1,52 | 1,40 | 1,55 | 1,25 | 1,54 |
| | Na | 0,40 | 0,55 | 0,50 | 2,64 | 2,62 | 2,57 | 2,57 | 2,59 | 2,54 | 2,40 | 2,49 | 2,49 | 2,49 | 2,52 | 2,99 | 2,46 | 2,61 | 2,43 | 2,86 | 2,44 |
| | K | 3,81 | 3,70 | 3,75 | 0,05 | 0,05 | 0,04 | 0,04 | 0,05 | 0,06 | 0,05 | 0,07 | 0,07 | 0,06 | 0,06 | 0,04 | 0,04 | 0,05 | 0,04 | 0,05 | 0,05 |
| | *Total* | *20,24* | *20,26* | *20,26* | *20,20* | *20,21* | *20,18* | *20,16* | *20,23* | *20,21* | *20,17* | *20,17* | *20,19* | *20,17* | *20,19* | *20,17* | *20,15* | *20,17* | *20,17* | *20,22* | *20,18* |
| | ***End Members*** | | | | | | | | | | | | | | | | | | | | |
| | Or | 90,18 | 86,84 | 88,01 | 1,23 | 1,22 | 0,99 | 0,92 | 1,09 | 1,39 | 1,28 | 1,73 | 1,66 | 1,58 | 1,37 | 1,04 | 0,99 | 1,25 | 1,02 | 1,13 | 1,21 |
| | Ab | 9,53 | 12,91 | 11,86 | 63,74 | 63,04 | 62,84 | 63,33 | 62,14 | 61,59 | 59,27 | 61,53 | 61,04 | 61,88 | 61,59 | 72,78 | 61,29 | 64,35 | 60,50 | 68,80 | 60,52 |
| | An | 0,29 | 0,25 | 0,12 | 35,03 | 35,74 | 36,17 | 35,75 | 36,77 | 37,02 | 39,45 | 36,74 | 37,30 | 36,54 | 37,03 | 26,18 | 37,72 | 34,40 | 38,48 | 30,07 | 38,27 |
| | *Total* | *100* | *100* | *100* | *100* | *100* | *100* | *100* | *100* | *100* | *100* | *100* | *100* | *100* | *100* | *100* | *100* | *100* | *100* | *100* | *100* |

Table D.5 EPMA results of feldspar minerals from Edremit field (cont'd)

| | **Sample No.** | **EDR-1032** | | | | | | | | | | | | | | |
|---|---|---|---|---|---|---|---|---|---|---|---|---|---|---|---|---|
| Feldspar | Region/Mineral | 1/1 | | | | 2/1 | | | | 2/2 | | | | | 2/3 | |
| | Spot No. | 1 | 2 | 3 | 4 | 1 | 2 | 3 | 4 | 1 | 2 | 3 | 4 | 5 | 1 | 4 |
| | $SiO_2$ | 57,08 | 57,80 | 56,48 | 57,18 | 62,53 | 55,95 | 55,28 | 63,09 | 55,66 | 55,53 | 57,60 | 54,75 | 56,17 | 54,78 | 58,61 |
| | $TiO_2$ | 0,01 | 0,00 | 0,00 | 0,01 | 0,00 | 0,01 | 0,00 | 0,00 | 0,01 | 0,00 | 0,00 | 0,00 | 0,00 | 0,01 | 0,00 |
| | $Al_2O_3$ | 26,70 | 26,18 | 26,46 | 28,50 | 19,26 | 27,40 | 27,63 | 19,32 | 27,12 | 27,89 | 26,66 | 28,63 | 28,15 | 28,03 | 26,15 |
| | FeO | 0,25 | 0,25 | 0,23 | 0,23 | 0,07 | 0,20 | 0,21 | 0,10 | 0,19 | 0,14 | 0,19 | 0,24 | 0,17 | 0,25 | 0,10 |
| | MnO | 0,00 | 0,00 | 0,00 | 0,00 | 0,00 | 0,00 | 0,00 | 0,00 | 0,00 | 0,00 | 0,00 | 0,00 | 0,00 | 0,00 | 0,00 |
| | MgO | 0,01 | 0,02 | 0,01 | 0,05 | 0,00 | 0,00 | 0,00 | 0,00 | 0,00 | 0,02 | 0,01 | 0,01 | 0,01 | 0,01 | 0,00 |
| | CaO | 6,91 | 6,45 | 6,83 | 7,43 | 0,05 | 7,33 | 7,46 | 0,07 | 7,52 | 7,92 | 6,48 | 8,25 | 7,46 | 7,83 | 5,70 |
| | $Na_2O$ | 7,90 | 8,02 | 7,75 | 7,45 | 1,34 | 7,50 | 7,22 | 1,61 | 7,36 | 7,17 | 8,09 | 6,61 | 7,47 | 6,92 | 8,53 |
| | $K_2O$ | 0,27 | 0,22 | 0,26 | 0,21 | 15,82 | 0,19 | 0,21 | 15,37 | 0,26 | 0,22 | 0,26 | 0,24 | 0,21 | 0,21 | 0,15 |
| | $SO_3$ | 0,01 | 0,00 | 0,00 | 0,02 | 0,00 | 0,00 | 0,01 | 0,02 | 0,00 | 0,03 | 0,01 | 0,01 | 0,02 | 0,01 | 0,02 |
| | *Total* | *99,15* | *98,93* | *98,01* | *101,09* | *99,06* | *98,58* | *98,01* | *99,57* | *98,12* | *98,90* | *99,29* | *98,73* | *99,66* | *98,04* | *99,25* |
| | ***Formula*** | | | | | | | | | | | | | | | |
| | Si | 10,33 | 10,45 | 10,33 | 10,14 | 11,73 | 10,19 | 10,12 | 11,75 | 10,19 | 10,09 | 10,39 | 9,97 | 10,12 | 10,04 | 10,54 |
| | Al | 5,69 | 5,58 | 5,70 | 5,96 | 4,26 | 5,88 | 5,97 | 4,24 | 5,85 | 5,97 | 5,67 | 6,14 | 5,98 | 6,05 | 5,54 |
| | Ti | 0,00 | 0,00 | 0,00 | 0,00 | 0,00 | 0,00 | 0,00 | 0,00 | 0,00 | 0,00 | 0,00 | 0,00 | 0,00 | 0,00 | 0,00 |
| | Fe | 0,04 | 0,04 | 0,04 | 0,03 | 0,01 | 0,03 | 0,03 | 0,01 | 0,03 | 0,02 | 0,03 | 0,04 | 0,03 | 0,04 | 0,01 |
| | Mn | 0,00 | 0,00 | 0,00 | 0,00 | 0,00 | 0,00 | 0,00 | 0,00 | 0,00 | 0,00 | 0,00 | 0,00 | 0,00 | 0,00 | 0,00 |
| | Mg | 0,00 | 0,01 | 0,00 | 0,01 | 0,00 | 0,00 | 0,00 | 0,00 | 0,00 | 0,00 | 0,00 | 0,00 | 0,00 | 0,00 | 0,00 |
| | Ca | 1,34 | 1,25 | 1,34 | 1,41 | 0,01 | 1,43 | 1,46 | 0,01 | 1,48 | 1,54 | 1,25 | 1,61 | 1,44 | 1,54 | 1,10 |
| | Na | 2,77 | 2,81 | 2,75 | 2,56 | 0,49 | 2,65 | 2,56 | 0,58 | 2,61 | 2,53 | 2,83 | 2,34 | 2,61 | 2,46 | 2,97 |
| | K | 0,06 | 0,05 | 0,06 | 0,05 | 3,78 | 0,04 | 0,05 | 3,65 | 0,06 | 0,05 | 0,06 | 0,06 | 0,05 | 0,05 | 0,03 |
| | *Total* | *20,24* | *20,19* | *20,22* | *20,18* | *20,28* | *20,22* | *20,20* | *20,25* | *20,22* | *20,21* | *20,22* | *20,15* | *20,22* | *20,18* | *20,20* |
| | ***End Members*** | | | | | | | | | | | | | | | |
| | Or | 1,51 | 1,23 | 1,46 | 1,20 | 88,38 | 1,06 | 1,18 | 85,99 | 1,47 | 1,23 | 1,44 | 1,40 | 1,17 | 1,20 | 0,84 |
| | Ab | 66,40 | 68,38 | 66,27 | 63,69 | 11,38 | 64,24 | 62,88 | 13,69 | 62,97 | 61,32 | 68,33 | 58,36 | 63,69 | 60,76 | 72,40 |
| | An | 32,08 | 30,39 | 32,27 | 35,11 | 0,23 | 34,69 | 35,94 | 0,32 | 35,56 | 37,44 | 30,24 | 40,23 | 35,15 | 38,04 | 26,76 |
| | *Total* | *100* | *100* | *100* | *100* | *100* | *100* | *100* | *100* | *100* | *100* | *100* | *100* | *100* | *100* | *100* |

# Table D.6 EPMA results of amphibole minerals from Edremit field

| Amphibole | **Sample No.** | **EDR-912** | | | | **EDR-958** | | | **EDR-964** | | | | | | | | | | | |
|---|---|---|---|---|---|---|---|---|---|---|---|---|---|---|---|---|---|---|---|---|
| | Region/Mineral | 2/1 | | | | 1/1 | | | 1/1 | | | | | | 1/3 | | | | | |
| | Spot No. | 1 | 2 | 3 | 5 | 1 | 3 | 4 | 1 | 2 | 3 | 4 | 5 | 6 | 1 | 2 | 3 | 4 | 5 | 6 |
| | $SiO_2$ | 46,25 | 46,65 | 46,38 | 55,13 | 58,13 | 54,53 | 55,52 | 45,21 | 46,37 | 45,14 | 45,57 | 45,31 | 47,92 | 46,96 | 45,96 | 44,75 | 42,43 | 42,50 | 44,50 |
| | $TiO_2$ | 1,60 | 1,54 | 1,64 | 0,03 | 0,00 | 0,00 | 0,004 | 1,41 | 1,07 | 1,37 | 1,31 | 1,29 | 1,07 | 1,05 | 1,20 | 1,72 | 2,50 | 2,39 | 1,94 |
| | $Al_2O_3$ | 6,89 | 6,74 | 6,90 | 25,81 | 24,87 | 27,13 | 27,12 | 6,31 | 5,89 | 6,31 | 6,15 | 6,21 | 5,52 | 5,20 | 6,01 | 7,01 | 9,16 | 8,75 | 7,79 |
| | $Cr_2O_3$ | 0,01 | 0,01 | 0,00 | 0,01 | 0,02 | 0,00 | 0,00 | 0,00 | 0,007 | 0,00 | 0,00 | 0,006 | 0,00 | 0,00 | 0,006 | 0,00 | 0,003 | 0,002 | 0,00 |
| | FeO | 14,83 | 14,68 | 14,49 | 1,86 | 0,11 | 0,20 | 0,21 | 17,06 | 16,00 | 16,99 | 17,01 | 16,92 | 15,86 | 16,25 | 15,98 | 15,45 | 16,77 | 16,67 | 16,33 |
| | MnO | 0,00 | 0,00 | 0,00 | 0,00 | 0,00 | 0,00 | 0,00 | 0,00 | 0,00 | 0,00 | 0,00 | 0,00 | 0,00 | 0,00 | 0,00 | 0,00 | 0,00 | 0,00 | 0,00 |
| | MgO | 14,04 | 14,54 | 14,38 | 0,24 | 0,01 | 0,00 | 0,00 | 12,76 | 13,24 | 12,64 | 12,65 | 12,85 | 13,81 | 13,49 | 13,47 | 13,30 | 11,89 | 11,86 | 12,75 |
| | CaO | 11,04 | 10,91 | 11,18 | 6,73 | 6,12 | 8,83 | 8,56 | 11,39 | 11,75 | 11,37 | 11,38 | 11,39 | 11,37 | 11,59 | 11,32 | 11,18 | 11,27 | 11,47 | 11,34 |
| | $Na_2O$ | 1,47 | 1,49 | 1,47 | 7,58 | 8,74 | 7,17 | 7,30 | 1,22 | 0,84 | 1,22 | 1,14 | 1,23 | 1,07 | 1,01 | 1,28 | 1,58 | 1,80 | 1,63 | 1,60 |
| | $K_2O$ | 0,69 | 0,73 | 0,72 | 0,39 | 0,48 | 0,23 | 0,26 | 0,66 | 0,57 | 0,68 | 0,60 | 0,68 | 0,48 | 0,55 | 0,65 | 0,68 | 0,95 | 0,94 | 0,80 |
| | *Total* | *96,81* | *97,29* | *97,15* | *97,77* | *98,47* | *98,09* | *98,96* | *96,03* | *95,73* | *95,71* | *95,81* | *95,88* | *97,09* | *96,10* | *95,88* | *95,66* | *96,76* | *96,21* | *97,05* |
| | O | 23,00 | 23,00 | 23,00 | 23,00 | 23,00 | 23,00 | 23,00 | 23,00 | 23,00 | 23,00 | 23,00 | 23,00 | 23,00 | 23,00 | 23,00 | 23,00 | 23,00 | 23,00 | 23,00 |
| | Cation | 15,00 | 15,00 | 15,00 | 15,00 | 15,00 | 15,00 | 15,00 | 15,00 | 15,00 | 15,00 | 15,00 | 15,00 | 15,00 | 15,00 | 15,00 | 15,00 | 15,00 | 15,00 | 15,00 |
| | ***Formula*** | | | | | | | | | | | | | | | | | | | |
| | Si | 6,85 | 6,87 | 6,84 | 7,77 | 8,12 | 7,70 | 7,75 | 6,85 | 6,96 | 6,86 | 6,90 | 6,87 | 7,07 | 7,06 | 6,93 | 6,77 | 6,41 | 6,45 | 6,66 |
| | Ti | 0,18 | 0,17 | 0,18 | 0,003 | 0,00 | 0,00 | 0,00 | 0,16 | 0,12 | 0,16 | 0,15 | 0,15 | 0,12 | 0,12 | 0,14 | 0,20 | 0,28 | 0,27 | 0,22 |
| | Al-iv | 1,15 | 1,13 | 1,16 | 0,23 | 0,00 | 0,30 | 0,25 | 1,15 | 1,04 | 1,14 | 1,10 | 1,13 | 0,93 | 0,94 | 1,07 | 1,23 | 1,59 | 1,55 | 1,34 |
| | Al-vi | 0,05 | 0,04 | 0,04 | 4,05 | 4,09 | 4,21 | 4,22 | -0,02 | 0,00 | -0,01 | 0,00 | -0,02 | 0,03 | -0,02 | 0,00 | 0,02 | 0,04 | 0,02 | 0,03 |
| | Cr | 0,001 | 0,001 | 0,00 | 0,001 | 0,002 | 0,00 | 0,00 | 0,00 | 0,001 | 0,00 | 0,00 | 0,001 | 0,00 | 0,00 | 0,001 | 0,00 | 0,00 | 0,00 | 0,00 |
| | $Fe^{3+}$ | 0,37 | 0,33 | 0,35 | -2,66 | -3,09 | -3,06 | -3,04 | 0,28 | 0,45 | 0,31 | 0,35 | 0,29 | 0,38 | 0,25 | 0,29 | 0,29 | 0,41 | 0,40 | 0,37 |
| | $Fe^{2+}$ | 1,46 | 1,48 | 1,44 | 2,87 | 3,10 | 3,08 | 3,06 | 1,88 | 1,56 | 1,85 | 1,81 | 1,86 | 1,58 | 1,79 | 1,72 | 1,66 | 1,70 | 1,72 | 1,67 |
| | Mn | 0,00 | 0,00 | 0,00 | 0,00 | 0,00 | 0,00 | 0,00 | 0,00 | 0,00 | 0,00 | 0,00 | 0,00 | 0,00 | 0,00 | 0,00 | 0,00 | 0,00 | 0,00 | 0,00 |
| | Mg | 3,10 | 3,19 | 3,16 | 0,05 | 0,00 | 0,00 | 0,00 | 2,88 | 2,96 | 2,86 | 2,86 | 2,91 | 3,04 | 3,02 | 3,03 | 3,00 | 2,68 | 2,68 | 2,84 |
| | Ca | 1,75 | 1,72 | 1,77 | 1,02 | 0,92 | 1,34 | 1,28 | 1,85 | 1,89 | 1,85 | 1,85 | 1,85 | 1,80 | 1,87 | 1,83 | 1,81 | 1,82 | 1,87 | 1,82 |
| | Na | 0,42 | 0,43 | 0,42 | 2,07 | 2,37 | 1,96 | 1,98 | 0,36 | 0,24 | 0,36 | 0,33 | 0,36 | 0,31 | 0,29 | 0,37 | 0,46 | 0,53 | 0,48 | 0,46 |
| | K | 0,13 | 0,14 | 0,14 | 0,07 | 0,09 | 0,04 | 0,05 | 0,13 | 0,11 | 0,13 | 0,12 | 0,13 | 0,09 | 0,10 | 0,12 | 0,13 | 0,18 | 0,18 | 0,15 |
| | *Total* | *15,46* | *15,49* | *15,49* | *15,48* | *15,60* | *15,58* | *15,54* | *15,52* | *15,34* | *15,51* | *15,45* | *15,53* | *15,34* | *15,43* | *15,50* | *15,57* | *15,64* | *15,62* | *15,56* |
| | CaB | 1,75 | 1,72 | 1,77 | 1,02 | 0,92 | 1,34 | 1,28 | 1,85 | 1,89 | 1,85 | 1,85 | 1,85 | 1,80 | 1,87 | 1,83 | 1,81 | 1,82 | 1,87 | 1,82 |
| | NaB | 0,09 | 0,07 | 0,07 | 0,98 | 1,08 | 0,66 | 0,72 | -0,04 | 0,01 | -0,02 | 0,00 | -0,03 | 0,06 | -0,03 | 0,00 | 0,03 | 0,07 | 0,04 | 0,05 |
| | NaA | 0,33 | 0,35 | 0,35 | 1,09 | 1,28 | 1,30 | 1,26 | 0,40 | 0,24 | 0,38 | 0,34 | 0,40 | 0,25 | 0,33 | 0,38 | 0,43 | 0,46 | 0,44 | 0,41 |
| | KA | 0,13 | 0,14 | 0,14 | 0,07 | 0,09 | 0,04 | 0,05 | 0,13 | 0,11 | 0,13 | 0,12 | 0,13 | 0,09 | 0,10 | 0,12 | 0,13 | 0,18 | 0,18 | 0,15 |

Table D.6 EPMA results of amphibole minerals from Edremit field (cont'd)

| | **Sample No.** | **EDR-964** | | | | | **EDR-994** | | **EDR-1008** | | | | | | | | |
|---|---|---|---|---|---|---|---|---|---|---|---|---|---|---|---|---|---|
| Amphibole | Region/Mineral | 2/1 | | | | | 2/1 | | 1/1 | | | | | | | | |
| | Spot No. | 1 | 2 | 3 | 4 | 5 | 2 | 3 | 1 | 2 | 3 | 4 | 5 | 6 | 7 | 8 | 9 |
| | $SiO_2$ | 45,04 | 45,63 | 48,99 | 47,83 | 49,76 | 46,19 | 46,92 | 44,23 | 45,31 | 46,23 | 44,68 | 48,90 | 49,50 | 47,04 | 46,11 | 45,80 |
| | $TiO_2$ | 1,52 | 1,49 | 0,57 | 0,42 | 0,46 | 1,54 | 1,60 | 1,45 | 1,54 | 1,63 | 1,52 | 0,60 | 0,59 | 1,04 | 1,21 | 1,50 |
| | $Al_2O_3$ | 6,75 | 6,71 | 4,62 | 4,53 | 4,93 | 6,71 | 7,05 | 6,63 | 6,82 | 7,19 | 6,85 | 4,54 | 4,16 | 5,26 | 6,28 | 6,64 |
| | $Cr_2O_3$ | 0,006 | 0,002 | 0,007 | 0,00 | 0,00 | 0,003 | 0,00 | 0,005 | 0,00 | 0,009 | 0,007 | 0,00 | 0,00 | 0,00 | 0,003 | 0,00 |
| | FeO | 16,83 | 16,61 | 15,10 | 15,60 | 15,10 | 16,49 | 16,54 | 16,18 | 15,29 | 15,07 | 16,12 | 14,24 | 14,04 | 15,35 | 15,76 | 14,97 |
| | MnO | 0,00 | 0,00 | 0,00 | 0,00 | 0,00 | 0,00 | 0,00 | 0,00 | 0,00 | 0,00 | 0,00 | 0,00 | 0,00 | 0,00 | 0,00 | 0,00 |
| | MgO | 12,53 | 12,94 | 14,10 | 13,92 | 14,74 | 13,16 | 13,32 | 12,82 | 13,78 | 14,12 | 12,63 | 14,87 | 14,97 | 13,96 | 13,61 | 14,02 |
| | CaO | 11,57 | 11,41 | 11,82 | 11,99 | 11,88 | 11,17 | 11,22 | 11,01 | 11,03 | 11,05 | 11,06 | 11,68 | 11,69 | 11,25 | 11,40 | 10,99 |
| | $Na_2O$ | 1,13 | 1,21 | 0,78 | 0,74 | 0,88 | 1,39 | 1,58 | 1,25 | 1,44 | 1,58 | 1,40 | 0,70 | 0,73 | 1,14 | 1,20 | 1,47 |
| | $K_2O$ | 0,69 | 0,65 | 0,31 | 0,32 | 0,33 | 0,63 | 0,64 | 0,66 | 0,64 | 0,70 | 0,67 | 0,31 | 0,33 | 0,47 | 0,63 | 0,67 |
| | *Total* | *96,06* | *96,65* | *96,30* | *95,34* | *98,07* | *97,29* | *98,86* | *94,22* | *95,85* | *97,57* | *94,93* | *95,84* | *96,00* | *95,50* | *96,21* | *96,05* |
| | O | 23,00 | 23,00 | 23,00 | 23,00 | 23,00 | 23,00 | 23,00 | 23,00 | 23,00 | 23,00 | 23,00 | 23,00 | 23,00 | 23,00 | 23,00 | 23,00 |
| | Cation | 15,00 | 15,00 | 15,00 | 15,00 | 15,00 | 15,00 | 15,00 | 15,00 | 15,00 | 15,00 | 15,00 | 15,00 | 15,00 | 15,00 | 15,00 | 15,00 |
| | ***Formula*** | | | | | | | | | | | | | | | | |
| | Si | 6,80 | 6,83 | 7,23 | 7,18 | 7,20 | 6,86 | 6,84 | 6,80 | 6,81 | 6,80 | 6,81 | 7,23 | 7,30 | 7,07 | 6,90 | 6,85 |
| | Ti | 0,17 | 0,17 | 0,06 | 0,05 | 0,05 | 0,17 | 0,18 | 0,17 | 0,17 | 0,18 | 0,17 | 0,07 | 0,07 | 0,12 | 0,14 | 0,17 |
| | Al-iv | 1,20 | 1,17 | 0,77 | 0,82 | 0,80 | 1,14 | 1,16 | 1,20 | 1,19 | 1,20 | 1,19 | 0,77 | 0,70 | 0,93 | 1,10 | 1,15 |
| | Al-vi | 0,00 | 0,01 | 0,03 | -0,02 | 0,04 | 0,03 | 0,06 | 0,00 | 0,01 | 0,04 | 0,03 | 0,02 | 0,02 | 0,00 | 0,01 | 0,02 |
| | Cr | 0,001 | 0,00 | 0,001 | 0,00 | 0,00 | 0,00 | 0,00 | 0,001 | 0,00 | 0,001 | 0,001 | 0,00 | 0,00 | 0,00 | 0,00 | 0,00 |
| | $Fe^{3+}$ | 0,40 | 0,39 | 0,45 | 0,40 | 0,50 | 0,37 | 0,39 | 0,36 | 0,34 | 0,38 | 0,40 | 0,43 | 0,36 | 0,29 | 0,38 | 0,32 |
| | $Fe^{2+}$ | 1,73 | 1,69 | 1,41 | 1,56 | 1,33 | 1,68 | 1,63 | 1,72 | 1,58 | 1,48 | 1,66 | 1,33 | 1,37 | 1,64 | 1,59 | 1,55 |
| | Mn | 0,00 | 0,00 | 0,00 | 0,00 | 0,00 | 0,00 | 0,00 | 0,00 | 0,00 | 0,00 | 0,00 | 0,00 | 0,00 | 0,00 | 0,00 | 0,00 |
| | Mg | 2,82 | 2,89 | 3,10 | 3,12 | 3,18 | 2,91 | 2,90 | 2,94 | 3,09 | 3,10 | 2,87 | 3,28 | 3,29 | 3,13 | 3,04 | 3,13 |
| | Ca | 1,87 | 1,83 | 1,87 | 1,93 | 1,84 | 1,78 | 1,75 | 1,81 | 1,78 | 1,74 | 1,80 | 1,85 | 1,85 | 1,81 | 1,83 | 1,76 |
| | Na | 0,33 | 0,35 | 0,22 | 0,21 | 0,25 | 0,40 | 0,45 | 0,37 | 0,42 | 0,45 | 0,41 | 0,20 | 0,21 | 0,33 | 0,35 | 0,43 |
| | K | 0,13 | 0,12 | 0,06 | 0,06 | 0,06 | 0,12 | 0,12 | 0,13 | 0,12 | 0,13 | 0,13 | 0,06 | 0,06 | 0,09 | 0,12 | 0,13 |
| | *Total* | *15,46* | *15,45* | *15,22* | *15,31* | *15,24* | *15,46* | *15,46* | *15,50* | *15,51* | *15,50* | *15,48* | *15,23* | *15,23* | *15,41* | *15,45* | *15,51* |
| | CaB | 1,87 | 1,83 | 1,87 | 1,93 | 1,84 | 1,78 | 1,75 | 1,81 | 1,78 | 1,74 | 1,80 | 1,85 | 1,85 | 1,81 | 1,83 | 1,76 |
| | NaB | 0,01 | 0,02 | 0,07 | -0,03 | 0,07 | 0,06 | 0,10 | 0,00 | 0,03 | 0,08 | 0,06 | 0,03 | 0,04 | 0,01 | 0,02 | 0,05 |
| | NaA | 0,33 | 0,33 | 0,16 | 0,25 | 0,18 | 0,34 | 0,34 | 0,37 | 0,39 | 0,37 | 0,35 | 0,17 | 0,17 | 0,32 | 0,33 | 0,38 |
| | KA | 0,13 | 0,12 | 0,06 | 0,06 | 0,06 | 0,12 | 0,12 | 0,13 | 0,12 | 0,13 | 0,13 | 0,06 | 0,06 | 0,09 | 0,12 | 0,13 |

Table D.6 EPMA results of amphibole minerals from Edremit field (cont'd)

| Amphibole | **Sample No.** | **EDR-1008** | | | | | | | | | | | | | | | | | | |
|---|---|---|---|---|---|---|---|---|---|---|---|---|---|---|---|---|---|---|---|---|
| | Region/Mineral | 2/1 | | | | | | | | | | 3/1 | | | | | | | | |
| | Spot No. | 1 | 2 | 3 | 4 | 5 | 6 | 7 | 8 | 9 | 10 | 1 | 2 | 3 | 4 | 5 | 6 | 7 | 8 | 9 |
| | $SiO_2$ | 45,59 | 44,62 | 45,06 | 45,58 | 45,12 | 45,01 | 45,25 | 45,73 | 44,72 | 45,12 | 45,99 | 45,63 | 46,04 | 45,65 | 47,71 | 46,00 | 46,10 | 45,33 | 45,54 |
| | $TiO_2$ | 1,63 | 1,66 | 1,65 | 1,60 | 1,60 | 1,62 | 1,48 | 1,29 | 1,55 | 1,63 | 1,36 | 1,49 | 1,55 | 1,42 | 0,86 | 1,50 | 1,57 | 1,66 | 1,65 |
| | $Al_2O_3$ | 6,65 | 6,71 | 6,90 | 6,68 | 6,75 | 6,92 | 6,93 | 6,37 | 6,81 | 6,81 | 6,59 | 6,49 | 6,78 | 6,70 | 5,35 | 6,73 | 6,77 | 7,14 | 7,12 |
| | $Cr_2O_3$ | 0,002 | 0,006 | 0,01 | 0,00 | 0,003 | 0,001 | 0,01 | 0,00 | 0,01 | 0,01 | 0,00 | 0,00 | 0,001 | 0,00 | 0,005 | 0,00 | 0,004 | 0,002 | 0,005 |
| | FeO | 15,09 | 15,24 | 15,37 | 15,05 | 15,18 | 15,27 | 15,99 | 15,87 | 15,66 | 14,93 | 15,99 | 14,78 | 15,09 | 15,34 | 15,03 | 16,23 | 14,67 | 15,20 | 14,94 |
| | MnO | 0,00 | 0,00 | 0,00 | 0,00 | 0,00 | 0,00 | 0,00 | 0,00 | 0,00 | 0,00 | 0,00 | 0,00 | 0,00 | 0,00 | 0,00 | 0,00 | 0,00 | 0,00 | 0,00 |
| | MgO | 13,61 | 13,11 | 13,31 | 13,90 | 13,51 | 13,47 | 13,16 | 13,40 | 13,35 | 13,80 | 13,44 | 13,88 | 13,80 | 13,46 | 14,09 | 13,15 | 14,22 | 13,57 | 13,55 |
| | CaO | 11,11 | 11,17 | 11,12 | 11,01 | 11,04 | 10,94 | 10,97 | 11,14 | 10,88 | 11,14 | 11,35 | 11,17 | 11,19 | 11,46 | 11,63 | 11,40 | 11,26 | 11,23 | 11,12 |
| | $Na_2O$ | 1,56 | 1,58 | 1,49 | 1,50 | 1,54 | 1,58 | 1,57 | 1,39 | 1,48 | 1,54 | 1,39 | 1,42 | 1,40 | 1,22 | 0,99 | 1,12 | 1,46 | 1,50 | 1,44 |
| | $K_2O$ | 0,67 | 0,69 | 0,64 | 0,64 | 0,66 | 0,66 | 0,65 | 0,62 | 0,68 | 0,64 | 0,61 | 0,62 | 0,64 | 0,61 | 0,49 | 0,61 | 0,59 | 0,68 | 0,62 |
| | *Total* | *95,90* | *94,79* | *95,56* | *95,95* | *95,39* | *95,48* | *96,03* | *95,81* | *95,13* | *95,63* | *96,72* | *95,47* | *96,49* | *95,86* | *96,15* | *96,73* | *96,64* | *96,31* | *95,98* |
| | O | 23,00 | 23,00 | 23,00 | 23,00 | 23,00 | 23,00 | 23,00 | 23,00 | 23,00 | 23,00 | 23,00 | 23,00 | 23,00 | 23,00 | 23,00 | 23,00 | 23,00 | 23,00 | 23,00 |
| | Cation | 15,00 | 15,00 | 15,00 | 15,00 | 15,00 | 15,00 | 15,00 | 15,00 | 15,00 | 15,00 | 15,00 | 15,00 | 15,00 | 15,00 | 15,00 | 15,00 | 15,00 | 15,00 | 15,00 |
| | ***Formula*** | | | | | | | | | | | | | | | | | | | |
| | Si | 6,85 | 6,81 | 6,80 | 6,84 | 6,82 | 6,80 | 6,81 | 6,89 | 6,79 | 6,80 | 6,86 | 6,87 | 6,85 | 6,84 | 7,09 | 6,85 | 6,84 | 6,77 | 6,80 |
| | Ti | 0,18 | 0,19 | 0,19 | 0,18 | 0,18 | 0,18 | 0,17 | 0,15 | 0,18 | 0,19 | 0,15 | 0,17 | 0,17 | 0,16 | 0,10 | 0,17 | 0,18 | 0,19 | 0,19 |
| | Al-iv | 1,15 | 1,19 | 1,20 | 1,16 | 1,18 | 1,20 | 1,19 | 1,11 | 1,21 | 1,20 | 1,14 | 1,13 | 1,15 | 1,16 | 0,91 | 1,15 | 1,16 | 1,23 | 1,20 |
| | Al-vi | 0,03 | 0,02 | 0,03 | 0,02 | 0,02 | 0,03 | 0,03 | 0,02 | 0,01 | 0,01 | 0,02 | 0,02 | 0,04 | 0,02 | 0,02 | 0,03 | 0,02 | 0,03 | 0,05 |
| | Cr | 0,00 | 0,001 | 0,001 | 0,00 | 0,00 | 0,00 | 0,002 | 0,00 | 0,001 | 0,002 | 0,00 | 0,00 | 0,00 | 0,00 | 0,001 | 0,00 | 0,00 | 0,00 | 0,001 |
| | $Fe^{3+}$ | 0,27 | 0,26 | 0,34 | 0,29 | 0,30 | 0,32 | 0,37 | 0,34 | 0,32 | 0,28 | 0,37 | 0,31 | 0,38 | 0,43 | 0,40 | 0,45 | 0,34 | 0,37 | 0,43 |
| | $Fe^{2+}$ | 1,62 | 1,69 | 1,60 | 1,59 | 1,62 | 1,60 | 1,64 | 1,66 | 1,67 | 1,60 | 1,63 | 1,55 | 1,50 | 1,49 | 1,46 | 1,57 | 1,48 | 1,53 | 1,43 |
| | Mn | 0,00 | 0,00 | 0,00 | 0,00 | 0,00 | 0,00 | 0,00 | 0,00 | 0,00 | 0,00 | 0,00 | 0,00 | 0,00 | 0,00 | 0,00 | 0,00 | 0,00 | 0,00 | 0,00 |
| | Mg | 3,05 | 2,98 | 2,99 | 3,11 | 3,04 | 3,03 | 2,95 | 3,01 | 3,02 | 3,10 | 2,99 | 3,11 | 3,06 | 3,01 | 3,12 | 2,92 | 3,15 | 3,02 | 3,02 |
| | Ca | 1,79 | 1,83 | 1,80 | 1,77 | 1,79 | 1,77 | 1,77 | 1,80 | 1,77 | 1,80 | 1,81 | 1,80 | 1,78 | 1,84 | 1,85 | 1,82 | 1,79 | 1,80 | 1,78 |
| | Na | 0,45 | 0,47 | 0,44 | 0,44 | 0,45 | 0,46 | 0,46 | 0,40 | 0,44 | 0,45 | 0,40 | 0,41 | 0,40 | 0,35 | 0,29 | 0,32 | 0,42 | 0,44 | 0,42 |
| | K | 0,13 | 0,14 | 0,12 | 0,12 | 0,13 | 0,13 | 0,13 | 0,12 | 0,13 | 0,12 | 0,12 | 0,12 | 0,12 | 0,12 | 0,09 | 0,12 | 0,11 | 0,13 | 0,12 |
| | *Total* | *15,53* | *15,57* | *15,51* | *15,52* | *15,53* | *15,54* | *15,52* | *15,49* | *15,54* | *15,55* | *15,48* | *15,50* | *15,46* | *15,42* | *15,34* | *15,39* | *15,49* | *15,51* | *15,44* |
| | CaB | 1,79 | 1,83 | 1,80 | 1,77 | 1,79 | 1,77 | 1,77 | 1,80 | 1,77 | 1,80 | 1,81 | 1,80 | 1,78 | 1,84 | 1,85 | 1,82 | 1,79 | 1,80 | 1,78 |
| | NaB | 0,05 | 0,03 | 0,05 | 0,03 | 0,04 | 0,05 | 0,06 | 0,03 | 0,02 | 0,02 | 0,03 | 0,04 | 0,07 | 0,05 | 0,04 | 0,05 | 0,04 | 0,06 | 0,10 |
| | NaA | 0,40 | 0,43 | 0,39 | 0,40 | 0,41 | 0,41 | 0,39 | 0,37 | 0,41 | 0,43 | 0,37 | 0,38 | 0,33 | 0,31 | 0,24 | 0,27 | 0,37 | 0,38 | 0,32 |
| | KA | 0,13 | 0,14 | 0,12 | 0,12 | 0,13 | 0,13 | 0,13 | 0,12 | 0,13 | 0,12 | 0,12 | 0,12 | 0,12 | 0,12 | 0,09 | 0,12 | 0,11 | 0,13 | 0,12 |

Table D.6 EPMA results of amphibole minerals from Edremit field (cont'd)

| | **Sample No.** | **EDR-1008** | | | | | **EDR-1032** | | | | | | | | | |
|---|---|---|---|---|---|---|---|---|---|---|---|---|---|---|---|---|
| | Region/Mineral | 3/2 | | | | | 1/1 | | 2/1 | | | | 2/2 | | | |
| | Spot No. | 1 | 2 | 3 | 4 | 5 | 2 | 4 | 1 | 2 | 3 | 4 | 1 | 2 | 3 | 4 |
| Amphibole | $SiO_2$ | 45,65 | 47,62 | 45,11 | 45,33 | 46,18 | 46,83 | 47,19 | 46,73 | 47,48 | 46,09 | 46,89 | 47,82 | 47,28 | 48,20 | 45,66 |
| | $TiO_2$ | 1,43 | 0,99 | 1,54 | 1,54 | 1,38 | 1,57 | 1,57 | 1,55 | 1,50 | 1,57 | 1,57 | 1,18 | 1,35 | 1,13 | 1,58 |
| | $Al_2O_3$ | 6,80 | 5,34 | 6,85 | 6,88 | 6,50 | 6,67 | 6,79 | 6,58 | 6,59 | 6,52 | 6,57 | 5,29 | 6,14 | 4,95 | 6,78 |
| | $Cr_2O_3$ | 0,00 | 0,01 | 0,005 | 0,004 | 0,004 | 0,00 | 0,007 | 0,003 | 0,00 | 0,02 | 0,00 | 0,005 | 0,00 | 0,00 | 0,003 |
| | FeO | 16,83 | 15,85 | 16,41 | 16,26 | 15,82 | 15,98 | 15,31 | 15,98 | 15,38 | 15,16 | 15,17 | 14,39 | 14,97 | 14,70 | 15,60 |
| | MnO | 0,00 | 0,00 | 0,00 | 0,00 | 0,00 | 0,00 | 0,00 | 0,00 | 0,00 | 0,00 | 0,00 | 0,00 | 0,00 | 0,00 | 0,00 |
| | MgO | 12,82 | 13,60 | 12,71 | 12,66 | 13,29 | 13,30 | 13,80 | 13,63 | 14,13 | 13,89 | 14,14 | 14,53 | 14,25 | 14,50 | 13,14 |
| | CaO | 11,29 | 11,63 | 11,28 | 11,23 | 11,03 | 11,52 | 11,33 | 11,22 | 11,12 | 11,24 | 11,13 | 11,42 | 11,28 | 11,31 | 11,18 |
| | $Na_2O$ | 1,30 | 0,91 | 1,31 | 1,24 | 1,42 | 1,32 | 1,39 | 1,49 | 1,64 | 1,49 | 1,59 | 1,06 | 1,31 | 1,15 | 1,50 |
| | $K_2O$ | 0,65 | 0,49 | 0,66 | 0,66 | 0,57 | 0,63 | 0,59 | 0,62 | 0,59 | 0,59 | 0,62 | 0,47 | 0,57 | 0,43 | 0,62 |
| | *Total* | *96,77* | *96,45* | *95,87* | *95,79* | *96,19* | *97,82* | *97,97* | *97,80* | *98,43* | *96,56* | *97,68* | *96,16* | *97,15* | *96,36* | *96,07* |
| | O | 23,00 | 23,00 | 23,00 | 23,00 | 23,00 | 23,00 | 23,00 | 23,00 | 23,00 | 23,00 | 23,00 | 23,00 | 23,00 | 23,00 | 23,00 |
| | Cation | 15,00 | 15,00 | 15,00 | 15,00 | 15,00 | 15,00 | 15,00 | 15,00 | 15,00 | 15,00 | 15,00 | 15,00 | 15,00 | 15,00 | 15,00 |
| | ***Formula*** | | | | | | | | | | | | | | | |
| | Si | 6,83 | 7,08 | 6,81 | 6,82 | 6,90 | 6,89 | 6,89 | 6,89 | 6,92 | 6,87 | 6,90 | 7,09 | 6,97 | 7,15 | 6,85 |
| | Ti | 0,16 | 0,11 | 0,17 | 0,17 | 0,16 | 0,17 | 0,17 | 0,17 | 0,16 | 0,18 | 0,17 | 0,13 | 0,15 | 0,13 | 0,18 |
| | Al-iv | 1,17 | 0,92 | 1,19 | 1,18 | 1,10 | 1,11 | 1,11 | 1,11 | 1,08 | 1,13 | 1,10 | 0,91 | 1,03 | 0,85 | 1,15 |
| | Al-vi | 0,02 | 0,02 | 0,02 | 0,04 | 0,05 | 0,04 | 0,06 | 0,03 | 0,05 | 0,02 | 0,04 | 0,02 | 0,03 | 0,02 | 0,05 |
| | Cr | 0,00 | 0,001 | 0,001 | 0,00 | 0,00 | 0,00 | 0,001 | 0,00 | 0,00 | 0,002 | 0,00 | 0,001 | 0,00 | 0,00 | 0,00 |
| | $Fe^{3+}$ | 0,42 | 0,39 | 0,40 | 0,46 | 0,40 | 0,39 | 0,43 | 0,31 | 0,32 | 0,28 | 0,29 | 0,30 | 0,34 | 0,23 | 0,36 |
| | $Fe^{2+}$ | 1,69 | 1,58 | 1,67 | 1,59 | 1,58 | 1,57 | 1,44 | 1,66 | 1,55 | 1,61 | 1,58 | 1,48 | 1,50 | 1,59 | 1,59 |
| | Mn | 0,00 | 0,00 | 0,00 | 0,00 | 0,00 | 0,00 | 0,00 | 0,00 | 0,00 | 0,00 | 0,00 | 0,00 | 0,00 | 0,00 | 0,00 |
| | Mg | 2,86 | 3,02 | 2,86 | 2,84 | 2,96 | 2,92 | 3,01 | 3,00 | 3,07 | 3,09 | 3,10 | 3,21 | 3,13 | 3,21 | 2,94 |
| | Ca | 1,81 | 1,85 | 1,82 | 1,81 | 1,77 | 1,82 | 1,77 | 1,77 | 1,74 | 1,80 | 1,75 | 1,81 | 1,78 | 1,80 | 1,80 |
| | Na | 0,38 | 0,26 | 0,38 | 0,36 | 0,41 | 0,38 | 0,39 | 0,42 | 0,46 | 0,43 | 0,45 | 0,31 | 0,37 | 0,33 | 0,44 |
| | K | 0,12 | 0,09 | 0,13 | 0,13 | 0,11 | 0,12 | 0,11 | 0,12 | 0,11 | 0,11 | 0,12 | 0,09 | 0,11 | 0,08 | 0,12 |
| | *Total* | *15,46* | *15,32* | *15,46* | *15,40* | *15,43* | *15,41* | *15,39* | *15,48* | *15,47* | *15,51* | *15,50* | *15,36* | *15,42* | *15,38* | *15,47* |
| | CaB | 1,81 | 1,85 | 1,82 | 1,81 | 1,77 | 1,82 | 1,77 | 1,77 | 1,74 | 1,80 | 1,75 | 1,81 | 1,78 | 1,80 | 1,80 |
| | NaB | 0,05 | 0,03 | 0,05 | 0,08 | 0,09 | 0,08 | 0,12 | 0,06 | 0,10 | 0,03 | 0,07 | 0,04 | 0,06 | 0,03 | 0,08 |
| | NaA | 0,33 | 0,23 | 0,34 | 0,28 | 0,32 | 0,29 | 0,28 | 0,37 | 0,36 | 0,40 | 0,38 | 0,27 | 0,31 | 0,30 | 0,35 |
| | KA | 0,12 | 0,09 | 0,13 | 0,13 | 0,11 | 0,12 | 0,11 | 0,12 | 0,11 | 0,11 | 0,12 | 0,09 | 0,11 | 0,08 | 0,12 |

# Table D.7 EPMA results of mica minerals from Edremit field

| Mica | **Sample No.** | **EDR-912** | | | | | | | | | | | | | **EDR-994** | | | | |
|---|---|---|---|---|---|---|---|---|---|---|---|---|---|---|---|---|---|---|---|
| | Region/Mineral | 1/1 | | | 1/2 | | | | | 3/1 | | | | | 1/1 | | | | |
| | Spot No. | 1 | 4 | 5 | 1 | 2 | 3 | 4 | 5 | 1 | 3 | 5 | 6 | 7 | 1 | 2 | 3 | 4 | 5 |
| | $SiO_2$ | 35,38 | 34,52 | 34,47 | 35,97 | 35,07 | 34,33 | 35,96 | 34,77 | 34,90 | 33,66 | 33,20 | 33,93 | 33,18 | 34,44 | 34,42 | 35,43 | 35,31 | 34,62 |
| | $TiO_2$ | 4,70 | 4,69 | 3,74 | 4,20 | 4,43 | 4,50 | 4,54 | 4,59 | 4,76 | 4,19 | 4,73 | 4,57 | 4,57 | 4,62 | 4,65 | 4,50 | 3,62 | 4,02 |
| | $Al_2O_3$ | 15,28 | 14,17 | 14,52 | 14,96 | 14,50 | 13,88 | 14,83 | 14,14 | 13,90 | 13,00 | 13,47 | 13,72 | 13,65 | 13,75 | 13,80 | 14,53 | 14,21 | 13,88 |
| | FeO | 24,56 | 24,94 | 24,12 | 23,44 | 23,35 | 23,24 | 23,08 | 22,99 | 26,91 | 25,66 | 26,83 | 27,82 | 28,25 | 22,87 | 22,63 | 23,24 | 23,21 | 23,27 |
| | MnO | 0,00 | 0,00 | 0,00 | 0,00 | 0,00 | 0,00 | 0,00 | 0,00 | 0,00 | 0,00 | 0,00 | 0,00 | 0,00 | 0,00 | 0,00 | 0,00 | 0,00 | 0,00 |
| | MgO | 9,21 | 8,75 | 9,29 | 10,38 | 10,23 | 9,72 | 10,37 | 9,98 | 8,45 | 9,52 | 7,95 | 7,68 | 7,34 | 10,35 | 10,35 | 10,47 | 10,65 | 10,26 |
| | CaO | 0,14 | 0,06 | 0,09 | 0,02 | 0,04 | 0,06 | 0,02 | 0,02 | 0,09 | 0,14 | 0,07 | 0,08 | 0,08 | 0,09 | 0,08 | 0,09 | 0,12 | 0,13 |
| | $Na_2O$ | 0,24 | 0,18 | 0,22 | 0,20 | 0,16 | 0,17 | 0,12 | 0,11 | 0,15 | 0,09 | 0,13 | 0,14 | 0,13 | 0,17 | 0,21 | 0,20 | 0,21 | 0,23 |
| | $K_2O$ | 8,73 | 9,22 | 8,77 | 9,71 | 9,51 | 9,79 | 9,86 | 9,94 | 9,55 | 8,10 | 9,46 | 9,48 | 9,38 | 9,58 | 9,58 | 9,66 | 9,70 | 9,44 |
| | $Cr_2O_3$ | 0,03 | 0,01 | 0,02 | 0,02 | 0,03 | 0,02 | 0,03 | 0,03 | 0,02 | 0,004 | 0,02 | 0,002 | 0,002 | 0,00 | 0,003 | 0,01 | 0,00 | 0,001 |
| | $SO_3$ | 0,08 | 0,07 | 0,07 | 0,05 | 0,06 | 0,08 | 0,05 | 0,04 | 0,10 | 0,07 | 0,06 | 0,09 | 0,08 | 0,09 | 0,11 | 0,12 | 0,12 | 0,14 |
| | *Total* | *98,34* | *96,60* | *95,32* | *98,95* | *97,37* | *95,79* | *98,85* | *96,60* | *98,82* | *94,42* | *95,92* | *97,51* | *96,65* | *95,96* | *95,83* | *98,24* | *97,16* | *95,99* |
| | ***Formula*** | | | | | | | | | | | | | | | | | | |
| | Si | 5,36 | 5,38 | 5,41 | 5,41 | 5,38 | 5,38 | 5,41 | 5,38 | 5,37 | 5,38 | 5,30 | 5,33 | 5,29 | 5,37 | 5,37 | 5,38 | 5,43 | 5,40 |
| | Al-iv | 2,64 | 2,60 | 2,59 | 2,59 | 2,62 | 2,56 | 2,59 | 2,58 | 2,52 | 2,45 | 2,53 | 2,54 | 2,56 | 2,53 | 2,54 | 2,60 | 2,57 | 2,55 |
| | Al-vi | 0,10 | 0,00 | 0,10 | 0,07 | 0,00 | 0,00 | 0,04 | 0,00 | 0,00 | 0,00 | 0,00 | 0,00 | 0,00 | 0,00 | 0,00 | 0,00 | 0,01 | 0,00 |
| | Ti | 0,54 | 0,55 | 0,44 | 0,48 | 0,51 | 0,53 | 0,51 | 0,53 | 0,55 | 0,50 | 0,57 | 0,54 | 0,55 | 0,54 | 0,55 | 0,51 | 0,42 | 0,47 |
| | Cr | 0,003 | 0,001 | 0,002 | 0,002 | 0,004 | 0,002 | 0,003 | 0,003 | 0,002 | 0,001 | 0,002 | 0,00 | 0,00 | 0,00 | 0,00 | 0,001 | 0,00 | 0,00 |
| | $Fe^{+2}$ | 3,12 | 3,25 | 3,17 | 2,95 | 2,99 | 3,05 | 2,90 | 2,98 | 3,46 | 3,43 | 3,58 | 3,66 | 3,76 | 2,98 | 2,95 | 2,95 | 2,99 | 3,04 |
| | Mn | 0,00 | 0,00 | 0,00 | 0,00 | 0,00 | 0,00 | 0,00 | 0,00 | 0,00 | 0,00 | 0,00 | 0,00 | 0,00 | 0,00 | 0,00 | 0,00 | 0,00 | 0,00 |
| | Mg | 2,08 | 2,03 | 2,17 | 2,33 | 2,34 | 2,27 | 2,33 | 2,30 | 1,94 | 2,27 | 1,89 | 1,80 | 1,74 | 2,41 | 2,41 | 2,37 | 2,44 | 2,39 |
| | Ca | 0,02 | 0,01 | 0,01 | 0,004 | 0,01 | 0,01 | 0,003 | 0,004 | 0,02 | 0,02 | 0,01 | 0,01 | 0,01 | 0,02 | 0,01 | 0,01 | 0,02 | 0,02 |
| | Na | 0,07 | 0,05 | 0,07 | 0,06 | 0,05 | 0,05 | 0,04 | 0,03 | 0,05 | 0,03 | 0,04 | 0,04 | 0,04 | 0,05 | 0,06 | 0,06 | 0,06 | 0,07 |
| | K | 1,69 | 1,83 | 1,75 | 1,86 | 1,86 | 1,96 | 1,89 | 1,96 | 1,87 | 1,65 | 1,93 | 1,90 | 1,91 | 1,91 | 1,91 | 1,87 | 1,90 | 1,88 |
| | *Total* | *15,61* | *15,71* | *15,72* | *15,75* | *15,76* | *15,81* | *15,72* | *15,79* | *15,78* | *15,73* | *15,85* | *15,83* | *15,86* | *15,80* | *15,80* | *15,77* | *15,84* | *15,82* |
| | Fe/Fe+Mg | 0,60 | 0,62 | 0,59 | 0,56 | 0,56 | 0,57 | 0,56 | 0,56 | 0,64 | 0,60 | 0,65 | 0,67 | 0,68 | 0,55 | 0,55 | 0,55 | 0,55 | 0,56 |
| | Fe+Mn+Ti | 3,65 | 3,80 | 3,61 | 3,42 | 3,50 | 3,58 | 3,42 | 3,51 | 4,01 | 3,93 | 4,15 | 4,20 | 4,31 | 3,52 | 3,50 | 3,47 | 3,41 | 3,51 |
| | Mg-Li | 2,08 | 2,03 | 2,17 | 2,33 | 2,34 | 2,27 | 2,33 | 2,30 | 1,94 | 2,27 | 1,89 | 1,80 | 1,74 | 2,41 | 2,41 | 2,37 | 2,44 | 2,39 |

# Table D.7 EPMA results of mica minerals from Edremit field (cont'd)

|  |  |  |  |  |  |  |  |  |  |  |  |  |  |  |  |  |  |  |  |
|---|---|---|---|---|---|---|---|---|---|---|---|---|---|---|---|---|---|---|---|
| Mica | **Sample No.** | **EDR-994** |  |  |  |  |  |  |  |  |  |  |  | **EDR-1008** |  |  |  |  |  |
|  | Region/Mineral | 1/1 |  |  |  | 1/2 |  |  |  |  |  |  | 2/1 | 1/1 |  |  |  |  |  |
|  | Spot No. | 6 | 7 | 8 | 9 | 1 | 2 | 3 | 4 | 5 | 6 | 7 | 2 | 2 | 3 | 4 | 5 | 6 | 7 |
|  | $SiO_2$ | 35,04 | 34,22 | 35,11 | 34,53 | 35,70 | 35,45 | 34,63 | 35,08 | 35,42 | 35,56 | 33,41 | 34,72 | 34,08 | 33,91 | 34,02 | 33,45 | 33,54 | 33,67 |
|  | $TiO_2$ | 4,34 | 4,34 | 4,37 | 4,33 | 3,34 | 3,80 | 4,07 | 4,17 | 4,32 | 4,42 | 4,09 | 4,39 | 4,37 | 4,33 | 4,44 | 4,06 | 3,47 | 4,61 |
|  | $Al_2O_3$ | 14,17 | 13,84 | 14,08 | 13,91 | 14,27 | 14,08 | 13,32 | 13,49 | 13,77 | 13,56 | 12,89 | 13,55 | 13,39 | 13,60 | 13,40 | 13,24 | 13,41 | 13,33 |
|  | FeO | 23,45 | 23,48 | 23,37 | 23,12 | 22,57 | 22,68 | 22,99 | 22,80 | 22,62 | 22,24 | 20,58 | 22,93 | 23,07 | 22,98 | 23,05 | 22,98 | 22,67 | 23,09 |
|  | MnO | 0,00 | 0,00 | 0,00 | 0,00 | 0,00 | 0,00 | 0,00 | 0,00 | 0,00 | 0,00 | 0,00 | 0,00 | 0,00 | 0,00 | 0,00 | 0,00 | 0,00 | 0,00 |
|  | MgO | 10,30 | 9,98 | 10,30 | 10,21 | 11,32 | 11,18 | 10,68 | 10,86 | 11,14 | 11,27 | 10,64 | 10,46 | 10,43 | 10,40 | 10,34 | 10,31 | 10,75 | 10,25 |
|  | CaO | 0,09 | 0,10 | 0,12 | 0,14 | 0,03 | 0,03 | 0,07 | 0,10 | 0,05 | 0,10 | 0,06 | 0,04 | 0,06 | 0,09 | 0,03 | 0,05 | 0,10 | 0,04 |
|  | $Na_2O$ | 0,35 | 0,23 | 0,21 | 0,24 | 0,19 | 0,17 | 0,30 | 0,17 | 0,16 | 0,20 | 0,16 | 0,13 | 0,25 | 0,24 | 0,30 | 0,26 | 0,43 | 0,33 |
|  | $K_2O$ | 9,54 | 9,60 | 9,53 | 9,53 | 10,05 | 9,99 | 9,93 | 9,87 | 9,97 | 9,99 | 9,33 | 9,71 | 9,66 | 9,67 | 9,62 | 9,91 | 9,75 | 9,75 |
|  | $Cr_2O_3$ | 0,01 | 0,00 | 0,00 | 0,00 | 0,007 | 0,01 | 0,006 | 0,002 | 0,02 | 0,002 | 0,007 | 0,003 | 0,00 | 0,003 | 0,002 | 0,00 | 0,00 | 0,007 |
|  | $SO_3$ | 0,13 | 0,10 | 0,09 | 0,11 | 0,06 | 0,07 | 0,06 | 0,14 | 0,10 | 0,11 | 0,08 | 0,07 | 0,10 | 0,11 | 0,09 | 0,10 | 0,47 | 0,13 |
|  | *Total* | *97,42* | *95,88* | *97,17* | *96,11* | *97,54* | *97,45* | *96,06* | *96,67* | *97,57* | *97,45* | *91,24* | *96,00* | *95,41* | *95,34* | *95,29* | *94,35* | *94,60* | *95,21* |
|  | ***Formula*** |  |  |  |  |  |  |  |  |  |  |  |  |  |  |  |  |  |  |
|  | Si | 5,38 | 5,36 | 5,40 | 5,38 | 5,45 | 5,43 | 5,41 | 5,43 | 5,42 | 5,44 | 5,44 | 5,41 | 5,37 | 5,34 | 5,36 | 5,35 | 5,36 | 5,33 |
|  | Al-iv | 2,57 | 2,56 | 2,55 | 2,56 | 2,55 | 2,54 | 2,45 | 2,46 | 2,48 | 2,45 | 2,48 | 2,49 | 2,49 | 2,53 | 2,49 | 2,49 | 2,52 | 2,49 |
|  | Al-vi | 0,00 | 0,00 | 0,00 | 0,00 | 0,02 | 0,00 | 0,00 | 0,00 | 0,00 | 0,00 | 0,00 | 0,00 | 0,00 | 0,00 | 0,00 | 0,00 | 0,00 | 0,00 |
|  | Ti | 0,50 | 0,51 | 0,51 | 0,51 | 0,38 | 0,44 | 0,48 | 0,49 | 0,50 | 0,51 | 0,50 | 0,51 | 0,52 | 0,51 | 0,53 | 0,49 | 0,42 | 0,55 |
|  | Cr | 0,001 | 0,00 | 0,00 | 0,00 | 0,001 | 0,001 | 0,001 | 0,00 | 0,002 | 0,00 | 0,001 | 0,00 | 0,00 | 0,00 | 0,00 | 0,00 | 0,00 | 0,001 |
|  | $Fe^{+2}$ | 3,01 | 3,08 | 3,01 | 3,01 | 2,88 | 2,90 | 3,00 | 2,95 | 2,89 | 2,84 | 2,80 | 2,99 | 3,04 | 3,03 | 3,04 | 3,07 | 3,03 | 3,06 |
|  | Mn | 0,00 | 0,00 | 0,00 | 0,00 | 0,00 | 0,00 | 0,00 | 0,00 | 0,00 | 0,00 | 0,00 | 0,00 | 0,00 | 0,00 | 0,00 | 0,00 | 0,00 | 0,00 |
|  | Mg | 2,36 | 2,33 | 2,36 | 2,37 | 2,58 | 2,55 | 2,49 | 2,51 | 2,54 | 2,57 | 2,58 | 2,43 | 2,45 | 2,44 | 2,43 | 2,46 | 2,56 | 2,42 |
|  | Ca | 0,01 | 0,02 | 0,02 | 0,02 | 0,005 | 0,005 | 0,01 | 0,02 | 0,01 | 0,02 | 0,01 | 0,01 | 0,01 | 0,02 | 0,005 | 0,01 | 0,02 | 0,01 |
|  | Na | 0,11 | 0,07 | 0,06 | 0,07 | 0,06 | 0,05 | 0,09 | 0,05 | 0,05 | 0,06 | 0,05 | 0,04 | 0,08 | 0,07 | 0,09 | 0,08 | 0,13 | 0,10 |
|  | K | 1,87 | 1,92 | 1,87 | 1,89 | 1,96 | 1,95 | 1,98 | 1,95 | 1,95 | 1,95 | 1,94 | 1,93 | 1,94 | 1,94 | 1,94 | 2,02 | 1,99 | 1,97 |
|  | *Total* | *15,82* | *15,84* | *15,78* | *15,82* | *15,89* | *15,87* | *15,92* | *15,85* | *15,84* | *15,83* | *15,81* | *15,81* | *15,88* | *15,89* | *15,88* | *15,97* | *16,02* | *15,91* |
|  | Fe/Fe+Mg | 0,56 | 0,57 | 0,56 | 0,56 | 0,53 | 0,53 | 0,55 | 0,54 | 0,53 | 0,53 | 0,52 | 0,55 | 0,55 | 0,55 | 0,56 | 0,56 | 0,54 | 0,56 |
|  | Fe+Mn+Ti | 3,52 | 3,59 | 3,51 | 3,52 | 3,27 | 3,34 | 3,48 | 3,44 | 3,39 | 3,35 | 3,31 | 3,50 | 3,56 | 3,54 | 3,57 | 3,56 | 3,45 | 3,60 |
|  | Mg-Li | 2,36 | 2,33 | 2,36 | 2,37 | 2,58 | 2,55 | 2,49 | 2,51 | 2,54 | 2,57 | 2,58 | 2,43 | 2,45 | 2,44 | 2,43 | 2,46 | 2,56 | 2,42 |

Table D.7 EPMA results of mica minerals from Edremit field (cont'd)

| | **Sample No.** | **EDR-1032** | | | | | | | | | | | | | | | | | |
|---|---|---|---|---|---|---|---|---|---|---|---|---|---|---|---|---|---|---|---|
| Mica | Region/Mineral | 1/1 | | | | | | | 1/2 | | | | | 2/1 | | | 2/2 | | |
| | Spot No. | 1 | 2 | 4 | 5 | 6 | 10 | 11 | 1 | 2 | 3 | 4 | 5 | 1 | 2 | 3 | 1 | 2 | 3 |
| | $SiO_2$ | 36,03 | 36,16 | 34,48 | 36,00 | 36,80 | 36,07 | 35,10 | 34,94 | 34,53 | 35,27 | 34,59 | 36,97 | 35,01 | 35,72 | 35,23 | 34,82 | 35,00 | 35,68 |
| | $TiO_2$ | 4,31 | 4,35 | 3,94 | 4,51 | 4,62 | 3,82 | 3,88 | 4,26 | 4,38 | 4,53 | 4,18 | 3,73 | 4,36 | 4,41 | 4,08 | 4,09 | 3,98 | 3,55 |
| | $Al_2O_3$ | 14,53 | 14,46 | 14,41 | 14,22 | 14,39 | 14,63 | 14,43 | 13,96 | 13,81 | 14,14 | 14,11 | 14,97 | 14,05 | 14,64 | 14,07 | 14,12 | 14,07 | 14,40 |
| | FeO | 21,88 | 22,18 | 22,69 | 21,91 | 21,58 | 21,79 | 22,24 | 22,16 | 21,72 | 21,57 | 22,20 | 21,73 | 21,04 | 21,22 | 20,98 | 20,99 | 20,88 | 20,44 |
| | MnO | 0,00 | 0,00 | 0,00 | 0,00 | 0,00 | 0,00 | 0,00 | 0,00 | 0,00 | 0,00 | 0,00 | 0,00 | 0,00 | 0,00 | 0,00 | 0,00 | 0,00 | 0,00 |
| | MgO | 11,51 | 11,48 | 11,62 | 11,28 | 11,46 | 11,86 | 11,93 | 11,13 | 10,88 | 10,99 | 11,29 | 12,01 | 11,22 | 11,58 | 11,62 | 11,55 | 11,59 | 12,19 |
| | CaO | 0,05 | 0,04 | 0,09 | 0,04 | 0,05 | 0,03 | 0,08 | 0,03 | 0,09 | 0,53 | 0,03 | 0,05 | 0,03 | 0,03 | 0,02 | 0,03 | 0,03 | 0,02 |
| | $Na_2O$ | 0,13 | 0,12 | 0,10 | 0,14 | 0,16 | 0,15 | 0,17 | 0,10 | 0,11 | 0,17 | 0,11 | 0,09 | 0,25 | 0,14 | 0,16 | 0,18 | 0,17 | 0,15 |
| | $K_2O$ | 9,82 | 9,85 | 8,74 | 10,08 | 9,81 | 9,79 | 9,28 | 9,72 | 9,84 | 9,21 | 9,48 | 9,84 | 9,90 | 9,97 | 9,93 | 9,91 | 10,04 | 10,22 |
| | $Cr_2O_3$ | 0,00 | 0,004 | 0,003 | 0,00 | 0,00 | 0,007 | 0,00 | 0,001 | 0,01 | 0,01 | 0,01 | 0,00 | 0,005 | 0,00 | 0,01 | 0,00 | 0,01 | 0,004 |
| | $SO_3$ | 0,07 | 0,06 | 0,06 | 0,07 | 0,05 | 0,07 | 0,10 | 0,04 | 0,06 | 0,10 | 0,06 | 0,06 | 0,07 | 0,05 | 0,06 | 0,07 | 0,07 | 0,05 |
| | *Total* | *98,34* | *98,70* | *96,13* | *98,23* | *98,92* | *98,22* | *97,20* | *96,35* | *95,43* | *96,51* | *96,06* | *99,44* | *95,94* | *97,76* | *96,15* | *95,74* | *95,83* | *96,71* |
| | ***Formula*** | | | | | | | | | | | | | | | | | | |
| | Si | 5,42 | 5,43 | 5,33 | 5,44 | 5,48 | 5,43 | 5,36 | 5,40 | 5,39 | 5,41 | 5,36 | 5,48 | 5,41 | 5,40 | 5,43 | 5,39 | 5,41 | 5,45 |
| | Al-iv | 2,58 | 2,56 | 2,62 | 2,53 | 2,52 | 2,57 | 2,60 | 2,54 | 2,54 | 2,56 | 2,58 | 2,52 | 2,56 | 2,60 | 2,55 | 2,58 | 2,57 | 2,55 |
| | Al-vi | 0,00 | 0,00 | 0,00 | 0,00 | 0,01 | 0,03 | 0,00 | 0,00 | 0,00 | 0,00 | 0,00 | 0,09 | 0,00 | 0,01 | 0,00 | 0,00 | 0,00 | 0,04 |
| | Ti | 0,49 | 0,49 | 0,46 | 0,51 | 0,52 | 0,43 | 0,45 | 0,49 | 0,51 | 0,52 | 0,49 | 0,42 | 0,51 | 0,50 | 0,47 | 0,48 | 0,46 | 0,41 |
| | Cr | 0,00 | 0,00 | 0,00 | 0,00 | 0,00 | 0,001 | 0,00 | 0,00 | 0,001 | 0,002 | 0,002 | 0,00 | 0,001 | 0,00 | 0,001 | 0,00 | 0,001 | 0,00 |
| | $Fe^{+2}$ | 2,75 | 2,79 | 2,93 | 2,77 | 2,69 | 2,74 | 2,84 | 2,86 | 2,84 | 2,77 | 2,88 | 2,69 | 2,72 | 2,68 | 2,70 | 2,72 | 2,70 | 2,61 |
| | Mn | 0,00 | 0,00 | 0,00 | 0,00 | 0,00 | 0,00 | 0,00 | 0,00 | 0,00 | 0,00 | 0,00 | 0,00 | 0,00 | 0,00 | 0,00 | 0,00 | 0,00 | 0,00 |
| | Mg | 2,58 | 2,57 | 2,68 | 2,54 | 2,55 | 2,66 | 2,71 | 2,56 | 2,53 | 2,51 | 2,61 | 2,65 | 2,59 | 2,61 | 2,67 | 2,67 | 2,67 | 2,77 |
| | Ca | 0,01 | 0,01 | 0,01 | 0,01 | 0,01 | 0,004 | 0,01 | 0,01 | 0,02 | 0,09 | 0,01 | 0,01 | 0,005 | 0,005 | 0,004 | 0,01 | 0,005 | 0,003 |
| | Na | 0,04 | 0,03 | 0,03 | 0,04 | 0,05 | 0,04 | 0,05 | 0,03 | 0,03 | 0,05 | 0,03 | 0,03 | 0,08 | 0,04 | 0,05 | 0,05 | 0,05 | 0,05 |
| | K | 1,89 | 1,89 | 1,72 | 1,94 | 1,87 | 1,88 | 1,81 | 1,92 | 1,96 | 1,80 | 1,87 | 1,86 | 1,95 | 1,92 | 1,95 | 1,96 | 1,98 | 1,99 |
| | *Total* | *15,76* | *15,76* | *15,78* | *15,78* | *15,69* | *15,80* | *15,83* | *15,81* | *15,82* | *15,71* | *15,82* | *15,74* | *15,81* | *15,77* | *15,82* | *15,85* | *15,86* | *15,87* |
| | Fe/Fe+Mg | 0,52 | 0,52 | 0,52 | 0,52 | 0,51 | 0,51 | 0,51 | 0,53 | 0,53 | 0,52 | 0,52 | 0,50 | 0,51 | 0,51 | 0,50 | 0,50 | 0,50 | 0,48 |
| | Fe+Mn+Ti | 3,24 | 3,28 | 3,39 | 3,28 | 3,21 | 3,18 | 3,29 | 3,36 | 3,35 | 3,29 | 3,36 | 3,11 | 3,23 | 3,18 | 3,17 | 3,19 | 3,16 | 3,02 |
| | Mg-Li | 2,58 | 2,57 | 2,68 | 2,54 | 2,55 | 2,66 | 2,71 | 2,56 | 2,53 | 2,51 | 2,61 | 2,65 | 2,59 | 2,61 | 2,67 | 2,67 | 2,67 | 2,77 |

Table D.8 EPMA results of pyroxene minerals from Edremit field

| Pyroxene | **Sample No.** | **EDR-994** | **EDR-1032** | |
|---|---|---|---|---|
| | Region/Mineral | 2/1 | 1/1 | |
| | Spot No. | 1 | 1 | 3 |
| | $SiO_2$ | 48,95 | 48,18 | 48,39 |
| | $TiO_2$ | 1,27 | 1,53 | 1,62 |
| | $Al_2O_3$ | 7,25 | 6,97 | 7,29 |
| | $Cr_2O_3$ | 0,003 | 0,00 | 0,002 |
| | FeO | 17,46 | 15,96 | 15,63 |
| | MnO | 0,00 | 0,00 | 0,00 |
| | MgO | 13,58 | 14,05 | 14,15 |
| | CaO | 11,53 | 11,52 | 11,20 |
| | $Na_2O$ | 1,24 | 1,27 | 1,38 |
| | $K_2O$ | 0,68 | 0,64 | 0,67 |
| | *Total* | *101,96* | *100,12* | *100,33* |
| | O | 6 | 6 | 6 |
| | Cation | 4 | 4 | 4 |
| | ***Formula*** | | | |
| | Si | 1,82 | 1,82 | 1,81 |
| | Ti | 0,04 | 0,04 | 0,05 |
| | Al | 0,32 | 0,31 | 0,32 |
| | Cr | 0,00 | 0,00 | 0,00 |
| | Fe | 0,54 | 0,50 | 0,49 |
| | Mn | 0,00 | 0,00 | 0,00 |
| | Mg | 0,75 | 0,79 | 0,79 |
| | Ca | 0,46 | 0,47 | 0,45 |
| | Na | 0,09 | 0,09 | 0,10 |
| | K | 0,03 | 0,03 | 0,03 |
| | ***End Members*** | | | |
| | Es | 42,88 | 44,91 | 45,70 |
| | Wo | 26,18 | 26,47 | 25,99 |
| | Fs | 30,94 | 28,62 | 28,31 |
| | *Total* | *100* | *100* | *100* |

# E. General Views of EPMA from two Samples of Akköy and Edremit

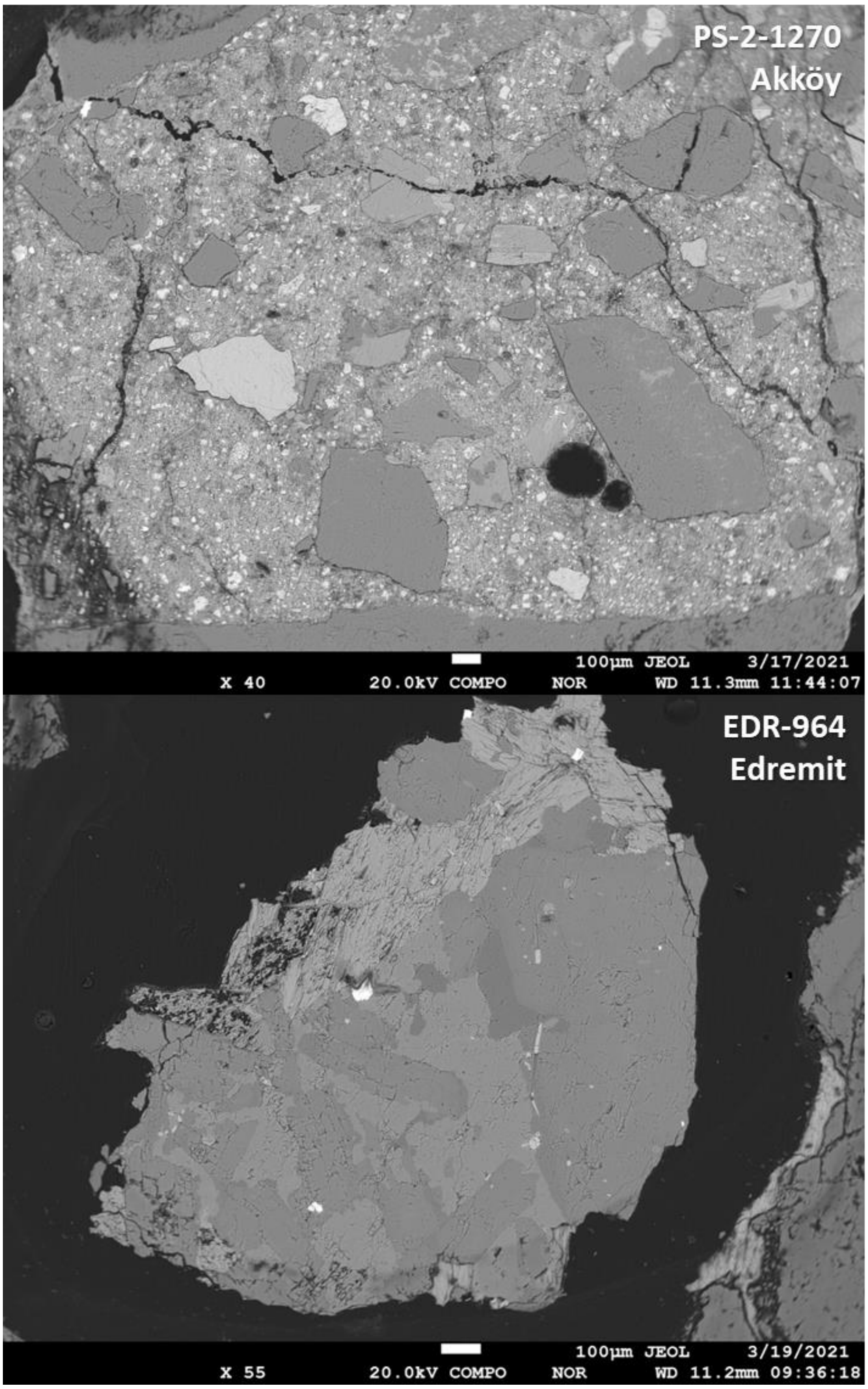

Figure E.1. EPMA views of two samples from Akköy and Edremit fields

# F. XRF Analyses Results of Akköy and Edremit Fields

Table F.1 XRF analyses results of samples from Akköy field

| Element | depth | $Na_2O$ | MgO | $Al_2O_3$ | $SiO_2$ | $P_2O_5$ | $SO_3$ | Cl | $K_2O$ | CaO | $TiO_2$ | $V_2O_5$ | $Cr_2O_3$ | MnO | $Fe_2O_3$ | LOI | Total |
|---|---|---|---|---|---|---|---|---|---|---|---|---|---|---|---|---|---|
| **Sample No\Dimension** | **m** | **%** | **%** | **%** | **%** | **%** | **%** | **%** | **%** | **%** | **%** | **%** | **%** | **%** | **%** | **%** | **%** |
| ADK-PS1-1300 | 1300 | 0,058 | 4,94 | 14,19 | 55,63 | 0,0687 | 0,3646 | 0,0002 | 1,451 | 7,943 | 0,6226 | 0,0245 | 0,0978 | 0,0685 | 8,129 | 6,23 | 99,82 |
| ADK-PS1-1305 | 1305 | 0,051 | 4,208 | 12,883 | 46,7 | 0,0724 | 0,3335 | 0,01627 | 1,273 | 12,26 | 0,4924 | 0,0224 | 0,0551 | 0,1925 | 12,55 | 8,62 | 99,73 |
| ADK-PS1-1310 | 1310 | 0,31 | 2,7 | 14,69 | 61,89 | 0,0754 | 0,3904 | 0,0002 | 1,774 | 4,085 | 0,7459 | 0,0301 | 0,1065 | 0,0337 | 7,398 | 5,82 | 100,05 |
| ADK-PS1-1315 | 1315 | 0,05 | 7,298 | 11,966 | 46,49 | 0,0637 | 0,3197 | 0,00324 | 1,15 | 14,55 | 0,4547 | 0,0178 | 0,0507 | 0,1186 | 7,827 | 8,92 | 99,28 |
| ADK-PS1-1320 | 1320 | 0,13 | 3,965 | 13,66 | 59,81 | 0,0634 | 1,557 | 0,0002 | 1,411 | 6,699 | 0,6032 | 0,0329 | 0,1734 | 0,0366 | 6,169 | 5,99 | 100,30 |
| ADK-PS1-1325 | 1325 | 0,05 | 4,498 | 10,17 | 58,44 | 0,0778 | 0,5638 | 0,00884 | 1,511 | 9,695 | 0,5815 | 0,0215 | 0,0899 | 0,0541 | 4,991 | 9,62 | 100,37 |
| ADK-PS1-1330 | 1330 | 0,05 | 5,356 | 10,08 | 53,2 | 0,077 | 1,206 | 0,02224 | 1,443 | 10,88 | 0,5983 | 0,0233 | 0,0817 | 0,063 | 6,73 | 10,63 | 100,44 |
| ADK-PS1-1335 | 1335 | 0,051 | 3,958 | 8,365 | 51,81 | 0,0629 | 0,5534 | 0,00249 | 1,236 | 10,56 | 0,4593 | 0,0191 | 0,0575 | 0,2109 | 9,626 | 12,84 | 99,81 |
| ADK-PS1-1340 | 1340 | 0,049 | 4,429 | 7,744 | 59,44 | 0,0679 | 0,8012 | 0,0002 | 1,031 | 10,18 | 0,519 | 0,0184 | 0,2663 | 0,0659 | 5,285 | 10,83 | 100,73 |
| ADK-PS1-1345 | 1345 | 0,053 | 5,39 | 9,158 | 54,83 | 0,0911 | 1,119 | 0,00014 | 1,072 | 11,22 | 0,6707 | 0,0235 | 0,0883 | 0,0615 | 6,038 | 10,44 | 100,26 |
| ADK-PS1-1350 | 1350 | 0,049 | 4,221 | 9,835 | 53,5 | 0,0775 | 0,5187 | 0,00006 | 1,385 | 11,94 | 0,6247 | 0,0248 | 0,0749 | 0,0918 | 6,085 | 11,554 | 99,98 |
| ADK-PS1-1355 | 1355 | 0,049 | 5,382 | 7,87 | 52,1 | 0,0586 | 0,5285 | 0,00139 | 1,122 | 12,91 | 0,4814 | 0,0182 | 0,1578 | 0,1106 | 6,651 | 12,53 | 99,97 |
| ADK-PS1-1360 | 1360 | 0,053 | 5,282 | 8,6 | 59,42 | 0,0736 | 0,3231 | 0,01193 | 1,182 | 13,78 | 0,5163 | 0,0187 | 0,1013 | 0,1543 | 7,801 | 2,48 | 99,80 |
| ADK-PS1-1365 | 1365 | 0,051 | 5,277 | 8,397 | 51,12 | 0,0655 | 0,2905 | 0,00551 | 1,213 | 12,86 | 0,5121 | 0,0186 | 0,1448 | 0,1021 | 7,043 | 12,99 | 100,09 |
| ADK-PS1-1370 | 1370 | 0,052 | 4,06 | 9,006 | 53,25 | 0,0765 | 0,3209 | 0,00006 | 0,975 | 10,54 | 0,5952 | 0,0234 | 0,1753 | 0,1237 | 8,327 | 12,74 | 100,27 |
| ADK-PS1-1375 | 1375 | 0,051 | 3,509 | 9,355 | 53,69 | 0,0831 | 0,3808 | 0,00006 | 1,217 | 11,96 | 0,6226 | 0,0221 | 0,0966 | 0,0677 | 5,791 | 13,85 | 100,70 |
| ADK-PS1-1380 | 1380 | 0,052 | 4,578 | 8,295 | 48,08 | 0,0684 | 0,3555 | 0,00008 | 1,099 | 15,76 | 0,4709 | 0,0168 | 0,1019 | 0,1172 | 7,089 | 14,11 | 100,19 |
| ADK-PS1-1385 | 1385 | 0,051 | 4,956 | 8,873 | 58,99 | 0,062 | 0,3818 | 0,00013 | 1,242 | 14,72 | 0,5022 | 0,0191 | 0,0859 | 0,0928 | 6,965 | 3,74 | 100,68 |
| ADK-PS1-1390 | 1390 | 0,053 | 4,918 | 8,345 | 60,59 | 0,0675 | 0,4409 | 0,009 | 1,194 | 13,35 | 0,4712 | 0,0131 | 0,0831 | 0,104 | 6,782 | 3,24 | 99,66 |
| ADK-PS1-1395 | 1395 | 0,051 | 6,013 | 6,832 | 59,16 | 0,057 | 0,2894 | 0,00075 | 0,9462 | 17,33 | 0,4399 | 0,0151 | 0,0572 | 0,098 | 5,578 | 3,29 | 100,16 |
| ADK-PS1-1400 | 1400 | 0,049 | 5,787 | 7,352 | 60,35 | 0,0597 | 0,3227 | 0,00014 | 0,991 | 17,07 | 0,4613 | 0,0171 | 0,0596 | 0,1273 | 7,309 | 0,33 | 100,29 |
| ADK-PS1-1405 | 1405 | 0,051 | 6,608 | 7,107 | 55,28 | 0,053 | 0,3365 | 0,00014 | 0,9115 | 17,39 | 0,4631 | 0,0189 | 0,0797 | 0,0759 | 5,117 | 6,24 | 99,73 |
| ADK-PS1-1410 | 1410 | 0,052 | 4,947 | 8,657 | 51,08 | 0,0724 | 0,3873 | 0,0001 | 1,141 | 14,66 | 0,5387 | 0,0195 | 0,0807 | 0,087 | 5,752 | 12,55 | 100,02 |

Table F.1 XRF analyses results of samples from Akköy field (cont'd)

| **Element** | **depth** | **$Na_2O$** | **MgO** | **$Al_2O_3$** | **$SiO_2$** | **$P_2O_5$** | **$SO_3$** | **Cl** | **$K_2O$** | **CaO** | **$TiO_2$** | **$V_2O_5$** | **$Cr_2O_3$** | **MnO** | **$Fe_2O_3$** | **LOI** | **Total** |
|---|---|---|---|---|---|---|---|---|---|---|---|---|---|---|---|---|---|
| **Sample No\Dimension** | **m** | **%** | **%** | **%** | **%** | **%** | **%** | **%** | **%** | **%** | **%** | **%** | **%** | **%** | **%** | **%** | **%** |
| ADK-PS1-1415 | 1415 | 0,051 | 5,011 | 7,421 | 53,58 | 0,0433 | 0,2931 | 0,00182 | 0,962 | 19,73 | 0,4598 | 0,0164 | 0,0654 | 0,0844 | 5,012 | 7,98 | 100,71 |
| ADK-PS1-1420 | 1420 | 0,049 | 5,918 | 6,676 | 56,85 | 0,06 | 0,5154 | 0,00013 | 0,8236 | 17,34 | 0,4301 | 0,0182 | 0,063 | 0,0932 | 5,573 | 6,03 | 100,44 |
| ADK-PS1-1425 | 1425 | 0,14 | 4,811 | 8,705 | 52,47 | 0,0598 | 0,3385 | 0,00005 | 1,057 | 15,57 | 0,55 | 0,0169 | 0,0946 | 0,0586 | 4,525 | 11,44 | 99,84 |
| ADK-PS1-1430 | 1430 | 0,049 | 5,21 | 7,994 | 57,7 | 0,0627 | 0,2812 | 0,0001 | 1,035 | 17,24 | 0,4885 | 0,0189 | 0,0537 | 0,0854 | 4,854 | 4,82 | 99,89 |
| ADK-PS1-1435 | 1435 | 0,047 | 6,199 | 7,919 | 56,57 | 0,0651 | 0,2093 | 0,0001 | 0,878 | 16,95 | 0,5251 | 0,0211 | 0,101 | 0,0753 | 4,604 | 5,86 | 100,02 |
| ADK-PS1-1440 | 1440 | 0,051 | 5,568 | 8,512 | 58,76 | 0,0589 | 0,2239 | 0,00008 | 1,032 | 15,26 | 0,5081 | 0,0199 | 0,0654 | 0,0834 | 5,728 | 4,53 | 100,40 |
| ADK-PS1-1445 | 1445 | 0,05 | 5,433 | 8,474 | 58,13 | 0,0613 | 0,232 | 0,0001 | 1,105 | 15,69 | 0,5378 | 0,0202 | 0,0881 | 0,0886 | 5,357 | 4,27 | 99,54 |
| ADK-PS1-1450 | 1450 | 0,049 | 5,937 | 6,843 | 53,26 | 0,0485 | 0,3473 | 0,01101 | 0,9105 | 17,95 | 0,4367 | 0,0219 | 0,0984 | 0,0852 | 5,067 | 9,72 | 100,79 |
| ADK-PS1-1455 | 1455 | 0,05 | 5,311 | 7,1 | 56,24 | 0,0542 | 0,4349 | 0,0001 | 0,8923 | 18,92 | 0,4854 | 0,0176 | 0,1098 | 0,0935 | 4,854 | 6,82 | 101,38 |
| ADK-PS1-1460 | 1460 | 0,048 | 4,252 | 5,789 | 52,75 | 0,0505 | 0,3168 | 0,00336 | 0,7162 | 22,3 | 0,3752 | 0,0178 | 0,1041 | 0,1507 | 5,736 | 7,83 | 100,44 |
| ADK-PS1-1465 | 1465 | 0,05 | 3,975 | 5,489 | 40,26 | 0,0495 | 0,3344 | 0,00949 | 0,6353 | 24,1 | 0,3702 | 0,0141 | 0,1109 | 0,1576 | 6,244 | 18,93 | 100,73 |
| ADK-PS1-1470 | 1470 | 0,05 | 4,939 | 7,082 | 45,15 | 0,0615 | 0,2884 | 0,00342 | 0,8918 | 18,51 | 0,4674 | 0,0146 | 0,0858 | 0,1199 | 5,795 | 17,33 | 100,79 |
| ADK-PS1-1475 | 1475 | 0,049 | 3,951 | 7,581 | 48,31 | 0,0576 | 0,2696 | 0,00007 | 0,8849 | 17,49 | 0,4686 | 0,0164 | 0,0916 | 0,121 | 5,553 | 15,39 | 100,23 |
| ADK-PS1-1480 | 1480 | 0,049 | 2,796 | 8,964 | 56,07 | 0,062 | 0,3568 | 0,00125 | 0,8366 | 13,87 | 0,5965 | 0,024 | 0,1289 | 0,0866 | 5,016 | 11,54 | 100,40 |
| ADK-PS1-1485 | 1485 | 0,05 | 2,376 | 7,849 | 44,99 | 0,0659 | 0,6395 | 0,00919 | 0,9724 | 22,36 | 0,4992 | 0,0201 | 0,0828 | 0,0775 | 4,64 | 16,03 | 100,66 |
| ADK-PS1-1490 | 1490 | 0,051 | 2,672 | 9,568 | 49,71 | 0,0739 | 0,9109 | 0,0002 | 1,3 | 17,39 | 0,5761 | 0,023 | 0,0903 | 0,0567 | 4,624 | 12,57 | 99,62 |
| ADK-PS1-1495 | 1495 | 0,05 | 2,912 | 8,706 | 47,29 | 0,0539 | 0,6962 | 0,00007 | 1,127 | 18,22 | 0,5157 | 0,0157 | 0,0765 | 0,0599 | 4,518 | 15,58 | 99,82 |
| ADK-PS1-1500 | 1500 | 0,05 | 3,836 | 8,122 | 48,6 | 0,0621 | 0,5361 | 0,00011 | 1,042 | 16,58 | 0,5438 | 0,0223 | 0,1021 | 0,0915 | 5,541 | 14,55 | 99,68 |
| ADK-PS1-1505 | 1505 | 0,05 | 3,903 | 9,109 | 49,75 | 0,0569 | 0,5241 | 0,1047 | 1,095 | 15,43 | 0,5587 | 0,0222 | 0,096 | 0,0657 | 4,884 | 14,64 | 100,29 |
| ADK-PS1-1510 | 1510 | 0,049 | 3,111 | 11,07 | 54,55 | 0,0674 | 0,6096 | 0,00004 | 1,243 | 12,86 | 0,6131 | 0,021 | 0,1432 | 0,0615 | 4,976 | 10,37 | 99,74 |
| ADK-PS1-1515 | 1515 | 0,052 | 3,679 | 8,733 | 51,56 | 0,0693 | 0,7455 | 0,00006 | 1,078 | 14,8 | 0,5591 | 0,0204 | 0,087 | 0,1079 | 6,353 | 12,58 | 100,42 |
| ADK-PS1-1520 | 1520 | 0,051 | 4,792 | 7,72 | 58,24 | 0,0714 | 0,3928 | 0,00305 | 0,9309 | 17,86 | 0,4384 | 0,0185 | 0,0914 | 0,2249 | 5,327 | 3,73 | 99,89 |
| ADK-PS1-1525 | 1525 | 0,051 | 3,642 | 9,067 | 50,13 | 0,0785 | 0,6291 | 0,00004 | 1,163 | 16,7 | 0,5337 | 0,0229 | 0,0915 | 0,1639 | 5,727 | 12,88 | 100,88 |

Table F.1 XRF analyses results of samples from Akköy field (cont'd)

| Element | depth | Co | Ni | Cu | Zn | Ga | Ge | As | Se | Br | Rb | Sr | Y | Zr | Nb | Mo | Cd | In |
|---|---|---|---|---|---|---|---|---|---|---|---|---|---|---|---|---|---|---|
| Sample No\Dimension | m | ppm | ppm | ppm | ppm | ppm | ppm | ppm | ppm | ppm | ppm | ppm | ppm | ppm | ppm | ppm | ppm | ppm |
| ADK-PS1-1300 | 1300 | 76,4 | 663,3 | 31,8 | 65,3 | 14,5 | 1,9 | 10,5 | 0,3 | 0,4 | 62,7 | 296,1 | 17,1 | 125,9 | 13,2 | 4 | 0,8 | 0,7 |
| ADK-PS1-1305 | 1305 | 96 | 599 | 20,6 | 121,5 | 11,6 | 2,2 | 5,7 | 0,3 | 1,4 | 57,9 | 378 | 23,6 | 126 | 12,6 | 3,8 | 1,3 | 0,8 |
| ADK-PS1-1310 | 1310 | 87,7 | 661,8 | 40,8 | 60,9 | 18,3 | 1,7 | 11,4 | 0,3 | 0,2 | 76,2 | 288,3 | 19,3 | 165,2 | 14,2 | 3,9 | 0,8 | 0,8 |
| ADK-PS1-1315 | 1315 | 53,9 | 451 | 27,3 | 74,8 | 12,6 | 1,3 | 7,6 | 0,3 | 0,8 | 52,2 | 398,1 | 17 | 111,5 | 7,9 | 3,1 | 0,9 | 0,8 |
| ADK-PS1-1320 | 1320 | 95 | 896 | 32,5 | 46 | 16,2 | 1,9 | 66,5 | 0,5 | 0,5 | 56,2 | 272,9 | 15,2 | 126,5 | 13,6 | 8 | 0,8 | 0,9 |
| ADK-PS1-1325 | 1325 | 48,2 | 453,9 | 22,9 | 49,7 | 14,4 | 1,4 | 16,6 | 0,3 | 0,7 | 65,1 | 338,5 | 18,9 | 177,7 | 11,5 | 2,7 | 0,8 | 0,7 |
| ADK-PS1-1330 | 1330 | 68,3 | 469,2 | 22,4 | 63,1 | 14,9 | 1,7 | 16,7 | 0,3 | 0,3 | 59,1 | 319 | 19 | 129,7 | 13 | 3,1 | 0,8 | 0,7 |
| ADK-PS1-1335 | 1335 | 89 | 701,7 | 19,8 | 76,3 | 10,7 | 1,1 | 9,6 | 0,3 | 0,5 | 53,8 | 272 | 16,8 | 100,3 | 16,3 | 3,5 | 0,9 | 0,9 |
| ADK-PS1-1340 | 1340 | 69,3 | 555,1 | 20,6 | 52 | 10,2 | 1,6 | 11,6 | 0,3 | 0,6 | 40,4 | 273 | 14,6 | 136 | 11,1 | 2,9 | 0,8 | 0,8 |
| ADK-PS1-1345 | 1345 | 94 | 652,9 | 30,6 | 51,1 | 11,6 | 1,3 | 13,9 | 0,3 | 0,3 | 42,5 | 483,7 | 17,4 | 121,5 | 11,8 | 3,4 | 0,9 | 0,8 |
| ADK-PS1-1350 | 1350 | 79,1 | 498,5 | 25,6 | 51,4 | 15,8 | 1,2 | 12 | 0,3 | 0,8 | 57,4 | 313,5 | 16,4 | 132 | 9,3 | 3 | 0,8 | 0,8 |
| ADK-PS1-1355 | 1355 | 44,2 | 524,2 | 21,1 | 52,6 | 9,9 | 2 | 9,5 | 0,3 | 0,3 | 46,6 | 367,9 | 14,6 | 127,5 | 12,4 | 3,4 | 0,9 | 0,8 |
| ADK-PS1-1360 | 1360 | 63,1 | 486 | 20,6 | 62,7 | 12,2 | 0,8 | 6,5 | 0,4 | 0,8 | 50,1 | 375,8 | 18 | 155 | 12,9 | 4 | 0,9 | 0,8 |
| ADK-PS1-1365 | 1365 | 62,6 | 492,6 | 19,7 | 55,5 | 12,3 | 1,3 | 5,4 | 0,3 | 0,6 | 51,4 | 346,8 | 17,3 | 153,4 | 17,6 | 4,5 | 0,9 | 0,9 |
| ADK-PS1-1370 | 1370 | 87 | 855 | 29,9 | 64,4 | 11,1 | 1,2 | 7,9 | 0,3 | 0,2 | 40,7 | 279,3 | 17,4 | 128,2 | 5,8 | 3 | 0,8 | 0,8 |
| ADK-PS1-1375 | 1375 | 38,6 | 513,9 | 20,4 | 43,7 | 13,6 | 0,5 | 10,3 | 0,3 | 0,2 | 49,3 | 287,5 | 17,9 | 135,3 | 10,9 | 3,5 | 0,8 | 0,8 |
| ADK-PS1-1380 | 1380 | 66,6 | 616,9 | 26,5 | 54,6 | 11,6 | 0,6 | 20,7 | 0,3 | 0,7 | 46,3 | 343,4 | 17,9 | 109,6 | 13,6 | 3,4 | 0,9 | 0,9 |
| ADK-PS1-1385 | 1385 | 97 | 570,8 | 20,8 | 56,1 | 11,8 | 2,2 | 9,3 | 0,3 | 0,6 | 55 | 348,4 | 17,6 | 121,3 | 10,7 | 3,5 | 0,9 | 0,8 |
| ADK-PS1-1390 | 1390 | 68,4 | 528,5 | 20,8 | 53,4 | 12,6 | 1,5 | 14,2 | 0,3 | 0,8 | 49,7 | 303,3 | 15 | 118,2 | 10,8 | 6,4 | 2 | 1 |
| ADK-PS1-1395 | 1395 | 70,1 | 437,8 | 19 | 45,5 | 9,1 | 0,6 | 5,2 | 0,3 | 0,7 | 39,2 | 372,1 | 15,8 | 105,3 | 6,7 | 2,6 | 0,8 | 0,7 |
| ADK-PS1-1400 | 1400 | 56,8 | 476 | 19,9 | 60,2 | 10,8 | 0,6 | 7,2 | 0,3 | 0,7 | 43,4 | 338,8 | 16,6 | 97,4 | 3,2 | 2,8 | 0,8 | 0,8 |
| ADK-PS1-1405 | 1405 | 77,3 | 440,9 | 20,1 | 44,3 | 10,4 | 0,5 | 7,2 | 0,3 | 1,1 | 39,8 | 449,2 | 13,5 | 98,8 | 9,9 | 5 | 0,8 | 0,8 |
| ADK-PS1-1410 | 1410 | 66,4 | 508,4 | 19,8 | 43,3 | 11,6 | 1,8 | 11,6 | 0,3 | 0,6 | 49,9 | 352 | 17,8 | 125 | 11,7 | 4,5 | 0,9 | 0,9 |

Table F.1 XRF analyses results of samples from Akköy field (cont’d)

| Element | depth | Sn | Sb | Te | I | Cs | Ba | La | Ce | Hf | Ta | W | Hg | Tl | Pb | Bi | Th | U |
|---|---|---|---|---|---|---|---|---|---|---|---|---|---|---|---|---|---|---|
| Sample No\Dimension | m | ppm | ppm | ppm | ppm | ppm | ppm | ppm | ppm | ppm | ppm | ppm | ppm | ppm | ppm | ppm | ppm | ppm |
| ADK-PS1-1300 | 1300 | 1,8 | 0,8 | 0,4 | 3,3 | 7 | 181,2 | 30,6 | 51,2 | 3,4 | 5,1 | 18,2 | 0,9 | 0,9 | 13,2 | 1 | 1,1 | 8,3 |
| ADK-PS1-1305 | 1305 | 1,1 | 1 | 1,2 | 2,3 | 5,4 | 237,5 | 29,6 | 42,1 | 3,4 | 5,4 | 5,6 | 1,1 | 1 | 19 | 0,7 | 4,1 | 14,9 |
| ADK-PS1-1310 | 1310 | 1,4 | 0,8 | 1,2 | 2,2 | 10,3 | 209 | 23,7 | 61,7 | 4,1 | 5,2 | 15 | 0,8 | 0,9 | 16,1 | 0,4 | 5,1 | 7 |
| ADK-PS1-1315 | 1315 | 1,8 | 0,9 | 1,2 | 8,4 | 8,9 | 176,9 | 23,6 | 32,1 | 3,2 | 4,7 | 12,2 | 0,9 | 0,9 | 15,7 | 0,6 | 3,6 | 6,9 |
| ADK-PS1-1320 | 1320 | 1,5 | 0,9 | 1,1 | 2,9 | 9 | 172,5 | 31,1 | 51,4 | 3,2 | 5,5 | 38,8 | 1 | 1,3 | 14,4 | 0,7 | 1,2 | 7,4 |
| ADK-PS1-1325 | 1325 | 1,9 | 0,9 | 1,1 | 2,1 | 6,3 | 298,3 | 40,6 | 68,5 | 3,3 | 4,5 | 27,1 | 0,9 | 0,9 | 19,7 | 0,6 | 7,9 | 7,1 |
| ADK-PS1-1330 | 1330 | 0,9 | 0,9 | 1,1 | 2,1 | 5 | 250,8 | 34,6 | 42,2 | 2,5 | 4,5 | 21,1 | 1 | 0,9 | 16,8 | 1,6 | 3,5 | 7,9 |
| ADK-PS1-1335 | 1335 | 0,8 | 0,9 | 1,2 | 2,6 | 7,5 | 270,7 | 23,8 | 46,4 | 3,3 | 5,1 | 28,5 | 1 | 1 | 13,6 | 0,6 | 0,7 | 8,2 |
| ADK-PS1-1340 | 1340 | 1,3 | 0,8 | 1,1 | 1,9 | 3 | 159,1 | 33,4 | 24,5 | 2,2 | 4,6 | 50,2 | 1 | 0,7 | 10,9 | 0,6 | 1,7 | 6,3 |
| ADK-PS1-1345 | 1345 | 0,6 | 0,8 | 1,3 | 2,3 | 3,8 | 860,6 | 16,9 | 41,8 | 3,1 | 5,1 | 26,5 | 0,9 | 0,9 | 13,3 | 0,6 | 0,5 | 7,8 |
| ADK-PS1-1350 | 1350 | 0,9 | 1 | 1,2 | 2,1 | 4,7 | 245,7 | 20 | 45,6 | 3 | 4,6 | 31 | 0,9 | 0,9 | 16,5 | 0,7 | 2,7 | 8,5 |
| ADK-PS1-1355 | 1355 | 1,3 | 0,9 | 1,3 | 2 | 6,8 | 162,5 | 27,7 | 35,4 | 3,7 | 5,1 | 23,6 | 1 | 0,9 | 11,9 | 0,6 | 1 | 7,9 |
| ADK-PS1-1360 | 1360 | 1,6 | 0,9 | 1,2 | 2,5 | 9,6 | 173,8 | 23,8 | 29 | 3 | 4,7 | 21 | 1 | 0,9 | 14,8 | 0,6 | 4 | 7,8 |
| ADK-PS1-1365 | 1365 | 1,7 | 1,2 | 1,2 | 2,1 | 8,7 | 177,9 | 32,1 | 51,7 | 2,9 | 4,5 | 43 | 1,1 | 0,9 | 14,7 | 0,6 | 4,5 | 9,9 |
| ADK-PS1-1370 | 1370 | 0,9 | 0,8 | 1,1 | 2 | 6,8 | 183,6 | 23 | 38,3 | 3,1 | 5,6 | 23,3 | 1 | 1,3 | 11,9 | 0,6 | 0,6 | 7,7 |
| ADK-PS1-1375 | 1375 | 1,6 | 1 | 1,1 | 2,1 | 3,6 | 285,7 | 23,9 | 42,6 | 2,7 | 4,4 | 34 | 0,9 | 0,8 | 11,8 | 0,6 | 0,5 | 7,5 |
| ADK-PS1-1380 | 1380 | 1,9 | 0,9 | 1,3 | 2,2 | 3,8 | 501,5 | 24,9 | 20,6 | 3,4 | 5 | 37,2 | 1 | 1 | 13,1 | 0,6 | 0,6 | 8,9 |
| ADK-PS1-1385 | 1385 | 1,4 | 0,9 | 1,1 | 5,3 | 6,2 | 234,9 | 23,2 | 31,8 | 3,1 | 4,7 | 25,1 | 1 | 0,9 | 14 | 0,6 | 2,8 | 7,3 |
| ADK-PS1-1390 | 1390 | 0,8 | 0,9 | 1,3 | 2,3 | 3,8 | 876,5 | 15,1 | 10 | 3,1 | 4,5 | 34,8 | 1 | 0,9 | 11,9 | 1,2 | 1,5 | 10 |
| ADK-PS1-1395 | 1395 | 1,6 | 0,8 | 1,1 | 2,4 | 6,3 | 229,8 | 27,8 | 25,2 | 2,9 | 4,4 | 43,2 | 1 | 0,9 | 13,9 | 1,1 | 0,6 | 8,2 |
| ADK-PS1-1400 | 1400 | 0,7 | 0,9 | 0,5 | 2,9 | 5,3 | 240,1 | 25,3 | 23 | 2,9 | 4,6 | 21,8 | 0,7 | 0,9 | 13 | 0,6 | 1 | 7,5 |
| ADK-PS1-1405 | 1405 | 2,2 | 0,9 | 1,1 | 3,9 | 3,4 | 330 | 20,6 | 27,9 | 2,9 | 4,4 | 29,2 | 0,9 | 0,8 | 10 | 0,6 | 1,5 | 7,7 |
| ADK-PS1-1410 | 1410 | 1 | 0,9 | 1,2 | 2,1 | 7 | 211,6 | 28,2 | 29,7 | 2,8 | 4,6 | 38,9 | 1,1 | 0,8 | 12,6 | 0,6 | 2 | 7,6 |

Table F.1 XRF analyses results of samples from Akköy field (cont’d)

| Element | depth | Co | Ni | Cu | Zn | Ga | Ge | As | Se | Br | Rb | Sr | Y | Zr | Nb | Mo | Cd | In |
|---|---|---|---|---|---|---|---|---|---|---|---|---|---|---|---|---|---|---|
| Sample No\Dimension | m | ppm | ppm | ppm | ppm | ppm | ppm | ppm | ppm | ppm | ppm | ppm | ppm | ppm | ppm | ppm | ppm | ppm |
| ADK-PS1-1415 | 1415 | 40,1 | 387,2 | 15,9 | 40,6 | 10,6 | 0,8 | 4 | 0,3 | 0,4 | 44,4 | 412 | 12,9 | 97 | 9,3 | 3,6 | 0,9 | 0,8 |
| ADK-PS1-1420 | 1420 | 70,6 | 497,8 | 19,8 | 44,3 | 9,4 | 1,6 | 14,6 | 0,3 | 0,8 | 35,7 | 370,7 | 14,8 | 83,7 | 3,5 | 2,7 | 0,8 | 0,8 |
| ADK-PS1-1425 | 1425 | 55,6 | 565 | 24,2 | 40 | 10,7 | 0,8 | 4,1 | 0,3 | 1 | 44,8 | 396,8 | 12,2 | 122 | 11,3 | 2,9 | 0,8 | 0,8 |
| ADK-PS1-1430 | 1430 | 57,6 | 414,8 | 18,5 | 38,4 | 10,2 | 1,1 | 6,8 | 0,3 | 0,9 | 44,1 | 400,7 | 15,4 | 97,8 | 10,2 | 2,9 | 0,8 | 0,7 |
| ADK-PS1-1435 | 1435 | 43 | 375,4 | 26,1 | 39,6 | 11,3 | 0,5 | 4,8 | 0,3 | 1,3 | 38,5 | 437,1 | 13,6 | 101,1 | 10,9 | 2,9 | 0,8 | 0,8 |
| ADK-PS1-1440 | 1440 | 53,6 | 442,9 | 25,4 | 51,6 | 12 | 0,6 | 6 | 0,3 | 0,9 | 45,7 | 388,2 | 15,2 | 128,8 | 9,3 | 2,1 | 0,8 | 0,7 |
| ADK-PS1-1445 | 1445 | 29,6 | 367,9 | 25,4 | 44,1 | 11,3 | 0,5 | 4 | 0,3 | 1 | 48,4 | 410,5 | 14,9 | 108,8 | 3,4 | 3 | 0,8 | 0,8 |
| ADK-PS1-1450 | 1450 | 68,4 | 338 | 18,3 | 39,8 | 9,2 | 0,6 | 2,9 | 0,3 | 1 | 40,1 | 429,8 | 13,2 | 101,1 | 3,2 | 2,7 | 0,8 | 0,8 |
| ADK-PS1-1455 | 1455 | 48,9 | 406,8 | 19,7 | 38,5 | 11,5 | 1 | 15 | 0,3 | 1,2 | 37,5 | 427,3 | 13,4 | 109 | 10,5 | 3 | 0,8 | 0,8 |
| ADK-PS1-1460 | 1460 | 49,4 | 379,8 | 12,1 | 45 | 7,6 | 0,7 | 4,5 | 0,3 | 0,7 | 30,7 | 434,9 | 11,3 | 92,5 | 3,5 | 3,3 | 0,9 | 0,9 |
| ADK-PS1-1465 | 1465 | 45,8 | 417,6 | 16,2 | 46,7 | 7,7 | 0,9 | 4,3 | 0,3 | 0,9 | 26,9 | 450,4 | 11,4 | 100,5 | 6,4 | 3,6 | 0,9 | 0,8 |
| ADK-PS1-1470 | 1470 | 49,1 | 384,5 | 15,5 | 43,8 | 10,3 | 0,6 | 3,7 | 0,3 | 1 | 38,1 | 373,1 | 14,8 | 100,9 | 8,1 | 3,3 | 0,9 | 0,7 |
| ADK-PS1-1475 | 1475 | 26,7 | 431,8 | 21,4 | 39,7 | 11,9 | 0,6 | 3,4 | 0,3 | 0,6 | 38,5 | 371,8 | 14,2 | 85,2 | 7,7 | 2,7 | 0,8 | 0,7 |
| ADK-PS1-1480 | 1480 | 74 | 565,2 | 29,4 | 42,3 | 11,9 | 1,8 | 6,6 | 0,3 | 0,9 | 34 | 295,3 | 12,1 | 98 | 6,4 | 2,9 | 0,8 | 0,7 |
| ADK-PS1-1485 | 1485 | 49,1 | 436,6 | 14,8 | 42,2 | 9,7 | 2,8 | 10,7 | 0,3 | 2,6 | 42,2 | 362,9 | 13,6 | 123,6 | 7,8 | 3,3 | 0,8 | 0,8 |
| ADK-PS1-1490 | 1490 | 73,7 | 586,1 | 22,2 | 52,6 | 12,6 | 3,2 | 17,6 | 0,7 | 1,7 | 55,7 | 386,8 | 15,3 | 124,8 | 10,6 | 5,2 | 0,9 | 0,8 |
| ADK-PS1-1495 | 1495 | 42,9 | 480,9 | 20,8 | 45 | 11,6 | 1,5 | 10,6 | 0,7 | 1,2 | 50,9 | 336,8 | 12,8 | 108,2 | 11,5 | 4,3 | 0,8 | 0,8 |
| ADK-PS1-1500 | 1500 | 75,1 | 531,7 | 19,8 | 49,4 | 11,4 | 1,5 | 7,9 | 0,3 | 1 | 45,4 | 298,4 | 15 | 120,5 | 9,7 | 3,5 | 0,8 | 0,8 |
| ADK-PS1-1505 | 1505 | 50,5 | 544,2 | 34,1 | 50,8 | 13,1 | 1,2 | 6,9 | 0,5 | 0,9 | 50,1 | 332,7 | 13,1 | 116,5 | 8,1 | 3 | 0,8 | 0,8 |
| ADK-PS1-1510 | 1510 | 58,6 | 549,5 | 27,4 | 50,6 | 14,9 | 1,7 | 7,8 | 0,3 | 0,9 | 58,7 | 350,4 | 15 | 132,9 | 9 | 3,4 | 0,8 | 0,8 |
| ADK-PS1-1515 | 1515 | 74,9 | 551,2 | 20,8 | 51,5 | 12,6 | 1,4 | 8,8 | 0,3 | 0,8 | 48,3 | 334,2 | 14,3 | 94,6 | 7,1 | 3,9 | 0,8 | 0,7 |
| ADK-PS1-1520 | 1520 | 41,2 | 450 | 28,6 | 52,4 | 10,3 | 0,5 | 4,8 | 0,3 | 0,3 | 41,2 | 307,5 | 18,1 | 85,9 | 3,5 | 2,6 | 0,8 | 0,8 |
| ADK-PS1-1525 | 1525 | 57,4 | 549,5 | 28 | 51,5 | 12,2 | 0,5 | 7,8 | 0,3 | 0,9 | 49 | 330 | 17,7 | 112,3 | 3,6 | 3,2 | 0,8 | 0,9 |

Table F.1 XRF analyses results of samples from Akköy field (cont’d)

| Element | depth | Sn | Sb | Te | I | Cs | Ba | La | Ce | Hf | Ta | W | Hg | Tl | Pb | Bi | Th | U |
|---|---|---|---|---|---|---|---|---|---|---|---|---|---|---|---|---|---|---|
| Sample No\Dimension | m | ppm | ppm | ppm | ppm | ppm | ppm | ppm | ppm | ppm | ppm | ppm | ppm | ppm | ppm | ppm | ppm | ppm |
| ADK-PS1-1415 | 1415 | 0,9 | 0,9 | 1,2 | 3,5 | 7,6 | 322,4 | 23 | 30,5 | 3 | 4 | 15,1 | 0,9 | 0,6 | 9,5 | 0,6 | 2,3 | 8,5 |
| ADK-PS1-1420 | 1420 | 0,9 | 0,9 | 0,9 | 2 | 3,4 | 179,5 | 30,2 | 33,7 | 2,4 | 4,5 | 36,9 | 1,1 | 0,4 | 9,7 | 0,6 | 0,6 | 7,6 |
| ADK-PS1-1425 | 1425 | 1,5 | 0,9 | 1,2 | 2,2 | 3,6 | 194,8 | 16,9 | 34,9 | 4,4 | 4,7 | 43,7 | 1 | 0,8 | 11,6 | 0,6 | 0,5 | 7,7 |
| ADK-PS1-1430 | 1430 | 1 | 0,8 | 1,2 | 5,2 | 3,6 | 371,8 | 16,2 | 27,4 | 2,9 | 4,2 | 23,1 | 0,9 | 0,8 | 11,1 | 0,6 | 1,5 | 7,1 |
| ADK-PS1-1435 | 1435 | 2,5 | 0,8 | 1,2 | 7,7 | 3,6 | 212,6 | 28,3 | 41,6 | 3,1 | 4,5 | 22,7 | 0,8 | 0,8 | 9,9 | 0,6 | 2,5 | 7,6 |
| ADK-PS1-1440 | 1440 | 1,7 | 0,9 | 0,8 | 3,7 | 3,5 | 182,8 | 28,2 | 41,2 | 3 | 4,6 | 36,5 | 1 | 0,8 | 11,6 | 0,6 | 1,8 | 8,1 |
| ADK-PS1-1445 | 1445 | 1,9 | 0,9 | 1,2 | 3,3 | 3,6 | 206,9 | 24 | 25,6 | 6,5 | 4,3 | 20,1 | 0,9 | 0,8 | 11,3 | 0,6 | 1,2 | 7,5 |
| ADK-PS1-1450 | 1450 | 0,9 | 0,8 | 1,1 | 4,3 | 3,7 | 290,3 | 20,4 | 18,6 | 3 | 4,1 | 34,1 | 1 | 0,8 | 10,5 | 0,6 | 0,9 | 7,5 |
| ADK-PS1-1455 | 1455 | 1,8 | 0,8 | 1,1 | 5,5 | 7,1 | 226,7 | 26 | 20,5 | 2,8 | 4,3 | 32,2 | 1 | 0,9 | 10,6 | 0,6 | 1,3 | 11,6 |
| ADK-PS1-1460 | 1460 | 1 | 1,1 | 1,2 | 2,2 | 3,6 | 190,6 | 29,3 | 20,5 | 4,9 | 4 | 32,6 | 1,1 | 0,9 | 7,9 | 0,6 | 0,6 | 8,7 |
| ADK-PS1-1465 | 1465 | 1,8 | 1 | 1,5 | 5,5 | 5,7 | 185,8 | 20,2 | 27,2 | 3 | 4,5 | 35,2 | 1,1 | 0,9 | 6,5 | 0,6 | 0,6 | 17,2 |
| ADK-PS1-1470 | 1470 | 0,5 | 0,9 | 1,1 | 2,1 | 4,3 | 390,3 | 23,3 | 22,2 | 2,9 | 4,4 | 26,6 | 1 | 0,9 | 10,6 | 0,6 | 1 | 10,9 |
| ADK-PS1-1475 | 1475 | 0,9 | 0,9 | 1,1 | 3,3 | 3,5 | 191,4 | 24,6 | 41,3 | 2,9 | 4,4 | 39,6 | 1,1 | 0,8 | 8,4 | 0,6 | 0,6 | 7,3 |
| ADK-PS1-1480 | 1480 | 0,8 | 1 | 1,1 | 4,3 | 3,4 | 268,2 | 18,3 | 22,1 | 3,1 | 5 | 37,6 | 1 | 0,8 | 5,4 | 0,6 | 0,5 | 6,6 |
| ADK-PS1-1485 | 1485 | 1,9 | 0,9 | 1,2 | 6,5 | 5,3 | 258,3 | 27,4 | 27,8 | 2,8 | 4,4 | 31,3 | 1,1 | 0,9 | 8,5 | 0,6 | 0,6 | 10,5 |
| ADK-PS1-1490 | 1490 | 1,5 | 0,9 | 1,2 | 2,1 | 5,1 | 262,6 | 26,7 | 48,2 | 2,9 | 4,8 | 19,5 | 1 | 0,9 | 12,2 | 0,6 | 1,6 | 8,6 |
| ADK-PS1-1495 | 1495 | 1,6 | 2,4 | 1,1 | 7,6 | 8,6 | 235,2 | 26,6 | 39,8 | 2,4 | 4,5 | 40,3 | 1,1 | 0,5 | 10,1 | 0,5 | 2 | 8,1 |
| ADK-PS1-1500 | 1500 | 0,4 | 0,8 | 1,1 | 2 | 8,1 | 222 | 18,4 | 36,2 | 3 | 4,7 | 34,6 | 1 | 0,8 | 11,6 | 0,6 | 1,3 | 8,1 |
| ADK-PS1-1505 | 1505 | 0,9 | 1 | 0,4 | 2 | 7,2 | 185,3 | 22,8 | 30,7 | 2,8 | 4,8 | 24 | 0,9 | 0,8 | 10,5 | 0,8 | 0,5 | 7,9 |
| ADK-PS1-1510 | 1510 | 1,2 | 1,7 | 1,2 | 2,1 | 3,7 | 464,1 | 25,8 | 32,1 | 3,8 | 4,7 | 9,9 | 0,8 | 0,8 | 10,2 | 0,6 | 0,8 | 8,5 |
| ADK-PS1-1515 | 1515 | 1,4 | 0,9 | 1,2 | 2,1 | 5,5 | 326,5 | 28,5 | 28 | 2,3 | 4,7 | 38 | 1,1 | 0,5 | 11,8 | 0,4 | 0,6 | 7,9 |
| ADK-PS1-1520 | 1520 | 0,9 | 0,8 | 1,1 | 2,1 | 10,3 | 190,2 | 21,2 | 30,3 | 2,6 | 4,9 | 28,3 | 1 | 0,8 | 7 | 0,5 | 0,6 | 8,1 |
| ADK-PS1-1525 | 1525 | 1,2 | 1 | 1,2 | 2,1 | 3,7 | 299,3 | 20,1 | 40,5 | 3,1 | 4,9 | 20,8 | 0,9 | 0,6 | 8,6 | 0,6 | 0,6 | 8,4 |

Table F.1 XRF analyses results of samples from Akköy field (cont'd)

| Element | depth | $Na_2O$ | MgO | $Al_2O_3$ | $SiO_2$ | $P_2O_5$ | $SO_3$ | Cl | $K_2O$ | CaO | $TiO_2$ | $V_2O_5$ | $Cr_2O_3$ | MnO | $Fe_2O_3$ | LOI | Total |
|---|---|---|---|---|---|---|---|---|---|---|---|---|---|---|---|---|---|
| Sample No\Dimension | m | % | % | % | % | % | % | % | % | % | % | % | % | % | % | % | % |
| ADK-PS2-755 | 755 | 0,05 | 4,756 | 5,445 | 31,46 | 0,0435 | 0,3899 | 0,03953 | 0,9845 | 23,82 | 0,3559 | 0,0117 | 0,0673 | 0,0593 | 3,895 | 28,63 | 100,01 |
| ADK-PS2-760 | 760 | 0,046 | 1,879 | 6,051 | 38,38 | 0,0657 | 0,2728 | 0,01788 | 1,271 | 23,91 | 0,3485 | 0,0074 | 0,0374 | 0,053 | 2,596 | 24,99 | 99,93 |
| ADK-PS2-765 | 765 | 0,051 | 2,257 | 7,675 | 37,95 | 0,0808 | 0,2482 | 0,01624 | 1,571 | 20,86 | 0,4451 | 0,0116 | 0,0343 | 0,0482 | 3,487 | 24,87 | 99,61 |
| ADK-PS2-770 | 770 | 0,05 | 1,492 | 4,718 | 33,47 | 0,0506 | 0,3494 | 0,0287 | 0,962 | 27,86 | 0,2956 | 0,0068 | 0,0439 | 0,041 | 1,876 | 28,73 | 99,97 |
| ADK-PS2-775 | 775 | 0,17 | 1,555 | 4,589 | 36,24 | 0,0584 | 0,449 | 0,04128 | 0,9907 | 26,09 | 0,3116 | 0,0057 | 0,0421 | 0,0442 | 1,673 | 28,05 | 100,31 |
| ADK-PS2-780 | 780 | 0,13 | 2,4 | 7,428 | 38,28 | 0,0625 | 1,114 | 0,01799 | 1,46 | 21,26 | 0,4568 | 0,015 | 0,05 | 0,045 | 2,844 | 24,53 | 100,09 |
| ADK-PS2-785 | 785 | 0,053 | 1,733 | 4,901 | 30,84 | 0,0585 | 1,504 | 0,02429 | 0,9953 | 29,11 | 0,3172 | 0,0081 | 0,0441 | 0,0419 | 1,921 | 27,89 | 99,44 |
| ADK-PS2-790 | 790 | 0,051 | 1,321 | 3,209 | 25,58 | 0,0403 | 0,9951 | 0,02407 | 0,7338 | 35,8 | 0,2125 | 0,0062 | 0,0321 | 0,0406 | 1,208 | 30,62 | 99,87 |
| ADK-PS2-795 | 795 | 0,049 | 1,821 | 4,978 | 35,14 | 0,0688 | 0,3079 | 0,01836 | 1,066 | 25,83 | 0,2977 | 0,0093 | 0,0338 | 0,0405 | 2,131 | 28,91 | 100,70 |
| ADK-PS2-800 | 800 | 0,052 | 1,23 | 4,21 | 34,87 | 0,0533 | 0,4969 | 0,02619 | 1,013 | 27,69 | 0,2709 | 0,0088 | 0,0406 | 0,0385 | 1,659 | 28,51 | 100,17 |
| ADK-PS2-805 | 805 | 0,15 | 1,319 | 5,092 | 39,93 | 0,0886 | 0,273 | 0,04066 | 1,03 | 24,25 | 0,4097 | 0,011 | 0,0819 | 0,0431 | 1,808 | 24,88 | 99,41 |
| ADK-PS2-810 | 810 | 0,049 | 1,575 | 5,839 | 37,95 | 0,0796 | 0,3221 | 0,03415 | 1,21 | 24,05 | 0,3781 | 0,0115 | 0,0476 | 0,0713 | 2,573 | 25,87 | 100,06 |
| ADK-PS2-815 | 815 | 0,048 | 2,701 | 10,29 | 47,1 | 0,1118 | 0,7558 | 0,0196 | 1,883 | 17,46 | 0,5514 | 0,0164 | 0,0395 | 0,0808 | 5,309 | 14,05 | 100,42 |
| ADK-PS2-820 | 820 | 0,05 | 2,694 | 11,75 | 51,66 | 0,1192 | 0,5445 | 0,01952 | 2,134 | 12,82 | 0,5763 | 0,016 | 0,0438 | 0,0944 | 6,104 | 11,63 | 100,26 |
| ADK-PS2-825 | 825 | 0,29 | 2,603 | 10,01 | 47,81 | 0,1022 | 1,001 | 0,02184 | 1,906 | 17,78 | 0,5383 | 0,0191 | 0,0357 | 0,0681 | 5,108 | 12,55 | 99,84 |
| ADK-PS2-830 | 830 | 0,051 | 1,861 | 7,443 | 32,03 | 0,0921 | 1,373 | 0,02239 | 1,543 | 25,91 | 0,4393 | 0,0149 | 0,0324 | 0,0516 | 3,572 | 25,52 | 99,96 |
| ADK-PS2-835 | 835 | 0,29 | 2,626 | 10,69 | 49,93 | 0,1071 | 1,18 | 0,01621 | 2,03 | 16,35 | 0,5848 | 0,0198 | 0,0383 | 0,0702 | 5,083 | 10,63 | 99,65 |
| ADK-PS2-840 | 840 | 0,049 | 2,621 | 11,91 | 51,84 | 0,1118 | 0,632 | 0,01523 | 2,212 | 13,37 | 0,5933 | 0,0192 | 0,0465 | 0,0751 | 5,709 | 10,77 | 99,97 |
| ADK-PS2-845 | 845 | 0,052 | 1,513 | 5,862 | 42,1 | 0,0729 | 1,261 | 0,03448 | 1,175 | 28,31 | 0,3819 | 0,0091 | 0,0451 | 0,0449 | 2,392 | 16,53 | 99,78 |
| ADK-PS2-850 | 850 | 0,051 | 1,366 | 5,081 | 27,48 | 0,0615 | 1,075 | 0,02768 | 1,067 | 31,93 | 0,3239 | 0,0105 | 0,0307 | 0,0486 | 2,183 | 29,73 | 100,47 |
| ADK-PS2-855 | 855 | 0,048 | 0,57 | 1,685 | 18,84 | 0,0464 | 0,9691 | 0,0078 | 0,4273 | 47,49 | 0,1153 | 0,0027 | 0,012 | 0,042 | 1,238 | 28,95 | 100,44 |
| ADK-PS2-860 | 860 | 0,05 | 0,437 | 2,021 | 15,18 | 0,038 | 0,8162 | 0,009 | 0,4604 | 46,61 | 0,1811 | 0,0035 | 0,0238 | 0,0494 | 1,424 | 32,62 | 99,92 |
| ADK-PS2-865 | 865 | 0,05 | 1,17 | 4,868 | 22,96 | 0,0614 | 0,9911 | 0,00934 | 0,9872 | 37,6 | 0,3215 | 0,0102 | 0,0309 | 0,0539 | 2,581 | 28,96 | 100,65 |
| ADK-PS2-870 | 870 | 0,047 | 0,295 | 1,457 | 21,32 | 0,0594 | 1,107 | 0,00995 | 0,4385 | 41,61 | 0,107 | 0,0046 | 0,0104 | 0,0581 | 0,9935 | 32,73 | 100,25 |
| ADK-PS2-875 | 875 | 0,05 | 1,805 | 8,171 | 39,74 | 0,0875 | 1,034 | 0,02934 | 1,616 | 21,64 | 0,4989 | 0,0141 | 0,0386 | 0,0563 | 3,435 | 21,74 | 99,96 |
| ADK-PS2-1255 | 1255 | 0,047 | 6,691 | 6,013 | 39,86 | 0,058 | 0,2563 | 0,00788 | 0,7825 | 22,99 | 0,378 | 0,0144 | 0,0482 | 0,0847 | 3,996 | 18,93 | 100,16 |
| ADK-PS2-1260 | 1260 | 0,05 | 8,098 | 6,486 | 41,65 | 0,0522 | 0,3945 | 0,00458 | 0,8685 | 19,45 | 0,4021 | 0,0159 | 0,0687 | 0,1269 | 5,675 | 16,73 | 100,07 |
| ADK-PS2-1265 | 1265 | 0,052 | 4,99 | 6,127 | 39,4 | 0,0714 | 0,2505 | 0,00736 | 0,7899 | 23,04 | 0,3972 | 0,0145 | 0,0489 | 0,2313 | 9,652 | 14,88 | 99,95 |
| ADK-PS2-1270 | 1270 | 0,049 | 3,83 | 8,058 | 44,83 | 0,0597 | 0,2955 | 0,00081 | 1,111 | 19,85 | 0,4802 | 0,0208 | 0,0789 | 0,104 | 7,059 | 14,72 | 100,55 |
| ADK-PS2-1275 | 1275 | 0,052 | 4,087 | 6,682 | 38,19 | 0,051 | 0,4555 | 0,00812 | 0,8652 | 19,71 | 0,3844 | 0,0167 | 0,047 | 0,2445 | 12,92 | 16,53 | 100,24 |
| ADK-PS2-1280 | 1280 | 0,052 | 3,768 | 8,247 | 45,19 | 0,0642 | 0,7556 | 0,01379 | 1,177 | 19,47 | 0,4907 | 0,0164 | 0,0716 | 0,101 | 7,093 | 13,64 | 100,15 |
| ADK-PS2-1285 | 1285 | 0,051 | 2,536 | 8,128 | 42,84 | 0,0695 | 0,7002 | 0,01155 | 1,233 | 20,62 | 0,4617 | 0,0183 | 0,0537 | 0,1136 | 7,776 | 15,88 | 100,49 |

Table F.1 XRF analyses results of samples from Akköy field (cont’d)

| **Element** | **depth** | **$Na_2O$** | **MgO** | **$Al_2O_3$** | **$SiO_2$** | **$P_2O_5$** | **$SO_3$** | **Cl** | **$K_2O$** | **CaO** | **$TiO_2$** | **$V_2O_5$** | **$Cr_2O_3$** | **MnO** | **$Fe_2O_3$** | **LOI** | **Total** |
|---|---|---|---|---|---|---|---|---|---|---|---|---|---|---|---|---|---|
| **Sample No\Dimension** | **m** | **%** | **%** | **%** | **%** | **%** | **%** | **%** | **%** | **%** | **%** | **%** | **%** | **%** | **%** | **%** | **%** |
| ADK-PS2-1290 | 1290 | 0,051 | 2,561 | 7,144 | 41,55 | 0,0721 | 0,7962 | 0,02113 | 1,035 | 24,22 | 0,405 | 0,0108 | 0,0492 | 0,115 | 6,504 | 15,62 | 100,15 |
| ADK-PS2-1295 | 1295 | 0,053 | 3,579 | 7,118 | 40,25 | 0,0637 | 0,6777 | 0,01348 | 1,077 | 23 | 0,4294 | 0,02 | 0,0561 | 0,1362 | 8,941 | 14,92 | 100,33 |
| ADK-PS2-1300 | 1300 | 0,054 | 3,694 | 6,642 | 38,7 | 0,0607 | 0,6058 | 0,01466 | 0,8663 | 20,61 | 0,3924 | 0,0182 | 0,0466 | 0,26 | 12,63 | 14,36 | 98,95 |
| ADK-PS2-1305 | 1305 | 0,05 | 3,142 | 4,907 | 36,76 | 0,0616 | 0,5247 | 0,01414 | 0,744 | 29,48 | 0,3051 | 0,0127 | 0,0768 | 0,1152 | 5,664 | 18,37 | 100,23 |
| ADK-PS2-1310 | 1310 | 0,048 | 4,864 | 1,856 | 19,97 | 0,0228 | 0,1954 | 0,01159 | 0,2895 | 35 | 0,1777 | 0,0089 | 0,0709 | 0,1095 | 3,961 | 34,28 | 100,87 |
| ADK-PS2-1315 | 1315 | 0,051 | 4,708 | 4,129 | 24,07 | 0,0451 | 0,286 | 0,0113 | 0,6727 | 29,26 | 0,2734 | 0,0103 | 0,0969 | 0,1184 | 5,969 | 30,62 | 100,32 |
| ADK-PS2-1320 | 1320 | 0,051 | 4,674 | 3,79 | 24,22 | 0,0353 | 0,2336 | 0,01205 | 0,595 | 30,19 | 0,2536 | 0,0096 | 0,0834 | 0,1007 | 4,831 | 30,51 | 99,59 |
| ADK-PS2-1325 | 1325 | 0,05 | 4,883 | 3,625 | 22,24 | 0,0342 | 0,2541 | 0,01453 | 0,5916 | 31,94 | 0,2333 | 0,011 | 0,1035 | 0,0835 | 4,504 | 31,73 | 100,30 |
| ADK-PS2-1330 | 1330 | 0,051 | 5,058 | 4,061 | 22,01 | 0,0374 | 0,3293 | 0,01346 | 0,6187 | 31,21 | 0,2561 | 0,0087 | 0,0575 | 0,093 | 4,544 | 31,48 | 99,83 |
| ADK-PS2-1335 | 1335 | 0,052 | 4,095 | 5,537 | 36,33 | 0,0496 | 0,6643 | 0,01581 | 0,7682 | 25,42 | 0,3251 | 0,0163 | 0,0654 | 0,1723 | 9,363 | 17,83 | 100,70 |
| ADK-PS2-1340 | 1340 | 0,049 | 8,14 | 4,135 | 30,19 | 0,0247 | 0,2106 | 0,00941 | 0,5597 | 28,37 | 0,2315 | 0,0104 | 0,0616 | 0,0722 | 4,104 | 23,62 | 99,79 |
| ADK-PS2-1345 | 1345 | 0,051 | 9,276 | 3,158 | 37,33 | 0,0217 | 0,3331 | 0,01382 | 0,3934 | 29,55 | 0,1868 | 0,0087 | 0,0402 | 0,1014 | 4,854 | 14,82 | 100,14 |
| ADK-PS2-1350 | 1350 | 0,054 | 2,425 | 5,055 | 27,18 | 0,0739 | 0,3024 | 0,01777 | 0,5977 | 30,47 | 0,6055 | 0,0138 | 0,0725 | 0,1081 | 5,114 | 27,53 | 99,62 |
| ADK-PS2-1355 | 1355 | 0,052 | 2,237 | 3,452 | 25,62 | 0,0508 | 0,2484 | 0,01033 | 0,4467 | 32,72 | 0,3544 | 0,0115 | 0,0535 | 0,1012 | 3,521 | 32,93 | 101,81 |
| ADK-PS2-1360 | 1360 | 0,054 | 2,071 | 4,674 | 31,31 | 0,1021 | 0,1511 | 0,01801 | 0,5471 | 27,9 | 0,7085 | 0,0154 | 0,0648 | 0,1258 | 5,162 | 27,82 | 100,72 |
| ADK-PS2-1365 | 1365 | 0,053 | 2,324 | 6,354 | 31,88 | 0,1 | 0,1384 | 0,00376 | 0,9688 | 24,32 | 0,5579 | 0,0134 | 0,0643 | 0,1289 | 6,953 | 25,921 | 99,78 |
| ADK-PS2-1370 | 1370 | 0,053 | 4,379 | 3,899 | 29,73 | 0,0717 | 0,1078 | 0,00821 | 0,3403 | 27,98 | 0,411 | 0,012 | 0,0647 | 0,1404 | 4,476 | 28,83 | 100,50 |
| ADK-PS2-1375 | 1375 | 0,051 | 5,14 | 4,477 | 30,4 | 0,0689 | 0,4832 | 0,01371 | 0,5781 | 26,34 | 0,294 | 0,0133 | 0,0622 | 0,1698 | 5,181 | 26,99 | 100,26 |
| ADK-PS2-1380 | 1380 | 0,051 | 4,945 | 4,814 | 30,08 | 0,0674 | 0,1566 | 0,01213 | 0,4924 | 26,02 | 0,386 | 0,0171 | 0,0979 | 0,1746 | 6,006 | 26,73 | 100,05 |
| ADK-PS2-1385 | 1385 | 0,055 | 1,869 | 1,418 | 10,2 | 0,0083 | 0,1048 | 0,02071 | 0,148 | 49,14 | 0,1493 | 0,0063 | 0,0376 | 0,0813 | 1,981 | 34,88 | 100,10 |
| ADK-PS2-1390 | 1390 | 0,052 | 1,456 | 1,43 | 12,7 | 0,0054 | 0,161 | 0,01933 | 0,192 | 46,73 | 0,1633 | 0,004 | 0,0224 | 0,0713 | 2,136 | 34,28 | 99,42 |
| ADK-PS2-1395 | 1395 | 0,053 | 0,314 | 0,607 | 3,784 | 0,0027 | 0,0637 | 0,0198 | 0,0053 | 57,29 | 0,0857 | 0,0062 | 0,0119 | 0,029 | 0,8574 | 36,73 | 99,86 |
| ADK-PS2-1400 | 1400 | 0,054 | 2,109 | 0,85 | 7,685 | 0,0069 | 0,0687 | 0,02105 | 0,1084 | 48,99 | 0,0932 | 0,0121 | 0,0243 | 0,0404 | 1,137 | 39,03 | 100,23 |
| ADK-PS2-1405 | 1405 | 0,054 | 2,026 | 1,286 | 10,13 | 0,017 | 0,0893 | 0,02278 | 0,162 | 47,78 | 0,1544 | 0,0067 | 0,0441 | 0,0689 | 1,748 | 36,82 | 100,41 |
| ADK-PS2-1410 | 1410 | 0,053 | 2,367 | 0,817 | 6,25 | 0,0029 | 0,0734 | 0,01877 | 0,1286 | 51,32 | 0,07 | 0,007 | 0,0198 | 0,0385 | 1,032 | 31,65 | 93,85 |
| ADK-PS2-1415 | 1415 | 0,051 | 0,042 | 1,378 | 3,966 | 0,0027 | 0,0596 | 0,01813 | 0,4311 | 56,8 | 0,0903 | 0,0014 | 0,0092 | 0,0176 | 0,5032 | 36,83 | 100,20 |
| ADK-PS2-1420 | 1420 | 0,05 | 0,115 | 0,506 | 1,859 | 0,0026 | 0,0629 | 0,02083 | 0,1437 | 55,02 | 0,0437 | 0,0014 | 0,005 | 0,01228 | 0,3152 | 41,48 | 99,64 |
| ADK-PS2-1425 | 1425 | 0,05 | 0,327 | 0,283 | 1,362 | 0,0026 | 0,0807 | 0,0226 | 0,0045 | 55,05 | 0,0189 | 0,0012 | 0,00295 | 0,01264 | 0,4424 | 42,48 | 100,14 |
| ADK-PS-2-1665 | 1665 | 0,047 | 1,066 | 0,838 | 4,8 | 0,0027 | 0,1864 | 0,02895 | 0,131 | 55,42 | 0,0686 | 0,006 | 0,005 | 0,0215 | 0,7437 | 35,73 | 99,09 |
| ADK-PS-2-2100 | 2100 | 0,053 | 1,618 | 4,797 | 26,91 | 0,0537 | 0,4222 | 0,01449 | 0,8931 | 31,9 | 0,4313 | 0,0074 | 0,00594 | 0,0456 | 3,655 | 29,73 | 100,54 |
| ADK-PS-2-2195 | 2195 | 0,054 | 1,984 | 6,35 | 31,65 | 0,0749 | 0,6386 | 0,04333 | 1,144 | 27,52 | 0,5106 | 0,0155 | 0,00622 | 0,0619 | 4,611 | 25,82 | 100,48 |

Table F.1 XRF analyses results of samples from Akköy field (cont'd)

| Element | depth | Co | Ni | Cu | Zn | Ga | Ge | As | Se | Br | Rb | Sr | Y | Zr | Nb | Mo | Cd | In |
|---|---|---|---|---|---|---|---|---|---|---|---|---|---|---|---|---|---|---|
| Sample No\Dimension | m | ppm | ppm | ppm | ppm | ppm | ppm | ppm | ppm | ppm | ppm | ppm | ppm | ppm | ppm | ppm | ppm | ppm |
| ADK-PS2-755 | 755 | 40,2 | 261,1 | 11,3 | 33 | 8,6 | 0,6 | 5,7 | 0,3 | 2,1 | 46,1 | 776,4 | 10 | 125,1 | 7,9 | 3,3 | 0,8 | 0,8 |
| ADK-PS2-760 | 760 | 26,5 | 120 | 6,5 | 29,3 | 8,6 | 1,8 | 8,3 | 0,4 | 1,9 | 47,5 | 661,8 | 14,2 | 124,3 | 11,1 | 3 | 0,8 | 0,8 |
| ADK-PS2-765 | 765 | 32,5 | 143,6 | 13 | 38,9 | 10,6 | 1,3 | 9,1 | 0,3 | 1,4 | 63,6 | 708 | 14,3 | 139,6 | 14,9 | 3,4 | 0,9 | 0,8 |
| ADK-PS2-770 | 770 | 30,5 | 84 | 5 | 18,4 | 7,2 | 0,7 | 5 | 0,3 | 0,8 | 37,7 | 639,6 | 11,5 | 130,5 | 10,4 | 6,2 | 0,8 | 0,9 |
| ADK-PS2-775 | 775 | 22,6 | 79 | 3,7 | 16,7 | 7,4 | 0,9 | 5,2 | 0,4 | 1,7 | 35,7 | 706,6 | 10,4 | 162,3 | 7,7 | 3,4 | 0,8 | 0,8 |
| ADK-PS2-780 | 780 | 32,1 | 160,7 | 10,5 | 35,7 | 9,9 | 0,7 | 10 | 0,3 | 0,9 | 60 | 775,4 | 16,7 | 173,8 | 11,3 | 2,7 | 0,9 | 0,8 |
| ADK-PS2-785 | 785 | 20,8 | 90,3 | 3,9 | 19,7 | 7,7 | 0,5 | 15,8 | 0,3 | 1,3 | 38,1 | 789,9 | 12,1 | 177,1 | 10,7 | 2,9 | 0,8 | 0,8 |
| ADK-PS2-790 | 790 | 25,7 | 49 | 2,8 | 11,4 | 6,3 | 0,7 | 25,3 | 0,4 | 1,5 | 27,8 | 866,6 | 7,3 | 139,9 | 3,6 | 3,6 | 0,9 | 0,9 |
| ADK-PS2-795 | 795 | 23,5 | 100 | 5,5 | 20,6 | 6,4 | 1,1 | 8,2 | 0,3 | 1,7 | 40,3 | 674 | 9,3 | 131,4 | 3,9 | 3,9 | 1,7 | 0,9 |
| ADK-PS2-800 | 800 | 19,9 | 62,8 | 2,7 | 16,9 | 5,6 | 0,8 | 9,9 | 0,4 | 1,7 | 36,4 | 693,1 | 8 | 124,5 | 8 | 2,7 | 0,8 | 0,8 |
| ADK-PS2-805 | 805 | 11,4 | 82,4 | 4,7 | 20,5 | 6,9 | 0,8 | 7,1 | 0,4 | 0,6 | 35,5 | 495,7 | 14,7 | 254,5 | 9,4 | 3,1 | 0,8 | 0,7 |
| ADK-PS2-810 | 810 | 38 | 119,6 | 4,3 | 28,7 | 9,5 | 0,7 | 11,4 | 0,4 | 1 | 48,5 | 528,9 | 14,5 | 220,9 | 8,9 | 3,2 | 0,9 | 0,8 |
| ADK-PS2-815 | 815 | 47,1 | 245,1 | 24,4 | 55,7 | 15,9 | 1,5 | 24,8 | 0,3 | 1,5 | 87,8 | 896,9 | 19,7 | 153,5 | 13,4 | 3,1 | 0,9 | 0,4 |
| ADK-PS2-820 | 820 | 43,2 | 251,2 | 24,3 | 65,6 | 16,3 | 0,8 | 25,9 | 0,3 | 1,4 | 98,3 | 633,7 | 21,7 | 200,6 | 17,5 | 3,4 | 1,8 | 0,9 |
| ADK-PS2-825 | 825 | 45,1 | 246 | 22,9 | 59,2 | 15,1 | 0,4 | 17,5 | 0,3 | 1,2 | 89,8 | 1179 | 16,4 | 145,2 | 13,7 | 3 | 0,9 | 0,8 |
| ADK-PS2-830 | 830 | 35,8 | 160,9 | 13,6 | 42,3 | 10,6 | 1,4 | 17,4 | 0,3 | 1,4 | 64 | 1250 | 14 | 149,1 | 14,2 | 3,9 | 0,8 | 0,8 |
| ADK-PS2-835 | 835 | 49,2 | 225,2 | 21,7 | 62,9 | 16,1 | 0,5 | 21,6 | 0,3 | 1,3 | 87,6 | 830,5 | 21,5 | 162,6 | 3,8 | 3,2 | 0,8 | 0,8 |
| ADK-PS2-840 | 840 | 36,5 | 258,5 | 25,6 | 68,3 | 16,5 | 0,8 | 18,8 | 1 | 1,1 | 102,6 | 805,8 | 22,6 | 175,8 | 12,6 | 3,2 | 0,9 | 0,8 |
| ADK-PS2-845 | 845 | 21,1 | 95,8 | 7,2 | 29,1 | 8,4 | 0,6 | 12,8 | 0,3 | 1,3 | 46,3 | 895,6 | 10,6 | 152,6 | 10,9 | 3,7 | 0,9 | 0,8 |
| ADK-PS2-850 | 850 | 14,6 | 98,6 | 9,1 | 25,4 | 7,6 | 0,6 | 8,8 | 0,3 | 1,6 | 45,6 | 1055 | 8,3 | 122,2 | 7,1 | 3,3 | 0,9 | 0,8 |
| ADK-PS2-855 | 855 | 19,3 | 76,2 | 1,2 | 9 | 3,5 | 0,5 | 6,5 | 0,3 | 1,6 | 18,6 | 1082 | 0,7 | 26,7 | 6,2 | 3,7 | 0,9 | 0,9 |
| ADK-PS2-860 | 860 | 24 | 45,7 | 1 | 10,1 | 4,4 | 0,8 | 5,6 | 0,4 | 1,2 | 17,2 | 840,5 | 4,9 | 86,5 | 4,2 | 6,1 | 0,5 | 1 |
| ADK-PS2-865 | 865 | 15,6 | 104,3 | 6 | 23,9 | 8,5 | 1,1 | 10,1 | 0,6 | 1,3 | 42,1 | 893,5 | 9,1 | 82,3 | 11,6 | 3,7 | 0,9 | 0,9 |
| ADK-PS2-870 | 870 | 15,6 | 27,3 | 1 | 4,5 | 3,4 | 0,8 | 5 | 0,4 | 0,3 | 15,7 | 579,4 | 3,4 | 50,6 | 3,5 | 3,2 | 0,9 | 0,8 |
| ADK-PS2-875 | 875 | 36 | 179,8 | 15,2 | 40,9 | 14 | 0,6 | 10,8 | 0,3 | 1,1 | 73,2 | 754 | 16,8 | 173,4 | 12,5 | 3 | 0,9 | 0,8 |
| ADK-PS2-1255 | 1255 | 28,8 | 237,7 | 11,7 | 33,3 | 9 | 0,4 | 2,3 | 0,3 | 1,4 | 33 | 308,2 | 14,5 | 87,2 | 9,1 | 3 | 0,9 | 0,8 |
| ADK-PS2-1260 | 1260 | 61,9 | 515,3 | 18,8 | 51,3 | 10,6 | 1,9 | 4 | 0,3 | 2,6 | 36,6 | 703,2 | 13,3 | 81,5 | 8,9 | 2,9 | 0,8 | 0,8 |
| ADK-PS2-1265 | 1265 | 93 | 587,5 | 25,3 | 82,2 | 6,7 | 0,6 | 1,8 | 0,3 | 0,3 | 33,4 | 401,2 | 22,8 | 106,4 | 9,7 | 4,2 | 1 | 0,8 |
| ADK-PS2-1270 | 1270 | 43,8 | 405,9 | 22,3 | 51,7 | 11,8 | 1,6 | 3,2 | 0,3 | 1 | 50,6 | 326,3 | 17,8 | 108,2 | 11,5 | 3,3 | 0,9 | 0,8 |
| ADK-PS2-1275 | 1275 | 119 | 684,3 | 28 | 96,2 | 9,2 | 0,6 | 1,3 | 0,3 | 1,2 | 43 | 346,7 | 20,3 | 81,3 | 11,3 | 5,8 | 1 | 0,9 |
| ADK-PS2-1280 | 1280 | 48,8 | 403,6 | 20,4 | 57,1 | 10,8 | 1,5 | 6,4 | 0,3 | 0,5 | 55 | 384,2 | 18,3 | 101,1 | 16,2 | 5,4 | 0,9 | 0,8 |
| ADK-PS2-1285 | 1285 | 67,2 | 454,8 | 23 | 62,6 | 13 | 0,4 | 4 | 0,3 | 0,3 | 62 | 415,1 | 16,4 | 118,2 | 11,5 | 3,9 | 0,9 | 0,8 |

Table F.1 XRF analyses results of samples from Akköy field (cont’d)

| **Element** | **depth** | **Sn** | **Sb** | **Te** | **I** | **Cs** | **Ba** | **La** | **Ce** | **Hf** | **Ta** | **W** | **Hg** | **Tl** | **Pb** | **Bi** | **Th** | **U** |
|---|---|---|---|---|---|---|---|---|---|---|---|---|---|---|---|---|---|---|
| **Sample No\Dimension** | **m** | **ppm** | **ppm** | **ppm** | **ppm** | **ppm** | **ppm** | **ppm** | **ppm** | **ppm** | **ppm** | **ppm** | **ppm** | **ppm** | **ppm** | **ppm** | **ppm** | **ppm** |
| ADK-PS2-755 | 755 | 1 | 1,5 | 1,2 | 8,3 | 5 | 239 | 20,5 | 38,9 | 2,7 | 3,8 | 39,6 | 1,1 | 0,8 | 10,9 | 0,9 | 3,3 | 8,4 |
| ADK-PS2-760 | 760 | 0,9 | 0,9 | 1,2 | 3,5 | 4,1 | 287,9 | 24 | 31,1 | 2,7 | 3 | 109,3 | 1,3 | 0,9 | 14,1 | 0,6 | 5,8 | 8,8 |
| ADK-PS2-765 | 765 | 1 | 0,9 | 1,2 | 4,2 | 3,7 | 321 | 29,8 | 35 | 2,6 | 3,2 | 42,9 | 1,1 | 0,8 | 17,8 | 0,6 | 5,7 | 8,5 |
| ADK-PS2-770 | 770 | 0,9 | 0,9 | 1,2 | 4,3 | 3,5 | 235,8 | 24,6 | 39,9 | 2,8 | 2,8 | 91,6 | 1,2 | 0,8 | 10,9 | 0,6 | 4,5 | 7,7 |
| ADK-PS2-775 | 775 | 0,9 | 1,5 | 1,2 | 2,3 | 3,5 | 243,6 | 21,2 | 41,3 | 3,5 | 2,8 | 152,8 | 1,5 | 0,7 | 11,6 | 0,6 | 5,1 | 8,6 |
| ADK-PS2-780 | 780 | 0,9 | 0,9 | 1,1 | 2,4 | 3,6 | 306,5 | 23 | 42,6 | 2,7 | 3,2 | 52,1 | 1,1 | 0,8 | 15,7 | 0,6 | 7,2 | 8,3 |
| ADK-PS2-785 | 785 | 0,9 | 1,9 | 1,1 | 4,9 | 3,5 | 253,2 | 20,8 | 25,7 | 2,8 | 2,8 | 69,2 | 1,2 | 0,9 | 12,1 | 1 | 5,8 | 7,5 |
| ADK-PS2-790 | 790 | 0,9 | 1 | 0,8 | 4,4 | 3,6 | 225,1 | 21,2 | 28,2 | 2,7 | 2,6 | 82,9 | 1,2 | 0,8 | 8 | 0,7 | 4 | 9,4 |
| ADK-PS2-795 | 795 | 0,7 | 1 | 1,2 | 4,3 | 4,7 | 225,6 | 26,5 | 29,8 | 4,7 | 2,8 | 75,2 | 1,2 | 0,9 | 11,8 | 0,4 | 5,5 | 14,6 |
| ADK-PS2-800 | 800 | 1,1 | 1,7 | 1,2 | 5 | 3,5 | 302 | 18,4 | 34,2 | 1,4 | 2,5 | 99,9 | 1,2 | 0,8 | 11,1 | 0,6 | 4,9 | 6,9 |
| ADK-PS2-805 | 805 | 2,1 | 0,9 | 1,7 | 2,9 | 3,6 | 224,8 | 19,8 | 18,5 | 3,7 | 3,3 | 112 | 1,3 | 0,8 | 11,1 | 0,6 | 5,6 | 7,7 |
| ADK-PS2-810 | 810 | 1,3 | 0,9 | 1,1 | 2,1 | 3,5 | 266,2 | 26,3 | 46,7 | 2,6 | 2,2 | 98,4 | 1,3 | 0,8 | 13,5 | 0,6 | 7,8 | 12 |
| ADK-PS2-815 | 815 | 3,2 | 2,6 | 1,2 | 2,1 | 6,2 | 363 | 30,9 | 61,9 | 2,9 | 4 | 6,8 | 0,9 | 0,7 | 22,7 | 0,4 | 9,7 | 7,8 |
| ADK-PS2-820 | 820 | 3,9 | 3,6 | 1,3 | 2,2 | 3,5 | 386,1 | 38 | 78,2 | 5,1 | 3,9 | 14,6 | 0,9 | 0,6 | 27,5 | 0,7 | 10,3 | 14,8 |
| ADK-PS2-825 | 825 | 2,1 | 1,8 | 1,2 | 1,7 | 3,2 | 363,5 | 20,6 | 35,8 | 3,1 | 4,1 | 7 | 0,9 | 0,9 | 25,2 | 0,7 | 9,2 | 8,3 |
| ADK-PS2-830 | 830 | 1,9 | 0,9 | 1,2 | 2,4 | 3,7 | 319,6 | 28,5 | 37,6 | 4,2 | 3,5 | 14,4 | 0,9 | 0,4 | 15,8 | 0,7 | 7,5 | 8,2 |
| ADK-PS2-835 | 835 | 1 | 1 | 1,2 | 2,6 | 6,8 | 382 | 35,5 | 49 | 4,5 | 3,9 | 13,5 | 0,9 | 1 | 25,6 | 0,7 | 9,6 | 11,9 |
| ADK-PS2-840 | 840 | 2,7 | 1,6 | 1,2 | 2,2 | 3,7 | 416 | 33,3 | 60,6 | 4,8 | 4 | 10,5 | 0,5 | 0,8 | 25,3 | 0,4 | 10,5 | 12,6 |
| ADK-PS2-845 | 845 | 1,4 | 0,6 | 1,2 | 2,1 | 6,6 | 260,7 | 22,9 | 41,3 | 2,6 | 2,9 | 43,2 | 1 | 1,2 | 12,9 | 0,6 | 6,9 | 8,6 |
| ADK-PS2-850 | 850 | 3,9 | 1,5 | 1,2 | 2,1 | 7,5 | 275,6 | 14,7 | 26 | 2,4 | 3,1 | 27,9 | 0,9 | 0,9 | 12,5 | 0,6 | 5,1 | 9,4 |
| ADK-PS2-855 | 855 | 1 | 0,9 | 1,2 | 2 | 3,4 | 101,1 | 7,2 | 9,9 | 2,9 | 3,1 | 2,9 | 0,9 | 0,9 | 5,4 | 0,7 | 2,7 | 14,8 |
| ADK-PS2-860 | 860 | 1,1 | 1 | 1,3 | 2,1 | 3,6 | 139,9 | 24,2 | 10 | 3,5 | 2,7 | 38,5 | 1,1 | 0,5 | 6,1 | 0,6 | 2,4 | 9,5 |
| ADK-PS2-865 | 865 | 1,1 | 1,2 | 1,2 | 5,9 | 3,6 | 199,7 | 14,4 | 30,5 | 2,1 | 3,2 | 14,4 | 1 | 0,4 | 11,7 | 0,7 | 4,8 | 16,5 |
| ADK-PS2-870 | 870 | 1 | 1 | 1,2 | 2,1 | 5,4 | 131,7 | 7,4 | 17,2 | 2,6 | 2,3 | 91,2 | 1,3 | 0,8 | 4,8 | 0,5 | 2,4 | 9,7 |
| ADK-PS2-875 | 875 | 2,7 | 2,7 | 1,2 | 2,2 | 5,5 | 393,8 | 25 | 53,2 | 3,2 | 3,5 | 28 | 1 | 0,9 | 18,4 | 0,6 | 10,5 | 8,3 |
| ADK-PS2-1255 | 1255 | 0,9 | 0,9 | 0,7 | 9 | 3,6 | 230,1 | 24 | 26,3 | 1,9 | 3,5 | 25,4 | 0,9 | 0,8 | 10,1 | 0,7 | 2,2 | 10 |
| ADK-PS2-1260 | 1260 | 1,5 | 0,9 | 1,2 | 10 | 3,5 | 184,1 | 19,4 | 29,5 | 2,9 | 4,5 | 6,1 | 0,9 | 0,7 | 12,1 | 0,6 | 0,6 | 8 |
| ADK-PS2-1265 | 1265 | 1,5 | 1 | 1,2 | 4,4 | 3,5 | 128,3 | 28,7 | 45,2 | 3,7 | 5,5 | 9,3 | 1 | 0,8 | 16,4 | 0,7 | 0,7 | 19,7 |
| ADK-PS2-1270 | 1270 | 1,4 | 1 | 0,7 | 2 | 12,6 | 163,2 | 7,5 | 39,4 | 3,1 | 4,5 | 9,1 | 1 | 0,9 | 13,3 | 0,6 | 3,1 | 12,7 |
| ADK-PS2-1275 | 1275 | 1,1 | 0,9 | 0,6 | 7,2 | 11,4 | 135,9 | 37,3 | 38,4 | 4 | 6,3 | 6,4 | 1,2 | 1,1 | 17,1 | 0,8 | 1 | 9,6 |
| ADK-PS2-1280 | 1280 | 2,5 | 1 | 1,2 | 2,1 | 4,5 | 259,9 | 25,4 | 39,1 | 3,2 | 4,6 | 12,1 | 1 | 0,9 | 15,4 | 0,7 | 2,6 | 9,2 |
| ADK-PS2-1285 | 1285 | 2,6 | 1 | 1,2 | 4,8 | 10,9 | 223,5 | 35,1 | 36,3 | 3,2 | 4,8 | 9,3 | 1 | 1 | 18,3 | 0,7 | 4,8 | 9 |

Table F.1 XRF analyses results of samples from Akköy field (cont'd)

| Element | depth | Co | Ni | Cu | Zn | Ga | Ge | As | Se | Br | Rb | Sr | Y | Zr | Nb | Mo | Cd | In |
|---|---|---|---|---|---|---|---|---|---|---|---|---|---|---|---|---|---|---|
| Sample No\Dimension | m | ppm | ppm | ppm | ppm | ppm | ppm | ppm | ppm | ppm | ppm | ppm | ppm | ppm | ppm | ppm | ppm | ppm |
| ADK-PS2-1290 | 1290 | 70 | 358,4 | 18,9 | 57,8 | 11,1 | 0,6 | 7 | 0,3 | 1,3 | 49,4 | 376,2 | 18,3 | 99,3 | 3,8 | 3,5 | 0,9 | 0,9 |
| ADK-PS2-1295 | 1295 | 31,3 | 502,4 | 20,9 | 64,6 | 10,4 | 0,6 | 5,8 | 0,3 | 1,4 | 51 | 368,7 | 17,2 | 98,7 | 10,6 | 13,6 | 0,9 | 0,9 |
| ADK-PS2-1300 | 1300 | 94 | 686,3 | 19 | 94,5 | 8,1 | 0,6 | 5 | 0,3 | 0,3 | 42,1 | 337,8 | 19,6 | 103,5 | 4,5 | 4,3 | 2,2 | 1 |
| ADK-PS2-1305 | 1305 | 38 | 426,9 | 16,4 | 46 | 8,7 | 0,6 | 4,6 | 0,3 | 0,7 | 35,8 | 330,5 | 12 | 97 | 6,3 | 3,7 | 0,9 | 0,9 |
| ADK-PS2-1310 | 1310 | 32,1 | 316,9 | 10,3 | 27,6 | 4,3 | 0,8 | 3,7 | 0,4 | 0,8 | 12,6 | 204,5 | 6,8 | 58,1 | 5,7 | 3,5 | 0,9 | 0,8 |
| ADK-PS2-1315 | 1315 | 70 | 553,2 | 10,7 | 37,7 | 6,3 | 0,5 | 5,2 | 0,6 | 0,3 | 31,2 | 273,4 | 10,8 | 67,9 | 3,4 | 9 | 0,9 | 0,8 |
| ADK-PS2-1320 | 1320 | 54,3 | 482,2 | 15,2 | 34,9 | 7,1 | 0,7 | 4,9 | 0,3 | 1,7 | 30,8 | 305,2 | 11,2 | 77,7 | 8,3 | 10,1 | 0,9 | 0,9 |
| ADK-PS2-1325 | 1325 | 55,3 | 487 | 15,3 | 32,8 | 5,2 | 0,6 | 5,3 | 0,3 | 1,6 | 29,9 | 273,9 | 9,1 | 79,9 | 4,6 | 3,5 | 0,9 | 0,9 |
| ADK-PS2-1330 | 1330 | 45 | 398,9 | 9,5 | 33,8 | 6,2 | 0,6 | 3,4 | 0,3 | 1,4 | 28,9 | 268,4 | 8,4 | 70,5 | 3,3 | 5,2 | 0,9 | 0,9 |
| ADK-PS2-1335 | 1335 | 80 | 578,1 | 21,1 | 69,9 | 9,7 | 0,8 | 5 | 0,4 | 0,9 | 37,6 | 299 | 15,7 | 84,3 | 8,4 | 4,2 | 0,9 | 0,9 |
| ADK-PS2-1340 | 1340 | 35,1 | 350 | 5,8 | 31,2 | 5,3 | 0,6 | 3,7 | 0,3 | 1 | 26,5 | 235,1 | 8,1 | 64 | 4,7 | 3 | 0,8 | 0,7 |
| ADK-PS2-1345 | 1345 | 63,3 | 313,5 | 11,3 | 34,1 | 4,7 | 0,6 | 5 | 0,3 | 1,5 | 19,8 | 228,2 | 8,9 | 51,4 | 3,1 | 3,1 | 0,9 | 0,8 |
| ADK-PS2-1350 | 1350 | 41,4 | 291,3 | 14 | 35,6 | 9,6 | 1,3 | 4,7 | 0,3 | 0,3 | 37,9 | 242,2 | 16,6 | 93,6 | 16,5 | 3,8 | 0,4 | 0,9 |
| ADK-PS2-1355 | 1355 | 26,7 | 206 | 9,3 | 24,4 | 6 | 0,8 | 3 | 0,3 | 0,3 | 25,3 | 236,5 | 14,1 | 62,6 | 9,5 | 3,3 | 0,9 | 0,8 |
| ADK-PS2-1360 | 1360 | 51,2 | 280,1 | 19,2 | 37,5 | 7,9 | 1 | 4,5 | 0,4 | 0,3 | 30,5 | 159,6 | 20,1 | 101,4 | 23,1 | 4 | 2,6 | 1 |
| ADK-PS2-1365 | 1365 | 53,2 | 560,6 | 21,7 | 58,9 | 9,6 | 0,7 | 4 | 0,4 | 0,7 | 51,3 | 305,1 | 15,4 | 103,2 | 4,1 | 3,6 | 1 | 0,9 |
| ADK-PS2-1370 | 1370 | 35,9 | 289,4 | 16,1 | 42,3 | 5,4 | 0,7 | 2,7 | 0,4 | 0,9 | 15,9 | 189 | 21 | 51,6 | 11,7 | 3,4 | 0,9 | 0,8 |
| ADK-PS2-1375 | 1375 | 34,6 | 313 | 26,2 | 36,5 | 5,8 | 0,7 | 5,4 | 0,3 | 0,9 | 25 | 226,6 | 15,4 | 54,4 | 2,7 | 3,2 | 0,8 | 0,8 |
| ADK-PS2-1380 | 1380 | 49,4 | 352,4 | 48,4 | 46,4 | 8,2 | 0,6 | 3,5 | 0,3 | 0,7 | 27,9 | 223,8 | 14,5 | 70,5 | 10 | 3,6 | 0,9 | 0,9 |
| ADK-PS2-1385 | 1385 | 21,5 | 120,9 | 9,9 | 13,5 | 2,5 | 0,6 | 2,3 | 0,3 | 0,3 | 8 | 332,5 | 6,9 | 25 | 3,9 | 3,2 | 1 | 0,9 |
| ADK-PS2-1390 | 1390 | 11,8 | 133,3 | 25,4 | 13,1 | 3,4 | 0,6 | 4,3 | 0,3 | 1,4 | 9,2 | 295,2 | 5,6 | 21,7 | 3,5 | 3,4 | 1 | 0,9 |
| ADK-PS2-1395 | 1395 | 15,8 | 34,1 | 0,9 | 4,1 | 2,3 | 0,5 | 1 | 0,3 | 0,7 | 4,9 | 184 | 3,5 | 9,9 | 3,6 | 3,4 | 1 | 0,8 |
| ADK-PS2-1400 | 1400 | 17,3 | 73 | 4,4 | 7,6 | 2,7 | 0,5 | 1,3 | 0,3 | 0,3 | 7,3 | 198,9 | 3,5 | 14,6 | 3,2 | 3 | 0,9 | 0,8 |
| ADK-PS2-1405 | 1405 | 16,4 | 109,4 | 5,7 | 10,5 | 3,9 | 0,6 | 1,9 | 0,3 | 1 | 7,4 | 193,6 | 6,7 | 19,5 | 3,5 | 3,3 | 0,9 | 0,9 |
| ADK-PS2-1410 | 1410 | 15,5 | 62,2 | 1,4 | 8,1 | 1,6 | 0,5 | 0,9 | 0,3 | 0,3 | 5,5 | 187,1 | 4,2 | 9,4 | 3,5 | 4,9 | 0,9 | 0,9 |
| ADK-PS2-1415 | 1415 | 27,9 | 18,1 | 6,5 | 3,7 | 3,6 | 0,6 | 1,5 | 0,3 | 0,3 | 16,4 | 156,5 | 4,5 | 15,5 | 3,4 | 3 | 0,8 | 0,9 |
| ADK-PS2-1420 | 1420 | 16,3 | 16,6 | 1 | 4,4 | 2 | 0,6 | 1,6 | 0,3 | 0,6 | 6,7 | 163,8 | 2,8 | 15,3 | 3,8 | 3,3 | 1 | 0,8 |
| ADK-PS2-1425 | 1425 | 24,6 | 2,7 | 1,2 | 0,6 | 2,6 | 0,5 | 0,4 | 0,3 | 0,3 | 1,9 | 132,6 | 1,3 | 5,5 | 3,3 | 3,1 | 0,9 | 0,9 |
| ADK-PS-2-1665 | 1665 | 21,5 | 38,1 | 49,1 | 4 | 2 | 0,6 | 1,8 | 0,3 | 0,3 | 5,6 | 150,4 | 1,2 | 17 | 3,4 | 3,2 | 0,9 | 0,8 |
| ADK-PS-2-2100 | 2100 | 34,3 | 21,9 | 13,9 | 36,9 | 7,8 | 1 | 2,3 | 0,5 | 0,3 | 31,6 | 165,1 | 12,6 | 80,5 | 4,9 | 3,3 | 0,8 | 0,8 |
| ADK-PS-2-2195 | 2195 | 38,5 | 40,5 | 20 | 57,5 | 7,7 | 1,1 | 4,6 | 0,4 | 0,7 | 36,9 | 170,9 | 16,1 | 122,7 | 10,2 | 3,4 | 0,9 | 0,8 |

Table F.1 XRF analyses results of samples from Akköy field (cont'd)

| Element | depth | Sn | Sb | Te | I | Cs | Ba | La | Ce | Hf | Ta | W | Hg | Tl | Pb | Bi | Th | U |
|---|---|---|---|---|---|---|---|---|---|---|---|---|---|---|---|---|---|---|
| Sample No\Dimension | m | ppm | ppm | ppm | ppm | ppm | ppm | ppm | ppm | ppm | ppm | ppm | ppm | ppm | ppm | ppm | ppm | ppm |
| ADK-PS2-1290 | 1290 | 1,3 | 1 | 1,2 | 2,2 | 3,6 | 400,2 | 21,2 | 45,5 | 3,2 | 4,5 | 27,6 | 1,1 | 1 | 18,3 | 0,7 | 3,6 | 19,2 |
| ADK-PS2-1295 | 1295 | 1,5 | 2,9 | 0,9 | 1,7 | 5,4 | 297,9 | 27,9 | 45,1 | 3,5 | 5,1 | 11,2 | 1 | 1,1 | 17,8 | 0,7 | 2,2 | 8,5 |
| ADK-PS2-1300 | 1300 | 1,1 | 0,9 | 0,9 | 6,7 | 3,6 | 252,8 | 29,1 | 51,9 | 3,5 | 5,9 | 7,1 | 1,2 | 1,2 | 15,8 | 0,7 | 0,9 | 25 |
| ADK-PS2-1305 | 1305 | 0,7 | 1 | 1,2 | 4,9 | 3,6 | 261 | 17,7 | 26,8 | 3,1 | 4,6 | 18,5 | 0,7 | 1 | 13,3 | 0,7 | 0,5 | 9,6 |
| ADK-PS2-1310 | 1310 | 1 | 1 | 1,2 | 3,3 | 3,5 | 68,4 | 18,1 | 10 | 3 | 4 | 74,6 | 1,3 | 0,9 | 7 | 0,6 | 0,6 | 8,7 |
| ADK-PS2-1315 | 1315 | 1 | 0,6 | 1,2 | 5,7 | 3,5 | 195,4 | 24,2 | 16,8 | 3 | 4,7 | 12,8 | 1,1 | 0,9 | 10,7 | 0,6 | 0,6 | 8,1 |
| ADK-PS2-1320 | 1320 | 0,9 | 1,5 | 1,2 | 4,7 | 3,6 | 163,7 | 23,4 | 22,5 | 3 | 4,6 | 34,7 | 1,1 | 0,9 | 10,4 | 0,5 | 0,6 | 8,3 |
| ADK-PS2-1325 | 1325 | 0,4 | 0,9 | 1,2 | 6,8 | 8,2 | 172,5 | 21,2 | 24,7 | 2,9 | 4,6 | 26,4 | 1,1 | 0,9 | 11,4 | 0,6 | 0,5 | 8,3 |
| ADK-PS2-1330 | 1330 | 1 | 1 | 1,2 | 5,7 | 4,3 | 154,3 | 21,8 | 20,8 | 2,8 | 4,1 | 17,2 | 1 | 0,8 | 9,1 | 0,6 | 0,5 | 9,2 |
| ADK-PS2-1335 | 1335 | 1,7 | 1,8 | 1,2 | 2,1 | 3,8 | 149,1 | 22,8 | 32,3 | 3,4 | 5,5 | 33 | 1,2 | 1,1 | 13,7 | 0,5 | 0,7 | 9,5 |
| ADK-PS2-1340 | 1340 | 1,3 | 1 | 1,1 | 2 | 3,5 | 177,6 | 15,8 | 13,2 | 2 | 3,9 | 17,2 | 0,9 | 0,8 | 6,7 | 0,6 | 0,4 | 6,1 |
| ADK-PS2-1345 | 1345 | 1 | 0,9 | 1,1 | 7,2 | 3,5 | 121,3 | 7,4 | 20,7 | 2,9 | 4 | 26,3 | 1 | 0,8 | 7,5 | 0,6 | 0,5 | 8,1 |
| ADK-PS2-1350 | 1350 | 1 | 1,6 | 1,2 | 2 | 11,1 | 126,9 | 39,7 | 23,8 | 2,9 | 4,1 | 37,4 | 1,1 | 1 | 8,4 | 0,7 | 0,4 | 11,2 |
| ADK-PS2-1355 | 1355 | 1,1 | 0,9 | 1,2 | 3,9 | 3,5 | 81,7 | 26,2 | 24 | 2,7 | 3,7 | 77,6 | 1,2 | 0,9 | 7,6 | 0,6 | 1,5 | 19,5 |
| ADK-PS2-1360 | 1360 | 1 | 1 | 1,3 | 2,1 | 6 | 64,9 | 25,9 | 32,8 | 3,2 | 4,2 | 88,1 | 1,3 | 0,5 | 11,9 | 0,6 | 2 | 17,1 |
| ADK-PS2-1365 | 1365 | 1,1 | 0,8 | 1,2 | 2,1 | 7,3 | 237,1 | 29 | 55,4 | 3,3 | 5,2 | 59,4 | 1,2 | 1 | 13,7 | 0,6 | 0,6 | 17 |
| ADK-PS2-1370 | 1370 | 1 | 0,9 | 1,2 | 3,7 | 7,2 | 61,6 | 20 | 35,8 | 2,8 | 4,2 | 80,8 | 1,2 | 0,8 | 9,3 | 0,6 | 0,5 | 9,7 |
| ADK-PS2-1375 | 1375 | 0,9 | 0,9 | 1,2 | 1,9 | 4,4 | 152,2 | 28,3 | 24,4 | 3,2 | 4,5 | 42,6 | 1,1 | 0,9 | 8 | 0,5 | 0,6 | 8,4 |
| ADK-PS2-1380 | 1380 | 0,9 | 0,9 | 1,2 | 3,3 | 3,6 | 102,4 | 17,8 | 40,1 | 4 | 5,2 | 39,3 | 1,1 | 0,9 | 7,5 | 0,6 | 0,6 | 13,1 |
| ADK-PS2-1385 | 1385 | 1 | 1 | 1,2 | 2 | 6,8 | 37 | 15,5 | 16,3 | 3,4 | 3,6 | 22,6 | 1 | 0,9 | 5,3 | 0,7 | 1,3 | 10 |
| ADK-PS2-1390 | 1390 | 1 | 0,9 | 1,2 | 2 | 3,5 | 49,3 | 7,4 | 23,5 | 3,5 | 4,2 | 34,4 | 1,1 | 0,9 | 6,7 | 0,6 | 0,8 | 9,9 |
| ADK-PS2-1395 | 1395 | 1 | 1 | 1,2 | 2 | 3,5 | 31,2 | 7,4 | 10 | 3 | 2,8 | 9,2 | 0,9 | 0,9 | 3,5 | 0,7 | 1 | 9 |
| ADK-PS2-1400 | 1400 | 0,9 | 0,9 | 1,1 | 2 | 3,5 | 35,8 | 15,5 | 10 | 2,8 | 2,9 | 15,8 | 0,9 | 0,8 | 3,9 | 0,6 | 1,6 | 9,2 |
| ADK-PS2-1405 | 1405 | 0,9 | 0,9 | 1,2 | 2 | 4,5 | 42,6 | 14,2 | 10 | 2,9 | 3,1 | 20,1 | 1 | 0,6 | 6,6 | 0,6 | 1,3 | 8,1 |
| ADK-PS2-1410 | 1410 | 1 | 0,9 | 1 | 3,9 | 3,5 | 41,7 | 15,4 | 15,6 | 2,7 | 2,8 | 20 | 0,9 | 0,8 | 6,8 | 0,6 | 0,8 | 7,2 |
| ADK-PS2-1415 | 1415 | 0,9 | 1,9 | 1,1 | 2 | 3,5 | 45,5 | 27,9 | 12,3 | 2,9 | 3,1 | 16 | 0,9 | 0,8 | 8,7 | 0,6 | 3 | 9,5 |
| ADK-PS2-1420 | 1420 | 1 | 1 | 1,2 | 2 | 3,5 | 27,9 | 7,4 | 10 | 3 | 3,8 | 21,8 | 1 | 0,8 | 5,4 | 0,6 | 2,6 | 9,8 |
| ADK-PS2-1425 | 1425 | 1,8 | 1 | 2 | 2 | 3,5 | 28,4 | 23,7 | 12,1 | 2,8 | 2,3 | 15 | 0,9 | 0,7 | 3 | 0,6 | 1,9 | 9,5 |
| ADK-PS-2-1665 | 1665 | 1 | 0,9 | 1,1 | 2 | 3,4 | 50,7 | 13,3 | 17,2 | 4,3 | 4,9 | 14,2 | 0,9 | 0,8 | 2,5 | 0,7 | 1,2 | 9,4 |
| ADK-PS-2-2100 | 2100 | 0,9 | 0,9 | 1,1 | 2 | 3,4 | 179,3 | 24,5 | 26,8 | 2,6 | 2,7 | 160,3 | 1,6 | 1,1 | 4,4 | 0,6 | 6 | 9,1 |
| ADK-PS-2-2195 | 2195 | 1 | 0,9 | 1,1 | 1,3 | 3,4 | 218,8 | 19,4 | 33,8 | 2,5 | 3,4 | 118,5 | 1,5 | 0,9 | 6,1 | 0,6 | 5,7 | 7,9 |

# Table F.2 XRF analyses results of samples from Edremit Field

| Element | depth | $Na_2O$ | MgO | $Al_2O_3$ | $SiO_2$ | $P_2O_5$ | $SO_3$ | Cl | $K_2O$ | CaO | $TiO_2$ | $V_2O_5$ | $Cr_2O_3$ | MnO | $Fe_2O_3$ | LOI | Total |
|---|---|---|---|---|---|---|---|---|---|---|---|---|---|---|---|---|---|
| Sample No\Dimension | m | % | % | % | % | % | % | % | % | % | % | % | % | % | % | % | % |
| EDR-900 | 900 | 1,82 | 1,359 | 9,82 | 75,5 | 0,0729 | 1,131 | 0,0002 | 2,846 | 3,881 | 0,3038 | 0,0094 | 0,00458 | 0,082 | 2,606 | 0,82 | 100,26 |
| EDR-902 | 902 | 1,49 | 1,426 | 9,863 | 72,52 | 0,0737 | 1,013 | 0,0002 | 2,84 | 4,019 | 0,3021 | 0,01 | 0,00625 | 0,0756 | 2,617 | 3,22 | 99,48 |
| EDR-904 | 904 | 1,8 | 1,329 | 9,604 | 75,32 | 0,0774 | 1,132 | 0,0002 | 2,843 | 3,74 | 0,3008 | 0,0135 | 0,00388 | 0,0803 | 2,69 | 1,55 | 100,48 |
| EDR-906 | 906 | 1,68 | 1,565 | 10,05 | 74,53 | 0,074 | 1,052 | 0,0002 | 2,844 | 4,112 | 0,3086 | 0,0127 | 0,00316 | 0,0847 | 2,659 | 1,76 | 100,74 |
| EDR-908 | 908 | 1,81 | 1,007 | 8,556 | 76,49 | 0,0617 | 0,6829 | 0,0002 | 2,712 | 5,459 | 0,2055 | 0,0097 | 0,00339 | 0,0636 | 1,983 | 0,35 | 99,39 |
| EDR-910 | 910 | 1,76 | 1,316 | 8,674 | 74,81 | 0,0713 | 0,6922 | 0,0002 | 2,59 | 4,789 | 0,2264 | 0,0085 | 0,00441 | 0,0952 | 2,212 | 2,55 | 99,80 |
| EDR-912 | 912 | 1,93 | 1,368 | 8,861 | 74,92 | 0,0663 | 0,6838 | 0,0002 | 2,697 | 4,442 | 0,2303 | 0,0062 | 0,0053 | 0,0936 | 2,277 | 2,71 | 100,29 |
| EDR-914 | 914 | 1,72 | 1,308 | 9,703 | 73,03 | 0,0944 | 1,024 | 0,0002 | 2,591 | 5,575 | 0,3171 | 0,0148 | 0,00268 | 0,1072 | 3,012 | 1,64 | 100,14 |
| EDR-916 | 916 | 1,6 | 1,277 | 9,806 | 73,06 | 0,0794 | 0,8162 | 0,0002 | 2,608 | 6,307 | 0,3215 | 0,0094 | 0,00519 | 0,1056 | 2,883 | 1,85 | 100,73 |
| EDR-918 | 918 | 1,51 | 1,399 | 9,73 | 70,59 | 0,081 | 1,077 | 0,0002 | 2,731 | 7,064 | 0,3197 | 0,0114 | 0,00435 | 0,113 | 3,105 | 2,56 | 100,30 |
| EDR-920 | 920 | 1,48 | 1,319 | 9,483 | 71,79 | 0,0898 | 0,8812 | 0,0002 | 2,751 | 7,221 | 0,3114 | 0,0084 | 0,00472 | 0,1033 | 2,832 | 1,86 | 100,14 |
| EDR-922 | 922 | 1,42 | 1,37 | 9,09 | 73,03 | 0,0831 | 0,6532 | 0,0002 | 2,565 | 8,358 | 0,2852 | 0,0118 | 0,00438 | 0,1027 | 2,544 | 0,13 | 99,65 |
| EDR-924 | 924 | 1,22 | 1,448 | 9,836 | 67,43 | 0,0935 | 0,893 | 0,0002 | 2,312 | 10,75 | 0,3599 | 0,0101 | 0,00795 | 0,1492 | 3,64 | 1,56 | 99,71 |
| EDR-926 | 926 | 1,33 | 1,53 | 9,707 | 65,68 | 0,1028 | 0,8991 | 0,0002 | 2,349 | 11,04 | 0,3459 | 0,0138 | 0,0042 | 0,1557 | 3,652 | 3,82 | 100,63 |
| EDR-928 | 928 | 1,01 | 1,322 | 9,453 | 67,2 | 0,0984 | 0,878 | 0,0002 | 2,15 | 12,17 | 0,3115 | 0,0101 | 0,0131 | 0,1407 | 3,612 | 1,35 | 99,72 |
| EDR-930 | 930 | 2,26 | 0,96 | 8,301 | 76,77 | 0,062 | 0,5424 | 0,0002 | 1,829 | 3,811 | 0,177 | 0,0066 | 0,00412 | 0,0463 | 1,787 | 3,21 | 99,77 |
| EDR-932 | 932 | 1,69 | 0,907 | 8,258 | 76,71 | 0,056 | 0,5647 | 0,0002 | 1,877 | 3,808 | 0,1625 | 0,0067 | 0,0383 | 0,0536 | 1,946 | 3,95 | 100,03 |
| EDR-934 | 934 | 1,83 | 0,644 | 6,392 | 82,44 | 0,0363 | 0,3446 | 0,0002 | 1,849 | 3,497 | 0,0909 | 0,0047 | 0,0026 | 0,0381 | 1,123 | 1,55 | 99,84 |
| EDR-936 | 936 | 1,47 | 0,803 | 7,463 | 76,59 | 0,0381 | 0,47 | 0,0002 | 1,95 | 6,147 | 0,1457 | 0,0078 | 0,0024 | 0,0506 | 1,518 | 3,44 | 100,10 |
| EDR-938 | 938 | 0,85 | 0,613 | 7,015 | 79,94 | 0,0383 | 0,3496 | 0,0002 | 2,004 | 6,413 | 0,1077 | 0,0027 | 0,00195 | 0,0352 | 1,333 | 1,54 | 100,24 |
| EDR-940 | 940 | 1,85 | 0,669 | 6,938 | 79,49 | 0,0404 | 0,357 | 0,0002 | 2,037 | 6,221 | 0,0923 | 0,0061 | 0,00417 | 0,0362 | 1,306 | 0,23 | 99,28 |
| EDR-942 | 942 | 1,83 | 0,828 | 6,971 | 76,7 | 0,0348 | 0,4437 | 0,0002 | 2,016 | 6,104 | 0,1098 | 0,0046 | 0,00412 | 0,0492 | 1,581 | 3,42 | 100,10 |
| EDR-944 | 944 | 1,68 | 0,735 | 6,979 | 82,34 | 0,0347 | 0,4839 | 0,0002 | 1,954 | 3,559 | 0,1074 | 0,0043 | 0,00148 | 0,0506 | 1,535 | 0,73 | 100,19 |
| EDR-946 | 946 | 1,41 | 0,812 | 7,176 | 79,44 | 0,035 | 0,5191 | 0,0002 | 2,005 | 4,471 | 0,1152 | 0,0054 | 0,00141 | 0,0614 | 1,594 | 1,46 | 99,11 |
| EDR-948 | 948 | 1,48 | 0,668 | 7,589 | 79,89 | 0,046 | 0,49 | 0,0002 | 2,952 | 3,252 | 0,1246 | 0,0037 | 0,00105 | 0,0436 | 1,42 | 2,57 | 100,53 |
| EDR-950 | 950 | 1,62 | 0,635 | 7,37 | 81,03 | 0,0441 | 0,5709 | 0,0002 | 2,872 | 3,349 | 0,1065 | 0,0053 | 0,00221 | 0,0425 | 1,381 | 0,83 | 99,86 |
| EDR-952 | 952 | 1,51 | 0,702 | 7,353 | 79,85 | 0,05 | 0,5547 | 0,0002 | 2,792 | 3,885 | 0,1257 | 0,0057 | 0,001 | 0,0552 | 1,507 | 1,56 | 99,95 |
| EDR-954 | 954 | 1,37 | 0,721 | 7,397 | 80,77 | 0,0438 | 0,4907 | 0,0002 | 2,88 | 3,252 | 0,11 | 0,0038 | 0,00221 | 0,0459 | 1,326 | 1,75 | 100,16 |
| EDR-956 | 956 | 1,53 | 1,113 | 8,255 | 78,94 | 0,0354 | 0,6716 | 0,0002 | 2,298 | 4,407 | 0,1512 | 0,0063 | 0,00482 | 0,0617 | 1,749 | 0,73 | 99,95 |
| EDR-958 | 958 | 1,73 | 0,979 | 7,991 | 79,76 | 0,0537 | 0,6427 | 0,0002 | 2,313 | 4,07 | 0,1626 | 0,0038 | 0,00532 | 0,0479 | 1,51 | 0,88 | 100,15 |
| EDR-960 | 960 | 1,82 | 0,979 | 7,768 | 79,1 | 0,0526 | 0,6339 | 0,0002 | 2,125 | 3,906 | 0,159 | 0,0054 | 0,00317 | 0,0473 | 1,521 | 1,45 | 99,57 |
| EDR-962 | 962 | 1,48 | 1,098 | 8,097 | 78,03 | 0,0529 | 0,5926 | 0,0002 | 2,265 | 3,847 | 0,1816 | 0,0088 | 0,01035 | 0,0534 | 1,643 | 1,86 | 99,22 |
| EDR-964 | 964 | 1,64 | 1,113 | 8,55 | 77,47 | 0,0593 | 1,066 | 0,0002 | 1,654 | 4,988 | 0,1807 | 0,0049 | 0,00236 | 0,0927 | 2,616 | 0,73 | 100,17 |
| EDR-966 | 966 | 1,35 | 1,02 | 8,516 | 76,72 | 0,0791 | 1,277 | 0,0002 | 1,609 | 4,069 | 0,2172 | 0,0109 | 0,0259 | 0,0792 | 2,679 | 2,55 | 100,20 |
| EDR-968 | 968 | 1,49 | 0,811 | 7,824 | 76,78 | 0,0674 | 1,127 | 0,0002 | 1,556 | 3,848 | 0,187 | 0,0082 | 0,00491 | 0,0783 | 2,266 | 3,02 | 99,07 |

Table F.2 XRF analyses results of samples from Edremit field (cont’d)

| Element | depth | $Na_2O$ | MgO | $Al_2O_3$ | $SiO_2$ | $P_2O_5$ | $SO_3$ | Cl | $K_2O$ | CaO | $TiO_2$ | $V_2O_5$ | $Cr_2O_3$ | MnO | $Fe_2O_3$ | LOI | Total |
|---|---|---|---|---|---|---|---|---|---|---|---|---|---|---|---|---|---|
| Sample No\Dimension | m | % | % | % | % | % | % | % | % | % | % | % | % | % | % | % | % |
| EDR-970 | 970 | 1,88 | 0,647 | 7,592 | 77,9 | 0,0365 | 0,8211 | 0,0002 | 1,677 | 2,735 | 0,1374 | 0,0075 | 0,00584 | 0,047 | 1,52 | 4,29 | 99,30 |
| EDR-972 | 972 | 1,62 | 0,862 | 9,046 | 77,68 | 0,0616 | 0,6942 | 0,0002 | 2,428 | 3,585 | 0,1958 | 0,0082 | 0,00828 | 0,0557 | 2,12 | 1,85 | 100,21 |
| EDR-974 | 974 | 1,59 | 0,837 | 8,781 | 77,4 | 0,053 | 0,6582 | 0,0002 | 2,515 | 3,37 | 0,167 | 0,0059 | 0,00343 | 0,052 | 1,765 | 2,57 | 99,77 |
| EDR-976 | 976 | 1,63 | 1,982 | 16,79 | 65,24 | 0,0868 | 1,373 | 0,0002 | 3,644 | 3,234 | 0,4378 | 0,0149 | 0,00725 | 0,0778 | 3,753 | 1,96 | 100,23 |
| EDR-978 | 978 | 1,6 | 1,861 | 16,58 | 64,91 | 0,0841 | 1,651 | 0,0002 | 3,664 | 3,199 | 0,4542 | 0,0153 | 0,00734 | 0,082 | 3,958 | 1,74 | 99,81 |
| EDR-980 | 980 | 1,81 | 1,903 | 16,49 | 65,47 | 0,0842 | 1,467 | 0,0002 | 3,73 | 3,393 | 0,4395 | 0,0139 | 0,00387 | 0,0837 | 3,804 | 1,88 | 100,57 |
| EDR-982 | 982 | 1,61 | 1,971 | 16,89 | 65,76 | 0,0839 | 1,544 | 0,0002 | 3,801 | 2,981 | 0,4569 | 0,0155 | 0,00799 | 0,0821 | 3,948 | 0,63 | 99,78 |
| EDR-984 | 984 | 1,79 | 1,978 | 15,76 | 63,4 | 0,0863 | 1,615 | 0,00091 | 3,111 | 4,531 | 0,4615 | 0,0178 | 0,003 | 0,0909 | 4,255 | 2,77 | 99,87 |
| EDR-986 | 986 | 2,11 | 1,872 | 14,97 | 66,38 | 0,1102 | 1,347 | 0,00293 | 2,522 | 5,18 | 0,4633 | 0,0152 | 0,0036 | 0,0955 | 4,093 | 0,83 | 99,99 |
| EDR-988 | 988 | 2,37 | 1,845 | 14,88 | 63,87 | 0,1078 | 1,16 | 0,00412 | 2,585 | 6,943 | 0,4509 | 0,0146 | 0,0164 | 0,1006 | 4,088 | 1,57 | 100,01 |
| EDR-990 | 990 | 2,74 | 1,865 | 14,72 | 66,54 | 0,116 | 1,366 | 0,0002 | 2,381 | 4,938 | 0,4183 | 0,0141 | 0,00119 | 0,0911 | 4,216 | 0,75 | 100,16 |
| EDR-992 | 992 | 3,59 | 2,039 | 15,38 | 63,46 | 0,1561 | 0,9157 | 0,00942 | 2,072 | 6,358 | 0,4714 | 0,0148 | 0,00093 | 0,0944 | 4,686 | 0,66 | 99,91 |
| EDR-994 | 994 | 3,11 | 2,054 | 15,19 | 63,47 | 0,1442 | 0,7229 | 0,01276 | 2,099 | 6,409 | 0,5182 | 0,013 | 0,00099 | 0,103 | 4,695 | 1,57 | 100,11 |
| EDR-996 | 996 | 3,78 | 1,962 | 16,18 | 63,19 | 0,1366 | 0,6951 | 0,00951 | 2,167 | 6,036 | 0,4801 | 0,0185 | 0,00093 | 0,0921 | 4,633 | 0,73 | 100,11 |
| EDR-998 | 998 | 3,34 | 2,04 | 15,1 | 64,78 | 0,1462 | 0,817 | 0,01464 | 2,143 | 5,522 | 0,4634 | 0,0185 | 0,00525 | 0,0907 | 4,85 | 0,86 | 100,19 |
| EDR-1000 | 1000 | 3,19 | 1,916 | 14,43 | 65,03 | 0,1445 | 0,821 | 0,01199 | 2,097 | 5,609 | 0,4287 | 0,0159 | 0,00157 | 0,0839 | 4,474 | 1,84 | 100,09 |
| EDR-1002 | 1002 | 2,47 | 2,064 | 13,26 | 63,9 | 0,1445 | 0,6144 | 0,01806 | 1,995 | 5,929 | 0,4359 | 0,0159 | 0,0247 | 0,0987 | 4,624 | 4,22 | 99,81 |
| EDR-1004 | 1004 | 3,05 | 1,815 | 13,74 | 58,7 | 0,1409 | 0,4809 | 0,01476 | 2,068 | 5,618 | 0,4378 | 0,0163 | 0,00095 | 0,0842 | 4,256 | 9,73 | 100,15 |
| EDR-1006 | 1006 | 3,2 | 1,989 | 14,92 | 65,75 | 0,1652 | 0,6714 | 0,02062 | 2,257 | 5,628 | 0,4688 | 0,0186 | 0,00714 | 0,0913 | 4,878 | 0,12 | 100,19 |
| EDR-1008 | 1008 | 3,46 | 1,85 | 14,96 | 64,84 | 0,1506 | 0,5356 | 0,01605 | 1,927 | 6,224 | 0,4514 | 0,0141 | 0,001 | 0,0859 | 4,418 | 1,46 | 100,39 |
| EDR-1010 | 1010 | 3,42 | 1,917 | 14,49 | 66,48 | 0,1432 | 0,5516 | 0,01088 | 2,045 | 5,876 | 0,4265 | 0,0159 | 0,00315 | 0,0933 | 4,33 | 0,53 | 100,33 |
| EDR-1012 | 1012 | 3,67 | 1,861 | 15,62 | 63,87 | 0,1304 | 0,3895 | 0,01462 | 2,218 | 5,785 | 0,4377 | 0,0145 | 0,00161 | 0,0792 | 4,119 | 1,47 | 99,68 |
| EDR-1014 | 1014 | 3,88 | 1,701 | 15,62 | 64,18 | 0,1386 | 0,4101 | 0,01137 | 2,191 | 6,022 | 0,4411 | 0,0151 | 0,00097 | 0,0792 | 4,195 | 1,35 | 100,24 |
| EDR-1016 | 1016 | 3,46 | 1,824 | 15,53 | 64,8 | 0,1367 | 0,2941 | 0,01359 | 2,222 | 5,982 | 0,4354 | 0,0123 | 0,00097 | 0,0807 | 3,984 | 1,37 | 100,15 |
| EDR-1018 | 1018 | 3,74 | 1,731 | 15,46 | 65,64 | 0,1317 | 0,3128 | 0,01058 | 2,191 | 5,983 | 0,4383 | 0,0172 | 0,00323 | 0,0788 | 4,137 | 0,18 | 100,05 |
| EDR-1020 | 1020 | 3,73 | 1,7 | 15,16 | 64,72 | 0,1282 | 0,3475 | 0,01492 | 2,154 | 5,808 | 0,4307 | 0,0133 | 0,00336 | 0,0771 | 3,995 | 1,44 | 99,72 |
| EDR-1022 | 1022 | 3,69 | 1,695 | 15,62 | 64,88 | 0,1518 | 0,4916 | 0,01091 | 2,162 | 6,158 | 0,4213 | 0,015 | 0,00229 | 0,0839 | 4,316 | 0,45 | 100,15 |
| EDR-1024 | 1024 | 3,37 | 1,822 | 14,2 | 63,75 | 0,1572 | 0,589 | 0,00647 | 2,011 | 5,846 | 0,4208 | 0,0167 | 0,001 | 0,0893 | 4,67 | 3,72 | 100,67 |
| EDR-1026 | 1026 | 3,55 | 1,853 | 14,8 | 63,21 | 0,1511 | 0,3545 | 0,00632 | 2,07 | 5,986 | 0,4378 | 0,0133 | 0,00135 | 0,1006 | 4,593 | 2,56 | 99,69 |
| EDR-1028 | 1028 | 3,2 | 1,96 | 14,44 | 64,85 | 0,1702 | 0,3839 | 0,00889 | 2,046 | 5,977 | 0,4435 | 0,0173 | 0,00099 | 0,0963 | 4,633 | 1,85 | 100,08 |
| EDR-1030 | 1030 | 3,87 | 1,742 | 14,95 | 65,41 | 0,1621 | 0,2721 | 0,00434 | 2,065 | 5,746 | 0,4283 | 0,0111 | 0,00096 | 0,0874 | 4,177 | 1,85 | 100,78 |
| EDR-1032 | 1032 | 4,12 | 1,561 | 16,2 | 63,8 | 0,1366 | 0,2283 | 0,0002 | 2,245 | 5,758 | 0,3738 | 0,0162 | 0,00187 | 0,0756 | 3,887 | 1,83 | 100,23 |
| EDR-1034 | 1034 | 3,75 | 1,493 | 15,47 | 65,71 | 0,1418 | 0,2827 | 0,0002 | 2,183 | 5,635 | 0,3779 | 0,0156 | 0,00094 | 0,0852 | 3,909 | 0,63 | 99,68 |
| EDR-1036 | 1036 | 4,11 | 1,602 | 15,93 | 64,88 | 0,1568 | 0,2593 | 0,00075 | 2,298 | 5,68 | 0,4117 | 0,0119 | 0,001 | 0,0806 | 4,058 | 0,24 | 99,72 |
| EDR-1038 | 1038 | 3,37 | 1,609 | 15,39 | 64,76 | 0,1642 | 0,3186 | 0,00173 | 2,16 | 5,827 | 0,3801 | 0,0136 | 0,0264 | 0,0776 | 4,035 | 1,55 | 99,68 |

Table F.2 XRF analyses results of samples from Edremit field (cont'd)

| Element | depth | Co | Ni | Cu | Zn | Ga | Ge | As | Se | Br | Rb | Sr | Y | Zr | Nb | Mo | Cd | In |
|---|---|---|---|---|---|---|---|---|---|---|---|---|---|---|---|---|---|---|
| Sample No\Dimension | m | ppm | ppm | ppm | ppm | ppm | ppm | ppm | ppm | ppm | ppm | ppm | ppm | ppm | ppm | ppm | ppm | ppm |
| EDR-900 | 900 | 60,2 | 14,8 | 28,5 | 180,5 | 13,2 | 1,3 | 67,8 | 0,6 | 0,5 | 91,9 | 181,9 | 16,5 | 127,9 | 12,2 | 14,1 | 0,8 | 0,8 |
| EDR-902 | 902 | 40,5 | 14,6 | 27,7 | 269,7 | 12,2 | 1,2 | 5,7 | 0,5 | 0,5 | 89,3 | 183,5 | 16,9 | 103,5 | 6,1 | 2,9 | 0,8 | 0,8 |
| EDR-904 | 904 | 55,9 | 16,6 | 25,2 | 211 | 14,2 | 1,6 | 6,5 | 0,7 | 0,7 | 92 | 183,8 | 16,4 | 109 | 8,2 | 3 | 0,7 | 0,7 |
| EDR-906 | 906 | 49,1 | 16,8 | 113,2 | 133,9 | 12,9 | 1,4 | 7,4 | 0,5 | 0,9 | 86,8 | 199,1 | 15,9 | 117,6 | 7,7 | 3,2 | 0,8 | 0,7 |
| EDR-908 | 908 | 60 | 16,9 | 15,7 | 53,1 | 10,1 | 1,2 | 13,1 | 0,6 | 0,9 | 80,2 | 172,3 | 11,9 | 86 | 9,8 | 5,7 | 0,6 | 0,8 |
| EDR-910 | 910 | 72,3 | 12,1 | 19,4 | 47,4 | 11,3 | 1,6 | 5,8 | 0,7 | 0,8 | 76,8 | 225,8 | 13,4 | 89 | 2,9 | 3,9 | 0,8 | 0,7 |
| EDR-912 | 912 | 58,6 | 18,1 | 28,1 | 38,3 | 12,6 | 1,5 | 14,4 | 0,6 | 1,2 | 76,9 | 226,8 | 13,7 | 90,7 | 5,8 | 5,1 | 0,8 | 0,8 |
| EDR-914 | 914 | 59,6 | 15,8 | 23,9 | 40,9 | 14,2 | 1,5 | 8,5 | 0,6 | 0,7 | 78,9 | 255 | 16,9 | 98,8 | 3,1 | 3,9 | 0,8 | 0,8 |
| EDR-916 | 916 | 46,6 | 16,5 | 22,7 | 39,9 | 13,8 | 1,3 | 5,9 | 0,5 | 0,6 | 79,3 | 259,7 | 15,9 | 98,7 | 6,7 | 3,1 | 0,7 | 0,7 |
| EDR-918 | 918 | 58,2 | 16,8 | 31 | 177,8 | 14,1 | 1,6 | 8,4 | 0,6 | 0,5 | 84,3 | 292,3 | 17 | 91,9 | 9 | 3,3 | 0,7 | 0,8 |
| EDR-920 | 920 | 47,5 | 13,2 | 41,2 | 102,9 | 13,9 | 1,1 | 8,3 | 0,5 | 0,9 | 85,2 | 302,4 | 16,3 | 101,4 | 11,7 | 3,3 | 0,8 | 0,9 |
| EDR-922 | 922 | 55,3 | 14,2 | 21,2 | 58,3 | 10 | 1,5 | 5,9 | 0,6 | 0,6 | 78,9 | 319,4 | 17,4 | 106,1 | 4,9 | 3,1 | 0,8 | 0,8 |
| EDR-924 | 924 | 50,7 | 18,8 | 29,6 | 147,4 | 13,3 | 1,2 | 6 | 0,5 | 0,3 | 75,4 | 372,8 | 17,3 | 112,3 | 7 | 3,5 | 0,8 | 0,8 |
| EDR-926 | 926 | 44,8 | 22,4 | 28 | 243,5 | 14,2 | 1 | 9,6 | 0,4 | 0,5 | 76,5 | 369,7 | 17 | 109,6 | 10 | 8,1 | 0,8 | 0,7 |
| EDR-928 | 928 | 55,2 | 32,7 | 31,5 | 157,6 | 13,6 | 1 | 4,9 | 0,5 | 1 | 69 | 401,2 | 17 | 111,6 | 3,3 | 13,1 | 0,8 | 0,9 |
| EDR-930 | 930 | 43,9 | 13,4 | 17,5 | 93,6 | 10,3 | 1,5 | 2,2 | 0,6 | 0,7 | 51,8 | 217,4 | 8,4 | 72,9 | 6,4 | 2,8 | 0,8 | 0,8 |
| EDR-932 | 932 | 64,8 | 11,8 | 18,9 | 91,3 | 9,7 | 1,5 | 2,4 | 0,6 | 0,7 | 50,3 | 211,4 | 8,8 | 72,3 | 4,4 | 4,5 | 0,8 | 0,8 |
| EDR-934 | 934 | 104,9 | 11,9 | 7,3 | 52,1 | 10 | 2,2 | 2,7 | 1,7 | 1,6 | 43,3 | 153,6 | 9,2 | 72,2 | 6 | 2,2 | 0,7 | 0,8 |
| EDR-936 | 936 | 44 | 13,5 | 9,3 | 42 | 10,4 | 1,3 | 2,1 | 0,5 | 0,8 | 45,4 | 185,8 | 10,3 | 95,9 | 7,5 | 3,4 | 0,8 | 0,9 |
| EDR-938 | 938 | 68,4 | 6,7 | 6,5 | 67,5 | 10,2 | 1,8 | 1,5 | 0,6 | 1,1 | 44 | 175,5 | 9,2 | 74,3 | 3,8 | 2,6 | 0,7 | 0,8 |
| EDR-940 | 940 | 73,1 | 7,3 | 8,5 | 32 | 9,6 | 1,7 | 1,9 | 0,7 | 1 | 44,7 | 167,2 | 9,2 | 72,3 | 8,5 | 6,7 | 0,7 | 0,8 |
| EDR-942 | 942 | 46,8 | 13,1 | 12,9 | 36 | 10 | 1,3 | 2,8 | 0,5 | 0,2 | 45,9 | 182,1 | 9,6 | 82,8 | 6,5 | 2,9 | 0,8 | 0,7 |
| EDR-944 | 944 | 97,5 | 7,4 | 9 | 34,9 | 11,8 | 2,2 | 3,4 | 0,9 | 1,7 | 46,9 | 177,3 | 10,7 | 86,7 | 2,8 | 2,7 | 0,8 | 0,7 |
| EDR-946 | 946 | 65,6 | 7,9 | 23,4 | 30 | 10,3 | 1,8 | 27,4 | 0,7 | 1,1 | 52,1 | 181,6 | 9,7 | 69,4 | 4,7 | 2,3 | 0,7 | 0,7 |
| EDR-948 | 948 | 81,9 | 11,8 | 4,9 | 116 | 9,9 | 1,6 | 1,9 | 0,8 | 1,4 | 78 | 168,4 | 9 | 85,8 | 6,4 | 5,8 | 0,7 | 0,7 |
| EDR-950 | 950 | 122,8 | 11,4 | 22,2 | 200,2 | 11,8 | 2,5 | 3,3 | 1 | 1,8 | 75,4 | 168,3 | 8,6 | 93,8 | 2,7 | 3 | 0,7 | 0,7 |
| EDR-952 | 952 | 83 | 9,6 | 19,2 | 113,2 | 11,9 | 2,1 | 3,4 | 1,8 | 1,5 | 73,7 | 171,1 | 9,3 | 88 | 6,5 | 2,9 | 0,7 | 0,8 |
| EDR-954 | 954 | 99,8 | 7,3 | 26,5 | 72,2 | 11,7 | 2,2 | 3,2 | 2,1 | 1,7 | 74,6 | 162,9 | 9,9 | 91,1 | 5,4 | 5,8 | 0,7 | 0,8 |
| EDR-956 | 956 | 72,6 | 10,5 | 12,1 | 85,6 | 10,8 | 1,8 | 6,1 | 0,7 | 1 | 56,2 | 240,2 | 9,4 | 87,2 | 2,7 | 2,8 | 0,7 | 0,7 |
| EDR-958 | 958 | 64,3 | 11,8 | 13,2 | 69,1 | 11,6 | 1,9 | 5,9 | 0,5 | 1,4 | 56,7 | 252,7 | 10,9 | 87,2 | 5,2 | 4,1 | 0,7 | 0,7 |
| EDR-960 | 960 | 55,3 | 7,1 | 13,5 | 38,6 | 11,4 | 1,5 | 5,5 | 0,6 | 0,7 | 51,4 | 217,7 | 9,3 | 89,6 | 8,3 | 3 | 0,8 | 0,8 |
| EDR-962 | 962 | 54,7 | 8,3 | 11,7 | 38,7 | 11,1 | 1,5 | 5,4 | 0,6 | 0,8 | 57 | 225,6 | 10,3 | 111,1 | 4,7 | 2,9 | 0,7 | 0,7 |
| EDR-964 | 964 | 79,4 | 7,3 | 31,9 | 49,6 | 12,9 | 1,6 | 4 | 0,6 | 0,8 | 43,7 | 232,2 | 11,6 | 100,8 | 9,4 | 3,9 | 1,8 | 0,8 |
| EDR-966 | 966 | 56,4 | 6,4 | 20,6 | 45,1 | 11,8 | 1,2 | 2 | 0,5 | 0,6 | 43,2 | 194,7 | 13 | 96,8 | 5,7 | 2,6 | 0,8 | 0,7 |
| EDR-968 | 968 | 64,8 | 6,6 | 12,4 | 39,8 | 12,2 | 1,7 | 1,9 | 0,7 | 0,8 | 44,3 | 193,9 | 12,3 | 105 | 4,9 | 2,7 | 0,8 | 0,7 |

Table F.2 XRF analyses results of samples from Edremit field (cont’d)

| Element | depth | Sn | Sb | Te | I | Cs | Ba | La | Ce | Hf | Ta | W | Hg | Tl | Pb | Bi | Th | U |
|---|---|---|---|---|---|---|---|---|---|---|---|---|---|---|---|---|---|---|
| Sample No\Dimension | m | ppm | ppm | ppm | ppm | ppm | ppm | ppm | ppm | ppm | ppm | ppm | ppm | ppm | ppm | ppm | ppm | ppm |
| EDR-900 | 900 | 2,2 | 0,8 | 1,1 | 2 | 2,8 | 411,3 | 19,7 | 33,3 | 2,6 | 8,1 | 682 | 2,5 | 1,7 | 8,1 | 1,7 | 6,5 | 7,6 |
| EDR-902 | 902 | 2 | 0,8 | 1,1 | 2 | 5,3 | 433,8 | 20 | 26 | 2,5 | 5,1 | 365,8 | 1,8 | 1,4 | 8,6 | 0,5 | 5 | 7,1 |
| EDR-904 | 904 | 0,8 | 0,8 | 1,1 | 1,9 | 3,4 | 424,6 | 14,7 | 25 | 2,5 | 5,4 | 763,9 | 2,6 | 1,7 | 8,4 | 2,3 | 6,9 | 7,1 |
| EDR-906 | 906 | 2,6 | 0,8 | 1,2 | 2 | 3,6 | 431,3 | 23,1 | 39,4 | 4,1 | 5,3 | 542,7 | 2,2 | 0,9 | 12,9 | 1,5 | 5,5 | 7,3 |
| EDR-908 | 908 | 1 | 0,8 | 0,9 | 2 | 3,5 | 468,4 | 16,5 | 22,9 | 2,1 | 8,7 | 693,5 | 2,4 | 1,7 | 8,9 | 0,6 | 5,4 | 10,2 |
| EDR-910 | 910 | 0,9 | 0,8 | 1,1 | 2 | 3,6 | 497,5 | 18,2 | 40 | 2,2 | 7,8 | 785,7 | 2,6 | 1,3 | 8 | 0,9 | 6,7 | 6,3 |
| EDR-912 | 912 | 1,5 | 0,8 | 0,4 | 2 | 3,5 | 488,9 | 20,5 | 31,6 | 2,5 | 3,4 | 635,2 | 2,3 | 1,1 | 8,8 | 1,3 | 8,2 | 8,5 |
| EDR-914 | 914 | 1,6 | 0,8 | 1,2 | 2 | 3,5 | 489,1 | 18,8 | 40 | 2,5 | 5,2 | 586,8 | 2,3 | 1,2 | 9,9 | 1 | 7 | 6,6 |
| EDR-916 | 916 | 0,9 | 0,8 | 1,1 | 2 | 3,5 | 495,3 | 7,2 | 45,7 | 2,4 | 7,2 | 448,3 | 2,1 | 1,7 | 8,5 | 0,8 | 8,1 | 6,3 |
| EDR-918 | 918 | 0,9 | 0,8 | 1,1 | 2 | 3,5 | 483,1 | 11,8 | 36,9 | 2,8 | 3,5 | 443,4 | 2,1 | 1,7 | 9,2 | 1,6 | 7,1 | 6,8 |
| EDR-920 | 920 | 1,7 | 0,8 | 1,1 | 2 | 3,5 | 491,6 | 22,4 | 27,8 | 3 | 3,7 | 448,5 | 2,1 | 1,7 | 7,8 | 0,8 | 7,4 | 10,4 |
| EDR-922 | 922 | 2,1 | 0,8 | 1,1 | 2 | 4,2 | 452,4 | 16,3 | 27,6 | 2,5 | 8,2 | 590,5 | 2,4 | 1,5 | 7,8 | 0,6 | 7,1 | 9,1 |
| EDR-924 | 924 | 2 | 0,9 | 1,1 | 2,1 | 4,2 | 436,4 | 21,1 | 43,1 | 2,8 | 6,9 | 337 | 1,9 | 1 | 8,6 | 0,9 | 7,5 | 6,7 |
| EDR-926 | 926 | 1,9 | 0,8 | 1,2 | 2 | 6,2 | 458,1 | 22,8 | 28,1 | 2,8 | 5 | 240,3 | 1,7 | 1,4 | 10,2 | 1,1 | 6,5 | 6,4 |
| EDR-928 | 928 | 2 | 0,9 | 1,2 | 2 | 6,7 | 411,4 | 20,4 | 41,9 | 3 | 4,9 | 329,7 | 1,9 | 1 | 8 | 0,6 | 8,7 | 8 |
| EDR-930 | 930 | 1,5 | 0,8 | 1,1 | 2 | 3,5 | 624,7 | 7,2 | 21,6 | 2,2 | 6,3 | 685 | 2,3 | 1,1 | 8,3 | 1 | 5,1 | 8,3 |
| EDR-932 | 932 | 1,1 | 0,8 | 1,2 | 2,1 | 3,6 | 628,1 | 13,7 | 36,8 | 2,2 | 3 | 644,1 | 2,3 | 1,6 | 10 | 0,8 | 4,2 | 6,3 |
| EDR-934 | 934 | 0,7 | 0,8 | 1,1 | 2 | 4,2 | 538,9 | 17,6 | 24,4 | 1,9 | 3,2 | 1571 | 3,5 | 2 | 5,5 | 2 | 4,1 | 6,5 |
| EDR-936 | 936 | 1 | 0,9 | 1,3 | 2,1 | 3,6 | 497,1 | 13,5 | 37,9 | 1,8 | 2,8 | 524,9 | 2 | 0,9 | 6,9 | 0,5 | 5 | 14,6 |
| EDR-938 | 938 | 0,8 | 0,8 | 1,1 | 2 | 3,5 | 504,9 | 16,5 | 24 | 1,9 | 2,4 | 870,8 | 2,7 | 1,1 | 7,6 | 0,5 | 3,2 | 6,9 |
| EDR-940 | 940 | 1,9 | 0,8 | 0,6 | 2 | 3,6 | 507 | 7,2 | 13,1 | 1,9 | 6,2 | 880,2 | 2,6 | 1,6 | 6,5 | 2,1 | 5,1 | 7 |
| EDR-942 | 942 | 0,9 | 0,8 | 1,1 | 2 | 3,5 | 477 | 7,2 | 17,1 | 2 | 2,6 | 525,7 | 2,1 | 1,6 | 4,9 | 1,5 | 3,7 | 16,2 |
| EDR-944 | 944 | 0,8 | 0,8 | 1,1 | 2 | 3,4 | 421,1 | 7 | 15,5 | 1,9 | 3,3 | 1623 | 3,6 | 1,7 | 6,2 | 2 | 4,3 | 9,8 |
| EDR-946 | 946 | 1,4 | 0,8 | 1,1 | 1,9 | 3,4 | 419 | 17,5 | 39,1 | 2,4 | 4,2 | 927,9 | 2,8 | 2,3 | 5 | 2,2 | 5,5 | 5,5 |
| EDR-948 | 948 | 0,8 | 0,8 | 1,1 | 2 | 3,4 | 533,2 | 13,9 | 15 | 1,7 | 9,7 | 1149 | 3 | 2,2 | 8,8 | 2,3 | 4,8 | 6,1 |
| EDR-950 | 950 | 1,8 | 0,5 | 0,9 | 2 | 3,4 | 513,9 | 7,1 | 22,5 | 2,3 | 6,9 | 1873 | 3,8 | 2,3 | 7,3 | 1,8 | 4,8 | 6,6 |
| EDR-952 | 952 | 0,8 | 0,8 | 1,1 | 2 | 3,4 | 503,8 | 16,7 | 29 | 2,2 | 3,4 | 1352 | 3,2 | 2,6 | 6,6 | 0,6 | 5,8 | 11,8 |
| EDR-954 | 954 | 1,4 | 0,8 | 1,1 | 2 | 3,5 | 498,8 | 11 | 21,6 | 2,3 | 8,2 | 1525 | 3,4 | 1,9 | 6,6 | 2,1 | 3,8 | 6,5 |
| EDR-956 | 956 | 1,5 | 0,8 | 1,1 | 2 | 3,5 | 527,3 | 13,7 | 19,2 | 2 | 7,5 | 944,6 | 2,8 | 1,4 | 7,5 | 2,4 | 4,7 | 6,4 |
| EDR-958 | 958 | 0,8 | 0,8 | 1,1 | 2 | 3,5 | 516,2 | 20,7 | 34 | 2,1 | 3,1 | 1098 | 3 | 1,9 | 7,5 | 0,6 | 7,2 | 6,9 |
| EDR-960 | 960 | 1 | 0,8 | 1,2 | 2 | 3,6 | 470,1 | 13,3 | 23,4 | 2,1 | 4,3 | 658 | 2,3 | 0,9 | 7,4 | 1,4 | 6,6 | 6,4 |
| EDR-962 | 962 | 1,5 | 0,8 | 1,1 | 2 | 3,5 | 519 | 18,6 | 25,4 | 2 | 3,6 | 670,7 | 2,3 | 0,8 | 8,1 | 0,6 | 6,4 | 6,6 |
| EDR-964 | 964 | 0,9 | 0,8 | 1,2 | 2 | 3,5 | 377,1 | 14,1 | 22,4 | 2,7 | 3,5 | 741,8 | 2,5 | 1,9 | 7 | 1,3 | 8,2 | 16,1 |
| EDR-966 | 966 | 2,1 | 0,8 | 1,1 | 1,2 | 3,4 | 323,4 | 23,3 | 25 | 2,3 | 2,9 | 410,8 | 1,9 | 1,3 | 6,5 | 1,1 | 6,9 | 5,6 |
| EDR-968 | 968 | 0,8 | 0,8 | 1,1 | 1,9 | 3,5 | 318 | 17,9 | 25,2 | 2 | 6 | 835,8 | 2,6 | 1,2 | 6,1 | 0,6 | 6,9 | 6,3 |

Table F.2 XRF analyses results of samples from Edremit field (cont’d)

| Element | depth | Co | Ni | Cu | Zn | Ga | Ge | As | Se | Br | Rb | Sr | Y | Zr | Nb | Mo | Cd | In |
|---|---|---|---|---|---|---|---|---|---|---|---|---|---|---|---|---|---|---|
| Sample No\Dimension | m | ppm | ppm | ppm | ppm | ppm | ppm | ppm | ppm | ppm | ppm | ppm | ppm | ppm | ppm | ppm | ppm | ppm |
| EDR-970 | 970 | 35,6 | 6,9 | 10,6 | 34,2 | 10,9 | 1,3 | 1,5 | 0,5 | 1,4 | 46,7 | 157,9 | 8,4 | 74,7 | 5,4 | 2,6 | 0,7 | 0,7 |
| EDR-972 | 972 | 57,3 | 24,4 | 18,3 | 72 | 12,2 | 1,7 | 3 | 0,7 | 0,9 | 65,7 | 190,6 | 13,5 | 100,6 | 5,7 | 8,6 | 0,7 | 0,7 |
| EDR-974 | 974 | 75,1 | 12,8 | 18,1 | 66,6 | 12,6 | 1,9 | 1,9 | 0,7 | 1,1 | 68,7 | 180 | 11,8 | 99,5 | 2,8 | 2,7 | 1,2 | 0,7 |
| EDR-976 | 976 | 45,1 | 16,2 | 39,6 | 44,8 | 23,9 | 1 | 20,3 | 0,5 | 0,2 | 102,3 | 170,7 | 23,5 | 194,6 | 20 | 5,5 | 2,4 | 0,9 |
| EDR-978 | 978 | 52,4 | 19 | 28,9 | 61,3 | 22,2 | 1,4 | 21,7 | 0,5 | 0,4 | 103,5 | 170,9 | 25,9 | 175,8 | 12,2 | 7,5 | 0,8 | 0,8 |
| EDR-980 | 980 | 48,7 | 17,2 | 34 | 59,1 | 22,1 | 2,5 | 25,6 | 0,6 | 1,2 | 105,2 | 162,9 | 25,7 | 198,5 | 16,2 | 4,4 | 0,8 | 0,8 |
| EDR-982 | 982 | 38,2 | 18,6 | 35,4 | 48,3 | 21,6 | 1,3 | 21,1 | 0,6 | 0,8 | 106 | 168,2 | 23,4 | 195,3 | 13,1 | 5,4 | 0,8 | 0,8 |
| EDR-984 | 984 | 17,8 | 19,4 | 65,7 | 38,4 | 22,1 | 1,8 | 51,2 | 0,4 | 0,6 | 93 | 228 | 21,3 | 192,2 | 15,9 | 4,5 | 0,8 | 0,8 |
| EDR-986 | 986 | 50,5 | 14,7 | 57,6 | 46,6 | 17,9 | 1,4 | 20,6 | 0,6 | 0,3 | 77,1 | 284,1 | 17,4 | 165,8 | 3 | 8 | 0,8 | 0,8 |
| EDR-988 | 988 | 54,5 | 13,7 | 53,9 | 70,2 | 20,3 | 1 | 23 | 0,4 | 0,6 | 77,4 | 297,4 | 16,7 | 154,3 | 12,9 | 8,8 | 0,8 | 0,8 |
| EDR-990 | 990 | 61 | 13,2 | 52,3 | 41,4 | 18,2 | 1,9 | 19 | 0,6 | 0,8 | 68,1 | 313,3 | 18,4 | 145,8 | 8,6 | 3,1 | 0,8 | 0,8 |
| EDR-992 | 992 | 50,9 | 8,7 | 52,3 | 56,5 | 17,9 | 1,4 | 39,1 | 0,6 | 0,3 | 56,4 | 443 | 15,4 | 105,8 | 2,9 | 6 | 0,8 | 0,7 |
| EDR-994 | 994 | 47,9 | 6,7 | 35,7 | 126,8 | 19,1 | 1,2 | 14,9 | 0,5 | 0,4 | 60,4 | 455,8 | 15,6 | 128,3 | 5,1 | 4,2 | 0,8 | 0,8 |
| EDR-996 | 996 | 79,3 | 12,7 | 41,3 | 112,6 | 21 | 1,5 | 9,3 | 0,6 | 0,7 | 63,5 | 453,6 | 14,3 | 138,1 | 3,1 | 3,6 | 0,8 | 0,8 |
| EDR-998 | 998 | 50 | 11,5 | 53 | 41 | 19,1 | 1,3 | 8,4 | 0,5 | 0,2 | 65,4 | 418 | 20,7 | 135,5 | 3,2 | 3,4 | 0,8 | 0,8 |
| EDR-1000 | 1000 | 41,3 | 5,2 | 54,9 | 41,7 | 18,6 | 0,9 | 11,9 | 0,4 | 0,7 | 64,8 | 406,4 | 17,7 | 121 | 3,2 | 3,2 | 0,9 | 0,8 |
| EDR-1002 | 1002 | 35,2 | 9,5 | 49,1 | 36,2 | 17,1 | 0,7 | 9,8 | 0,3 | 0,2 | 64,4 | 406,5 | 18,8 | 119,2 | 10,1 | 7,7 | 0,9 | 0,8 |
| EDR-1004 | 1004 | 57,4 | 5,7 | 36,1 | 41 | 18,1 | 1 | 4,5 | 0,4 | 0,2 | 62,2 | 408,8 | 18,9 | 156,1 | 6,7 | 3,3 | 0,8 | 1,1 |
| EDR-1006 | 1006 | 63,2 | 5,8 | 54,2 | 47,2 | 19,5 | 1,9 | 5 | 0,5 | 1,1 | 66,3 | 406,8 | 18,7 | 140,6 | 12,7 | 3,2 | 0,8 | 0,8 |
| EDR-1008 | 1008 | 37,5 | 7,7 | 77,6 | 38,5 | 18,6 | 1 | 10,8 | 0,4 | 0,2 | 64,1 | 483,4 | 16,4 | 142,6 | 4,2 | 4,9 | 0,9 | 0,8 |
| EDR-1010 | 1010 | 35,1 | 7,1 | 49,5 | 47,5 | 16,6 | 1,1 | 5,2 | 0,5 | 0,5 | 64,3 | 418,7 | 18,9 | 140 | 7 | 3,7 | 1,8 | 1,8 |
| EDR-1012 | 1012 | 39,4 | 9,1 | 30,9 | 48,3 | 18,1 | 1,2 | 3,5 | 0,5 | 0,9 | 68,1 | 476,4 | 14,7 | 131 | 9,4 | 2,3 | 0,8 | 0,9 |
| EDR-1014 | 1014 | 61,2 | 8,9 | 36,6 | 45,7 | 18,8 | 1,5 | 9,4 | 0,9 | 0,5 | 69,1 | 489 | 13,9 | 125 | 6,3 | 5,5 | 0,7 | 0,8 |
| EDR-1016 | 1016 | 54,7 | 7,7 | 27,5 | 47,8 | 18,4 | 1,4 | 3,1 | 0,9 | 0,9 | 66,9 | 481,2 | 14,6 | 133,8 | 3,5 | 3,7 | 0,8 | 0,8 |
| EDR-1018 | 1018 | 55,3 | 9,2 | 24,8 | 77,2 | 18,5 | 1,5 | 1,7 | 0,6 | 0,6 | 69,4 | 474,3 | 15,5 | 123,9 | 2,6 | 3,4 | 0,8 | 0,8 |
| EDR-1020 | 1020 | 56 | 6,5 | 25,7 | 47,3 | 15,9 | 1,2 | 5,9 | 0,5 | 0,3 | 65,8 | 476,4 | 14,6 | 103,1 | 10 | 9,1 | 0,8 | 0,8 |
| EDR-1022 | 1022 | 55,7 | 9,2 | 37,5 | 59,8 | 19,1 | 1,7 | 13,8 | 0,6 | 1,1 | 63,6 | 475,7 | 15,4 | 120,6 | 8,4 | 5,7 | 1,4 | 2,1 |
| EDR-1024 | 1024 | 58,2 | 4,2 | 27,8 | 43,6 | 15,6 | 1,4 | 3,2 | 0,6 | 0,5 | 60,5 | 443,4 | 17,4 | 125,8 | 3,1 | 3,3 | 0,8 | 0,8 |
| EDR-1026 | 1026 | 55 | 5 | 32,6 | 45,8 | 16,5 | 2,6 | 5,3 | 0,5 | 0,2 | 65,3 | 450,7 | 19,7 | 127,7 | 7,4 | 2,9 | 0,8 | 0,8 |
| EDR-1028 | 1028 | 51,5 | 6 | 33,3 | 46,4 | 16 | 1,2 | 4 | 0,5 | 0,4 | 63,7 | 442 | 20,5 | 164,7 | 5,8 | 3,5 | 0,9 | 0,9 |
| EDR-1030 | 1030 | 47 | 6,1 | 20,1 | 51,6 | 17,4 | 1 | 2,3 | 0,4 | 0,2 | 61,9 | 467,1 | 17,7 | 133,5 | 3,3 | 3,3 | 0,8 | 0,8 |
| EDR-1032 | 1032 | 51,1 | 8 | 15,1 | 68,7 | 18,3 | 1,6 | 4,1 | 0,5 | 1,1 | 65,3 | 502,8 | 13,9 | 116,6 | 2,9 | 3,3 | 0,8 | 0,8 |
| EDR-1034 | 1034 | 48,1 | 6,8 | 21,6 | 48,8 | 17,5 | 1,4 | 4,3 | 0,6 | 1 | 64,2 | 483,7 | 15 | 125,6 | 4,4 | 5 | 0,8 | 0,8 |
| EDR-1036 | 1036 | 62,1 | 3,9 | 18,1 | 44,8 | 17,4 | 1,4 | 2,9 | 0,6 | 0,2 | 67,1 | 496,2 | 14,5 | 131,2 | 7,8 | 5,3 | 1,5 | 1,5 |
| EDR-1038 | 1038 | 63,3 | 6,8 | 20,5 | 44,2 | 18,9 | 1,3 | 4,4 | 0,5 | 0,7 | 63,8 | 500,1 | 14,4 | 112,8 | 6 | 3,1 | 0,8 | 0,7 |

Table F.2 XRF analyses results of samples from Edremit field (cont’d)

| Element | depth | Sn | Sb | Te | I | Cs | Ba | La | Ce | Hf | Ta | W | Hg | Tl | Pb | Bi | Th | U |
|---|---|---|---|---|---|---|---|---|---|---|---|---|---|---|---|---|---|---|
| **Sample No\Dimension** | **m** | **ppm** | **ppm** | **ppm** | **ppm** | **ppm** | **ppm** | **ppm** | **ppm** | **ppm** | **ppm** | **ppm** | **ppm** | **ppm** | **ppm** | **ppm** | **ppm** | **ppm** |
| EDR-970 | 970 | 1 | 0,8 | 1,1 | 1,9 | 3,4 | 263,4 | 11,1 | 26,8 | 1,9 | 2,6 | 515 | 2 | 0,5 | 8,2 | 0,5 | 5,6 | 5,7 |
| EDR-972 | 972 | 0,8 | 0,8 | 1,1 | 2 | 3,4 | 404,7 | 25,4 | 40,6 | 2,1 | 6,2 | 826 | 2,6 | 2,1 | 8 | 3,5 | 7,2 | 8,7 |
| EDR-974 | 974 | 1,8 | 0,8 | 1,1 | 2 | 3,4 | 382,9 | 15,6 | 22,3 | 2,1 | 4,4 | 1044 | 2,9 | 1,6 | 9,5 | 2,6 | 5 | 21,9 |
| EDR-976 | 976 | 1 | 0,9 | 1,3 | 2,2 | 3,8 | 787,5 | 32,2 | 76,8 | 2,7 | 3,6 | 291,1 | 1,7 | 1,5 | 13,4 | 0,6 | 15,5 | 22,9 |
| EDR-978 | 978 | 1,3 | 0,8 | 1,2 | 2,1 | 3,7 | 836,9 | 34,2 | 78 | 2,8 | 4,4 | 394,6 | 2 | 1,9 | 14,9 | 0,6 | 16,4 | 15,6 |
| EDR-980 | 980 | 0,9 | 0,8 | 1,2 | 2,1 | 3,7 | 824,1 | 25,8 | 66,6 | 2,7 | 8,2 | 475,8 | 2,2 | 0,8 | 14,2 | 0,6 | 17,8 | 12,3 |
| EDR-982 | 982 | 0,9 | 0,8 | 1,1 | 2,1 | 3,7 | 876,7 | 32,8 | 65,2 | 2,8 | 7,7 | 290,3 | 1,7 | 1,3 | 13,8 | 0,5 | 15,8 | 6,6 |
| EDR-984 | 984 | 1,9 | 0,9 | 1,2 | 2,2 | 3,7 | 768,9 | 31,5 | 77,9 | 3,4 | 4,4 | 259 | 1,7 | 1,6 | 12,5 | 0,7 | 14,9 | 23,4 |
| EDR-986 | 986 | 0,4 | 0,8 | 1,1 | 2,1 | 3,6 | 753,9 | 24,4 | 51,6 | 3,4 | 7,4 | 490 | 2,2 | 1,2 | 11,4 | 1,1 | 10,3 | 6,4 |
| EDR-988 | 988 | 0,9 | 0,9 | 1,3 | 2,2 | 3,8 | 761,9 | 23,9 | 60,9 | 2,8 | 4 | 203,6 | 1,5 | 0,7 | 12,1 | 0,6 | 11,8 | 7,8 |
| EDR-990 | 990 | 1,3 | 0,9 | 1,2 | 2 | 3,6 | 624,5 | 27,4 | 60,6 | 3,3 | 4,1 | 440,5 | 2,1 | 1,8 | 10,8 | 1,6 | 11 | 6,6 |
| EDR-992 | 992 | 0,8 | 0,8 | 1,1 | 2 | 3,6 | 641,8 | 23 | 41,7 | 3,2 | 4,1 | 417,9 | 2,1 | 1,5 | 13,4 | 0,6 | 7,6 | 7,6 |
| EDR-994 | 994 | 1,1 | 0,9 | 1,2 | 2,1 | 3,7 | 685,4 | 19,7 | 23,5 | 2,8 | 3,6 | 272,9 | 1,8 | 0,7 | 17,1 | 1,4 | 5,6 | 8,4 |
| EDR-996 | 996 | 1,2 | 0,8 | 1,2 | 2,1 | 3,6 | 700,8 | 15,9 | 50,3 | 3,2 | 3,9 | 559,7 | 2,4 | 1,3 | 13 | 0,6 | 7,5 | 7 |
| EDR-998 | 998 | 2,4 | 0,8 | 1,2 | 2,1 | 3,7 | 712 | 25,7 | 55,8 | 3,3 | 5,6 | 387,9 | 2 | 0,8 | 11,1 | 0,6 | 10,6 | 7,1 |
| EDR-1000 | 1000 | 1,9 | 0,9 | 1,2 | 2,1 | 3,7 | 689,5 | 27,5 | 55,9 | 3,3 | 4,8 | 170,3 | 1,4 | 1,1 | 11,2 | 0,6 | 8,7 | 7,9 |
| EDR-1002 | 1002 | 0,9 | 0,9 | 1,3 | 2,1 | 3,8 | 719,3 | 11 | 47,6 | 4,7 | 3,7 | 74,9 | 1,1 | 0,9 | 11,3 | 0,8 | 12,4 | 8,2 |
| EDR-1004 | 1004 | 1,2 | 0,9 | 1,2 | 2,2 | 3,7 | 729,2 | 25,3 | 30 | 3,5 | 3,6 | 225,5 | 1,5 | 0,5 | 11,5 | 0,6 | 7,8 | 12,8 |
| EDR-1006 | 1006 | 0,9 | 0,8 | 1,1 | 2,1 | 3,5 | 706,2 | 21,6 | 42,3 | 3,5 | 4,1 | 349 | 2 | 1,6 | 11,5 | 0,9 | 7,9 | 10,5 |
| EDR-1008 | 1008 | 0,9 | 0,9 | 1,2 | 2,1 | 3,7 | 698,4 | 23,8 | 51,9 | 3,8 | 4,7 | 240,9 | 1,6 | 1,6 | 12,1 | 0,6 | 5,5 | 7,2 |
| EDR-1010 | 1010 | 4,5 | 0,7 | 1,3 | 2,1 | 3,7 | 625,4 | 24,2 | 62,1 | 3,2 | 3,6 | 288 | 1,8 | 1,7 | 10,1 | 0,5 | 6,8 | 22,4 |
| EDR-1012 | 1012 | 1,4 | 0,9 | 1,2 | 2,1 | 3,7 | 793,6 | 21,5 | 27,6 | 2,9 | 4,2 | 333,1 | 1,9 | 1 | 14 | 1,9 | 7,4 | 20,7 |
| EDR-1014 | 1014 | 0,8 | 0,8 | 1,1 | 2 | 3,6 | 802 | 12,8 | 19,3 | 2,9 | 3,8 | 498,8 | 2,3 | 1,7 | 13,8 | 0,6 | 6,8 | 7,1 |
| EDR-1016 | 1016 | 1 | 0,9 | 1,2 | 2,1 | 3,7 | 759,2 | 21,9 | 45,5 | 2,6 | 3,2 | 437,1 | 2,1 | 1,3 | 13,1 | 0,6 | 6,8 | 24,6 |
| EDR-1018 | 1018 | 0,9 | 0,9 | 1,2 | 2,1 | 3,7 | 761,7 | 21,2 | 29,1 | 2,7 | 5,3 | 495 | 2,3 | 2,5 | 13,1 | 11,9 | 7,4 | 12,7 |
| EDR-1020 | 1020 | 0,9 | 0,9 | 1,2 | 2,1 | 3,6 | 776,5 | 24,2 | 49,3 | 2,6 | 5,5 | 324,2 | 1,8 | 1,5 | 12,9 | 3,7 | 6,2 | 7,8 |
| EDR-1022 | 1022 | 0,9 | 0,8 | 1,2 | 2,2 | 3,6 | 756,4 | 19,4 | 21,2 | 3 | 3,7 | 482 | 2,3 | 1,1 | 13,9 | 2,3 | 6,3 | 18,6 |
| EDR-1024 | 1024 | 0,9 | 0,9 | 1,1 | 2,1 | 3,6 | 716,1 | 14,4 | 32,3 | 2,9 | 4,5 | 420,9 | 2,1 | 1,7 | 10,6 | 0,6 | 11,1 | 17 |
| EDR-1026 | 1026 | 0,4 | 0,8 | 1,1 | 2,1 | 3,6 | 703,3 | 23,1 | 56,6 | 2,8 | 8 | 377,8 | 2 | 1,7 | 12,8 | 0,8 | 9,2 | 8 |
| EDR-1028 | 1028 | 1,8 | 0,9 | 1,3 | 2,2 | 3,7 | 693,8 | 24,7 | 43,5 | 4,1 | 3,5 | 326,3 | 1,8 | 1,8 | 12,4 | 0,6 | 11,3 | 14,2 |
| EDR-1030 | 1030 | 1,8 | 0,9 | 1,2 | 2,1 | 3,7 | 750,3 | 19,6 | 37,9 | 2,9 | 2,7 | 265,5 | 1,6 | 0,9 | 13,2 | 0,6 | 8,1 | 15,4 |
| EDR-1032 | 1032 | 0,9 | 0,9 | 1,2 | 2,1 | 3,7 | 818,8 | 21,2 | 38,6 | 2,2 | 5 | 610,7 | 2,4 | 1 | 13,8 | 3 | 7 | 9,5 |
| EDR-1034 | 1034 | 0,8 | 0,9 | 1,2 | 2,1 | 3,6 | 817,9 | 23 | 49,8 | 2,5 | 4,3 | 477,8 | 2,2 | 1,2 | 13,2 | 0,6 | 9,5 | 7 |
| EDR-1036 | 1036 | 1,5 | 0,9 | 1,2 | 2,1 | 3,6 | 835,6 | 18 | 26,9 | 2,5 | 2,5 | 472,8 | 2,2 | 2,3 | 14,7 | 0,8 | 8,6 | 11,6 |
| EDR-1038 | 1038 | 0,9 | 0,8 | 1,2 | 2,1 | 3,6 | 807,4 | 15,9 | 37,6 | 2,4 | 3,1 | 439,1 | 2,1 | 0,9 | 14,2 | 0,6 | 8,3 | 9,3 |

## G. Reservoir Rock Mineralogy of the Representative Samples from Akköy and Edremit Fields Used in Modelling

Table G.1 Reservoir rock mineralogy of representative Akköy samples

| Mineral | PS-1-1315 | | PS-1-1375 | | PS-1-1415 | | PS-1-1480 | | PS-1-1495 | | PS-1-1515* | | PS-2-840* | | PS-2-1280 | | PS-2-1355 | | PS-2-1380* | |
|---|---|---|---|---|---|---|---|---|---|---|---|---|---|---|---|---|---|---|---|---|
| | **Vol. (%)** | **Amount (mol)** | **Vol. (%)** | **Amount (mol)** | **Vol. (%)** | **Amount (mol)** | **Vol. (%)** | **Amount (mol)** | **Vol. (%)** | **Amount (mol)** | **Vol. (%)** | **Amount (mol)** | **Vol. (%)** | **Amount (mol)** | **Vol. (%)** | **Amount (mol)** | **Vol. (%)** | **Amount (mol)** | **Vol. (%)** | **Amount (mol)** |
| Albite | 2,5 | 7,17 | - | - | - | - | 7,9 | 22,65 | - | - | 13 | 37,27 | 6,7 | 19,21 | - | - | 10,8 | 30,97 | - | - |
| Ankerite | - | - | - | - | - | - | 12,4 | 45,31 | - | - | - | - | - | - | 16,5 | 60,29 | - | - | - | - |
| Biotite | - | - | 7,1 | 10,46 | - | - | - | - | 8 | 11,79 | - | - | 7,9 | 11,64 | - | - | - | - | - | - |
| Calcite | - | - | 13,6 | 102,47 | 26,6 | 200,41 | 17,3 | 130,34 | 25,3 | 190,62 | 16,3 | 122,81 | 22,8 | 171,78 | 27,2 | 204,93 | 55,6 | 418,91 | 46,8 | 352,61 |
| Chlorite | - | - | - | - | - | - | - | - | 13,4 | 29,57 | 12,9 | 28 | - | - | - | - | - | - | 16,3 | 35,97 |
| Dolomite | 40,7 | 166,45 | 8,9 | 36,40 | 22,4 | 91,61 | - | - | 7,2 | 29,44 | 8,3 | 34 | - | - | - | - | 7,9 | 32,31 | 7,6 | 31,08 |
| Illite | 13,4 | 26,32 | 13,6 | 26,72 | 7,1 | 13,95 | - | - | 7,8 | 15,32 | - | - | 12,4 | 24,36 | 8,1 | 15,91 | - | - | - | - |
| Kaolinite | - | - | - | - | 1 | 2,92 | 16 | 46,74 | 8,6 | 25,12 | 17,5 | 51 | - | - | - | - | - | - | 2 | 5,84 |
| Muscovite | 1,8 | 3,40 | 2,6 | 4,92 | 0,9 | 1,70 | 4,6 | 8,70 | - | - | 0,4 | 0,76 | 1,9 | 3,59 | 5,4 | 10,21 | 1,3 | 2,46 | 7,3 | 13,81 |
| Orthoclase | - | - | 17,1 | 46,33 | - | - | - | - | - | - | - | - | 13,7 | 37,12 | - | - | - | - | - | - |
| Quartz | 39 | 489,52 | 34,7 | 435,55 | 39,1 | 490,78 | 39,2 | 492,03 | 27,6 | 346,43 | 31,5 | 395,38 | 32,5 | 407,94 | 39,8 | 499,56 | 24,4 | 306,27 | 19,9 | 249,78 |
| Smectite | 2,5 | 4,81 | 2,4 | 4,62 | 2,9 | 5,58 | 2,7 | 5,19 | 2,1 | 4,04 | - | - | 2,2 | 4,23 | 3 | 5,77 | - | - | - | - |

*Simulated Samples

Table G.2 Reservoir rock mineralogy of representative Edremit samples

| Mineral | EDR-912* | | EDR-928 | | EDR-964 | | EDR-976 | | EDR-988* | | EDR-994 | | EDR-1008* | | EDR-1032 | |
|---|---|---|---|---|---|---|---|---|---|---|---|---|---|---|---|---|
| | Vol. (%) | Amount (mol) | Vol. (%) | Amount (mol) | Vol. (%) | Amount (mol) | Vol. (%) | Amount (mol) | Vol. (%) | Amount (mol) | Vol. (%) | Amount (mol) | Vol. (%) | Amount (mol) | Vol. (%) | Amount (mol) |
| Albite | - | - | 21,7 | 43,11 | - | - | - | - | 25,6 | 50,86 | - | - | - | - | - | - |
| Amphibole | - | - | - | - | - | - | - | - | - | - | 5,8 | 3,63 | - | - | - | - |
| Biotite | 14,3 | 17,91 | - | - | 12 | 15,03 | - | - | 6,3 | 7,89 | 20,5 | 25,67 | 10,2 | 12,77 | 14,3 | 17,91 |
| Bytownite | - | - | - | - | - | - | - | - | - | - | 18 | 34,20 | - | - | - | - |
| Calcite | 1,2 | 6,26 | 4 | 20,88 | - | - | - | - | 5 | 26,1 | - | - | - | - | 1,2 | 6,26 |
| Chlorite | - | - | - | - | - | - | - | - | 12 | 18,35 | - | - | - | - | - | - |
| Dolomite | 3,2 | 9,07 | 1,1 | 3,12 | - | - | - | - | 2 | 5,67 | 4,9 | 13,88 | - | - | 3,2 | 9,07 |
| Illite | - | - | 10,7 | 14,56 | 8 | 10,89 | 12,2 | 16,60 | - | - | 3,1 | 4,22 | 11,4 | 15,52 | - | - |
| Kaolinite | 3 | 6,07 | - | - | - | - | 9,4 | 19,03 | 10,2 | 20,64 | 4,5 | 9,11 | 0,6 | 1,21 | 3 | 6,07 |
| Labradorite | - | - | - | - | - | - | 29,8 | 57,28 | - | - | - | - | 32,8 | 63,05 | - | - |
| Orthoclase | 50 | 93,86 | 14 | 26,28 | 20,5 | 38,48 | - | - | - | - | 22,4 | 42,05 | 23,2 | 43,55 | 50 | 93,86 |
| Quartz | 28,3 | 246,12 | 48,5 | 421,79 | 59,5 | 517,46 | 48,6 | 422,66 | 38,9 | 338,3 | 20,9 | 181,76 | 21,8 | 189,59 | 28,3 | 246,12 |

*Simulated Samples

## H. Modelling Results of Samples PS-1-1315, PS-1-1375, PS-1-1415, PS-1-1480, PS-1-1495, PS-2-1280, PS-2-1355 from Akköy Field and EDR-928, EDR-964, EDR-976, EDR-994, EDR-1032 from Edremit Field

Table H.1 Equilibrium modelling results for sample ADK-PS-1-1315 from Akköy field (values are as moles)

| Mineral | PS-1-1315 | | |
|---|---|---|---|
| | Initial | Final | Delta |
| Albite | 7,17 | 0 | -7,17 |
| Ankerite | 0 | 0 | 0 |
| Biotite | 0 | 0 | 0 |
| Calcite | 0 | 0 | 0 |
| Chlorite | 0 | 0 | 0 |
| Dolomite | 166,45 | 166,5 | 0,05 |
| Illite | 26,32 | 26,27 | -0,05 |
| Kaolinite | 0 | 0 | 0 |
| Muscovite | 3,40 | 3,435 | 0,03 |
| Orthoclase | 0 | 0 | 0 |
| Quartz | 489,52 | 511,1 | 21,58 |
| Smectite | 4,81 | 4,808 | 0 |
| Dawsonite | 0 | 7,187 | 7,19 |
| Magnesite | 0 | 0 | 0 |
| Siderite | 0 | 0 | 0 |

Table H.2 Equilibrium modelling results of the water sample PS-1.2018 reacting with sample ADK-PS-1-1315 (Akköy field)

| mol/L | initial | final |
|---|---|---|
| Al | 7,48E-07 | 9,84E-06 |
| Total C | 0,02945 | 0,953 |
| Ca | 0,006629 | 0,0006575 |
| Cl | 0,002052 | 0,002356 |
| Fe | 6,27E-06 | 0,001186 |
| K | 0,003457 | 3,06E-09 |
| Mg | 0,002483 | 0,01319 |
| Na | 0,03068 | 0,01585 |
| $SO_4$ | 0,009349 | 0,01073 |
| Si | 0,0005351 | 0,001169 |

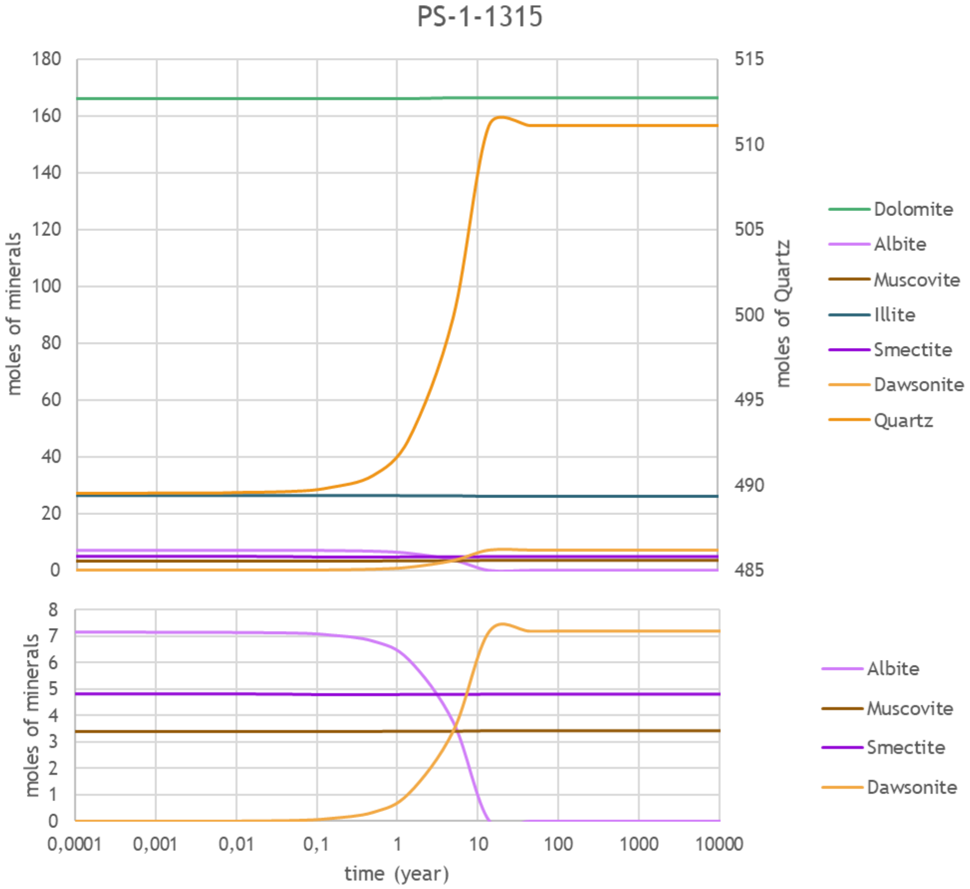

Figure H.1. Kinetic modelling results for sample ADK-PS-1-1315 from Akköy field

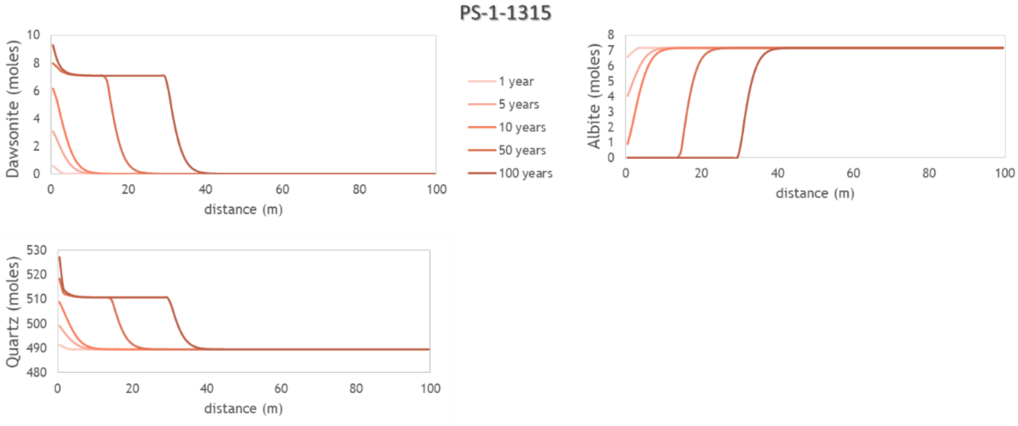

Figure H.2. Reactive transport modelling results for sample ADK-PS-1-1315 from Akköy field

Table H.3 Equilibrium modelling results for sample ADK-PS-1-1375 from Akköy field (values are as moles)

| **Mineral** | **PS-1-1375** | | |
|---|---|---|---|
| | **Initial** | **Final** | **Delta** |
| Albite | 0 | 0 | 0 |
| Ankerite | 0 | 47,8 | 47,80 |
| Biotite | 10,46 | 0 | -10,46 |
| Calcite | 102,47 | 58,27 | -44,20 |
| Chlorite | 0 | 0 | 0 |
| Dolomite | 36,40 | 32,9 | -3,50 |
| Illite | 26,72 | 0 | -26,72 |
| Kaolinite | 0 | 0 | 0 |
| Muscovite | 4,92 | 30,07 | 25,15 |
| Orthoclase | 46,33 | 48,58 | 2,25 |
| Quartz | 435,55 | 495,6 | 60,05 |
| Smectite | 4,62 | 0 | -4,62 |
| Dawsonite | 0 | 0 | 0 |
| Magnesite | 0 | 0 | 0 |
| Siderite | 0 | 0 | 0 |

Table H.4 Equilibrium modelling results of the water sample PS-1.2018 reacting with sample ADK-PS-1-1375 (Akköy field)

| mol/L | initial | final |
|---|---|---|
| Al | 7,48E-07 | 2,79E-07 |
| Total C | 0,02945 | 1,262 |
| Ca | 0,006629 | 1,27E-04 |
| Cl | 0,002052 | 0,001586 |
| Fe | 6,27E-06 | 1,26E-03 |
| K | 0,003457 | 0,01564 |
| Mg | 0,002483 | 4,37E-06 |
| Na | 0,03068 | 0,5594 |
| $SO_4$ | 0,009349 | 0,007227 |
| Si | 0,0005351 | 0,001186 |

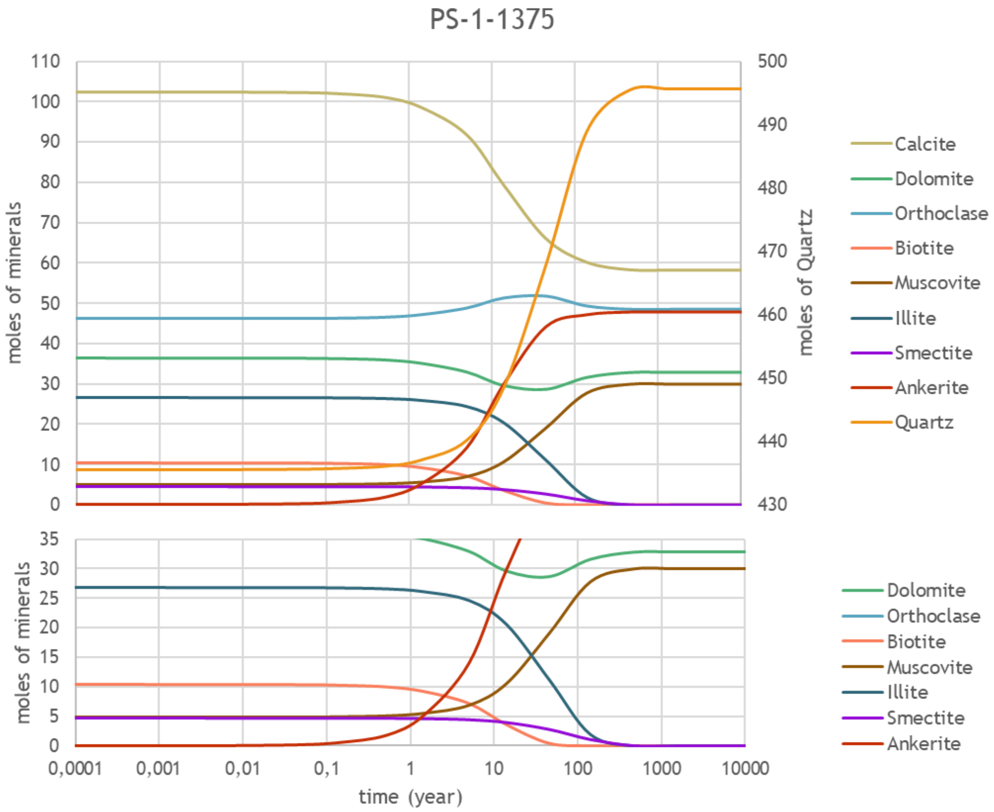

Figure H.3. Kinetic modelling results for sample ADK-PS-1-1375 from Akköy field

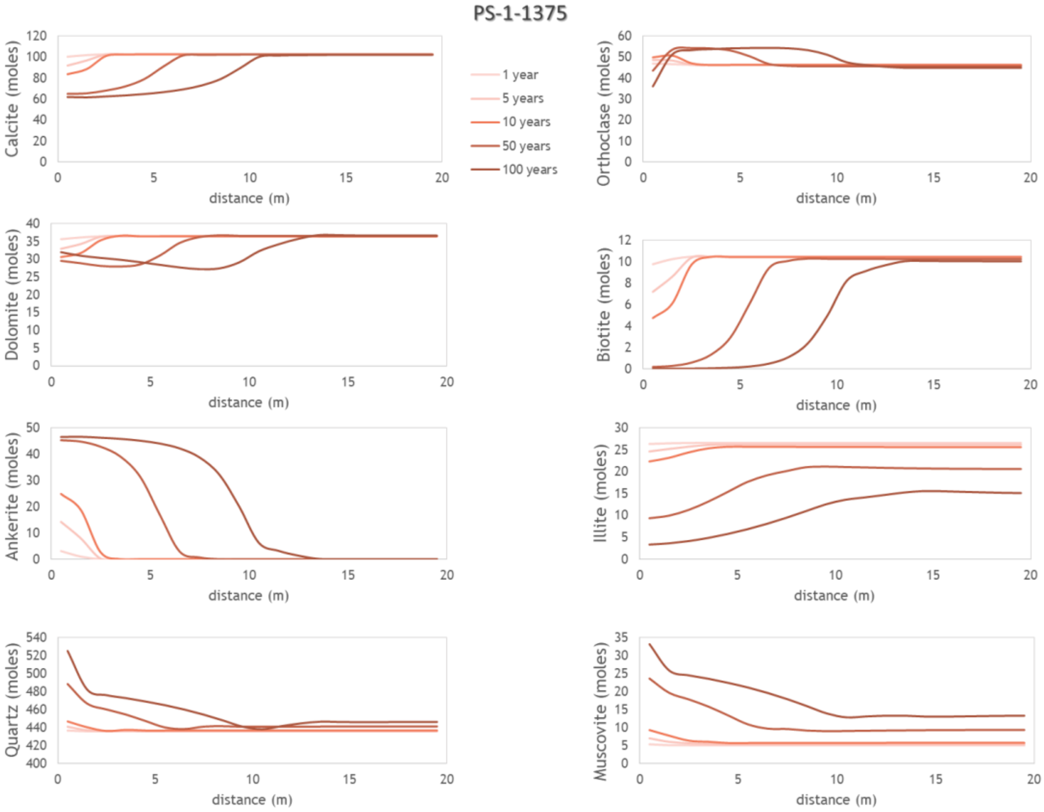

Figure H.4. Reactive transport modelling results for sample ADK-PS-1-1375 from Akköy field

Table H.5 Equilibrium modelling results for sample ADK-PS-1-1415 from Akköy field (values are as moles)

| **Mineral** | **PS-1-1415** | | |
|---|---|---|---|
| | **Initial** | **Final** | **Delta** |
| Albite | 0 | 0 | 0 |
| Ankerite | 0 | 3,584 | 3,58 |
| Biotite | 0 | 0 | 0 |
| Calcite | 200,41 | 189,5 | -10,91 |
| Chlorite | 0 | 0 | 0 |
| Dolomite | 91,61 | 99,05 | 7,44 |
| Illite | 13,95 | 0 | -13,95 |
| Kaolinite | 2,92 | 7,905 | 4,98 |
| Muscovite | 1,70 | 11,19 | 9,49 |
| Orthoclase | 0 | 0 | 0 |
| Quartz | 490,78 | 522,1 | 31,32 |
| Smectite | 5,58 | 0 | -5,58 |
| Dawsonite | 0 | 0,6252 | 0,63 |
| Magnesite | 0 | 0 | 0 |
| Siderite | 0 | 0 | 0 |

Table H.6 Equilibrium modelling results of the water sample PS-1.2018 reacting with sample ADK-PS-1-1415 (Akköy field)

| **mol/L** | **initial** | **final** |
|---|---|---|
| Al | 7,48E-07 | 3,21E-07 |
| Total C | 0,02945 | 1,281 |
| Ca | 0,006629 | 4,30E-04 |
| Cl | 0,002052 | 0,002076 |
| Fe | 6,27E-06 | 2,23E-03 |
| K | 0,003457 | 9,61E-04 |
| Mg | 0,002483 | 1,91E-05 |
| Na | 0,03068 | 0,2454 |
| $SO_4$ | 0,009349 | 0,00946 |
| Si | 0,0005351 | 0,001173 |

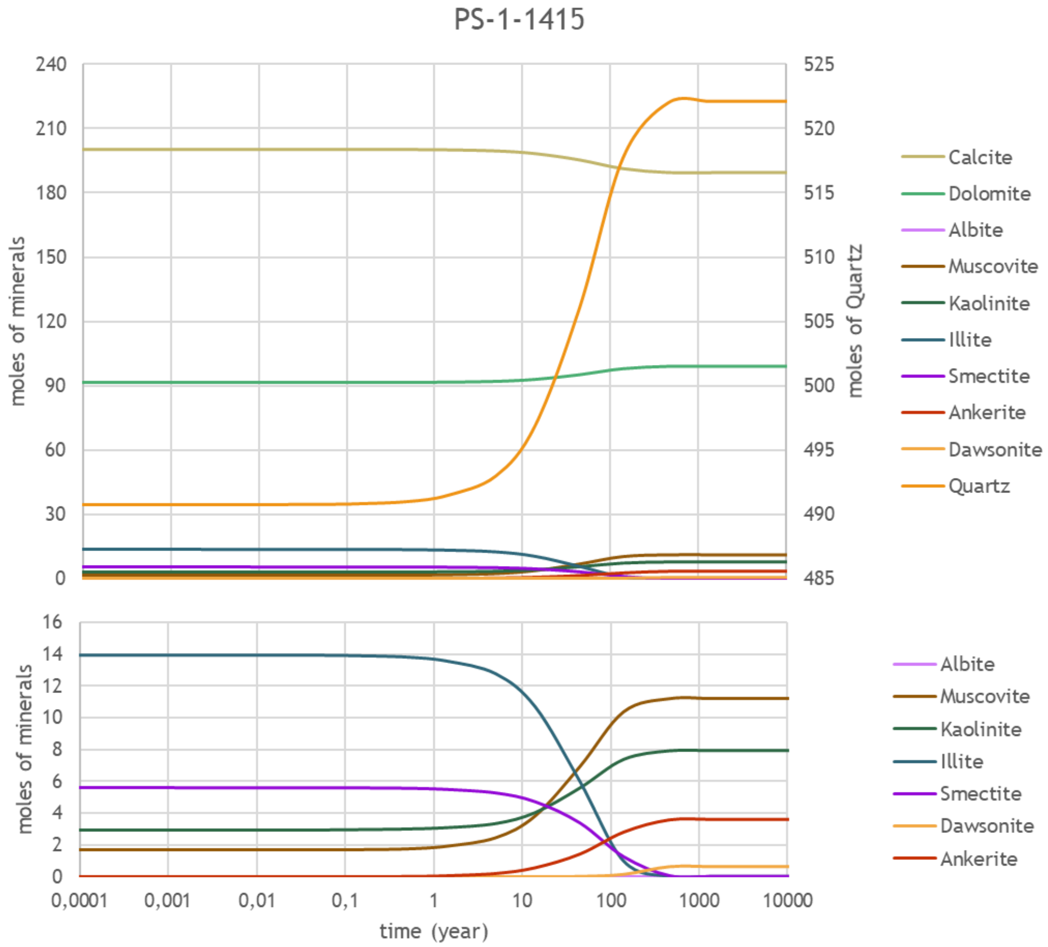

Figure H.5. Kinetic modelling results for sample ADK-PS-1-1415 from Akköy field

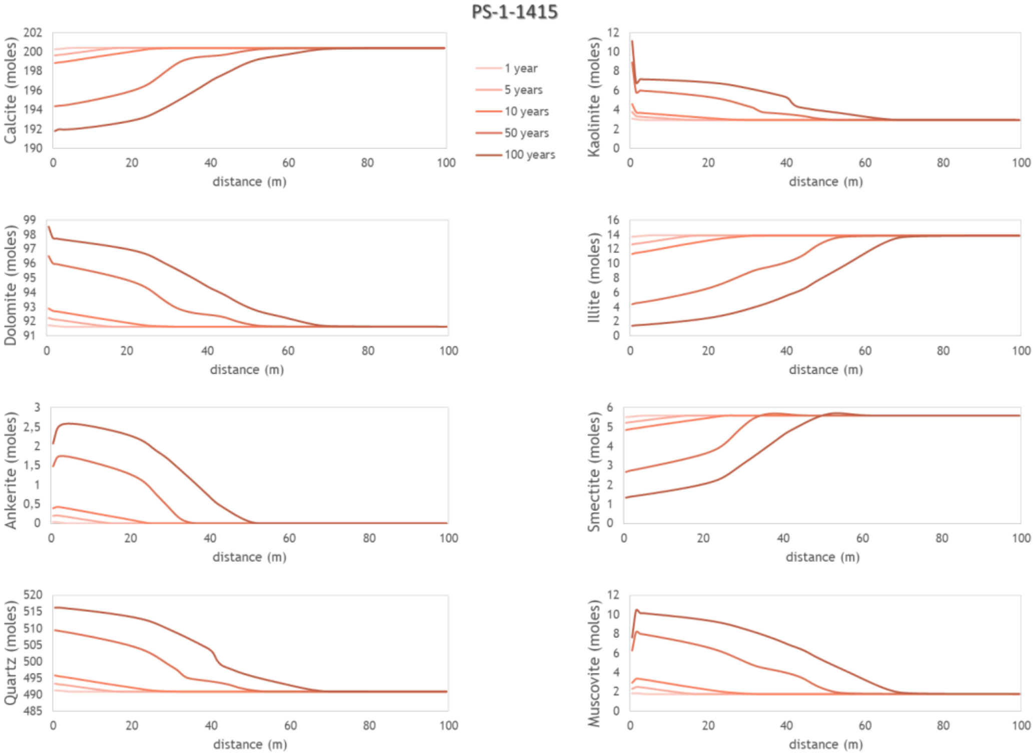

Figure H.6. Reactive transport modelling results for sample ADK-PS-1-1415 from Akköy field

Table H.7 Equilibrium modelling results for sample ADK-PS-1-1480 from Akköy field (values are as moles)

| **Mineral** | **PS-1-1480** | | |
|---|---|---|---|
| | **Initial** | **Final** | **Delta** |
| Albite | 22,65 | 0 | -22,65 |
| Ankerite | 45,31 | 48,64 | 3,33 |
| Biotite | 0 | 0 | 0 |
| Calcite | 130,34 | 123,4 | -6,94 |
| Chlorite | 0 | 0 | 0 |
| Dolomite | 0 | 3,673 | 3,67 |
| Illite | 0 | 0 | 0 |
| Kaolinite | 46,74 | 48,09 | 1,35 |
| Muscovite | 8,70 | 9,741 | 1,04 |
| Orthoclase | 0 | 0 | 0 |
| Quartz | 492,03 | 573,6 | 81,57 |
| Smectite | 5,19 | 0 | -5,19 |
| Dawsonite | 0 | 23,3 | 23,30 |
| Magnesite | 0 | 0 | 0 |
| Siderite | 0 | 0 | 0 |

Table H.8 Equilibrium modelling results of the water sample PS-1.2018 reacting with sample ADK-PS-1-1480 (Akköy field)

| **mol/L** | **initial** | **final** |
|---|---|---|
| Al | 7,48E-07 | 3,92E-07 |
| Total C | 0,02945 | 1,00E+00 |
| Ca | 0,006629 | 0,0003601 |
| Cl | 0,002052 | 0,003391 |
| Fe | 6,27E-06 | 0,002669 |
| K | 0,003457 | 7,85E-04 |
| Mg | 0,002483 | 1,85E-05 |
| Na | 0,03068 | 0,2551 |
| $SO_4$ | 0,009349 | 0,01545 |
| Si | 0,0005351 | 0,001173 |

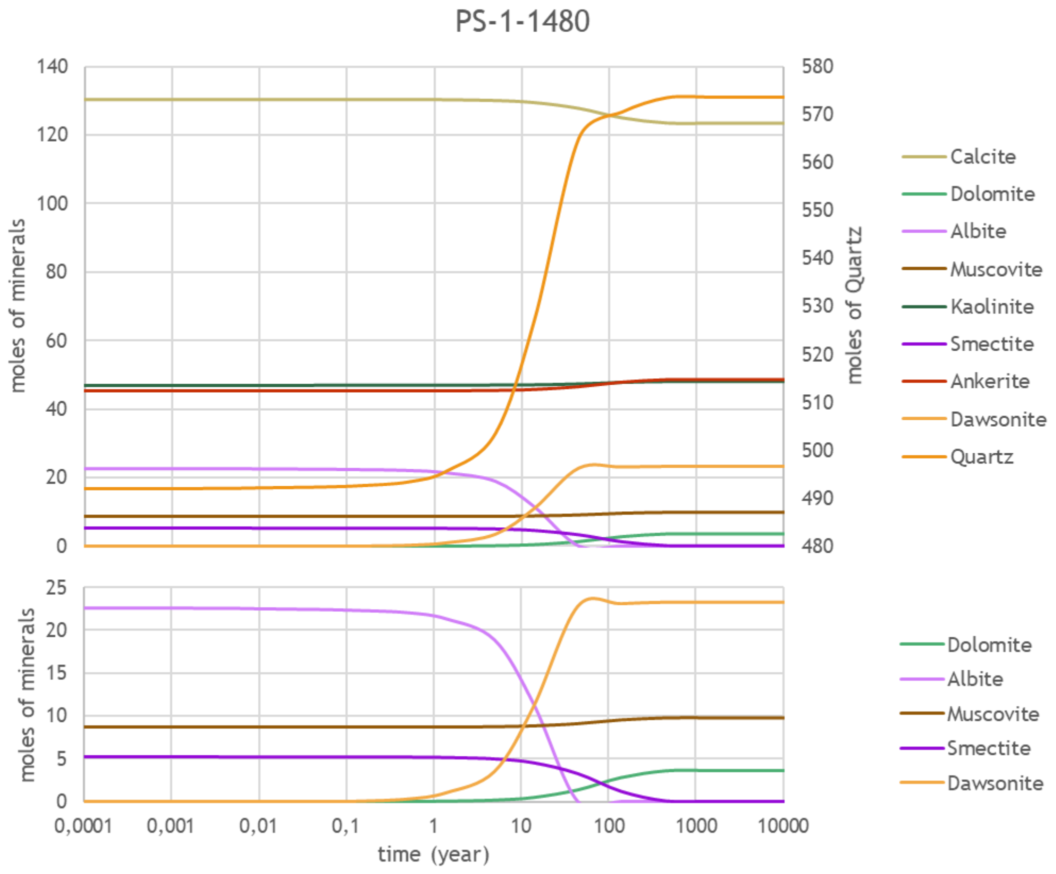

Figure H.7. Kinetic modelling results for sample ADK-PS-1-1480 from Akköy field

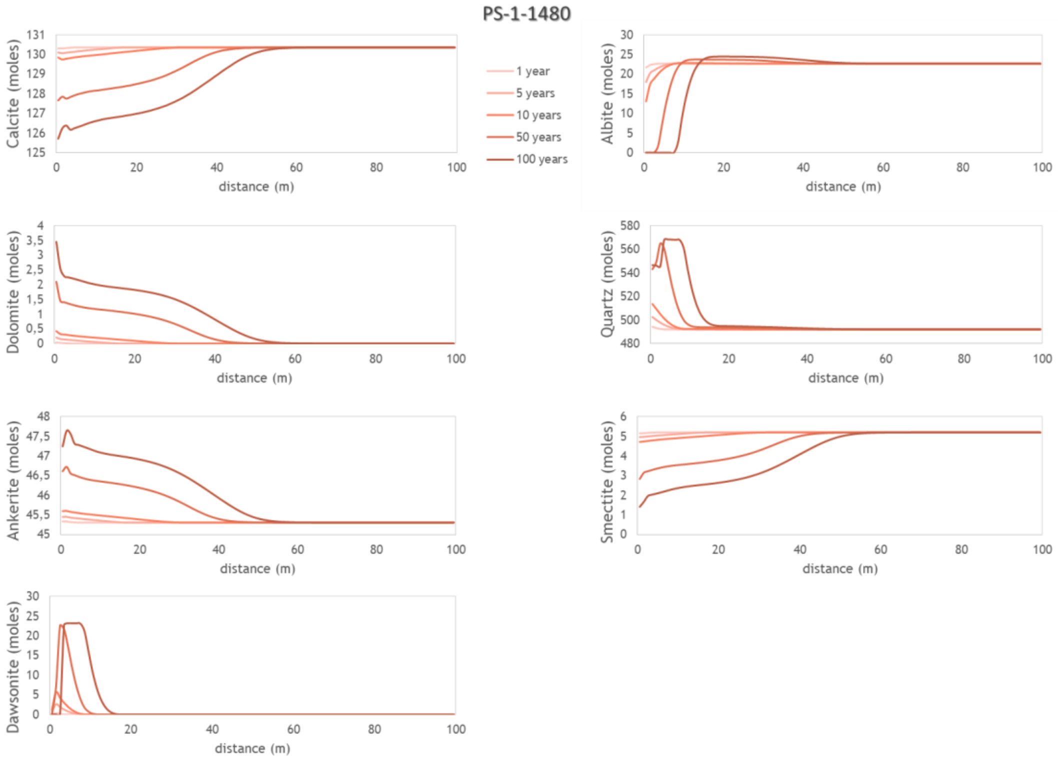

Figure H.8. Reactive transport modelling results for sample ADK-PS-1-1480 from Akköy field

Table H.9 Equilibrium modelling results for sample ADK-PS-1-1495 from Akköy field (values are as moles)

| **Mineral** | **PS-1-1495** | | |
|---|---|---|---|
| | **Initial** | **Final** | **Delta** |
| Albite | 0 | 0,002503 | 0 |
| Ankerite | 0 | 23,14 | 23,14 |
| Biotite | 11,79 | 20,98 | 9,19 |
| Calcite | 190,62 | 170,6 | -20,02 |
| Chlorite | 29,57 | 7,678 | -21,89 |
| Dolomite | 29,44 | 26,32 | -3,12 |
| Illite | 15,32 | 0 | -15,32 |
| Kaolinite | 25,12 | 60,02 | 34,90 |
| Muscovite | 0 | 0 | 0 |
| Orthoclase | 0 | 0 | 0 |
| Quartz | 346,43 | 324,5 | -21,93 |
| Smectite | 4,04 | 4,056 | 0,02 |
| Dawsonite | 0 | 0 | 0 |
| Magnesite | 0 | 0 | 0 |
| Siderite | 0 | 0 | 0 |

Table H.10 Equilibrium modelling results of the water sample PS-1.2018 reacting with sample ADK-PS-1-1495 (Akköy field)

| **mol/L** | **initial** | **final** |
|---|---|---|
| Al | 7,48E-07 | 4,79E-06 |
| Total C | 0,02945 | 0,006539 |
| Ca | 0,006629 | 0,0002712 |
| Cl | 0,002052 | 0,003198 |
| Fe | 6,27E-06 | 5,58E-07 |
| K | 0,003457 | 6,83E-06 |
| Mg | 0,002483 | 3,99E-05 |
| Na | 0,03068 | 0,04027 |
| $SO_4$ | 0,009349 | 0,01457 |
| Si | 0,0005351 | 0,001202 |

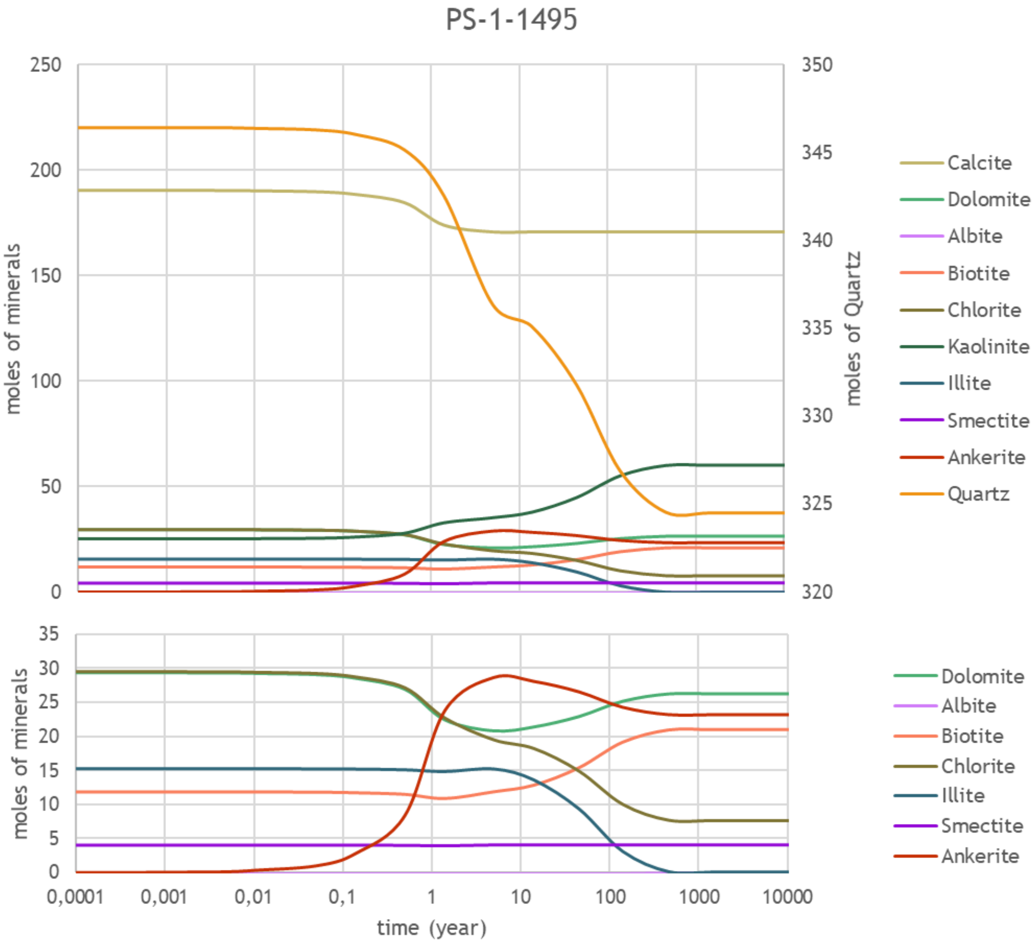

Figure H.9. Kinetic modelling results for sample ADK-PS-1-1495 from Akköy field

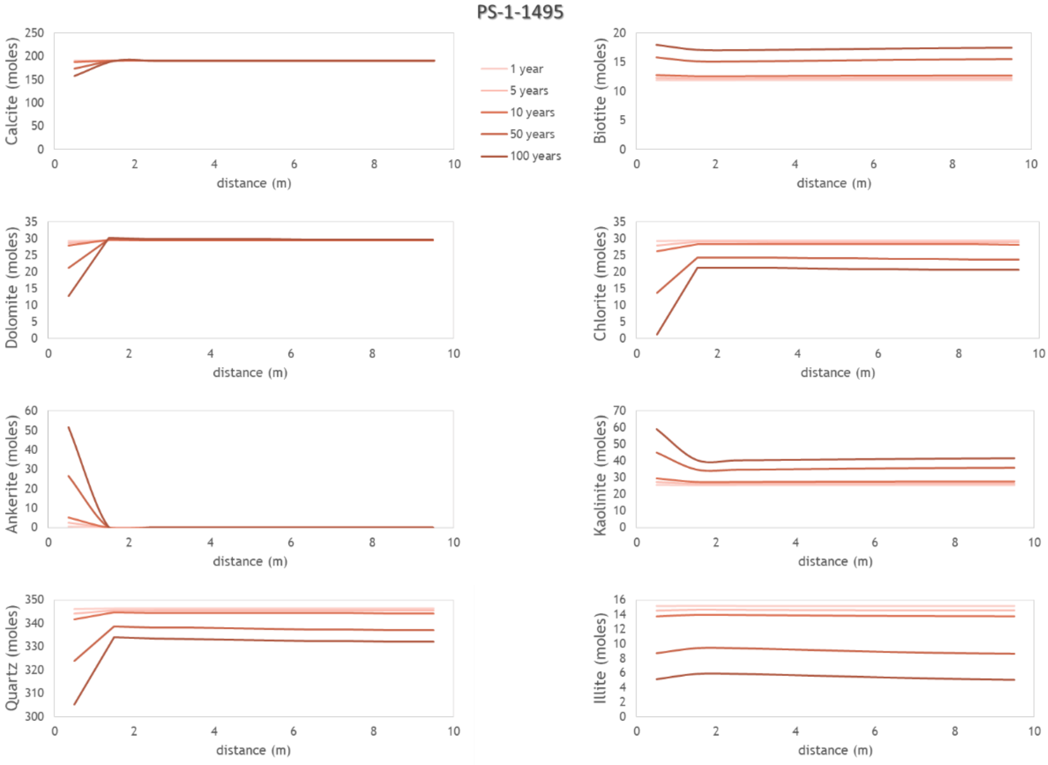

Figure H.10. Reactive transport modelling results for sample ADK-PS-1-1495 from Akköy field

Table H.11 Equilibrium modelling results for sample ADK-PS-2-1280 from Akköy field (values are as moles)

| **Mineral** | **PS-2-1280** | | |
|---|---|---|---|
| | **Initial** | **Final** | **Delta** |
| Albite | 0 | 0 | 0 |
| Ankerite | 60,29 | 63,97 | 3,68 |
| Biotite | 0 | 0 | 0 |
| Calcite | 204,93 | 198,7 | -6,23 |
| Chlorite | 0 | 0 | 0 |
| Dolomite | 0 | 2,667 | 2,67 |
| Illite | 15,91 | 21,61 | 5,70 |
| Kaolinite | 0 | 0 | 0 |
| Muscovite | 10,21 | 7,95 | -2,26 |
| Orthoclase | 0 | 0 | 0 |
| Quartz | 499,56 | 508 | 8,44 |
| Smectite | 5,77 | 0 | -5,77 |
| Dawsonite | 0 | 0,892 | 0,89 |
| Magnesite | 0 | 0 | 0 |
| Siderite | 0 | 0 | 0 |

Table H.12 Equilibrium modelling results of the water sample PS-1.2018 reacting with sample ADK-PS-2-1280 (Akköy field)

| **mol/L** | **initial** | **final** |
|---|---|---|
| Al | 7,48E-07 | 4,14E-05 |
| Total C | 0,02945 | 0,6607 |
| Ca | 0,006629 | 0,00756 |
| Cl | 0,002052 | 0,002001 |
| Fe | 6,27E-06 | 0,02123 |
| K | 0,003457 | 4,75E-11 |
| Mg | 0,002483 | 0,0006752 |
| Na | 0,03068 | 0,004066 |
| $SO_4$ | 0,009349 | 0,009115 |
| Si | 0,0005351 | 0,001169 |

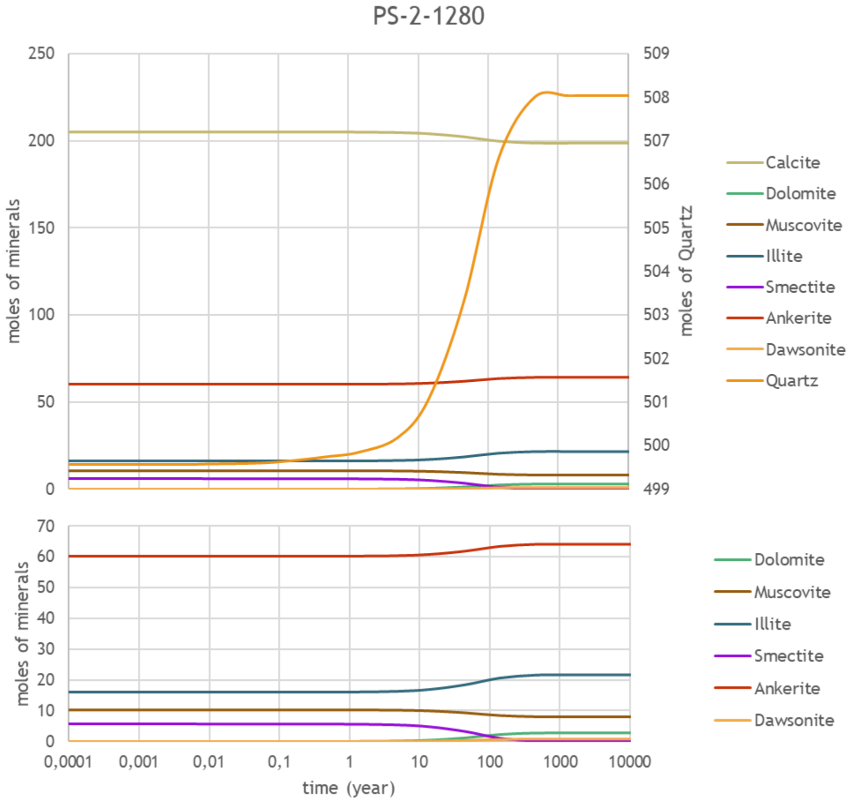

Figure H.11. Kinetic modelling results for sample ADK-PS-2-1280 from Akköy field

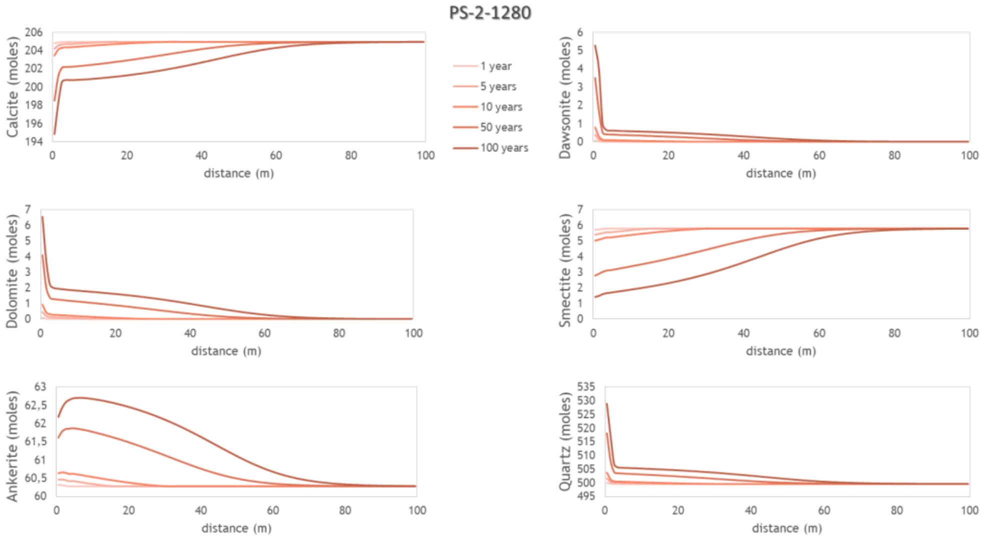

Figure H.12. Reactive transport modelling results for sample ADK-PS-2-1280 from Akköy field

Table H.13 Equilibrium modelling results for sample ADK-PS-2-1355 from Akköy field (values are as moles)

| Mineral | PS-2-1355 | | |
|---|---|---|---|
| | **Initial** | **Final** | **Delta** |
| Albite | 30,97 | 0,05782 | -30,91 |
| Ankerite | 0 | 0 | 0 |
| Biotite | 0 | 0 | 0 |
| Calcite | 418,91 | 418,9 | -0,01 |
| Chlorite | 0 | 0 | 0 |
| Dolomite | 32,31 | 32,31 | 0 |
| Illite | 0 | 0 | 0 |
| Kaolinite | 0 | 0 | 0 |
| Muscovite | 2,46 | 2,463 | 0 |
| Orthoclase | 0 | 0 | 0 |
| Quartz | 306,27 | 399 | 92,73 |
| Smectite | 0 | 0 | 0 |
| Dawsonite | 0 | 30,9 | 30,90 |
| Magnesite | 0 | 0 | 0 |
| Siderite | 0 | 0 | 0 |

Table H.14 Equilibrium modelling results of the water sample PS-1.2018 reacting with sample ADK-PS-2-1355 (Akköy field)

| mol/L | initial | final |
|---|---|---|
| Al | 7,48E-07 | 2,96E-06 |
| Total C | 0,02945 | 0,2687 |
| Ca | 0,006629 | 0,001271 |
| Cl | 0,002052 | 0,004627 |
| Fe | 6,27E-06 | 1,41E-05 |
| K | 0,003457 | 6,81E-07 |
| Mg | 0,002483 | 1,46E-04 |
| Na | 0,03068 | 0,09256 |
| $SO_4$ | 0,009349 | 0,02108 |
| Si | 0,0005351 | 0,001171 |

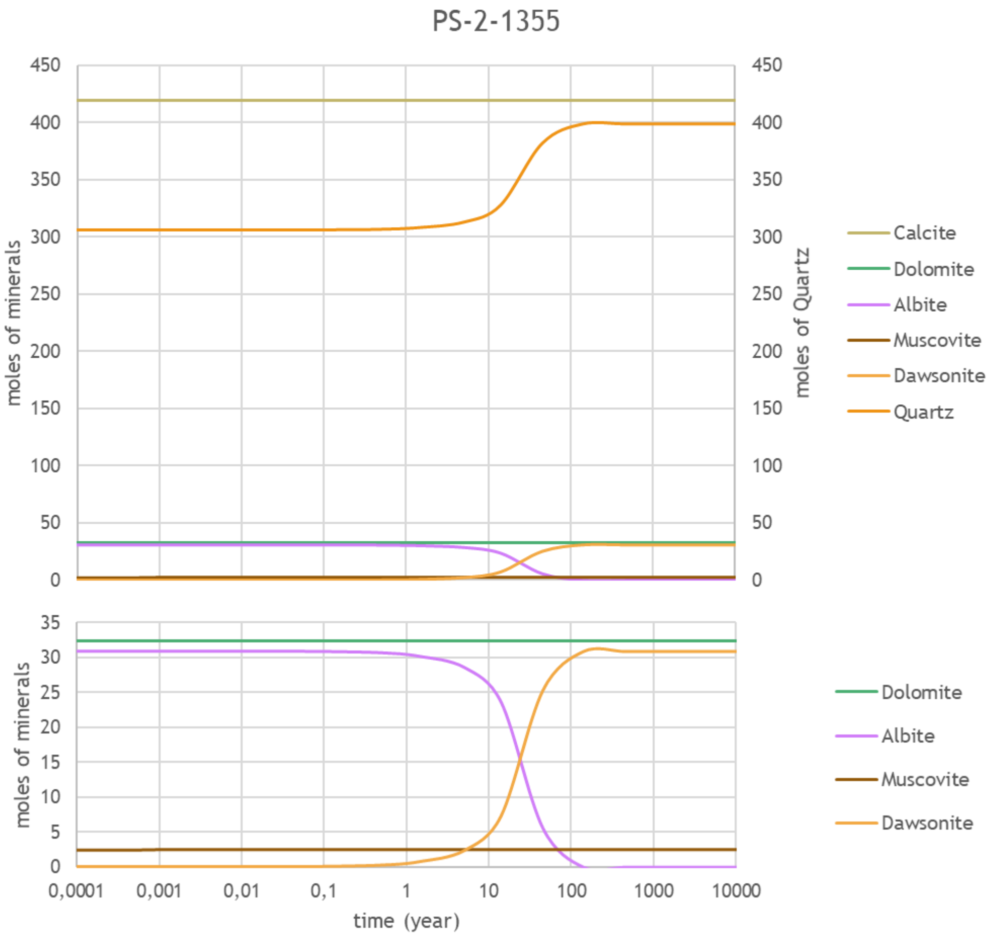

Figure H.13. Kinetic modelling results for sample ADK-PS-2-1355 from Akköy field

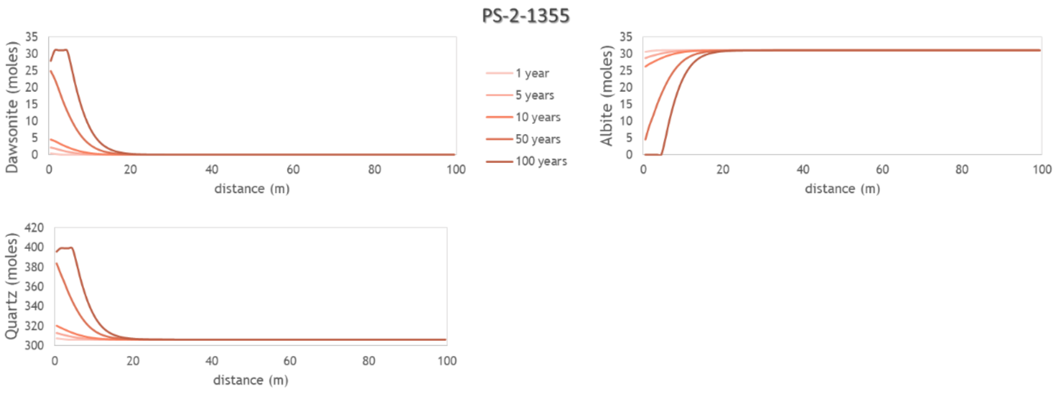

Figure H.14. Reactive transport modelling results for sample ADK-PS-2-1355 from Akköy field

Table H.15 Equilibrium modelling results for sample EDR-928 from Edremit field (values are as moles)

| **Mineral** | **EDR-928** | | |
|---|---|---|---|
| | **Initial** | **Final** | **Delta** |
| Albite | 43,11 | 43,03 | -0,08 |
| Amphibole | 0 | 0 | 0 |
| Biotite | 0 | 0 | 0 |
| Bytownite | 0 | 0 | 0 |
| Calcite | 20,88 | 17,24 | -3,64 |
| Chlorite | 0 | 0 | 0 |
| Dolomite | 3,12 | 6,76 | 3,64 |
| Illite | 14,56 | 0 | -14,56 |
| Kaolinite | 0 | 12,42 | 12,42 |
| Labradorite | 0 | 0 | 0 |
| Orthoclase | 26,28 | 35,01 | 8,73 |
| Quartz | 421,79 | 422 | 0,21 |
| Ankerite | 0 | 0 | 0 |
| Dawsonite | 0 | 0 | 0 |
| Magnesite | 0 | 0 | 0 |
| Siderite | 0 | 0 | 0 |

Table H.16 Equilibrium modelling results of the water sample EDJ-7 reacting with sample EDR-928 (Edremit field)

| **mol/L** | **initial** | **final** |
|---|---|---|
| Al | 3,26E-06 | 3,94E-06 |
| Total C | 6,07E-04 | 0,4418 |
| Ca | 9,74E-04 | 1,00E-04 |
| Cl | 0,001779 | 0,002185 |
| Fe | 1,42E-06 | 1,74E-06 |
| K | 1,46E-04 | 2,67E-03 |
| Mg | 4,12E-06 | 6,14E-06 |
| Na | 0,01071 | 0,1174 |
| $SO_4$ | 0,005211 | 0,006401 |
| Si | 0,0003739 | 0,001963 |

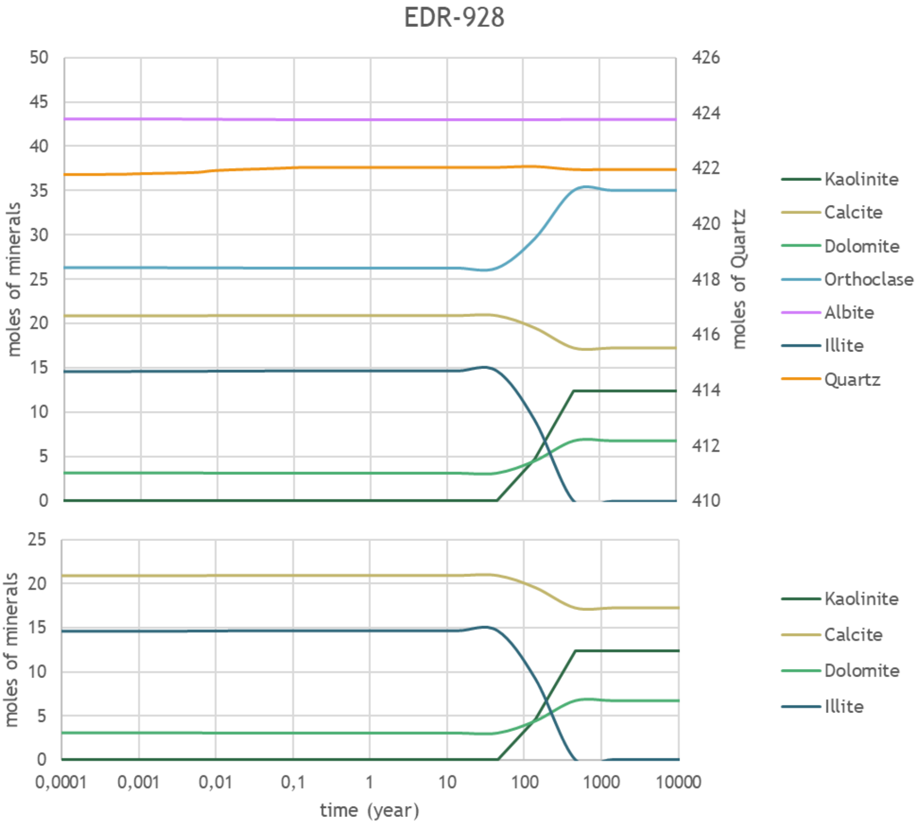

Figure H.15. Kinetic modelling results for sample EDR-928 from Edremit field

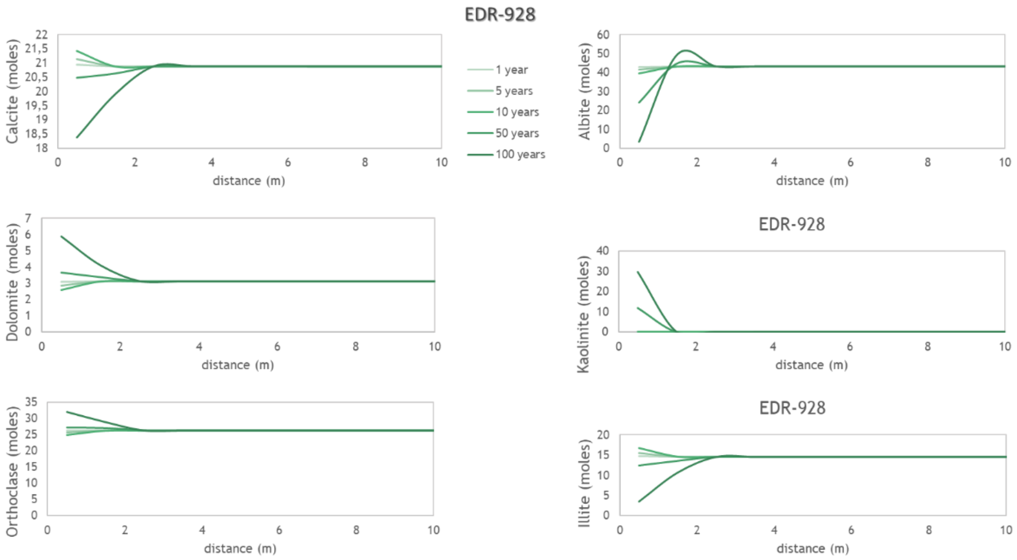

Figure H.16. Reactive transport modelling results for sample EDR-928 from Edremit field

Table H.17 Equilibrium modelling results for sample EDR-964 from Edremit field (values are as moles)

| **Mineral** | **EDR-964** | | |
|---|---|---|---|
| | **Initial** | **Final** | **Delta** |
| Albite | 0 | 0 | 0 |
| Amphibole | 0 | 0 | 0 |
| Biotite | 15,03 | 0 | -15,03 |
| Bytownite | 0 | 0 | 0 |
| Calcite | 0 | 0 | 0 |
| Chlorite | 0 | 0 | 0 |
| Dolomite | 0 | 0 | 0 |
| Illite | 10,89 | 10,9 | 0,01 |
| Kaolinite | 0 | 0 | 0 |
| Labradorite | 0 | 0 | 0 |
| Orthoclase | 38,48 | 53,48 | 15,00 |
| Quartz | 517,46 | 517,5 | 0,04 |
| Ankerite | 0 | 0 | 0 |
| Dawsonite | 0 | 0 | 0 |
| Magnesite | 0 | 45,08 | 45,08 |
| Siderite | 0 | 0 | 0 |

Table H.18 Equilibrium modelling results of the water sample EDJ-7 reacting with sample EDR-964 (Edremit field)

| **mol/L** | **initial** | **final** |
|---|---|---|
| Al | 3,26E-06 | 5,75E-07 |
| Total C | 6,07E-04 | 0,7205 |
| Ca | 9,74E-04 | 1,15E-04 |
| Cl | 0,001779 | 0,0014 |
| Fe | 1,42E-06 | 1,12E-06 |
| K | 1,46E-04 | 1,69E-02 |
| Mg | 4,12E-06 | 1,78E-03 |
| Na | 0,01071 | 0,008432 |
| $SO_4$ | 0,005211 | 0,004102 |
| Si | 0,0003739 | 0,001949 |

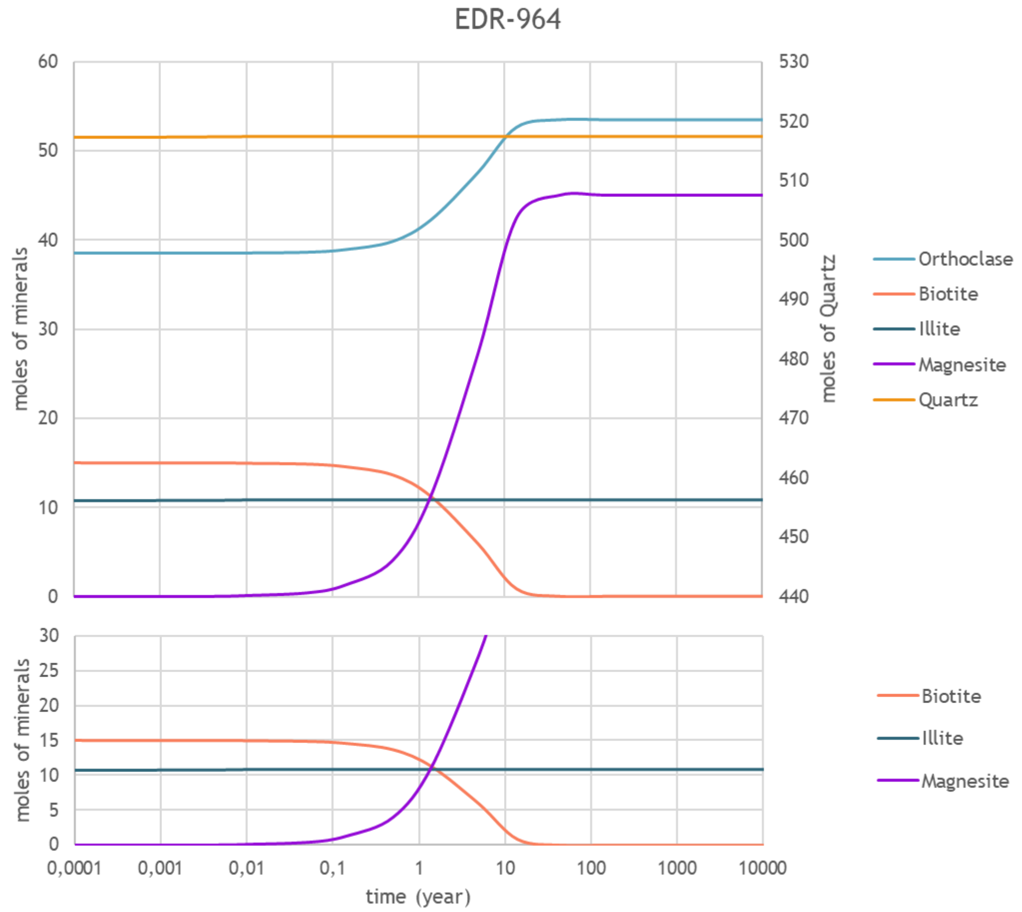

Figure H.17. Kinetic modelling results for sample EDR-964 from Edremit field

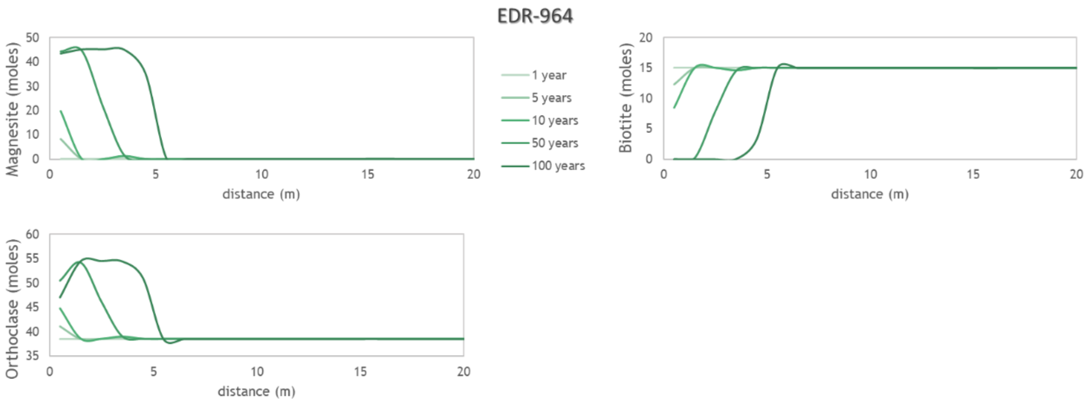

Figure H.18. Reactive transport modelling results for sample EDR-964 from Edremit field

Table H.19 Equilibrium modelling results for sample EDR-976 from Edremit field (values are as moles)

| Mineral | EDR-976 | | |
|---|---|---|---|
| | **Initial** | **Final** | **Delta** |
| Albite | 0,00 | 18,01 | 18,01 |
| Amphibole | 0,00 | 0 | 0,00 |
| Biotite | 0,00 | 0 | 0,00 |
| Bytownite | 0,00 | 0 | 0,00 |
| Calcite | 0,00 | 27 | 27,00 |
| Chlorite | 0,00 | 0 | 0,00 |
| Dolomite | 0,00 | 0 | 0,00 |
| Illite | 16,60 | 16,6 | 0,00 |
| Kaolinite | 19,03 | 46,03 | 27,00 |
| Labradorite | 57,28 | 12,27 | -45,01 |
| Orthoclase | 0,00 | 0 | 0,00 |
| Quartz | 422,66 | 422,6 | -0,06 |
| Ankerite | 0,00 | 0 | 0,00 |
| Dawsonite | 0,00 | 0 | 0,00 |
| Magnesite | 0,00 | 0 | 0,00 |
| Siderite | 0,00 | 0 | 0,00 |

Table H.20 Equilibrium modelling results of the water sample EDJ-7 reacting with sample EDR-976 (Edremit field)

| mol/L | initial | final |
|---|---|---|
| Al | 3,26E-06 | 4,23E-06 |
| Total C | 6,07E-04 | 4,32E-04 |
| Ca | 9,74E-04 | 1,43E-01 |
| Cl | 0,001779 | 0,06476 |
| Fe | 1,42E-06 | 5,16E-05 |
| K | 1,46E-04 | 5,73E-03 |
| Mg | 4,12E-06 | 3,25E-04 |
| Na | 0,01071 | 0,1492 |
| $SO_4$ | 0,005211 | 0,1897 |
| Si | 0,0003739 | 0,001964 |

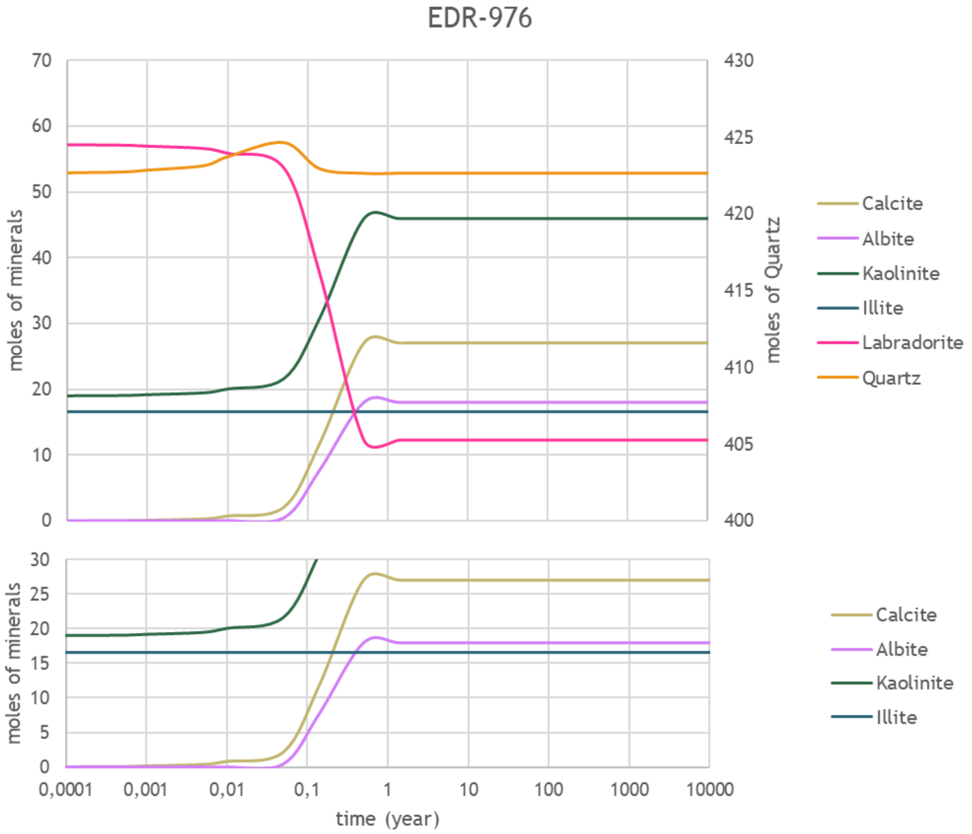

Figure H.19. Kinetic modelling results for sample EDR-976 from Edremit field

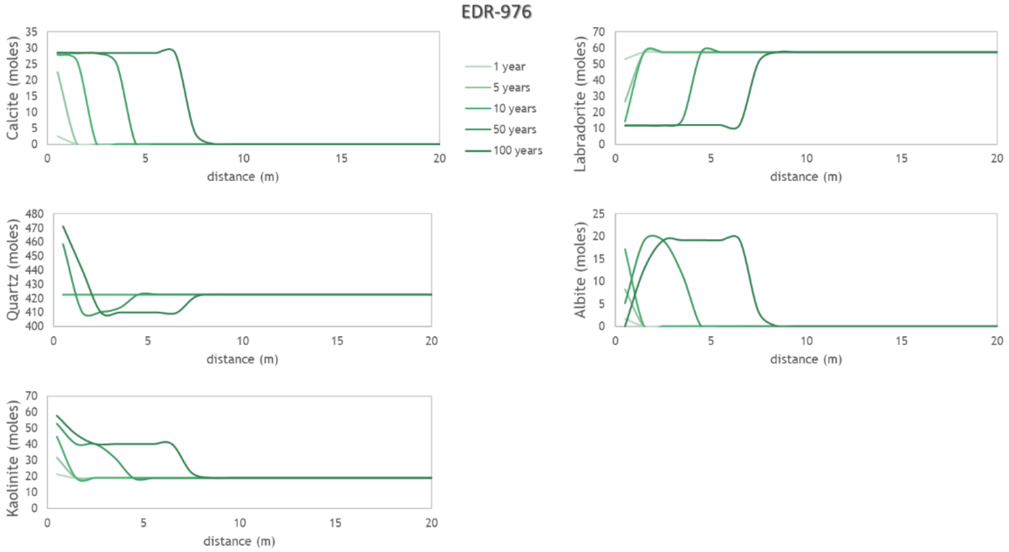

Figure H.20. Reactive transport modelling results for sample EDR-976 from Edremit field

Table H.21 Equilibrium modelling results for sample EDR-994 from Edremit field (values are as moles)

| **Mineral** | **EDR-994** | | |
|---|---|---|---|
| | **Initial** | **Final** | **Delta** |
| Albite | 0 | 10,46 | 10,46 |
| Amphibole | 3,63 | 0 | -3,63 |
| Biotite | 25,67 | 15,12 | -10,55 |
| Bytownite | 34,20 | 0 | -34,20 |
| Calcite | 0 | 0,2528 | 0,25 |
| Chlorite | 0 | 0 | 0 |
| Dolomite | 13,88 | 48,25 | 34,37 |
| Illite | 4,22 | 51,4 | 47,18 |
| Kaolinite | 9,11 | 0 | -9,11 |
| Labradorite | 0 | 0 | 0 |
| Orthoclase | 42,05 | 24,29 | -17,76 |
| Quartz | 181,76 | 185,4 | 3,64 |
| Ankerite | 0 | 0 | 0 |
| Dawsonite | 0 | 0 | 0 |
| Magnesite | 0 | 0 | 0 |
| Siderite | 0 | 0 | 0 |

Table H.22 Equilibrium modelling results of the water sample EDJ-7 reacting with sample EDR-994 (Edremit field)

| **mol/L** | **initial** | **final** |
|---|---|---|
| Al | 3,26E-06 | 1,31E-05 |
| Total C | 6,07E-04 | 1,58E-02 |
| Ca | 9,74E-04 | 8,99E-05 |
| Cl | 0,001779 | 2,42E-03 |
| Fe | 1,42E-06 | 1,93E-06 |
| K | 1,46E-04 | 5,79E-04 |
| Mg | 4,12E-06 | 1,79E-05 |
| Na | 0,01071 | 0,025 |
| $SO_4$ | 0,005211 | 0,007102 |
| Si | 0,0003739 | 0,001992 |

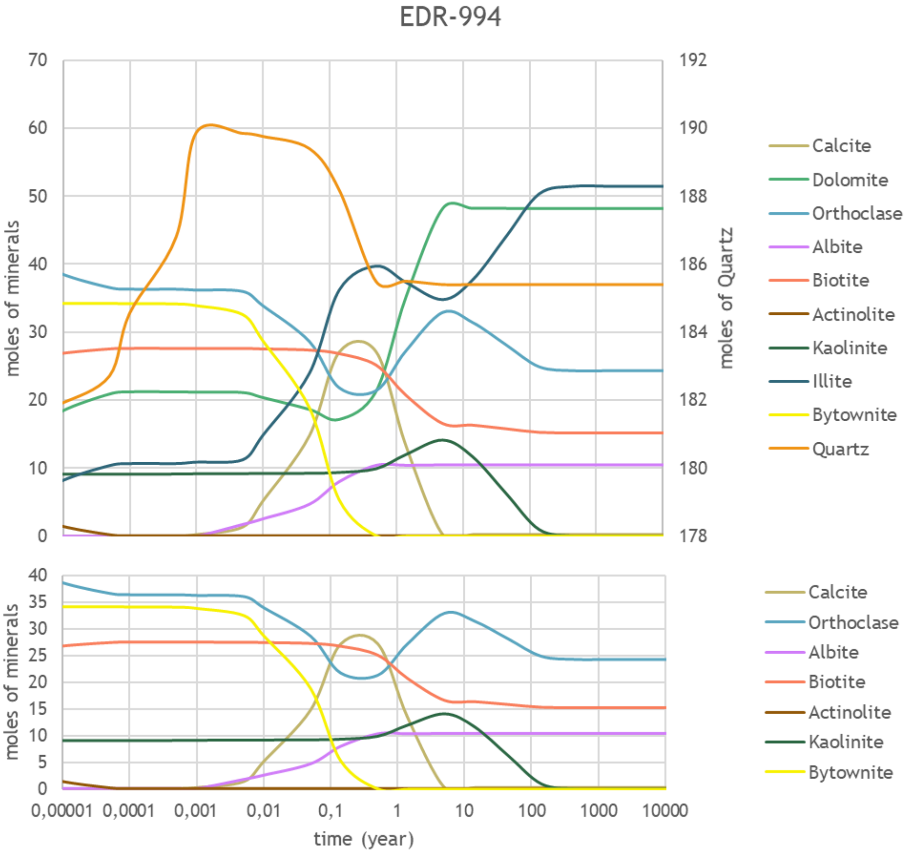

Figure H.21. Kinetic modelling results for sample EDR-994 from Edremit field

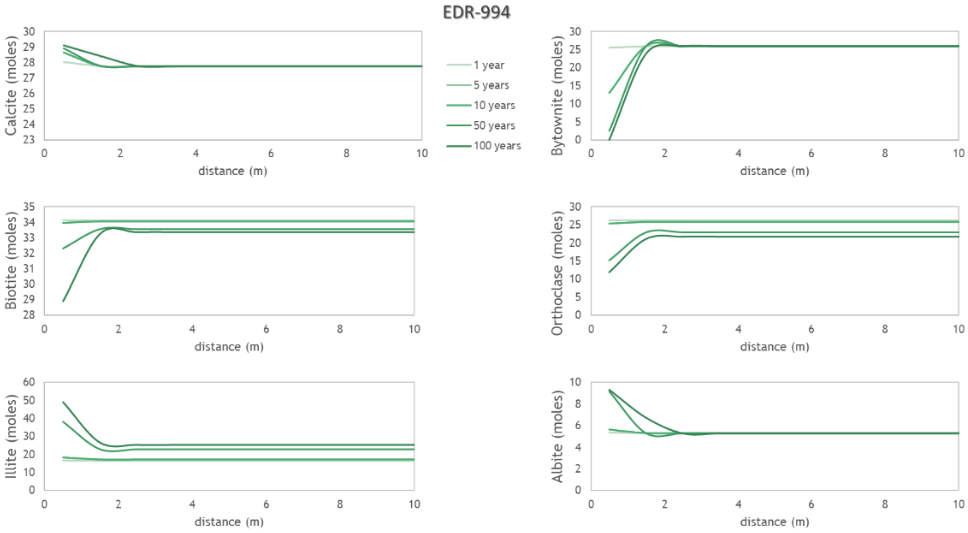

Figure H.22. Reactive transport modelling results for sample EDR-994 from Edremit field

Table H.23 Equilibrium modelling results for sample EDR-1032 from Edremit field (values are as moles)

| **Mineral** | **EDR-1032** | | |
|---|---|---|---|
| | **Initial** | **Final** | **Delta** |
| Albite | 0 | 0 | 0 |
| Amphibole | 0 | 0 | 0 |
| Biotite | 17,91 | 0 | -17,91 |
| Bytownite | 0 | 0 | 0 |
| Calcite | 6,26 | 0 | -6,26 |
| Chlorite | 0 | 0 | 0 |
| Dolomite | 9,07 | 15,33 | 6,26 |
| Illite | 0 | 0 | 0 |
| Kaolinite | 6,07 | 6,076 | 0 |
| Labradorite | 0 | 0 | 0 |
| Orthoclase | 93,86 | 111,8 | 17,94 |
| Quartz | 246,12 | 246,1 | -0,02 |
| Ankerite | 0 | 0 | 0 |
| Dawsonite | 0 | 0 | 0 |
| Magnesite | 0 | 47,47 | 47,47 |
| Siderite | 0 | 0 | 0 |

Table H.24 Equilibrium modelling results of the water sample EDJ-7 reacting with sample EDR-1032 (Edremit field)

| **mol/L** | **initial** | **final** |
|---|---|---|
| Al | 3,26E-06 | 8,25E-07 |
| Total C | 6,07E-04 | 2,06E-01 |
| Ca | 9,74E-04 | 8,00E-05 |
| Cl | 0,001779 | 1,35E-03 |
| Fe | 1,42E-06 | 1,07E-06 |
| K | 1,46E-04 | 9,62E-03 |
| Mg | 4,12E-06 | 1,55E-03 |
| Na | 0,01071 | 0,0081 |
| $SO_4$ | 0,005211 | 0,003941 |
| Si | 0,0003739 | 0,00195 |

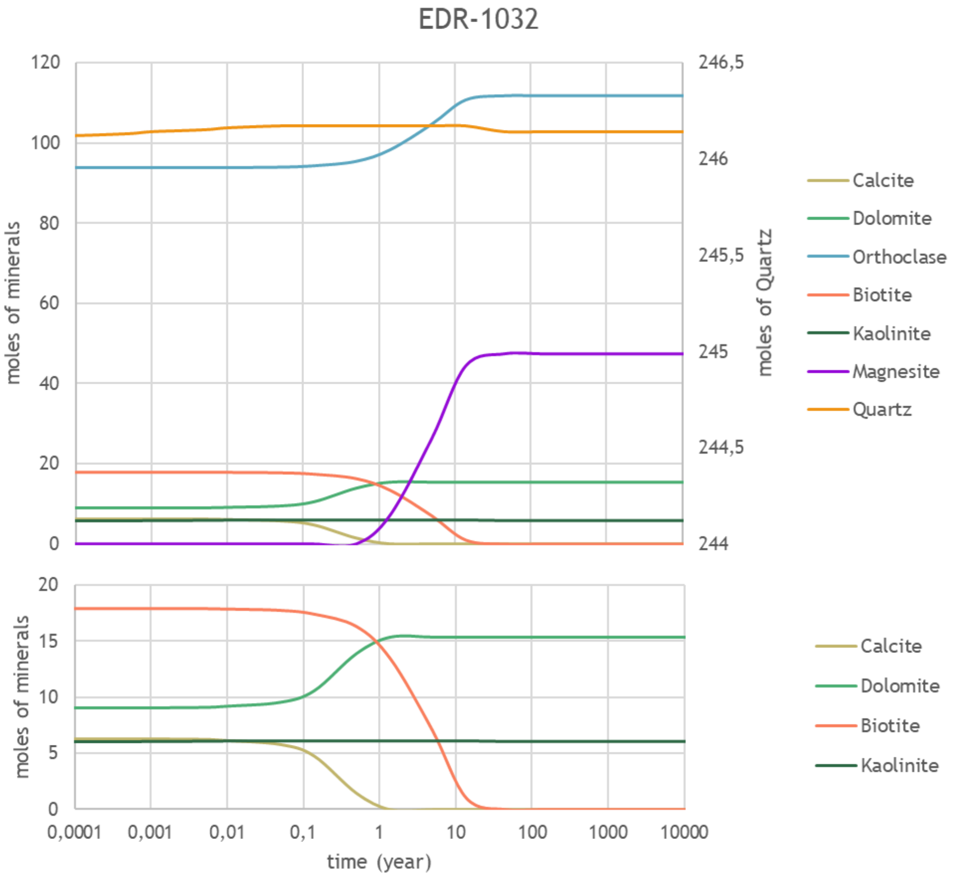

Figure H.23. Kinetic modelling results for sample EDR-1032 from Edremit field

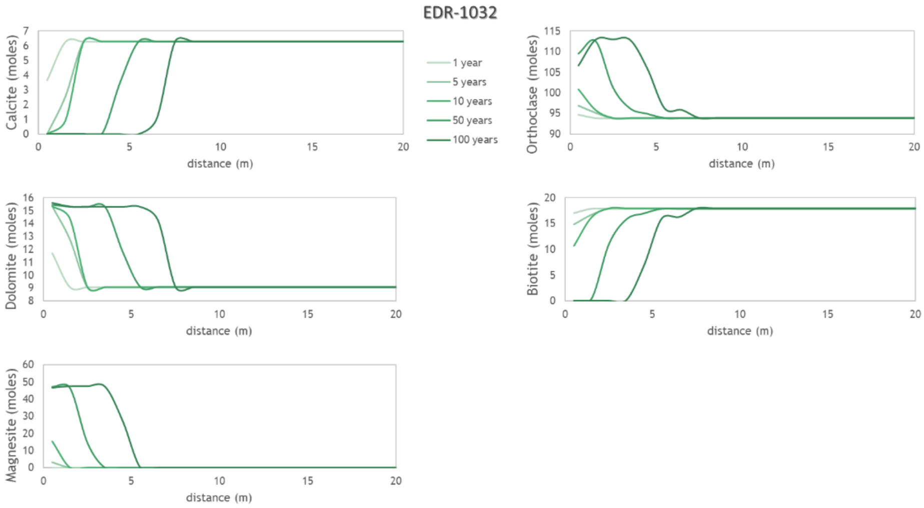

Figure H.24. Reactive transport modelling results for sample EDR-1032 from Edremit field

# CURRICULUM VITAE

Surname, Name: Elidemir, Sanem

## EDUCATION

| Degree | Institution | Year of Graduation |
|---|---|---|
| MS | METU Geological Engineering | 2014 |
| BS | METU Geological Engineering | 2011 |
| High School | Anıttepe Super High School, Ankara | 2006 |

## FOREIGN LANGUAGES

Advanced English, Intermediate French, Intermediate Italian, Beginner Japanese

## PUBLICATIONS

### Journal Papers

1. Elidemir, S., Güleç, N., Deniz, K. and Kadıoğlu, Y.K. (2022). Reservoir rock characterization in Edremit geothermal field: Geochemical implications for possible fault zones. *Applied Geochemistry 143*. DOI: https://doi.org/10.1016/j.apgeochem.2022.105388

2. Elidemir, S. and Güleç, N. (2018). Geochemical characterization of geothermal systems in western Anatolia (Turkey): implications for $CO_2$ trapping mechanisms in prospective $CO_2$-EGS sites. *Greenhouse Gases: Science and Technology 8, 63–76*. DOI: 10.1002/ghg.1747

### Conference Papers

1. Elidemir, S., Güleç, N., Deniz, K., and Kadıoğlu, Y. K. (2023) Implications for Possible Fault Zones Deduced from Lithogeochemical Characterization of Reservoir Levels of a Geothermal Field: Edremit Example, EGU General Assembly 2023, Vienna, Austria, 24–28 Apr 2023, EGU23-545, https://doi.org/10.5194/egusphere-egu23-545

2. Elidemir, S. and Güleç, N. (2021). Olası $CO_2$ Depolama Sahaları Olarak Akköy ve Edremit Jeotermal Sistemlerindeki Akışkan - Kayaç Etkileşimlerinin Jeokimyasal Modellemesi: Ön Çalışma Sonuçları/Geochemical Modelling of Fluid-Rock Interactions in Akköy and Edremit Geothermal Fields as Prospective $CO_2$ Storage Sites: Results of a Preliminary Study: *73rd Geological Congress of Turkey* (Online), 24-28 May 2021, Ankara, Turkey

3. Elidemir, S. and Güleç, N. (2020). Lithogeochemical Characterization of Akkoy and Edremit Geothermal Fields as Prospective $CO_2$ Storage Sites: A Preliminary Study: *EGU General Assembly 2020*, Online, 4-8 May 2020, EGU2020-452, DOI: 10.5194/egusphere-egu2020-452

4. Elidemir, S. and Güleç, N. (2020). Water-Rock Interactions in Geothermal Systems in the Framework of $CO_2$ Storage: *European Geothermal PhD Days-2020*, 24-26 February 2020, Denizli, Turkey

5. Elidemir, S. and Güleç, N. (2019). Geochemical Modelling of Fluid-Rock Interactions in Adaköy and Edremit Geothermal Fields as Prospective $CO_2$ Storage Sites: A Preliminary Study: *14th $CO_2$ GeoNet Open Forum*, 6-9 May 2019, Venice, Italy

6. Elidemir, S. and Güleç, N. (2017). Geothermal Systems as Natural Analogues for Geological Storage of $CO_2$: Implications for Trapping Mechanisms from Hydrogeochemistry of Western Anatolian Fluids (Turkey): *Goldschmidt 2017*, 13-18 August 2017, Paris, France (Goldschmidt Abstracts, 2017 1051)

7. Elidemir, S. and Güleç, N. (2016). Geochemical Characterization of Geothermal Systems in Turkey as Natural Analogues for Geological Storage of $CO_2$: *7th Geochemistry Symposium with International Participation*, 16-18 May 2016, Antalya, Turkey (Abstract Book p.213-214)